

Fe-Mg interdiffusion at high pressures
in mineral phases
relevant for the Earth's mantle

Inaugural-Dissertation
zur
Erlangung des Doktorgrades
der Mathematisch-Naturwissenschaftlichen Fakultät
der Universität zu Köln

vorgelegt von
Christian Holzapfel
aus Köln

Köln, 2004

Berichterstatter: Prof. Dr. H. Palme
Prof. Dr. D. C. Rubie
Prof. Dr. L. Bohaty
Tag der mündlichen Prüfung: 28.5.2004

Contents

Zusammenfassung	7
Abstract	15
1 Introduction	19
1.1 Motivation	19
1.2 Theory of diffusion	22
1.2.1 Definition of diffusion	22
1.2.2 Macroscopic theory of diffusion	22
1.2.3 Microscopic theory of diffusion	23
1.2.4 Oxygen fugacity dependence	26
1.2.5 Temperature dependence of diffusion	27
1.2.6 Pressure dependence of diffusion	28
1.2.7 Direction dependence of diffusion	29
1.3 Mineralogical model of the Earth's mantle	30
1.3.1 Phase stabilities and structures	30
1.3.2 Summary of existing diffusion data	34
1.4 Aims of the present study	38
2 Experimental Techniques	41
2.1 Introduction	41
2.2 High pressure experiments: Multi anvil technique	42
2.3 Diffusion Couples	43
2.3.1 Diffusion couples: General remarks	43

2.3.2	Diffusion couples: Olivine	45
2.3.3	Diffusion couples: Wadsleyite	46
2.3.4	Diffusion couples: Ferropericlasite	46
2.3.5	Diffusion couples: (Mg,Fe)SiO ₃ perovskite	48
2.4	Capsules	50
2.5	Assemblies used for high pressure diffusion experiments	53
3	Chemical analysis of diffusion profiles	59
3.1	Choice of analysis techniques	59
3.2	Electron microprobe analysis (EPMA)	60
3.3	Transmission electron microscopy	62
4	Mathematical treatment of diffusion profiles	67
4.1	General remarks	67
4.2	Two semi-infinite media, D constant	68
4.3	Semi-infinite media, D concentration-dependent	71
4.3.1	Boltzmann-Matano analysis	71
4.3.2	Numerical simulations: Finite difference method	73
5	Results	81
5.1	Introduction	81
5.2	Olivine	84
5.2.1	Conditions of experiments	84
5.2.2	Characterization of diffusion couples after the experiments	85
5.2.3	Profiles and diffusion coefficients	88
5.2.4	Pressure dependence at constant temperature (1673 K)	93
5.2.5	Temperature dependence at constant pressure (12 GPa)	98
5.2.6	Model of diffusion in olivine	104
5.2.7	Comparison with previous results	105
5.3	Wadsleyite	109
5.3.1	Conditions of experiments	109

5.3.2	Backscatter images and sample characterization	110
5.3.3	Profiles	113
5.3.4	Temperature dependence at 15 GPa	115
5.3.5	Summary: Fe-Mg interdiffusion in wadsleyite	119
5.4	Ferropericlae	121
5.4.1	Conditions of experiments	121
5.4.2	Sample characterization	122
5.4.3	Profiles and diffusion coefficients	123
5.4.4	Pressure dependence at constant temperature	128
5.4.5	Temperature dependence at constant pressure	129
5.4.6	Oxygen fugacity	132
5.4.7	Summary: Ferropericlae	132
5.5	(Fe _x Mg _{1-x})SiO ₃ Perovskite	135
5.5.1	Introduction, conditions of experiments	135
5.5.2	SEM and EPMA investigations of perovskite diffusion experiments . . .	135
5.5.3	TEM characterization of the samples	142
5.5.4	Profiles and diffusion coefficients	144
5.5.5	Temperature dependence of Fe-Mg interdiffusion at 24 GPa	150
5.6	Overview	154
5.7	Experimental complications	155
5.7.1	High pressure versus low pressure experiments	155
5.7.2	Temperature gradients	155
5.7.3	Heating effects	157
6	Discussion	159
6.1	Introduction	159
6.2	Extrapolations towards lower mantle conditions	160
6.2.1	Ferropericlae	160
6.2.2	Silicate perovskite	162
6.3	Fe-Mg interdiffusion along a present day geotherm	163

6.4	Time scales of Fe-Mg partitioning experiments	167
6.5	Applications to geological problems	169
6.5.1	Kinetics of the olivine-wadsleyite phase boundary	169
6.5.2	Two-phase aggregates	172
6.5.3	Reequilibration in the lower mantle	178
6.5.4	Interaction at the core-mantle boundary	182
6.5.5	Interaction during core formation	185
7	Conclusions	191
A	Multianvil Technique	193
B	TEMQuant: Quantifying EDX-TEM analysis	199
B.1	Principles of the program	199
B.2	Source code of TEMQuant	200
B.2.1	Header file of class TEMQuant	200
B.2.2	Definition of class methods for class TEMQuant	201
B.2.3	Main function	213
C	Finite difference simulation	215
C.1	Introduction	215
C.2	Source code	216
D	Example profile analyses	227
E	Example EDX-spectra of silicate perovskite	249
	Bibliography	252
	Index	272

Zusammenfassung

Zur Quantifizierung der Kinetik vieler Prozesse, wie z.B. Reäquilibration subduzierter Platten oder Phasenumwandlungen mehrkomponentiger Systeme, ist die Kenntnis von Diffusionskoeffizienten als Funktion von Druck (P), Temperatur (T), und Sauerstoffugazität (fO_2) unabdingbar. In dieser Arbeit werden Experimente zur Bestimmung von Fe-Mg Interdiffusionskoeffizienten D_{Fe-Mg} bei Drücken zwischen 6 und 23 GPa und Temperaturen von 1653 bis 2273 K bei reduzierenden und oxidierenden Bedingungen beschrieben. Dabei wurden Diffusionspaare von Mineralen, die einen wesentlichen Anteil am Mineralbestand des Erdmantels haben, untersucht: Olivin, Wadsleyit, Ferroperiklas und Silikat-Perowskit. Die wesentlichen Zielsetzungen der Arbeit lauteten:

- Bestimmung von Fe-Mg Interdiffusionskoeffizienten in Olivin im gesamten Druck-Stabilitätsbereich. Außerdem sollten Diffusionskoeffizienten der Spurenelemente Ni und Mn bestimmt werden
- Bestimmung der Aktivierungsenergie von Wadsleyit
- Bestimmung von Fe-Mg Interdiffusionskoeffizienten für Ferroperiklas, die zweithäufigste Phase des unteren Erdmantels
- Bestimmung von Fe-Mg Interdiffusionskoeffizienten für $(Fe,Mg)SiO_3$ Perowskit, der häufigsten Phase des unteren Erdmantels

Diffusion unter hohen Drücken kann im wesentlichen durch die folgende Gleichung beschrieben werden:

$$D = D_0 (fO_2)^{\frac{1}{n}} \exp(A X) \exp\left(-\frac{E_a - P\Delta V_a}{R T}\right), \quad (1)$$

wobei D den Diffusionskoeffizienten, D_0 den präexponentiellen Faktor, f_{O_2} die Sauerstoffugazität, n den Sauerstoffugazitätskoeffizienten, A den Koeffizienten der Zusammensetzungsabhängigkeit, E_a die Aktivierungsenergie, ΔV_a das Aktivierungsvolumen, P den Druck, T die Temperatur und R die Gaskonstante bezeichnen.

Die Hochdruckexperimente dieser Arbeit wurden mit der Vielstempel-Technologie (multi-anvil apparatus) am Bayerischen Geoinstitut in Bayreuth durchgeführt. Die Probe befindet sich in einem Oktaeder aus MgO, der innerhalb eines Satzes von 8 WC-Würfeln mit abgeschrägten Ecken komprimiert wird. Die charakteristischen Größen, die das Volumen der Proben und den maximal erreichbaren Druck charakterisieren sind die Kantenlänge K_o des Oktaeders und K_a der Abschrägungen des Würfels. Daher werden die verwendeten Oktaeder mit dem Tupel K_o/K_a bezeichnet. In dieser Arbeit wurden Oktaeder mit den Geometrien 18/11, 14/8 und 10/4 verwendet. Zum Heizen wurde eine Widerstandsheizung aus LaCrO_3 verwendet. Die Temperatur wurde während der Experimente mit einem W_{97}Re_3 - $\text{W}_{75}\text{Re}_{25}$ Thermoelement gemessen.

Für die Herstellung der Diffusionspaare von Olivin wurden für jeden Versuch ein Diffusionspaar aus denselben, in c -Richtung orientierten Einkristallen verwendet. Der Mg-reiche Kristall war ein synthetischer Forsterit und der Fe-reiche Kristall ein San Carlos Olivin mit $X_{\text{Fe}_2\text{SiO}_4} = 0.06$ ($X_{\text{Fe}_2\text{SiO}_4}$ bezeichnet den Molenbruch der Fayalit-Komponente im Olivin). Auch die Diffusionspaare von Ferroperiklas wurden aus Einkristallen hergestellt. Eisenhaltige (Mg,Fe)O Einkristalle mit einem nominalen Gehalt von $X_{\text{FeO}} = 0.07$ und $X_{\text{FeO}} = 0.35$ sind vor den Diffusionsversuchen von S. Mackwell mit dem in Holzapfel et al. (2003) beschriebenen Verfahren synthetisiert worden. Für Wadsleyit und Silikatperowskit wurden polykristalline Proben vor den eigentlichen Diffusionsversuchen synthetisiert, da es keine natürlichen Proben gibt und eine Einkristallsynthese nicht erfolgreich war.

Da der Diffusionskoeffizient nach Gleichung 1 von der Sauerstoffugazität abhängt, wurden im wesentlichen Kapselmaterialien verwendet, die eine Charakterisierung der Sauerstoffugazität während des Experiments zulassen. Zum einen wurden daher Ni-Kapseln mit einer Zugabe von NiO benutzt, die die Sauerstoffugazität nahe des Ni-NiO Gleichgewichts puffern. Desweiteren wurden bei den Perowskit-Versuchen auch MgO-Einkristallkapseln mit einer zusätzlichen Fe-Folie eingesetzt. Die Sauerstoffugazität ist dann durch die Lösung von FeO in MgO bestimmt.

Nur für einige Versuche mit Olivin wurden auch Au-Kapseln wie bei Chakraborty et al. (1999) verwendet. Die Redox-Bedingungen, die in diesen Kapseln vorherrschen, wurden durch Vergleich mit den Resultaten von Experimenten in Ni-NiO-Kapseln charakterisiert.

Nach den Hochdruckversuchen wurden die Diffusionspaare zur Messung mit mikroanalytischen Verfahren im Querschliff freigelegt. Für Profillängen größer als $8 \mu\text{m}$ wurde die Elektronenstrahl-Mikrosonde eingesetzt (EPMA). Bei einigen Proben, insbesondere bei Silikatperowskit, waren die Profile kürzer als die Auflösung die mit EPMA erreicht werden kann. Daher wurden diese Proben für transmissionselektronenmikroskopische Untersuchungen (TEM) gedünnt. Im Rastermodus (STEM) wurden dann Profilanalysen mit einem EDX-Detektor durchgeführt (EDX-STEM).

Aus den gemessenen Profilen wurden die Diffusionskoeffizienten mit Hilfe unterschiedlicher mathematischer Verfahren bestimmt. Für Olivin und Silikat-Perowskit wurden im wesentlichen symmetrische Profile beobachtet, die mit einer analytischen Lösung der Diffusionsgleichung für konzentrationsunabhängige Diffusion angepasst wurden. Konzentrationsabhängige Diffusion führte im Fall von Ferroperiklas und Wadsleyit zu asymmetrischen Profilen, für die keine analytische Lösung existiert. In diesem Fall wurden die Profile numerisch mit Hilfe der finiten Differenzmethode simuliert. Wadsleyit und Ferroperiklas mit $X_{FeO} > 0.07$ zeigen eine exponentielle Konzentrationsabhängigkeit des Diffusionskoeffizienten. Nur im Fall von Ferroperiklas mit $X_{FeO} < 0.07$ mußte nach Mackwell et al. (2004) ein zusätzlicher Term in die Konzentrationsabhängigkeit des Diffusionskoeffizienten eingeführt werden.

Für Olivin wird im wesentlichen eine lineare Abnahme des Fe-Mg Interdiffusionskoeffizienten bis 12 GPa beobachtet. Die Fe-Mg Interdiffusionskoeffizienten, die in Ni-NiO Kapseln beobachtet wurden, sind im Rahmen des Fehlers identisch mit den Ergebnissen von Versuchen in Au-Kapseln. Daher kann geschlussfolgert werden, daß die Sauerstoffugazität, die charakteristisch für die Goldkapseln ist, nahe bei der des Ni-NiO Puffers liegt. Eine Meßreihe mit Olivin bei 12 GPa und zwischen 1623 K und 1823 K ist ebenfalls kompatibel mit der Aktivierungsenergie bei 1 bar und einer Sauerstoffugazität nahe des Ni-NiO Puffers. Das Aktivierungsvolumen entlang des Ni-NiO Puffers ist $5.6 \pm 0.5 \text{ cm}^3 \text{ mol}^{-1}$. Wenn man die Sauerstoffugazität des Ni-NiO Puffers als Funktion von Druck und Temperatur mit der Annahme eines konstanten Reak-

tionsvolumens der Oxidationsreaktion von Ni berücksichtigt, erhält man ein Aktivierungsvolumen von $7.3 \pm 1.0 \text{ cm}^3 \text{ mol}^{-1}$ bei konstanter Sauerstoffugazität.

Fe-Mg Interdiffusion in Wadsleyit ist wesentlich schneller als in Olivin, wie auch schon bei Chakraborty et al. (1999) und Farber et al. (2000) beobachtet worden ist. In dieser Arbeit wird ein Sprung der Diffusivität um nahezu 4 Größenordnungen bei Bedingungen der 410 km Diskontinuität beobachtet. Die Aktivierungsenergie bei 15 GPa beträgt $260 \pm 30 \text{ kJ mol}^{-1}$ (ohne Korrektur für den Effekt der Sauerstoffugazität des Ni-NiO Puffers).

Für Ferroperiklas wurden Experimente zwischen 8 und 23 GPa bei 1663 K bis 2073 K durchgeführt. Die Ergebnisse sind in Übereinstimmung mit Experimenten bei 1 bar (Mackwell et al., 2004). Für Sauerstoffugazitäten entlang des Ni-NiO-Puffers wurde ein Aktivierungsvolumen von $3.3 \pm 0.1 \text{ cm}^3 \text{ mol}^{-1}$ und eine Aktivierungsenergie von 255 kJ mol^{-1} bestimmt. Das Aktivierungsvolumen bei konstanter Sauerstoffugazität beträgt $5 \pm 1 \text{ cm}^3 \text{ mol}^{-1}$. Die Zusammensetzungsabhängigkeit kann im Bereich zwischen 7 und 35 mol%, übereinstimmend mit Mackwell et al. (2004) mit einem exponentiellen Ansatz beschrieben werden: $D_{Fe-Mg} \propto \exp((132 \pm 13) \text{ kJ mol}^{-1} X_{FeO}/(RT))$.

Silikat-Perowskit zeigt deutlich niedrigere Diffusionskoeffizienten als die anderen betrachteten Systeme. Der präexponentielle Faktor bei Sauerstoffugazitäten entsprechend des Ni-NiO Puffers ist $(5.1 \pm 2.0) \times 10^{-8} \text{ m}^2 \text{ sec}^{-1}$ und die Aktivierungsenergie $404 \pm 144 \text{ kJ mol}^{-1}$. Damit sind die Diffusionskoeffizienten des Silikatperowskits, der die Hauptphase des unteren Erdmantels bildet, bei denselben P, T und fO_2 -Bedingungen um etwa einen Faktor 2×10^4 kleiner als die von Ferroperiklas. Weil Ferroperiklas nur ungefähr 20 vol% des unteren Erdmantels einnimmt, werden kinetische Prozesse, die durch Fe-Mg Interdiffusion bestimmt werden, dominiert durch D_{Fe-Mg} von Perowskit. Simulationen in Verbindung mit theoretischen Modellen zeigen, daß der effektive Diffusionskoeffizient des unteren Erdmantels $\sim 2.4 \times D_{pvsk}$ beträgt.

Die in dieser Arbeit bestimmten Diffusionskoeffizienten können in einer vielseitigen Weise zur Quantifizierung kinetischer Prozesse, die in der Erde ablaufen oder abgelaufen sind verwendet werden. Dabei verlaufen Prozesse, die von der Geschwindigkeit des Fe-Mg Austausches abhängen, am schnellsten im Stabilitätsfeld von Wadsleyit und Ringwoodit (410 - 670 km Tiefe). Olivin im oberen Mantel besitzt deutlich kleinere Diffusionskoeffizienten. Bei 12

GPa führt der Druckeffekt zu einer Verringerung der Diffusivität von Olivin um etwa zwei Größenordnungen im Vergleich zu $D_{\text{Fe-Mg}}$ bei 1 bar und derselben Temperatur. Daher sollte für kinetische Modellierungen der Druckeffekt nicht vernachlässigt werden. Modellierungen der Kinetik der Phasenumwandlung von Olivin nach Wadsleyit oder umgekehrt während Konvektion durch die 410 km Diskontinuität zeigen, dass die Diffusionskoeffizienten groß genug sind, um bei einer Konvektionsgeschwindigkeit von 5 cm/Jahr für eine Gleichgewichtseinstellung zu sorgen. Allerdings kann es bei deutlich niedrigeren Temperaturen zu einem metastabilen Überschreiten der Gleichgewichtsphasengrenzen und damit zu einer Verbreiterung der Diskontinuität kommen.

Für den unteren Erdmantel ($P > 23$ GPa) kann die Druckabhängigkeit der Fe-Mg Interdiffusion für Ferroperiklas mit Hilfe von ab initio Berechnungen für Migrations-Enthalpien und -Entropien von Ita and Cohen (1997) abgeschätzt werden. Allerdings wird bei diesen Abschätzungen vorausgesetzt, dass bzgl. der Druckabhängigkeit die Berechnung für Mg Selbstdiffusion zumindest annähernd auch für Fe-Mg Interdiffusion gelten. Es zeigt sich, dass nach Ita and Cohen (1997) die Druckabhängigkeit des präexponentiellen Vorfaktors vernachlässigbar ist. Damit kann die Druckabhängigkeit von ΔV_a mit einem einfachen quadratischen Ansatz beschrieben werden. Die Extrapolation des Fe-Mg Interdiffusionskoeffizienten führt entlang einer Manteladiabate zu einer Abnahme der Diffusivität im oberen Teil des unteren Erdmantels aufgrund des Druckeffektes. Im unteren Bereich des unteren Erdmantels geht das Aktivierungsvolumen nahezu gegen null und der Temperaturanstieg führt zu einer Zunahme des Diffusionskoeffizienten. Insgesamt variiert der so berechnete Interdiffusionskoeffizient von Ferroperiklas um weniger als einen Faktor von 10. Daher ist ein mittlerer Diffusionskoeffizient von $4 \times 10^{-14} \text{ m}^2 \text{ sec}^{-1}$ bei $X_{\text{FeO}} = 0.1$ und einer Sauerstofffugazität, die dem Ni-NiO Puffer entspricht, eine gute Näherung für $D_{\text{Fe-Mg}}$ im unteren Erdmantel.

Für Silikatperowskit konnte aufgrund des begrenzten Druckbereiches, der mit Hilfe der Vielstempel-Technik untersucht werden konnte, kein Aktivierungsvolumen bestimmt werden. Daher wurden in dieser Arbeit zwei Grenzfälle betrachtet: Der Druckeffekt wird vernachlässigt ($\Delta V_a = 0$) oder es wird ein Wert von $\Delta V_a = 2.1 \text{ cm}^3 \text{ mol}^{-1}$ (Wright and Price, 1993) angenommen. Im ersten Fall steigt entlang einer Manteladiabate die Diffusivität von $\sim 10^{-18} \text{ m}^2 \text{ sec}^{-1}$ bei 24 GPa auf $5 \times 10^{-15} \text{ m}^2 \text{ sec}^{-1}$ bei 136 GPa. Im zweiten Fall ($\Delta V_a = 2.1 \text{ cm}^3 \text{ sec}^{-1}$) wird auf-

grund des gegensätzlichen Temperatur- und Druckeffektes ein im wesentlichen konstanter Fe-Mg Interdiffusionskoeffizient ($\sim 10^{-18} \text{ m}^2 \text{ sec}^{-1}$) beobachtet. Diese Werte gelten bei einer Sauerstoffugazität entsprechend des Ni-NiO Puffers. Für reduzierende Verhältnisse, die ungefähr der heutigen Fe-Verteilung zwischen Kern und Mantel der Erde entsprechen, ist D_{Fe-Mg} um etwa einen Faktor 14 kleiner.

Da die Kinetik im unteren Mantel im wesentlichen von D_{Fe-Mg} von Silikatperowskit abhängt, zeigen die in dieser Arbeit bestimmten Diffusionskoeffizienten, daß keine effektive Reäquilibration im unteren Erdmantel durch reine Volumendiffusion stattfinden kann. Reäquilibrationstrecken sind selbst auf einer Zeitskala der gesamten Erdgeschichte nicht viel größer als 1 m. Da diese Werte mit Fe-Mg Interdiffusionskoeffizienten abgeschätzt wurden, sind für Elemente wie Ni oder Co ähnliche Werte zu erwarten. Für Elemente mit größerem Ionenradius und/oder höherer Wertigkeit wie Ca, Rb, Sr, Nd, Hf oder W werden noch kürzere Distanzen erwartet, weil im allgemeinen der Diffusionskoeffizient für diese Elemente kleiner als D_{Fe-Mg} ist. Damit könnten Teile der ozeanischen Kruste oder kontinentale Sedimente, die durch Subduktion in den unteren Mantel gelangen, sehr lange als eigenständige chemische Signatur bestehen, sofern kein anderer Äquilibrationmechanismus als Volumendiffusion wirksam wird.

Die maximal mögliche Entfernung eines chemischen Austausches an der Kern-Mantelgrenze beträgt ~ 800 m. Dieser Wert ist nur dann gültig, wenn für Silikatperowskit ein möglicher Druckeffekt vernachlässigt wird ($\Delta V_a = 0$) und die Temperatur in der thermischen Grenzschicht an der Kern-Mantel-Grenze bei etwa 5000 K liegt. Ansonsten werden wesentlich niedrigere Werte für die Austauschlänge abgeschätzt. Damit zeigen die Resultate dieser Arbeit, daß im Laufe der Erdgeschichte kein effektiver Austausch zwischen Erdkern und Erdmantel alleine durch Volumendiffusion stattgefunden haben kann.

Als letzter Punkt wird in dieser Arbeit eine mögliche Reäquilibration nach einer Gleichgewichtseinstellung von siderophilen Elementen unter hohen Drücken in einem Magmenozean betrachtet. Das flüssige Metall muß den festen unteren Erdmantel passieren, um den Kern der Erde zu bilden. Die Diffusionskoeffizienten, die in dieser Arbeit bestimmt wurden, zeigen, daß im Fall einer Separierung in Form großer Diapire keine signifikante Veränderung der Elementhäufigkeiten stattfindet, wohingegen im Falle der Perkolation sich eine neue Verteilung

einstellt und die ursprüngliche Signatur zerstört wird. In der Zukunft müssen weitere Studien durchgeführt werden, um die Frage der Benetzungswinkel im unteren Erdmantel eindeutig zu klären und damit eine bessere geochemische Antwort auf die Verteilung der siderophilen Elemente zwischen Erdkern und Erdmantel der Erde finden zu können.

Abstract

In this study Fe-Mg interdiffusion coefficients were determined at pressures between 6 and 26 GPa and temperatures between 1653 and 2273 K for various constituent minerals of the Earth's mantle employing a multianvil apparatus. Minerals investigated include olivine, wadsleyite, ferropericlase and (Mg,Fe)SiO₃ silicate perovskite. The main aims of this study were:

- To extend the existing diffusion data set for olivine to pressures in excess of 8 GPa.
- To constrain the activation energy for diffusion in wadsleyite over a larger temperature interval than that of the previous study of Chakraborty et al. (1999).
- To determine Fe-Mg interdiffusion coefficients for ferropericlase, the second most abundant phase in the Earth, over a wide pressure range up to 23 GPa.
- To determine Fe-Mg interdiffusion coefficients for silicate perovskite, the most abundant mineral in the Earth.

For ferropericlase and olivine, single crystal diffusion couples were used whereas for wadsleyite and silicate perovskite only presynthesized polycrystalline diffusion couples could be employed. In the case of olivine, diffusion along the *c* crystallographic direction was investigated. As capsule material, Au and Ni-NiO capsules were chosen for olivine and Ni-NiO capsules for wadsleyite, ferropericlase and silicate perovskite. In addition, in the case of perovskite, single crystal MgO capsules in contact with metallic Fe were employed. Therefore, because the oxygen fugacity was not fixed at a constant value but varied with the solid state buffers Ni-NiO and Fe-(Mg,Fe)O with pressure and temperature, activation energies and activation volumes include this variation in fO_2 . To retrieve activation energies and volumes at constant fO_2 , a correction

was performed but is subject to large uncertainties because of a lack of a calibration of the buffer systems at the conditions of the experiments.

Diffusion profiles were measured after the diffusion experiments either by electron microprobe analysis (EPMA) or for profiles $< 8 \mu\text{m}$ long by energy dispersive X-ray spectrometry on a transmission electron microscope equipped with a scanning unit (EDX-STEM). In the case of olivine and silicate perovskite, diffusion coefficients were found to be essentially constant within the compositional range investigated resulting in symmetrical diffusion profiles. In this case, the profiles were fitted with an analytical solution to the diffusion equation. On the other hand, wadsleyite and ferropericlasite exhibited strongly asymmetric profiles implying a strong composition dependence of Fe-Mg interdiffusion. For elucidating the compositional dependence, profiles were simulated using the finite difference method.

The activation volume of olivine along the Ni-NiO buffer was constrained to be $5.6 \pm 0.5 \text{ cm}^3 \text{ mol}^{-1}$. A $f\text{O}_2$ correction leads to an activation volume of $7.4 \pm 1.0 \text{ cm}^3 \text{ mol}^{-1}$ at constant $f\text{O}_2$. The temperature effect observed at 12 GPa in Au capsules is consistent with the 1 bar activation energy employing a pressure and $f\text{O}_2$ correction. This observation leads to the conclusion that results obtained from Au capsule experiments (Chakraborty et al., 1999) are consistent with an $f\text{O}_2$ at the Ni-NiO buffer.

Therefore, results obtained for wadsleyite at 15 GPa and 1673-1773 K in Ni-NiO capsules were combined with the previous results by Chakraborty et al. (1999) resulting in an activation energy of $260 \pm 30 \text{ kJ mol}^{-1}$ along the Ni-NiO buffer at 15 GPa. The compositional dependence of diffusion is stronger than for olivine and can be described by a factor of $\exp\{(11.8 \pm 1.5)X_{\text{Fe}_2\text{SiO}_4}\}$, where $X_{\text{Fe}_2\text{SiO}_4}$ is the mole fraction of Fe_2SiO_4 in the solid solution.

Ferropericlasite experiments were performed over a pressure range between 8 and 23 GPa leading to an activation volume of $3.3 \pm 0.1 \text{ cm}^3 \text{ mol}^{-1}$ along the Ni-NiO buffer. This value corresponds to an activation volume of $5 \pm 1 \text{ cm}^3 \text{ mol}^{-1}$ at constant $f\text{O}_2$. The activation energy was determined to be $255 \pm 16 \text{ kJ mol}^{-1}$ along the Ni-NiO buffer and the compositional dependence of $\exp\{(132 \pm 13) \text{ kJ mol}^{-1} X_{\text{FeO}}/(RT)\}$, where X_{FeO} is the mole fraction of FeO, was found to be consistent with a model at 1 bar of Mackwell et al. (2004).

Fe-Mg interdiffusion in $(\text{Mg,Fe})\text{SiO}_3$ perovskite is orders of magnitude slower than in the other investigated phases. At oxygen fugacity conditions of the Ni-NiO buffer, the preexponential factor is $(5.1 \pm 2.0) \times 10^{-8} \text{ m}^2 \text{ sec}^{-1}$ and the activation energy is $404 \pm 144 \text{ kJ mol}^{-1}$. Compared to ferropericlase with $X_{\text{FeO}} = 0.05 - 0.1$ the difference in the Fe-Mg interdiffusion coefficient is on the order of a factor of 2×10^4 , with the smaller diffusion coefficient in perovskite. Because perovskite is believed to be the dominant phase in the lower mantle ($\sim 80 \text{ vol\%}$), the effective diffusion coefficient D_{eff} of the lower mantle should be mainly determined by the diffusion coefficient of perovskite. An effective diffusion coefficient of $D_{\text{eff}} = 2.4 \times D_{\text{pvsk}}$ was estimated assuming that ferropericlase occurs as isolated grains.

The very low rates of diffusion in silicate perovskite and hence in the lower mantle implies that reequilibration kinetics in the lower mantle are very slow. Detailed calculations show that even on the time scale of the age of the Earth (4.5×10^9 years) the reequilibration distance is only $\sim 1 \text{ m}$. Therefore, chemical heterogeneities in the lower mantle, resulting for example from subduction, cannot effectively be erased by lattice diffusion alone. Only in the thermal boundary layer at the core-mantle boundary larger interaction distances ($\sim 10\text{-}800 \text{ m}$), depending on the model used, might exist. During core formation, extensive reequilibration of percolating liquid metal in the lower mantle occurs on timescales of ~ 100000 years whereas large diapirs would never reach a new equilibrium state with surrounding oxides and silicates.

Chapter 1

Introduction

1.1 Motivation

For a given chemical system at constant pressure and temperature, the Gibbs free energy is the thermodynamic potential that determines what phases are stable (e.g. Denbigh, 1981). In nature and technology, systems are often displaced in pressure and temperature space and the system has to reach a new equilibrium state. Such processes in the mantle of the Earth would be rising plumes, descending subduction slabs, or reequilibration of minerals with percolating fluids and melts. The time scale, over which reequilibration occurs, is determined by kinetics. Many such processes are rate limited by diffusion. Therefore understanding diffusion is essential in constraining time scales of processes and life times of heterogeneities and thermodynamic disequilibria.

Most diffusion studies on naturally occurring minerals have been performed at 1 bar, exploring the temperature and composition dependence (Section 1.3.2). In contrast, the pressure dependence is not well constrained due to experimental difficulties such as keeping pressure and temperature conditions of diffusion experiments constant for a long time or having large enough sample space to accommodate diffusion couples. Hence, the effect of pressure on diffusion is often neglected. For geological processes occurring in the Earth's crust, this assumption might be justified judging from previously reported activation volumes of diffusion, but ignoring the pressure dependence may lead to substantial errors for processes occurring at greater depth in the Earth's mantle or core. For example in Misener (1974) an activation volume for Fe-Mg interdiffusion of $5.5 \text{ cm}^3 \text{ mol}^{-1}$ was determined experimentally, leading to a decrease of diffusivity of 2 orders of

magnitude over a pressure interval of 12 GPa at 1673 K. Hence, the equilibration time t_{eq} would be 2 orders of magnitude longer in the upper mantle just above the transition zone for the same diffusional length scale x_{dif} as compared to processes occurring at the Earth's surface because $x_{dif} \propto \sqrt{Dt_{eq}}$, where D is the diffusion coefficient.

The effect of pressure on diffusion might influence, for example, calculations of entrapment of melt inclusions and subsequent polybaric reequilibration where normally pressure-independent expressions for diffusivity are applied (e.g. Cottrell et al., 2002; Gaetani and Watson, 2002). The simulation of Cottrell et al. (2002) shows that the results are very sensitive to small variations in the diffusion coefficient for small values of the reduced time $\tau = t \kappa_s R^{-2}$ where t is time, κ_s is the diffusion coefficient in the host phase and R is the radius of the inclusion. Another example from the $(\text{Mg,Fe})_2\text{SiO}_4$ system are studies of the kinetics of the phase boundary of the olivine \rightleftharpoons wadsleyite transition. The growth of wadsleyite from olivine should be rate limited by interdiffusion in olivine (Rubie, 1993). In the study of Solomatov and Stevenson (1994) an Fe-Mg interdiffusion coefficient of $10^{-10} \text{ m}^2 \text{ sec}^{-1}$ was used whereas, as shown above, extrapolation of diffusion data employing the activation volume determined at lower pressures would predict significantly smaller D values and therefore longer time scales.

Only few diffusion studies exist for high pressure phases, such as silicate perovskite. The reason for this lack of data is the difficulty of maintaining high pressure and temperature conditions to stabilize the high pressure phases for such a long time that diffusion profiles can be measured. Although the diamond anvil cell can reach pressures up to several 100 GPa, equivalent to conditions of the Earth's core, the sample volume is not big enough to accommodate diffusion couples. On the contrary, the multianvil apparatus is capable of fulfilling these requirements up to pressures of more than 25 GPa and temperatures well above 2000 K. In the last few years the setup of a new 5000 t multianvil press at the Bayerisches Geoinstitut lead to the possibility of performing multianvil experiments at stable pressure and temperature conditions on time scales up to several days with large volume samples (up to 3 mm^3 at 22 GPa, Frost et al., 2003). The experiments reported in this study were performed at pressures between 6 and 26 GPa at temperatures between 1623 K and 2273 K for time durations in the range of 5 minutes up to 3 days. In combination with microanalytical techniques (Chapter 3), such as the electron microprobe or

for smaller length scales the analytical transmission electron microscope (Meißner et al., 1998), interdiffusion coefficients on the order of $10^{-20} \text{ m}^2 \text{ sec}^{-1}$ can now be determined with diffusion couple experiments at pressures as high as 26 GPa with reasonable accuracy.

Only two studies of Fe-Mg interdiffusion in wadsleyite exist in the literature at present (Chakraborty et al., 1999; Farber et al., 2000). In the study of Chakraborty et al. (1999) two experiments are reported, that span a temperature range of only 100 K. The experiments of Farber et al. (2000) were all performed at one temperature. Therefore one aim of this study is to better constrain the activation energy of Fe-Mg interdiffusion in wadsleyite by performing experiments at higher temperatures than Chakraborty et al. (1999).

Numerous applications of diffusion coefficients exist, such that only a few can be highlighted in this paragraph. For example, the knowledge of interdiffusion coefficients of the phases forming the lower mantle will help in understanding such fundamental questions as the grain size in this part of the Earth. In a simulation of the grain size in the lower mantle by Solomatov et al. (2002), diffusion coefficients for Si self diffusion were taken from Yamazaki et al. (2000). But up to now it is not established what the slowest diffusing species in silicate perovskite is. For silicates with SiO_4 tetrahedra, Si diffusion is much slower than Fe-Mg interdiffusion (e.g. Brady, 1995). But the structure of silicate perovskite is quite different, containing SiO_6 octahedra, (Section 1.3.1) and therefore this assumption needs to be tested (for results from a theoretical study of relative diffusivities in perovskite see section 1.3.2). Fe-Mg partitioning experiments between magnesiowüstite and magnesium silicate perovskite already show that Fe-Mg exchange is a very slow process in perovskite at least at reducing conditions (Frost and Langenhorst, 2002). The data on diffusion will be used in section 6.5.5 to constrain kinetically some recently-proposed core forming scenarios. In these models a magma ocean exists at an early stage of Earth's history with a depth of approximately 1000 km. The current distribution of siderophile elements between the core and the mantle would be established by metal-silicate equilibration at the base of the magma ocean. Subsequently, after the equilibration event, the liquid metal has to descend through the solids forming the lower mantle either by large diapirs or by grain boundary wetting. The extent of reequilibration and hence obliteration of the siderophile element signature is controlled by diffusion in the solids and therefore the knowledge of diffusion coefficients becomes

essential in understanding this process.

Results of previous diffusion studies of olivine, wadsleyite, ferropericlase and silicate perovskite are summarized in Section 1.3.2. The most important aspects of the theory of diffusion, as needed as a background for this study, are given in the next section.

1.2 Theory of diffusion

1.2.1 Definition of diffusion

“Diffusion and mass flow or drift result from individual jumps of atoms and/or point defects in the solid” (Philibert, 1991). In the case of a crystalline solid, periodic jumps occur between distinct lattice sites (Shewmon, 1989). Random walk theory therefore provides the link between macroscopic diffusion coefficients, as defined below and experimentally determined in this study, and microscopic motion of individual atoms in the structure.

1.2.2 Macroscopic theory of diffusion

In a macroscopic linear theory, without considering the atomistic details of the diffusion process, the diffusion coefficient is defined by Fick’s first law (Fick, 1855):

$$\mathbf{J}_i = -D_i \nabla n_i \quad (1.1)$$

where \mathbf{J}_i is the flux of component i , in terms of the number of atoms crossing a unit area perpendicular to the flux-direction in unit time, n_i is the number of atoms i per unit volume and D_i is the diffusion coefficient for atoms i . Hence, the diffusion coefficient relates the vector \mathbf{J}_i to the vector ∇n_i , the gradient of the concentration, and is therefore a second rank tensor (Nye, 1985). When measuring diffusion coefficients in non-cubic materials, the direction dependence has to be taken into account (see section 1.2.7).

Equation 1.1 is valid at a local point in space and time. Due to the fact that local fluxes are difficult to determine directly, only in very special circumstances, in the case of a local steady state, can Equation 1.1 be used to determine the diffusion coefficient (e.g. permeation experiments as described in Philibert, 1991). In the non-steady state, where the concentration distribution is a function of time, which is the normal situation in a diffusion couple experiment as used in this

study (Chapter 2.3), Fick's second law is used for measuring the diffusion coefficient D_i :

$$\frac{\partial n_i}{\partial t} = \nabla \cdot (D_i \nabla n_i) \quad (1.2)$$

Equation 1.2 can be derived from Equation 1.1 by considering the conservation of atoms i during the diffusion process (see Allnatt and Lidiard, 1993, for details). Fick's second law is a parabolic partial differential equation of the second order, mathematically equivalent to Fourier's law of heat conduction, and solutions for many initial and boundary conditions are listed in Crank (1979) and Carslaw and Jaeger (1946). For other forces apart from a concentration gradient, Equation 1.1 has to be extended. For any force F produced by a potential gradient $F = -\nabla V$ it can be shown that Equation 1.2 has to be written as (Shewmon, 1989):

$$\frac{\partial n_i}{\partial t} = D_i \nabla \left[\nabla n_i + \frac{n_i \nabla V}{kT} \right] \quad (1.3)$$

if the diffusion coefficient D_i is position and concentration-independent. For limitations of the linear theory (Equation 1.1) see Allnatt and Lidiard (1993).

1.2.3 Microscopic theory of diffusion

Diffusion takes place by the hopping of atoms between lattice sites. For random jumps with equal probability of jump directions, following Einstein (1905), the diffusion coefficient D in one direction is related to the mean-square displacement $\langle X^2 \rangle$ in a time interval t by:

$$D = \frac{\langle X^2 \rangle}{2t} \quad (1.4)$$

A number of possible different diffusion mechanisms exist, for example direct exchange, vacancy, interstitial, or interstitialcy. Divalent cation diffusion in silicates and oxides is assumed to occur mostly by a vacancy mechanism. Vacancies are either intrinsically or extrinsically created. The abundance of intrinsic lattice vacancies varies with temperature and their presence is thermodynamically favored because the free energy of the system is lowered due to mixing effects, whereas extrinsic vacancies are created by aliovalent substitution or by oxidation of transition metal ions like Fe (Ganguly, 2002). In an Arrhenius plot a kink is observed with a steeper slope at high temperature for the intrinsic regime and a shallower slope for the extrinsic regime at lower temperature (e.g. in the NaCl system see: Mapother et al., 1950). Buening and Buseck (1973)

also observed such a kink in the olivine system, but this observation was later disproved by Chakraborty (1997, see section 1.3.2). In addition to the classical intrinsic and extrinsic regime, Chakraborty (1997) proposed an additional regime for Fe-bearing silicates due to the fact that unlike in a pure extrinsic case the concentration of point defects changes with temperature because, based on the redox reaction of Fe, the $\text{Fe}^{2+}/\text{Fe}^{3+}$ ratio changes with temperature as well. As a consequence the activation energy comprises a sum of a formation and a migration energy (like in the intrinsic case). This diffusion regime is termed “transition metal-extrinsic” (TaMED) by Chakraborty (1997). TaMED possesses both extrinsic (defect concentration is controlled by a chemical potential at a fixed P,T, and major element composition) and intrinsic (change of concentration of vacancies with P and T) character.

In the literature various types of diffusion coefficients are defined and often used inconsistently. The self diffusion coefficient of component A describes the diffusion of A in the absence of a concentration gradient. If the diffusion of a tracer is considered, depending on the kind of mechanism, successive jumps of an atom are correlated, and the diffusion coefficient of a tagged atom in a medium is then called a tracer diffusion coefficient: $D^* = f \cdot D_{random}$, where D^* is the tracer diffusion coefficient, f is the correlation factor describing the non-randomness of subsequent jumps, and D_{random} is the diffusion coefficient derived by uncorrelated random walk (Philibert, 1991). Often this process is also termed self-diffusion. In addition to the correlation effect when using a different isotope for the study of tracer diffusion, also the isotope effect (different isotopes have different masses and hence slightly different vibrational frequencies) might become important.

The tracer diffusion coefficient in its atomistic form depends in a complex way on a variety of parameters such as the underlying diffusion mechanism, temperature, and $f\text{O}_2$. As an example, for a vacancy controlled diffusion mechanism in a transition metal oxide, considering correlation of successive jumps, the tracer diffusion coefficient D^* for a cation can be written in its atomistic form as (Philibert, 1991):

$$D^* = fN_V D_V \quad (1.5)$$

where f is the correlation coefficient (Bardeen and Herring, 1952), D_V is the vacancy diffusion coefficient, and N_V is the vacancy concentration. Inserting the appropriate equations for the

vacancy diffusivity and the vacancy abundance (including the f_{O_2} dependence) in Eq. 1.5, the complete expression for the tracer diffusion coefficient is derived (Philibert, 1991)

$$D^* = \beta a^2 \nu f A_V (f_{O_2})^m \exp\left(\frac{S_V^m + S_V^f}{k}\right) \exp\left(-\frac{H_V^m + H_V^f}{kT}\right) \quad (1.6)$$

where β is a geometrical factor, a is the lattice constant, ν is a vibration frequency, A is a constant, m is a constant depending on the charge state of the vacancy, S_V^m is the vacancy migration entropy, S_V^f is the effective vacancy formation entropy (Philibert, 1991), H_V^m is the vacancy migration enthalpy, H_V^f is the effective vacancy formation enthalpy, k is Boltzmann's constant, and T is temperature (for the pressure dependence see section 1.2.6).

In computer simulations self-diffusion coefficients are calculated employing equations corresponding to Eq. 1.6 using a variety of computer simulation techniques (e.g. Ita and Cohen, 1997; Vočadlo et al., 1995; Wright and Price, 1989). Although a lot of assumptions have to be made in order to keep computation times reasonable, comparisons with experimentally determined diffusion coefficients are often relatively encouraging. Therefore, they may be used for extrapolation of experimentally determined values towards P and T conditions that are not reachable by experiment. This approach is used in Chapter 6 to extrapolate diffusion data to conditions of the lower mantle.

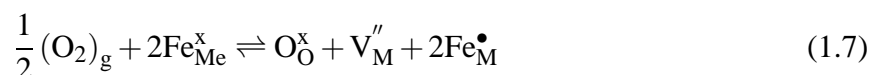
Most systems are thermodynamically nonideal and in addition to a concentration gradient other driving forces such as chemical potential gradients (or more precisely the nonideal part of the chemical potential gradient), stress gradients or temperature gradients exist (as already indicated in Section 1.2.2). The role of stress gradients and temperature gradients in the experiments of this study are investigated in section 5.7.

Fluxes of different species are usually coupled due to constraints of electroneutrality and conservation of lattice sites in a crystal. In this study minerals forming Fe-Mg solid solutions are investigated. Because the flux of Fe-atoms in one direction is coupled with a flux of Mg-atoms in the other direction (in the microscopic picture also with a flux of vacancies), in a single diffusion couple experiment, employing two endmember crystals with a different Fe-Mg concentration, only one independent Fe-Mg interdiffusion coefficient can be determined for each profile (Fe or Mg). In that context the term chemical diffusion is used. Chemical diffusion describes the exchange of chemical components (Brady, 1975a) and not structure elements in the sense of

Schmalzried (1995). Different equations exist for relating chemical diffusion coefficients determined in interdiffusion studies with microscopically defined self diffusion coefficients depending on the system under investigation (for metals: Darken (1948), for ionic compounds: Barrer et al. (1963); Brady (1975a); Manning (1968)). In all of these equations, for a dilute component in a diffusion couple, the ideal part of the chemical diffusion coefficient equals the tracer diffusion coefficient of the dilute component (Chakraborty, 1995). In a nonideal solid solution the situation becomes more complex because an additional thermodynamic factor has to be included (Chakraborty, 1995). In Section 5.2 not only Fe-Mg interdiffusion in olivine has been measured but also the diffusion of the dilute components Ni and Mn were determined.

1.2.4 Oxygen fugacity dependence

For most mineral systems in the Earth, it is assumed that cation diffusion occurs via vacancies. In the case of Fe-bearing solid-solutions the concentration of vacancies is a function of the oxygen fugacity. For example in ferropericlase, (Mg,Fe)O, one may write according to Chen and Peterson (1980) and Poirier (2000):



using the Kröger-Vink notation, where a structure element (Schmalzried, 1995) is described as S_l^q with S denotes the atom or point defect, q the electric charge with respect to the perfect lattice (x = neutral, $'$ = negative, \bullet = positive), and l the sublattice on which S resides. With the Fe^{3+} -ion an electron hole is associated and therefore the equilibrium constant $K_{1.7}$ of Equation 1.7 can be written as:

$$K_{1.7} = \frac{[V_{\text{M}}''] [h^{\bullet}]^2}{(f\text{O}_2)^{\frac{1}{2}}}. \quad (1.8)$$

The electroneutrality condition is:

$$2 [V_{\text{M}}''] = [h^{\bullet}]. \quad (1.9)$$

Combining Equations 1.8 and 1.9 and using $D \propto [V_{\text{M}}'']$ (compare with Eq. 1.5) leads to the ideal $f\text{O}_2$ dependence:

$$D \propto [V_{\text{M}}''] \propto (f\text{O}_2)^{\frac{1}{6}}. \quad (1.10)$$

An equivalent analysis for majority defects in other minerals can be made. A detailed study for olivine can be found in Nakamura and Schmalzried (1983, 1984). The treatment should be similar for the high pressure polymorphs of olivine. Silicate perovskite has a much higher Fe^{3+} content even at low oxygen fugacities. For this phase the situation is more complicated because Fe^{3+} can also be incorporated into the Si-site as a coupled substitution or charge balanced by O vacancies (Lauterbach et al., 2000; Frost and Langenhorst, 2002). No rigorous quantitative treatment of the point defect chemistry of Fe-bearing perovskite with respect to transport properties so far exists in the literature.

1.2.5 Temperature dependence of diffusion

The diffusion coefficient D depends strongly on temperature because diffusion is a thermally activated process. Often it is found experimentally that D follows an Arrhenius relationship:

$$D = D_0 \exp \left[-\frac{E_a}{RT} \right] \quad (1.11)$$

where D_0 is the preexponential factor, E_a is the activation energy, R is the universal molar gas constant, and T is temperature. Equation 1.11 implies that in a plot of $\log D$ versus the inverse temperature, a linear relationship is observed where the slope gives the activation energy (Fig. 1.1).

The dependence on temperature may be understood in the framework of the theory of the activated complex. Local fluctuations in energy, responsible for a successful jump of an atom to another crystal site, occur with a frequency dominated by a Boltzmann exponential factor (Allnatt and Lidiard, 1993). As shown in section 1.2.3 the concentration and mobility of vacancies depends exponentially on temperature. Hence a diffusion process with a vacancy mechanism should also be exponentially dependent on temperature (Eq. 1.5, 1.6).

Nevertheless one should be aware that the Arrhenius law is not universal, and might break down in cases where there is a change in diffusion mechanism (extrinsic to intrinsic diffusion transition, see Section 1.2.3), impurities or microstructural irregularities.

1.2.6 Pressure dependence of diffusion

A recent review about diffusion at high pressure with a detailed description of models for the effect of pressure on diffusion was given by B ejina et al. (2003). The pressure dependence of diffusion is derived by considering the free energy G_a of the activation process. The self-diffusion coefficient at variable pressure P and temperature T , $D(P, T)$, is then given by (Sammis et al., 1981):

$$D(P, T) = (D_0)' \exp \left[\frac{-\Delta G_a}{RT} \right] \quad (1.12)$$

where $D_0' = \beta a^2 v$ (see Eq. 1.6). The Gibbs free energy for activation can be expressed at variable temperature and pressure as:

$$\Delta G_a = \Delta H_a - T \cdot \Delta S_a, \quad \Delta H_a = E_a + P \cdot \Delta V_a \quad (1.13)$$

where ΔH_a is the activation enthalpy, E_a is the activation energy, ΔV_a is the activation volume and ΔS_a is the activation entropy. Equation 1.13 is inserted into Equation 1.12, giving:

$$D = \left\{ D_0' \exp \left[-\frac{\Delta S_a}{R} \right] \right\} \exp \left[-\frac{E_a + P \cdot \Delta V_a}{RT} \right] \quad (1.14)$$

where the expression inside the curly brackets is the conventional preexponential factor D_0 . The pressure dependence of the vibrational term is usually small (Philibert, 1991) and therefore neglected, although the equations used are normally only valid for very simple metals. If ΔS_a is assumed to be pressure independent, the activation volume becomes $\Delta V_a = -RT(\partial \ln D / \partial P) = \partial \Delta H_a / \partial P$ Poirier (2000). For chemical diffusion the same formalism as in Eq. 1.14 is applied for the interpretation of the diffusion data in Chapter 5.

The graphical determination of the apparent activation volume is shown in Fig. 1.1. If the activation volume and the activation energy are constant over the pressure and temperature regime studied, straight lines are observed if the logarithm of the diffusion coefficient is plotted versus inverse temperature or pressure. Otherwise, only the instantaneous activation energy at a certain temperature or the instantaneous activation volume at a certain pressure can be determined. If the dominant diffusion mechanism changes (for example a transition from extrinsic to intrinsic diffusion) a kink in the correlations shown in Figure 1.1 would be observed.

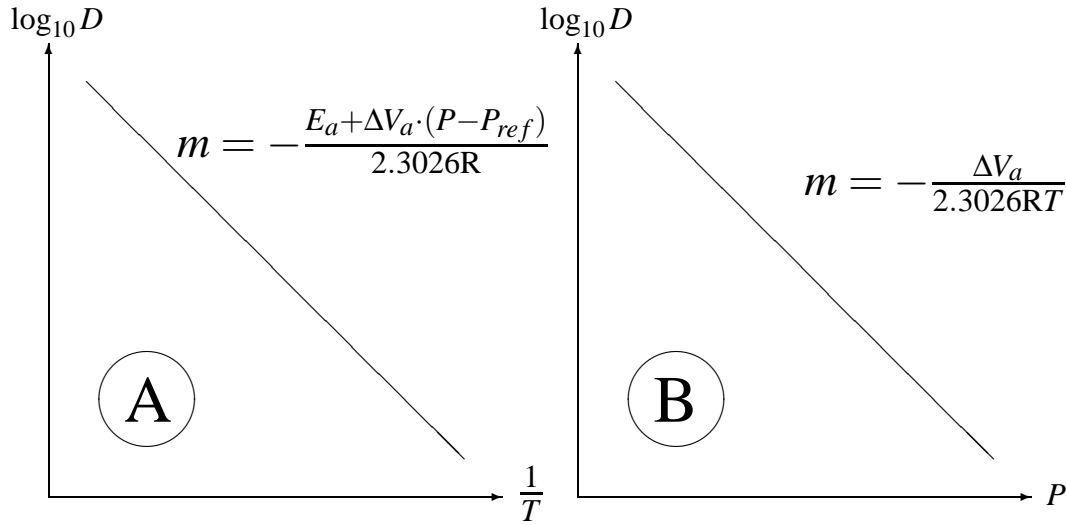


Figure 1.1: Graphical interpretation of the activation energy and the activation volume. A: The activation energy E_a is calculated from a slope of $\log D$ versus the inverse temperature T . At a pressure $P = P_{ref} = 1$ bar the slope directly gives the activation energy whereas at high pressure the slope gives the combined pressure and temperature effect. B: The activation volume V_a is calculated from the slope of $\log D$ versus the pressure.

1.2.7 Direction dependence of diffusion

In Eq. 1.1, Fick's first law, the diffusion coefficient relates the vector concentration gradient to the vector flux. Therefore the diffusion coefficient is a second rank tensor. Only for amorphous or cubic materials the diffusion coefficient is direction-independent. Equation 1.1 can be written as:

$$J_i = D_{ij}C_j \quad (1.15)$$

where J_i equals the flux in the i -direction, C_j is the concentration derivative in the j -direction, the D_{ij} are the corresponding components of the diffusion tensor, and the Einstein summation convention is assumed (*when a letter suffix occurs twice in the same term, summation with respect to that suffix from 1 to 3 is to be automatically understood*, Nye, 1985). The D_{ij} form a symmetric second rank tensor (Ganguly, 2002) and the independent components for each crystal system can be found in Nye (1985) or Haussühl (1983). As discussed in the next section, olivine, wadsleyite and silicate perovskite are orthorhombic, whereas ferropicrlase is cubic. Therefore, the diffusion coefficient as a second rank tensor does not depend on direction in ferropicrlase.

For the orthorhombic system three independent components exist, which are D_{11} , D_{22} , and D_{33} for the normal convention of the crystal-physical coordination system (Nye, 1985).

1.3 Mineralogical model of the Earth's mantle

1.3.1 Phase stabilities and structures

In Figure 1.2 a section through the Earth's mantle is shown, outlining the stability ranges of the most important mineral phases. The upper mantle is dominated by olivine which transforms at 410 km to its high pressure polymorph wadsleyite. Wadsleyite is stable down to a depth of approximately 520 km where it transforms to ringwoodite. The olivine phase diagram was determined by Akaogi et al. (1984), Akaogi et al. (1989), Katsura and Ito (1989), Morishima et al. (1994), and Suzuki et al. (2000). At 670 km ringwoodite decomposes into silicate perovskite and ferropericlase (Ito and Takahashi, 1989). The precise depth of this decomposition and the nature of the 670-km discontinuity is currently debated due to recent in situ multianvil and diamond anvil studies (Chudinovskikh and Boehler, 2001; Irifune et al., 1998; Katsura et al., 2003; Shim et al., 2001a). With increasing depth silicate perovskite becomes more Al-rich consuming the majoritic garnet (Wood, 2000). Pyroxenes are only stable at depths less than 480 km where they react to form majorite (Akaogi and Akimoto, 1977). At 580 km Ca-perovskite becomes stable taking the Ca-component from majoritic garnet (Liu, 1975). A more extensive review about phase stabilities and mantle discontinuities can be found in Poirier (2000).

As outlined in section 1.1 and is evident from the last paragraph, diffusion coefficients are needed for the minerals shown in Fig. 1.2 for constraining kinetic processes occurring in the Earth. This study focuses mainly on Fe-Mg interdiffusion as a function of pressure and temperature in olivine, wadsleyite, silicate perovskite and ferropericlase. In addition, Ni and Mn diffusion in olivine was also investigated.

Olivine crystallizes in the orthorhombic space group $Pbnm$. Thus diffusion in olivine is anisotropic (see section 1.2.7). The oxygen atoms form a distorted hexagonal array parallel to (100) planes. For the divalent cations two different octahedral sites M1 and M2 exist, where in $(Fe,Mg)_2SiO_4$ solid solutions the larger Fe^{2+} ion is incorporated preferentially into the smaller M1 site (Deer et al., 1992). The M1 octahedra form edge-sharing chains along the crystallo-

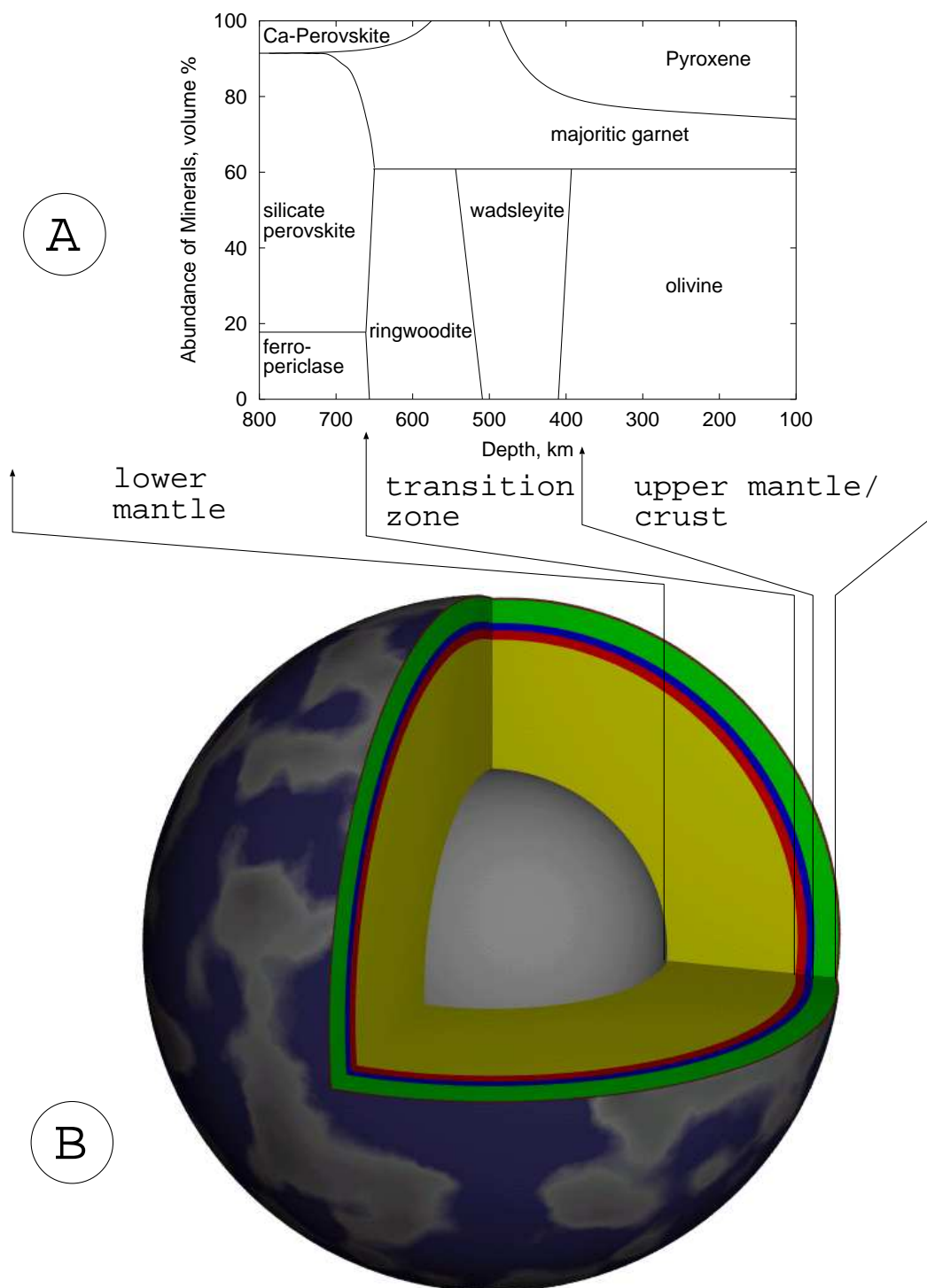


Figure 1.2: Section through the Earth's mantle. In (A) the abundance of minerals in the depth-interval 100 - 800 km (redrawn from Jackson and Rigden (1998) with original data from Irifune (1993, 1994)), and in (B) a schematical section through the whole mantle is shown.

graphic c-direction probably forming a relatively fast diffusion pathway because the c-direction is also the fastest diffusion direction. For a detailed discussion of the relation of diffusion and structure in olivine see Morioka and Nagasawa (1991).

The two high pressure polymorphs of olivine, wadsleyite and ringwoodite, have structures that are closely related to each other. Whereas ringwoodite has a normal spinel structure, wadsleyite has a modified spinel structure. The oxygen atoms are approximately cubic closed packed but the cations are on different positions than in a normal spinel. The modified spinel and the spinel structure can be understood by stacking of slabs parallel to (110) in the spinel structure (Putnis, 1992). The symmetry of wadsleyite is orthorhombic. As in olivine, edge sharing octahedra exist in wadsleyite running along the b-axis. In addition the structure consists also of double chains of octahedra oriented along the crystallographic a direction (Finger et al., 1993). From the structural point of view it is difficult to estimate the extent of anisotropy although the close relationship to the spinel structure might imply that it is not very pronounced and diffusion coefficients of wadsleyite and ringwoodite might be similar.

Ferropericlase crystallizes in the halite NaCl(B1) structure, space group Fm3m. The pure endmember periclase retains this structure into the megabar pressure range (Duffy et al., 1995; Dubrovinsky et al., 1998). Fe-bearing solid solutions show a disproportionation at pressures above 85 GPa and temperatures up to 1100 K in the externally heated diamond anvil experiments by Dubrovinsky et al. (2000a,b). The driving force for this decomposition was attributed either to the transition of the Fe-bearing endmember wüstite from the B1 to a NiAs or anti-NiAs (B8 or a-B8) or possible changes in the magnetic structure of Fe²⁺. For the diffusional properties a structure change from B1 to B8 would imply a change from isotropic to anisotropic diffusion. Recent results by Badro et al. (2003) show a change from high spin to low spin of Fe²⁺ in ferropericlase with $X_{FeO} = 0.17$ between 60 and 70 GPa. This phase change would change the diffusivity by altering the vibrational frequency term in Equation 1.6. In addition, due to a resulting change in the Fe-distribution between ferropericlase and coexisting perovskite, the diffusivity in the lower mantle would be changed by a compositional effect.

(Mg,Fe)SiO₃ silicate perovskite has the orthorhombic Pbnm GdFeO₃-structure. Hence, diffusion is anisotropic. An extensive review of the perovskite structure is given in the recent book

by Mitchell (2002). The ideal structure consists of corner linked SiO_6 octahedra forming 12-coordinated cation sites in between the octahedra. The deviation from cubic symmetry occurs by the tilting of the SiO_6 octahedra and displacement of Si from the center of an octahedron. With respect to diffusion this change in structure is minor when compared to the anisotropic arrangement of edge-sharing polyhedra chains e.g. in olivine (see above). Even in olivine the anisotropy is only approximately a factor of 6 between the slowest direction (b) and the fastest direction (c) at ~ 1373 K. Therefore the extent of anisotropy in silicate perovskite is expected to be very small.

In the literature is an ongoing debate about whether there are structural phase transitions for silicate perovskite at conditions of ~ 25 GPa and elevated temperatures (conditions of the multi-anvil press used in this study). Wang et al. (1992) concluded in their electron microscopy study of $(\text{Mg,Fe})\text{SiO}_3$ perovskite that, based on twin morphology, analog studies, and theoretically predicted twin laws, silicate perovskite might be cubic above 1873 K and 26 GPa. However, such a phase change is not detected in situ by X-ray diffraction in a diamond anvil cell. The most recent study by Shim et al. (2001b) only shows the possibility of a phase change from the orthorhombic space group Pbnm , stable at low pressures and temperatures, to either $\text{P2}_1/\text{m}$, Pmmn , or $\text{P4}_2/\text{nmc}$ above 83 GPa and 1973 K.

1.3.2 Summary of existing diffusion data

General remarks

The section about existing diffusion data should summarize diffusion data relevant for this study. This includes mainly Fe-Mg interdiffusion or cation diffusion studies for olivine, wadsleyite, ferropicrinite and silicate perovskite. Numerous studies for Si or O diffusion in olivine exist but are not explicitly cited here because these components were not further investigated in this study. General reviews for diffusion data covering a large variety of minerals and different species can be found in Brady (1995) and especially for other high pressure phases in B ejina et al. (2003). On the contrary, Mg, Si and O self-diffusion studies in ferropicrinite and silicate perovskite are described to some extent because they are the only existing high pressure data available for these phases. Especially interesting is the relative difference of Si and O self-diffusion compared to Fe-Mg interdiffusion in silicate perovskite.

Olivine

Several studies for diffusion of octahedral cations have been performed at 1 bar and elevated temperatures and varying oxygen fugacities (Clark and Long, 1971; Buening and Buseck, 1973; Misener, 1974; Hermeling and Schmalzried, 1984; Nakamura and Schmalzried, 1984; Jurewicz and Watson, 1988; Morioka and Nagasawa, 1991; Chakraborty, 1997; Ito et al., 1999; Petry, 1999a; Petry et al., 2003). Discrepancies that exist between the different datasets are thoroughly further discussed in Chakraborty (1997). High pressure Fe-Mg interdiffusion experiments have been performed at pressures up to 3.5 GPa by Misener (1974) and Farber et al. (2000). They derived activation volumes for Fe-Mg interdiffusion in olivine of 5.5 and 5.4 cm³ mol⁻¹ respectively. Between 3 and 9 GPa, Fe-Mg interdiffusion experiments were performed at very low temperatures, between 873 and 1173 K, by Jaoul et al. (1995). The experiments employed San Carlos olivine covered with a thin layer of fayalite and the diffusion profiles were analyzed by Rutherford backscattering. Errors for the diffusion coefficients reported in Jaoul et al. (1995) are up to two orders of magnitude. The activation volume deduced was essentially zero within the error of the experiments. Jaoul et al. (1995) attributed the difference in activation volume compared to the study of Misener (1974) to a change from extrinsic diffusion at low temperatures (Jaoul

et al., 1995) to intrinsic diffusion at higher temperatures (Misener, 1974). This conclusion is in contradiction with the results at 1 bar from Chakraborty (1997) because in his study diffusion at temperatures between 1253 K and 1573 K occurred in the TaMED regime (Section 1.2.3) and the transition to intrinsic diffusion would be at much higher temperature. In Chakraborty et al. (1994), Mg tracer diffusion experiments in pure Mg_2SiO_4 are reported. The activation volume for Mg tracer diffusion was found to be $1\text{-}3.5 \text{ cm}^3 \text{ mole}^{-1}$, although it should be emphasized that the point defect chemistry in pure forsterite is different from Fe-bearing olivine. The study of Chakraborty et al. (1999) investigated Fe-Mg interdiffusion at pressures between 9 and 15 GPa in olivine and wadsleyite. Because these experiments were performed in Au capsules the $f\text{O}_2$ is not directly buffered but was estimated to be approximately between 10^{-8} and 10^{-9} bars for experiments performed in the range 9-12 GPa, corresponding to a relative oxygen fugacity of $\sim \text{IW-1.7}$ (1.7 orders of magnitude smaller than the $f\text{O}_2$ imposed by the iron-wüstite buffer, calculated at 11 GPa using values from Ride, 1991, see also Chapter 5). Compared to 1 bar data at the same oxygen fugacity, the results would imply an activation volume for olivine which is close to zero. As stated in Note 9 of Chakraborty et al. (1999) the pressure effect for their thermodynamic calculations was neglected. Therefore, in this study, the olivine system was reinvestigated at high pressure using the same type of capsule and also using diffusion couples embedded in Ni capsules with an addition of NiO (Section 2.3). The results of the new experiments, given in Chapter 5, can then be used to estimate the oxygen fugacity conditions characteristic for the experiments employing Au capsules and allow a better estimation of the activation volume for olivine using data between 1 bar and 12 GPa.

Wadsleyite

Only two studies exist in which Fe-Mg interdiffusion coefficients for wadsleyite were measured. Both studies (Farber et al., 2000; Chakraborty et al., 1999) showed a marked increase in diffusivity by 2-3 orders of magnitude across the olivine-wadsleyite phase boundary. The experiments of Farber et al. (2000) suffer by the fact that diffusion occurs at the same time as phase transformations. In the study of Chakraborty et al. (1999) only two experiments at 1373 and 1473 K were performed on wadsleyite. These experiments used Au as capsule material providing a mechanically soft environment but leaving the oxygen fugacity unbuffered (see previous section). The

calibration of the fO_2 conditions inside the Au capsules, as outlined above for olivine, also helps in constraining the oxygen fugacity conditions in the experiments of Chakraborty et al. (1999) for wadsleyite. In this study experiments at higher temperatures than used by Chakraborty et al. (1999) were performed and the results are compared with their data in order to obtain a better estimate of the activation energy for diffusion in wadsleyite (section 5.3).

Ferropericlase

Most studies of diffusion in the system MgO-FeO have been performed on the end member MgO. Reviews of Mg and O self-diffusion data at 1 bar and variable temperatures can be found in Freer (1980) and Wuensch (1983). Vočadlo et al. (1995) investigated ionic diffusion in MgO by computer calculations via lattice dynamics.

Fe tracer diffusion experiments in (Mg,Fe)O solid solutions were performed by Chen and Peterson (1980). The oxygen fugacity dependence follows the ideal $fO_2^{1/6}$ -dependence (Equation 1.10) and the Fe tracer diffusion coefficient depends exponentially on composition. Only a few studies exist on Fe-Mg interdiffusion in the system MgO-FeO. Experiments employing polycrystalline diffusion couples or single crystals embedded in powders were performed by Bygdén et al. (1997), Rigby and Cutler (1965) and Blank and Pask (1969). The temperature range of these experiments was restricted to 1363 - 1588 K. The oxygen fugacity was not buffered directly and led to discrepancies in the results (see Bygdén et al. (1997) for a discussion and comparison of results).

Mackwell et al. (2004, in preparation) performed Fe-Mg interdiffusion experiments employing single crystal diffusion couples over a wide range of temperatures and oxygen fugacities at 1 bar. According to their results, diffusion depends on oxygen fugacity with an exponent of 0.22, slightly different from the ideal value 1/6 in Eq. 1.10, and depends exponentially on composition, and the interdiffusion coefficient is given by:

$$D_{Fe-Mg} = (D_{01} + D_{02} \cdot fO_2^m \cdot X_{FeO}^p) \cdot \exp\left(-\frac{E_A - \alpha \cdot X_{FeO}}{R \cdot T}\right) \quad (1.16)$$

where $D_{01} = 1.8 \times 10^{-8} \text{ m}^2 \text{ sec}^{-1}$, $D_{02} = 1.1 \times 10^{-4} \text{ m}^2 \text{ sec}^{-1}$, the activation energy $E_A = 206500 \text{ J mol}^{-1}$, $\alpha = 61950 \text{ J mol}^{-1}$, $m = 0.22$, $p = 1.17$, R is the molar gas constant, and T is temperature. This equation was derived by Mackwell et al. (2004, in preparation) using point

defect arguments and the values of its parameters are best fit values to their data. The power law dependence only plays a significant role at low iron concentrations, whereas for compositions with $X_{FeO} > 0.07$, diffusivities are primarily exponentially dependent on composition; Eq. 1.16 can then be approximated at constant temperature by:

$$D = D_0 \cdot \exp(a \cdot c(x)) \quad (1.17)$$

where the constant a controls the extent of asymmetry observed in the diffusion profiles and the preexponential factor includes the temperature and oxygen fugacity of the experiment which are constant for each individual experiment. A pure exponential compositional dependence was observed for Fe-Mg interdiffusion in ferropericlase by Bygdén et al. (1997), for Ni tracer diffusion from thin films into NiO-MgO single crystal solid solutions by Wei and Wuensch (1973) and in interdiffusion studies of NiO-MgO by Blank and Pask (1969), Appel and Pask (1971), and Jakobsson (1996). Also for olivine (Morioka and Nagasawa, 1991) a pure exponential dependence on composition was observed.

To understand transport processes in the lower mantle, where ferropericlase is an important constituent phase, diffusivities as a function of pressure are needed. $(Fe_xMg_{1-x})O$ ferropericlase is well suited for high pressure experiments due to the large stability field of this phase. Ita and Cohen (1997, 1998) performed a theoretical study on diffusion in pure MgO at high pressures. Calculated self-diffusion coefficients for Mg and O decrease with increasing pressure. Van Orman et al. (2003) performed multi-anvil experiments to measure Mg, Al and O self-diffusion in MgO between 15 and 25 GPa at a constant temperature of 2273 K. Their results agree with the theoretical work of Ita and Cohen (1998) and the experimentally determined activation volume for Mg diffusion is $3.0 \text{ cm}^3/\text{mole}$.

Yamazaki and Irifune (2003) recently determined Fe-Mg interdiffusion coefficients for ferropericlase. They derived an activation volume of $1.8 \text{ cm}^3 \text{ mol}^{-1}$ and an activation energy of 226 kJ mol^{-1} . The experiments were conducted mostly in Re capsules ($P < 30 \text{ GPa}$). In addition at 35 GPa a graphite capsule experiment was performed. Although it is assumed that the experiments follow a trend compatible with the Re-ReO₂ buffer this assumption was not tested and the results are therefore unconstrained with respect to oxygen fugacity.

Silicate perovskite

In spite of the fact that (Mg,Fe)SiO₃ is believed to be the most abundant mineral in the Earth there is an overall lack of experimental Fe-Mg interdiffusion studies for this mineral.

Computer simulations were performed by Wright and Price (1993) using an ab initio atomistic simulation. The calculated activation enthalpy for intrinsic Si diffusion is so high ($H_a = 1113 \text{ kJ mol}^{-1}$) that these authors conclude that Si diffusion in the lattice most likely occurs by an extrinsic process. For Mg an extrinsic activation enthalpy of $440.6 \text{ kJ mol}^{-1}$ at 0 GPa and $717.0 \text{ kJ mol}^{-1}$ at 125 GPa was derived. For the pressure effect of diffusion, activation volumes of 2.1 and $4.96 \text{ cm}^3 \text{ mol}^{-1}$ for extrinsic and intrinsic Mg diffusion respectively were derived, whereas for Si a negative activation volume for extrinsic diffusion was found implying that Mg becomes the slowest diffusing species in the deeper parts of the lower mantle.

The only experimental study performed so far was a study of silicon self-diffusion in pure MgSiO₃ by Yamazaki et al. (2000). These authors measured lattice and grain boundary diffusion coefficients (D_l and D_{gb}) and give for both types of diffusion an Arrhenius relationship:

$$D_l \text{ (m}^2 \text{ sec}^{-1}\text{)} = 2.74 \times 10^{-10} \exp\left(\frac{-336 \text{ (kJ mol}^{-1}\text{)}}{RT}\right) \quad (1.18)$$

$$\delta D_{gb} \text{ (m}^3 \text{ sec}^{-1}\text{)} = 7.12 \times 10^{-17} \exp\left(\frac{-311 \text{ (kJ mol}^{-1}\text{)}}{RT}\right) \quad (1.19)$$

where δ denotes effective grain boundary width, R is the gas constant, and T is temperature.

1.4 Aims of the present study

In order to have a better understanding of kinetic processes occurring in the Earth (Section 1.1), experimental diffusion studies in a multianvil apparatus were performed

- to investigate the whole pressure stability range of olivine for a better constraint of the activation volume for Fe-Mg interdiffusion and Mn and Ni diffusion,
- to determine the activation energy for Fe-Mg interdiffusion in olivine at pressures close to the stability limit,
- to constrain the activation energy of Fe-Mg interdiffusion in wadsleyite,

- to establish a database of Fe-Mg interdiffusion in ferropericlase at pressures between 6 and 23 GPa and temperatures between 1653 and 2073 K at controlled oxygen fugacity conditions,
- to derive for the first time Fe-Mg interdiffusion coefficients in (Mg,Fe)SiO₃ perovskite, the most abundant mineral of our planet.

Chapter 2

Experimental Techniques

2.1 Introduction

For the determination of Fe-Mg interdiffusion coefficients in olivine, wadsleyite, ferropericlase and silicate perovskite, diffusion couple experiments were performed at high pressure in a multianvil apparatus. For diffusion studies, diffusion couples should have sample sizes of at least $\sim 250 \mu\text{m}$ diameter and $\sim 100 \mu\text{m}$ thickness, otherwise handling of the samples becomes extremely difficult. Therefore, the multianvil apparatus is the most suitable technique for studying the pressure range of 6-26 GPa, investigated in this study, because samples with volumes of 1 mm^3 can be easily accommodated. The upper pressure limit that can be reached with this technique, employing sintered WC cubes as pressure transmitting medium, is about 27 GPa. With sintered diamond cubes the pressure range can be extended to about 40 GPa (Irifune et al., 2002). Although the diamond anvil cell (DAC) can provide much higher pressures, equivalent to the whole pressure range of the lower mantle (23 - 137 GPa) and to core conditions (136-360 GPa), the sample volume is in general too small for diffusion couple experiments (for a description of the DAC see e.g. Eremets, 1996). In addition, temperature gradients in laser heated DAC are too high for precise diffusion coefficient determinations because of the strong dependence of diffusivity on temperature (Section 1.2.5). In this chapter, after explaining the basics of the multianvil technique (Section 2.2), the setup and the compositions of the diffusion couples for the different mineral systems are described (Section 2.3). For high pressure experiments a suitable capsule material has to be selected that does not destabilize the sample and provides a mechanically suitable (low stress) environment. The choice for capsule materials employed in this study is

outlined in Section 2.4. Section 2.5 describes the assemblies used for the high pressure diffusion experiments.

2.2 High pressure experiments: Multi anvil technique

The multianvil technique is described in detail in a number of publications (Kawai and Endo, 1970; Kawai et al., 1973; Spain and Paauwe, 1977a; Graham, 1987; Ohtani et al., 1987; Walker et al., 1990; Liebermann and Wang, 1992; Rubie et al., 1993; Rubie, 1999; Irifune, 2002).

The principles of the multianvil apparatus are shown schematically in Figure 2.1. The force of a hydraulic press is exerted onto a set of 6 steel anvils that form a cubic gap filled with 8 WC cubes. Because the corners of the WC cubes are truncated, they form an octahedral pressure chamber, which is filled by an MgO octahedron containing the sample capsule. All presses installed at the Bayerisches Geoinstitut with axial forces between 500 and 5000 t were used for performing experiments in this study (Table A.1). More details of the technique are given in Appendix A.

The maximum pressure that can be reached in an experiment depends on the force applied, the edge length of the octahedron and the truncation edge length of the cubes. For synthesis, experiments have been performed to produce starting samples of the high pressure phases wadsleyite and $(\text{Mg,Fe})\text{SiO}_3$ perovskite (see Section 2.3 for details) employing 14/8 and 10/4 assemblies where the first number is the octahedron edge length and the second number is the truncation edge length. A schematic drawing of the synthesis assemblies is shown in Figure 2.2. Because of the wide range of pressures covered for diffusion experiments in this study, a large variety of assemblies were employed, to accommodate the diffusion couples, by modifying the standard assemblies used at the Bayerischen Geoinstitut. The details of these assemblies are explained in Section 2.5 after a description of diffusion couples (Section 2.3) and sample capsules (Section 2.4).

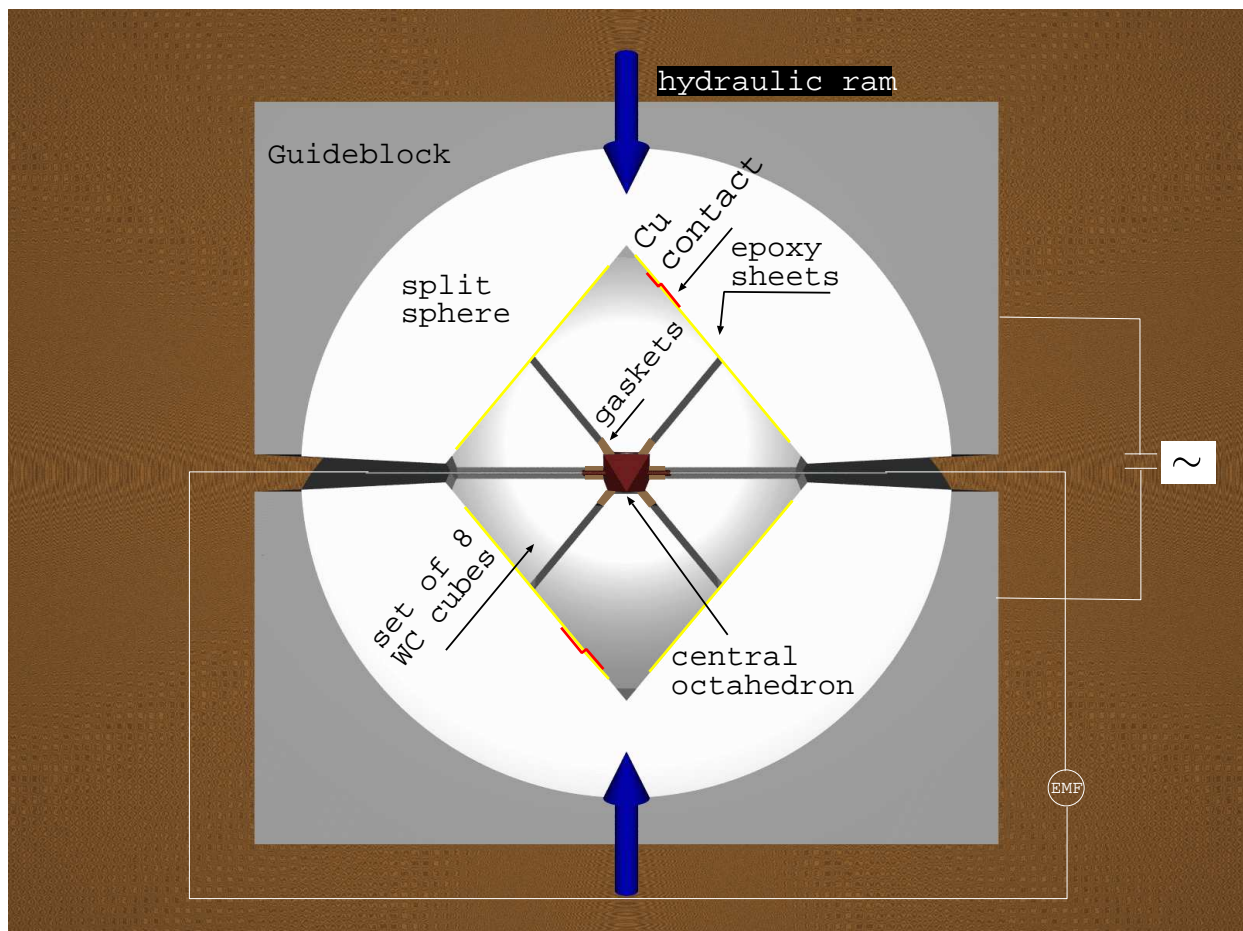


Figure 2.1: Schematic cross section of a multi-anvil apparatus. The hydraulic press is not shown, but the compression axis is indicated. The inner cubic gap of the first stage anvil system is filled with a set of 8 WC cubes used as second stage compression mechanism and leaving an octahedral pressure chamber filled with the sample assembly. Pyrophyllite gaskets separate the WC cubes and provide a pressure seal. The WC cubes are isolated from the steel anvils by epoxy sheets. The principal heating and thermocouple circuits are indicated by white lines.

2.3 Diffusion Couples

2.3.1 Diffusion couples: General remarks

The general strategy for an interdiffusion study is placing two single crystals or polycrystalline samples with different compositions in contact with each other and annealing this diffusion couple for a specific time that is long enough to generate a measurable compositional profile and short enough such that complete homogenization is avoided (for a general theory of diffusion

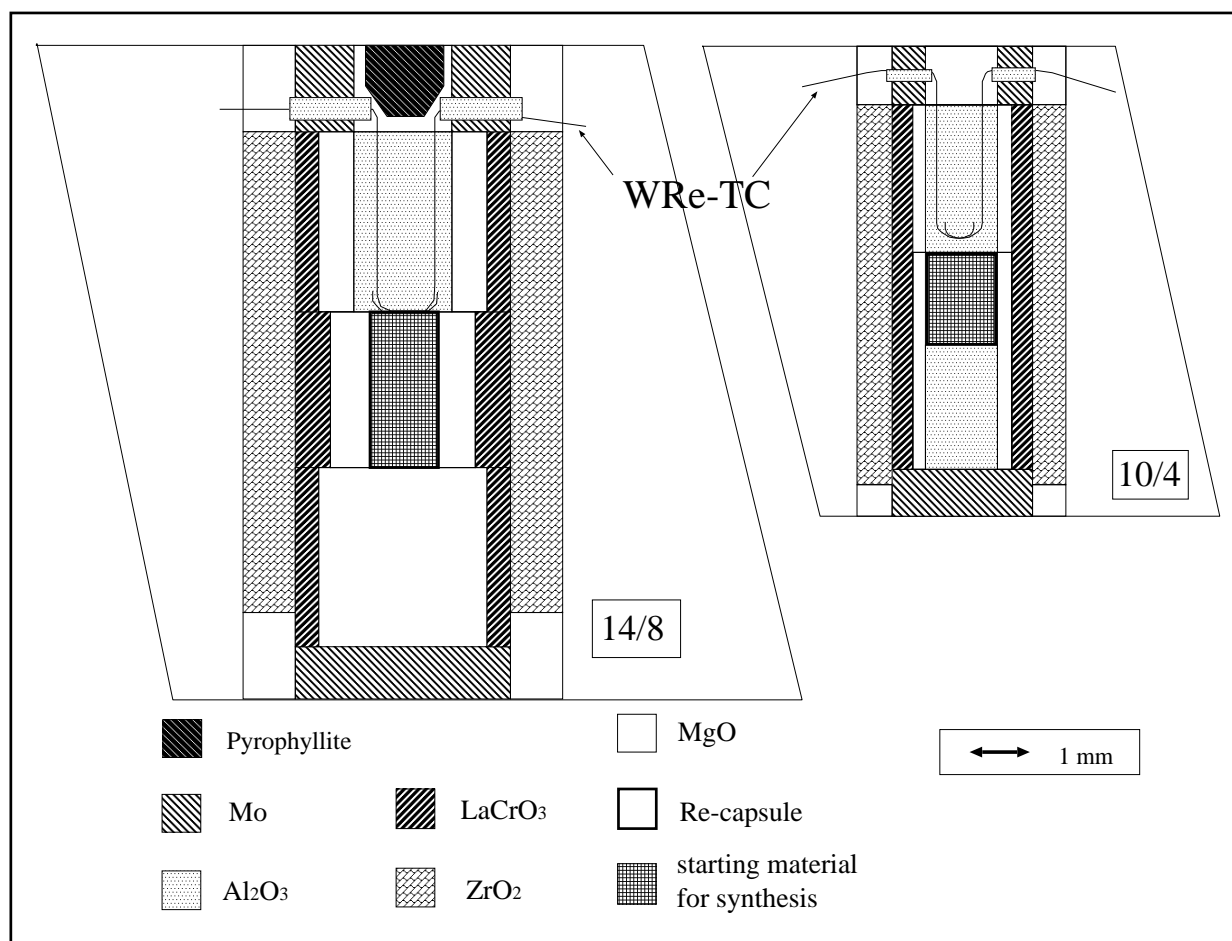


Figure 2.2: Assemblies used for synthesis experiments. The figure shows a cross section of the octahedron which is surrounded by WC cubes in Figure 2.1. WRe TC denotes W₉₇Re₃-W₇₅Re₂₅ thermocouple

couples and the atomistic details in an interdiffusion experiment, see e.g. Bocquet et al., 1983). The last requirement is, in general, difficult to achieve for studies of rapid diffusion occurring in silicate melts (Chakraborty, 1995) whereas the first requirement can be difficult to achieve for diffusion studies in crystalline solids. The experimental configuration of a diffusion couple is relatively close to the situation in nature where exchange of chemical components between two or more phases occur to reach a new equilibrium state (e.g. Chakraborty and Ganguly, 1992; Ganguly, 2002).

In order to determine accurate lattice diffusion coefficients, the use of single crystals is desirable for diffusion couples. When using polycrystalline samples, grain boundary diffusion may

also occur and either the experimental setup should allow for separation of the two effects or bulk diffusion should be the dominant process (for the theory of grain boundary diffusion see Herzig and Mishin, 1998). The last case is generally true for large grain sizes and high temperatures. In this study, single crystals were used in studies of olivine and ferroprecipitate, whereas for wadsleyite and perovskite, polycrystalline starting materials were synthesized prior to diffusion runs

The analysis of diffusion profiles after the diffusion experiments is described in Chapter 3 and the mathematical treatment of the diffusion profiles is described in Chapter 4.

2.3.2 Diffusion couples: Olivine

All olivine diffusion experiments utilized samples from the same two single crystals as starting materials. One endmember was synthetic pure Mg_2SiO_4 , forsterite, grown by the Czochralski method by H. Takei at Tohoku University. It is the same crystal (called Fo1) used by Chakraborty et al. (1994), where also trace element contents are given. The Fe content of this crystal is between 122 and 180 ppm. The Fe-bearing endmember was a natural single crystal from San Carlos with an average Mg-value $\text{Mg}/(\text{Mg} + \text{Fe}) = 0.94$ with 3000 ppm NiO and 1500 ppm MnO. Both crystals were oriented along the crystallographic c-direction by Laue backscatter diffraction such that the c axis is perpendicular to the diffusion interface. After the diffusion experiments the orientation of the two crystals was redetermined by electron backscatter diffraction (EBSD). The c-axes for both crystals were found in the diffusion plane perpendicular to the diffusion interface with an error of less than 4° .

For preparation of the diffusion couples the crystals were cut into polished thin slices with a thickness of $\sim 250 \mu\text{m}$. Discs were drilled out with a diameter of $250 \mu\text{m}$ (Au-capsule experiments) or $950 \mu\text{m}$ (Ni-NiO capsules). Polishing of the olivine slices (and wadsleyite as well) was performed with diamond spray (Struers) down to 0.25 microns. The two polished sides were then placed together and inserted into the capsule (see Section 2.4).

2.3.3 Diffusion couples: Wadsleyite

Wadsleyite diffusion couple experiments employing a single crystal as one endmember are described by Chakraborty et al. (1999), but the synthesis of crystals large enough for this study failed. Thus, polycrystalline wadsleyite samples were synthesized prior to diffusion runs as starting material. For all synthesis experiments a 14/8 assembly was used (for a description of the high pressure assemblies see Section 2.5). A polycrystalline pure Mg_2SiO_4 wadsleyite sample was prepared by annealing forsterite powder at 15 GPa and 1673 K in a 1000 t multi-anvil press employing a Re-foil capsule (Section 2.4). The powder with forsterite composition was kindly provided by D.J. Frost. For the Fe-bearing sample, a single crystal of olivine with $\text{Fe}/(\text{Mg} + \text{Fe}) = 0.84$ from San Carlos, kindly provided by S. Mackwell, was used. The conversion from olivine to wadsleyite was performed at 15 GPa and 1873 K, using a capsule prepared of Re-foil. Another Fe-bearing wadsleyite sample was synthesized from hot-pressed San Carlos olivine powder at 15 GPa and 1673 K in a Re-capsule. To confirm that the synthesized samples consisted of wadsleyite, the material was characterized by Raman spectroscopy (Fig. 2.3) using a LabRAM microraman instrument (Jobin Yvon GmbH). X-ray microdiffraction patterns could be easily indexed with the reference pattern of Moore and Smith (1970). The X-ray diffraction pattern contained only peaks that are attributable to wadsleyite. Unfortunately Moore and Smith (1970) only collected data for the interplanar spacing d_{obs} in the range $6.69 > d_{obs} > 0.9156$. Therefore assignment for low d-spacings (large θ) was not possible.

After synthesis the samples were removed from the high pressure assembly and the Re foil was withdrawn. Subsequently they were cut into discs $\sim 250 \mu\text{m}$ thick and mounted on glass slides to enable them to be polished in the same way as the olivine samples. After polishing, small discs were drilled out for use in diffusion couples as already described for olivine (Section 2.3.2).

2.3.4 Diffusion couples: Ferropericlase

Two ferropericlase single crystal slices ($500 \mu\text{m}$ thick) were obtained from S. Mackwell. They had been synthesized by embedding a slice of a pure synthetic single crystal of MgO in $(\text{Mg,Fe})\text{O}$ powder and annealing at controlled oxygen fugacity (Holzapfel et al., 2003). The resulting non-

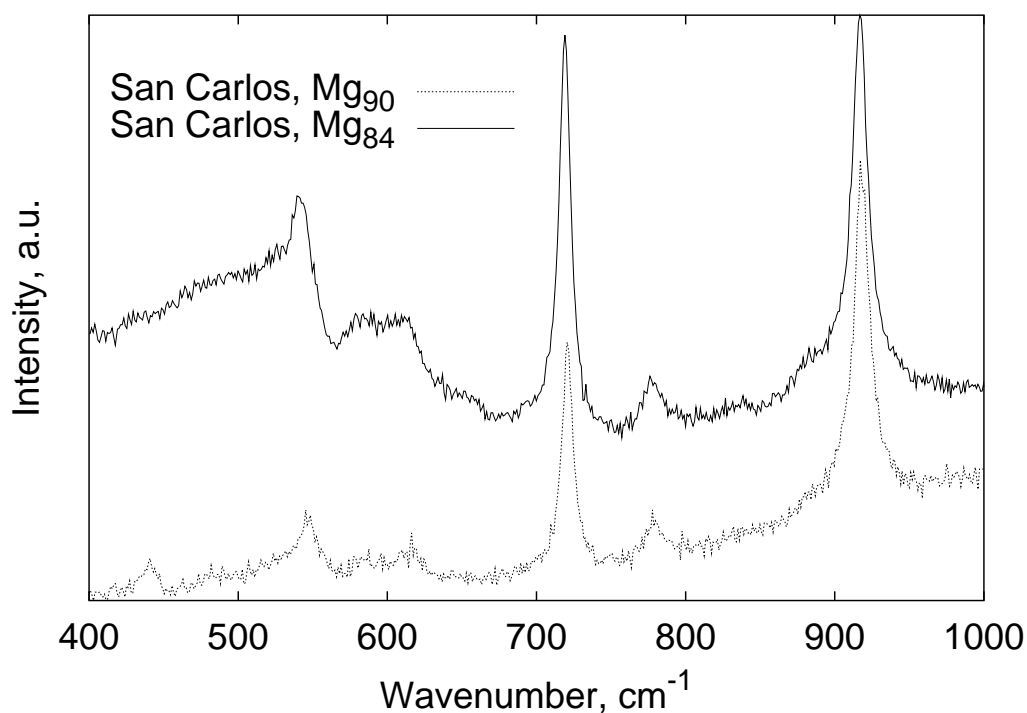


Figure 2.3: Raman spectra used to identify the $(\text{Mg,Fe})_2\text{SiO}_4$ phases produced in synthesis experiments for wadsleyite. Representative spectra from synthesis experiments performed at 15 GPa, 1873 K (Fo_{84}) and 1673 K (Fo_{90}) are shown. The Raman patterns can be identified as wadsleyite by comparing them to Raman patterns of wadsleyite and ringwoodite given in Figure 1 in McMillan and Akaogi (1987) and of forsterite using data from the web-based database of the California Institute of Technology at http://minerals.gps.caltech.edu/FILES/raman/Caltech_data.

inal compositions were $X_{\text{FeO}} = 0.07$ and $X_{\text{FeO}} = 0.35$, where X_{FeO} is mole fraction of FeO. The diffusion interface was polished with alumina powders to 0.3 microns. For the high-pressure diffusion experiments, discs 1 mm in diameter and 500 μm thick were drilled out as starting crystals. Electron microprobe traverses over the samples showed heterogeneities of less than ± 1.5 mole% FeO along the entire length of the crystal and less than ± 0.25 mole% over the 1 mm diameter of the diffusion couples. On one side of the low iron content crystal a well sintered layer with polycrystalline $(\text{Mg,Fe})\text{O}$ with the same composition and a Ca_2SiO_4 phase was observed after the experiments, possibly due to contamination during sample preparation.

2.3.5 Diffusion couples: (Mg,Fe)SiO₃ perovskite

Samples for diffusion runs were synthesized in Re-capsules, employing a 10/4 assembly (Figure 2.2), at 2073 K and 25 GPa using synthetic MgSiO₃ powder, (Mg,Fe)SiO₃ powder with varying Fe/Fe+Mg (kindly provided by D.J. Frost) and a single crystal of natural pyroxene (kindly provided by S. Mackwell) with $X_{\text{FeSiO}_3} = 0.136$. The pyroxene contains only trace amounts of aluminium and Calcium (850 ppm Al₂O₃ and 2200 ppm CaO), hence all compositions of the perovskite diffusion couples are restricted to the MgSiO₃-FeSiO₃ binary system.

The phase identity of the synthesis runs were checked by Raman spectroscopy. Typical spectra obtained by a Raman microscope are shown in Fig. 2.4. For Fe-bearing perovskite two relatively broad peaks occur at 727 and 894 wavenumbers. These are typical for samples containing Fe (C. Liebske and L. Dubrovinsky, pers. communication) and are probably attributable to a second order Raman effect due to disorder in the perovskite structure similar to that occurring in manganites or rare earth element perovskites (Dubrovinsky, pers. communication).

After the synthesis the samples were removed from the assembly and the Re-foil capsule, cut into discs $\sim 100 \mu\text{m}$ thick and mechanically polished. Because perovskites are unstable with respect to mechanical preparation, in addition to mechanical polishing, chemical polishing with a colloidal silica suspension (OP-S or OP-U suspension obtained from Struers A/S) was also performed. To test the crystallinity of the polished surfaces, orientation contrast imaging and electron backscatter diffraction (EBSD) were carried out using a LEO Gemini 1530 scanning electron microscope (SEM) equipped with a field emission gun (FEG). Both methods are based on scattering of electrons in the surface and hence can be used as a probe for surface crystallinity. Figure 2.5 shows an orientation contrast image of a pure MgSiO₃ sample. The orientation contrast observed, reveals the good crystallinity of the samples. If the area of observation is reduced significantly the surface becomes damaged by the electron beam and the orientation contrast quickly degrades. Yamazaki et al. (2000) reported that they observed EBSD patterns for their pure MgSiO₃ perovskite samples used to study Si self-diffusion although no example is given in their work. For the samples of this study very weak EBSD patterns only appeared for a very short time when scanning over a big crystal grain. A focused electron beam immediately destroys the surface of the crystal and no EBSD pattern can be obtained.

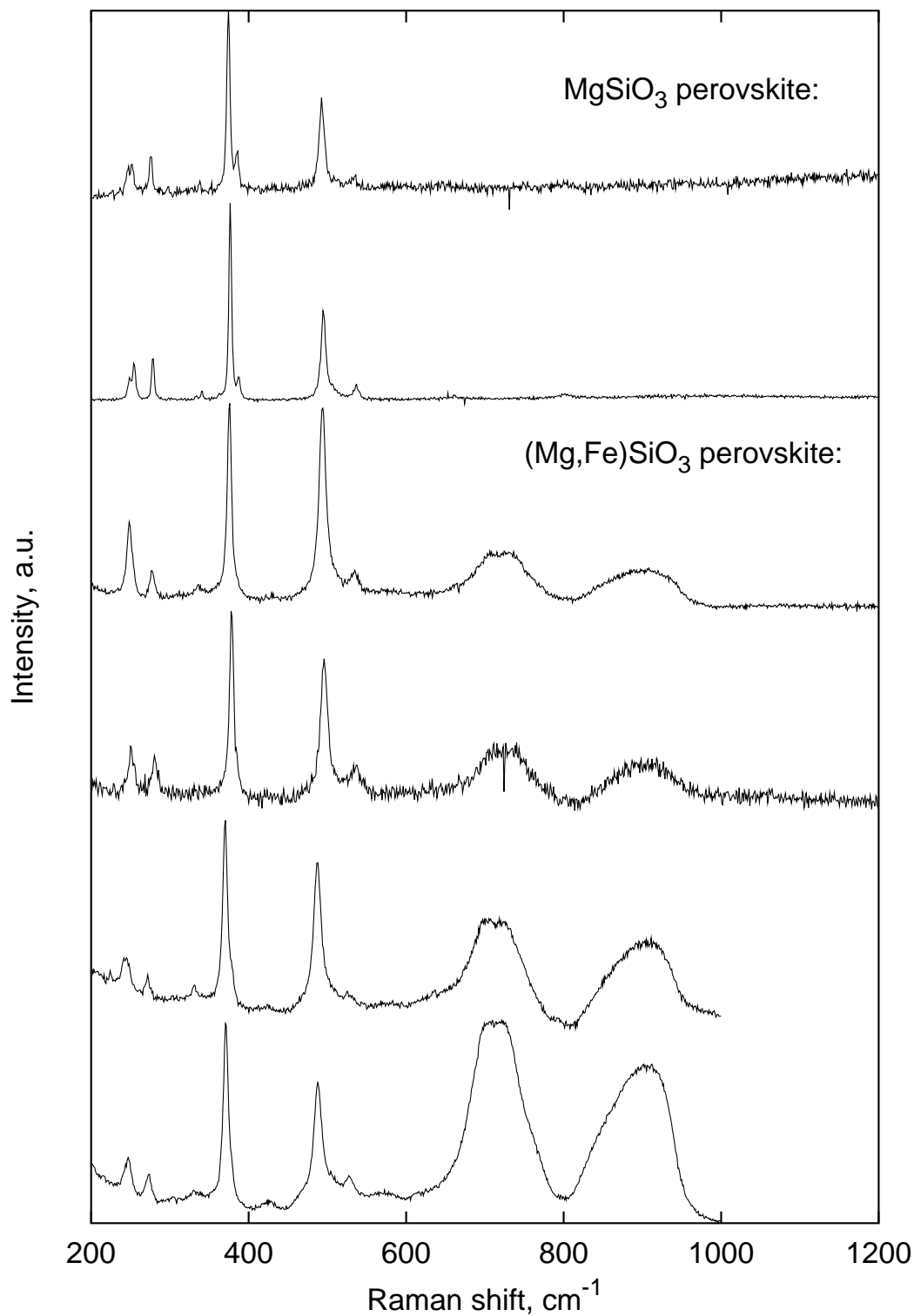


Figure 2.4: Typical Raman spectra from different synthesis runs. For Fe-bearing perovskite two broad bands appear at approximately 727 and 894 wavenumbers (see text for explanation).

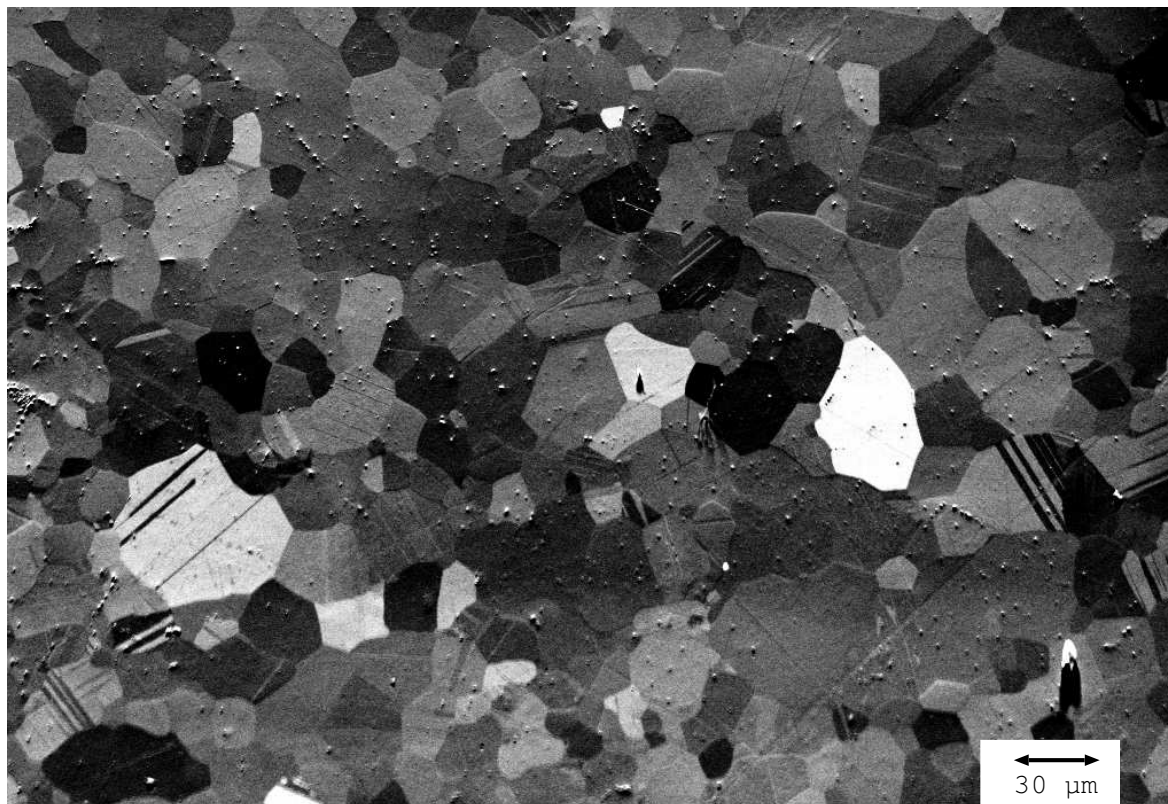


Figure 2.5: Orientation contrast image of a MgSiO₃ perovskite synthesized at 2073 K and 25 GPa for 2 hours. Ubiquitous twinning can be observed. The role of twinning and structural phase transitions is discussed in Sections 1.3.1 and 5.5.2

2.4 Capsules

Requirements for capsule materials

In previous studies of diffusion at high pressure several different capsule materials were employed (Béjina et al., 2003). The ideal capsule material does not interact chemically with the sample (for example no Fe loss), buffers the oxygen fugacity and is mechanically weak and thus provides a hydrostatic environment to minimize differential stresses imposed on the diffusion couple. It is difficult to meet all these requirements at the same time with any one capsule type. Therefore, different capsule materials were used in this study. For most of the olivine experiments, mechanically weak Au capsules were employed, as described in Chakraborty et al. (1999). To calibrate the oxygen fugacity conditions in the Au capsules some experiments were also performed using Ni capsules with added NiO. The addition of NiO buffers the f_{O_2} at the

	Au	Ni-NiO	MgO-Fe
ol	×	×	
wds		×	
fp		×	
pv		×	×

Table 2.1: Employment of the different capsule materials. The investigated minerals are olivine (ol), wadsleyite (wds), ferroperricite (fp), and silicate perovskite (pv). The capsule materials used are gold (Au), Ni-foil with added NiO (Ni-NiO) and MgO single crystals with an addition of Fe-foil (MgO-Fe). See text for further details.

Ni-NiO buffer. The Ni-NiO capsules were also used for ferroperricite, wadsleyite and some of the silicate perovskite experiments. In the case of silicate perovskite, for experiments at reducing conditions, MgO single crystal capsules with added iron foil were employed. The fO_2 in these capsules is fixed by the incorporation of Fe in MgO (Fe saturation). If a capsule is used that buffers the fO_2 it is necessary that the point defect chemistry of the phases investigated, reacts much faster than the actual diffusion process such that the point defect chemistry is in equilibrium. As argued by Chakraborty (1997), vacancy diffusion rates in olivine are much faster than cation diffusion (Nakamura and Schmalzried, 1983; Mackwell et al., 1988) resulting in a very fast point defect equilibration. In this study it is assumed that this can be generalized to the other mineral phases as well.

In the subsequent sections the details of the capsules are described, Fig. 2.6 shows a schematic view of the capsule types used for diffusion experiments and Table 2.1 lists which capsule materials have been used for different phases and conditions.

Re capsules

Re capsules were used solely for synthesis experiments for preparing the starting samples for the wadsleyite and perovskite diffusion couples (Section 2.3). Therefore, they are not listed in Table 2.1 or shown in Figure 2.6. The dimensions depended on the kind of assembly used (see section 2.5). In case of a 10/4 assembly the outer diameter is 1.2 mm and the length is 1.6-2.1 mm, in the case of a 14/8 assembly the outer diameter is 1.6 mm and the length is 2.7 mm. The preparation of these capsules was performed by first folding the ends of a cylindrical role of Re-foil and cleaning this container in an ultrasonic bath. Then the powder or crystal used in the synthesis

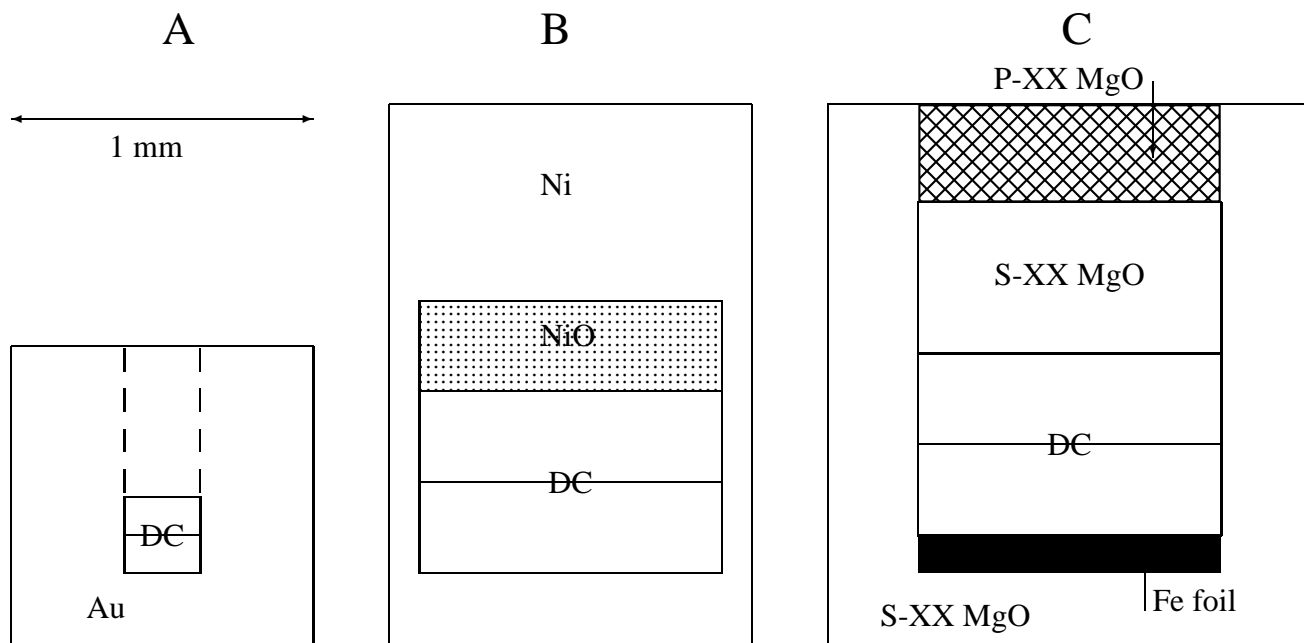


Figure 2.6: Graphical representation of the three different capsule types used for high pressure diffusion runs. A: Au capsule, B: Ni-NiO capsule, C: MgO-Fe capsule. P-XX denotes polycrystalline. S-XX denotes single crystal, and DC denotes diffusion couple.

run is added and in case of the powder slightly compressed with a steel rod. Subsequently the capsule is closed by folding the surmounting ends over and gently pressing it together.

Au capsules

For preparation of the capsules a Au wire of 1mm diameter was drilled with a hole of $250 \mu\text{m}$ diameter. Discs of the single crystals of olivine (see Section 2.3.2) were carefully inserted and the capsule closed. Figure 2.6 shows the capsule schematically. After insertion of the diffusion couple the sample was closed by deformation of the soft capsule (Chakraborty et al., 1999).

MgO-Fe capsules

This capsule type was used solely for a set of experiments on silicate perovskite. A cylinder was drilled out of a commercially available single crystal of MgO with a diameter of 1.5 mm. Into the cylinder an inner hole was drilled with a diameter of 1.0 mm. Into the bottom of the inner hole

an Fe disc was inserted on top of which the two slices of polycrystalline perovskite were placed. Another single crystal MgO disc was added to be able to study interaction of Fe with MgO as well, and then the rest of the capsule was filled with a polycrystalline MgO disc. The reducing conditions of this capsule type imposed by the Fe-distribution between Fe-metal and (Mg,Fe)O, formed on the rim of the capsule, should mimic oxygen fugacity conditions prevailing during core formation and at the present-day core-mantle boundary.

Ni-NiO capsules

This capsule type was used for all phases investigated in this study (Table 2.1). The Ni capsules were prepared by rolling Ni-foil (thickness 125 μm , 99.98%, Goodfellow) into a cylinder and folding one end over to form the bottom of the capsule. The two polycrystalline slices of wadsleyite or perovskite or single crystals of olivine or ferropericlase were inserted such that the polished sides were together. NiO powder was added on top of the diffusion couple. The NiO powder was previously dried at 1273 K in an Al_2O_3 -crucible to prevent water contamination. At these conditions the crucible did not react with the powder to form Ni-Al spinel as confirmed by microprobe analysis. The capsule was subsequently closed by folding the end of the foil and gently uniaxially compressing the capsule.

In this kind of capsule the oxygen fugacity should be close to the Ni-NiO buffer system. Ni+NiO was also used in the experiments of Farber et al. (2000) to buffer oxygen fugacity. These authors claim that the SiO_2 -activity was buffered by the equilibrium of NiO and Ni_2SiO_4 , which was also present in their experiments. By a similar reasoning silica activity in this study should be controlled in the case of olivine by formation of a Ni_2SiO_4 component due to Mg-Ni exchange at the NiO-olivine interface and subsequent SiO_2 buffering due to the equilibrium of Ni-metal and Ni_2SiO_4 dissolved in olivine.

2.5 Assemblies used for high pressure diffusion experiments

For experiments at pressures between 6 and 15 GPa a 14/8 type multianvil assembly and for pressures between 15 and 26 GPa a 10/4 type multianvil assembly were used. In the 5000 t press (Zwick, Table A.1), where sample volumes are significantly larger, an 18/8 multianvil assembly

	14/8	10/4	18/8
ol	6-12		
wds	15		
fp	8-12	16-23	
pv		25-26	22

Table 2.2: Range of use of the different octahedral assemblies. The numbers given for each combination of mineral phase (ol = olivine, wds = wadsleyite, fp = ferropericlase, pv = perovskite) and octahedral assembly (see text for explanation of assembly abbreviations) denote investigated pressure range in GPa.

could be employed for two silicate perovskite diffusion experiments at pressures of 22 GPa. Table 2.2 shows the assemblies used and the pressure range attained for the different minerals investigated in this study. For a detailed description of multianvil assemblies see also Liebermann and Wang (1992), Walter et al. (1995), and Rubie (1999).

Fig. 2.7-2.9 show the details of the multianvil assemblies for the different phases investigated. The details are described in Appendix A. The 10/4 assembly employs a straight LaCrO_3 resistance heater where temperature gradients can be as high as 100 K/mm (Trønnes, 2000), whereas all other assemblies use a stepped LaCrO_3 heater greatly reducing temperature gradients (Rubie et al., 1993). In all cases a W_{97}Re_3 - $\text{W}_{75}\text{Re}_{25}$ thermocouple was used and temperature was not corrected for the pressure effect on the electromotive force (for a discussion of the maximum error involved, see Appendix A).

For pressure calibration, known phase transition points are employed in order to calibrate the oil pressure of the hydraulic system against the pressure acting on the sample. For the 14/8 assembly (olivine, ferropericlase and wadsleyite experiments) the coesite \rightleftharpoons stishovite (Zhang et al., 1996) and the Mg_2SiO_4 $\alpha \rightleftharpoons \beta$ (Morishima et al., 1994) phase transformations at 1473 K were employed. The calibration for the 10/4 assembly (ferropericlase, $(\text{Mg,Fe})\text{SiO}_3$ perovskite experiments) was based on the phase boundaries of $\gamma \rightleftharpoons$ perovskite + MgO, $\beta \rightleftharpoons \gamma$, and $\alpha \rightleftharpoons \beta$ in Mg_2SiO_4 (Akaogi et al., 1989; Morishima et al., 1994; Suzuki et al., 2000) as well as the ilmenite \rightleftharpoons perovskite phase boundary in the system MgSiO_3 (Ono et al., 2001). For the 18/8 assembly the Mg_2SiO_4 $\alpha \rightleftharpoons \beta$, the Mg_2SiO_4 $\beta \rightleftharpoons \gamma$ phase boundaries both at 1673 K (Morishima et al., 1994), with the additional constraint of an unbracketed occurrence of MgSiO_3 perovskite at 2273 K were used.

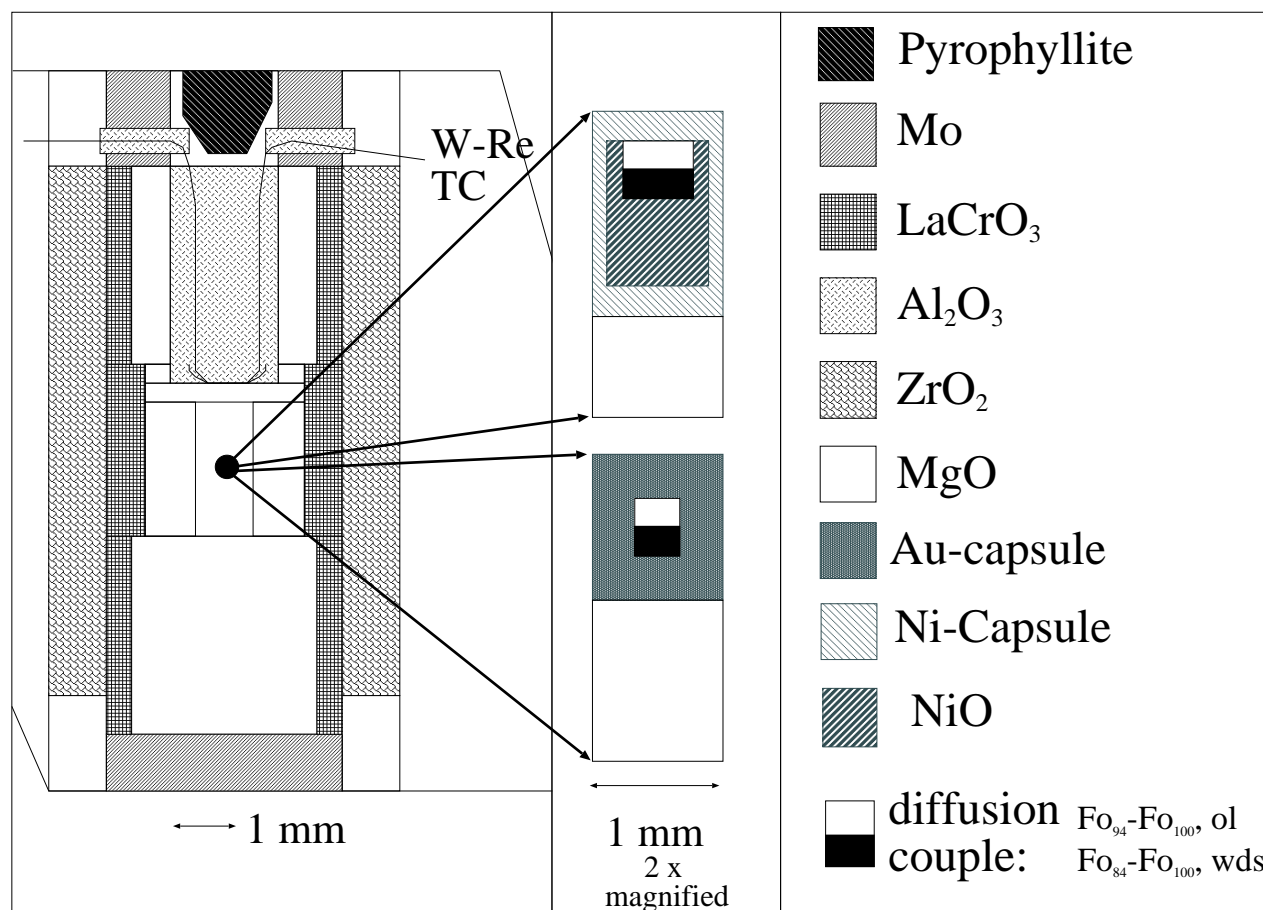


Figure 2.7: Pressure assembly used for olivine (ol) and wadsleyite (wds) diffusion experiments in this study. All dimensions are given in mm. For olivine, the sample consists either of a diffusion couple of two single crystals enclosed in a Au capsule or a single crystal diffusion couple in a Ni-NiO capsule. For wadsleyite, experiments were performed employing polycrystalline diffusion couples in a Ni-NiO capsule. W-Re TC denotes $\text{W}_{97}\text{Re}_3\text{-W}_{75}\text{Re}_{25}$ thermocouple, the composition of the diffusion couples is given as e.g. Fo_{94} = 94 mol% forsterite component.

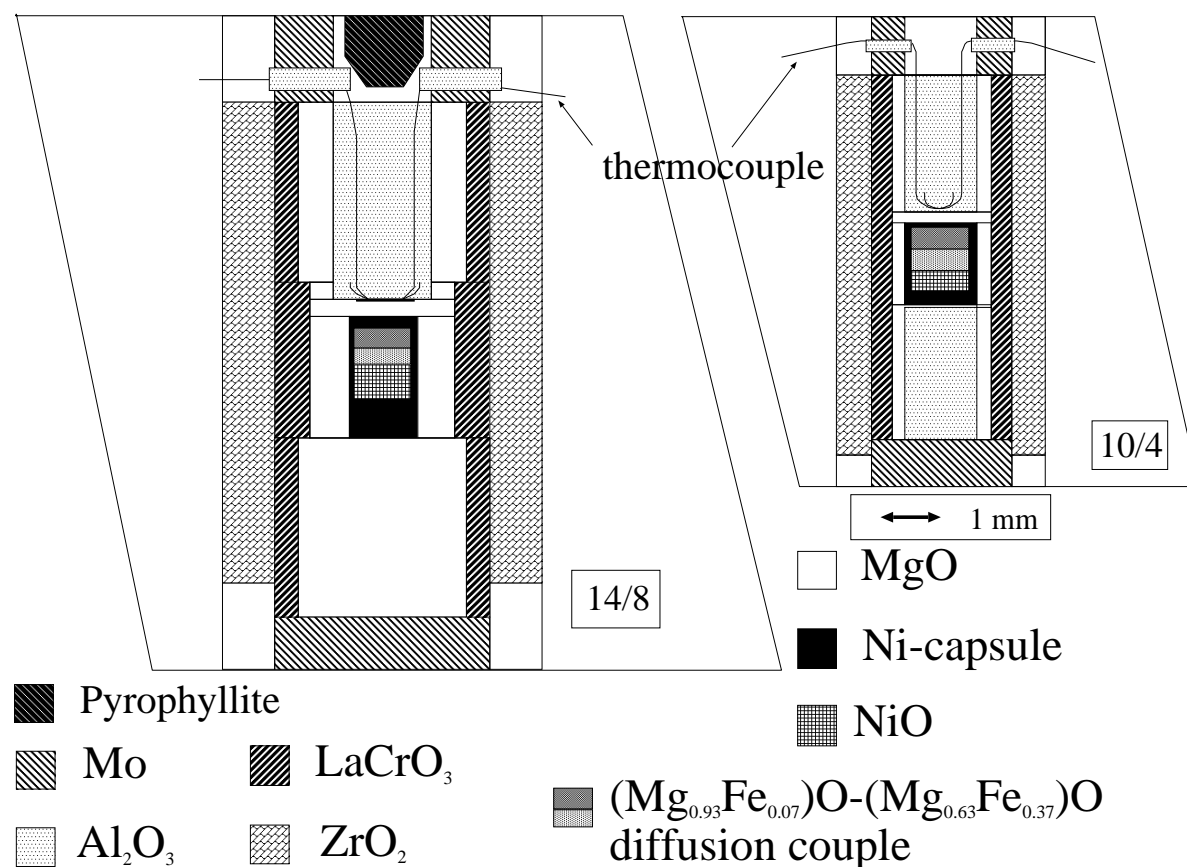


Figure 2.8: Pressure assemblies for multianvil experiments used in this study for ferropericlase. At $P < 16$ GPa a 14/8 assembly (14 mm edge length of the octahedron, WC cubes with 8 mm edge length corner truncations) and at $P \geq 16$ GPa a 10/4 assembly were used. The sample capsule consists of Ni foil with the addition of NiO to buffer f_{O_2}

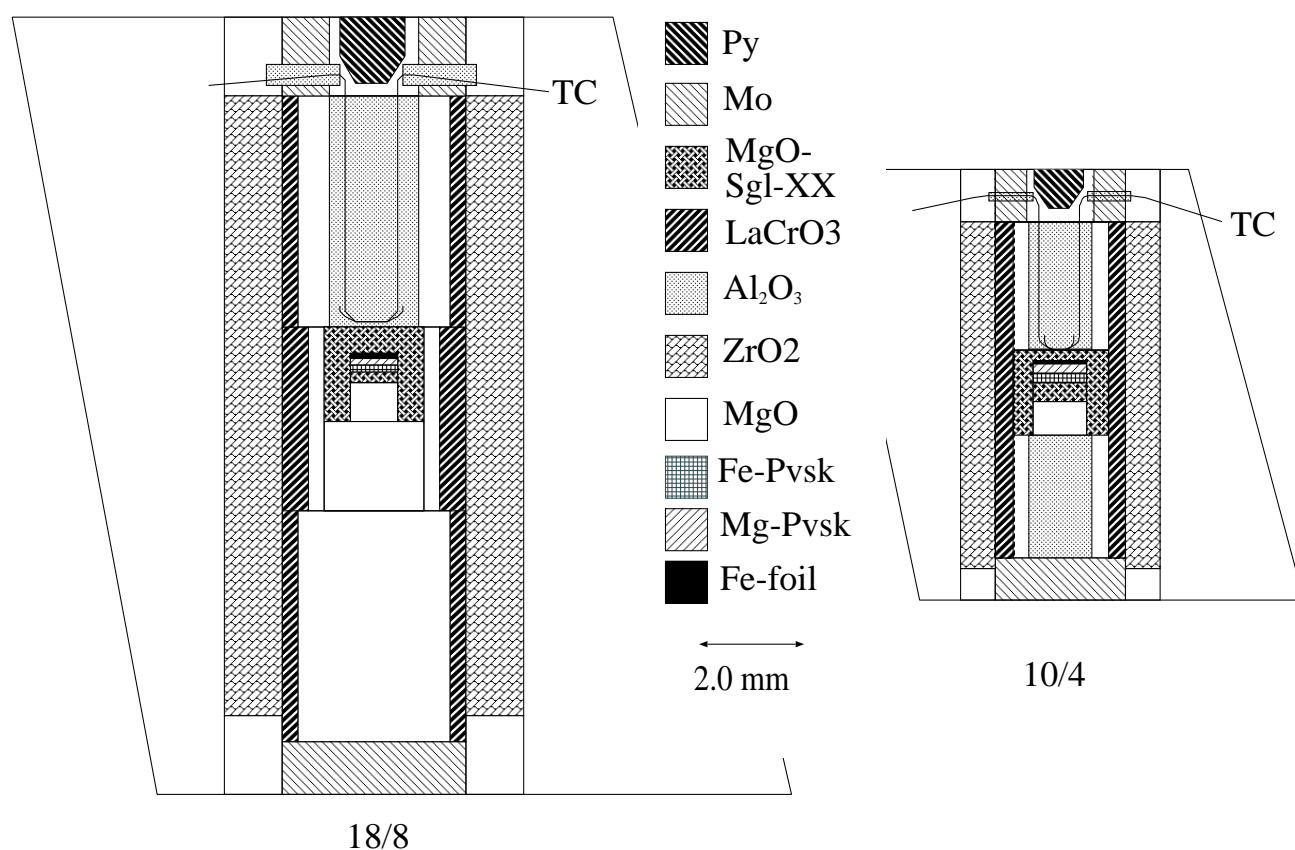


Figure 2.9: Pressure assembly used for perovskite diffusion experiments in this study. An 18/8 assembly was employed in a 5000 t press at 22 GPa for temperatures higher than 2273 K. For lower temperatures a 10/4 assembly was used at pressures of 25-26 GPa in a 1000 t or 1200 t press. Sgl-XX denotes single crystal, TC denotes W₉₇Re₃-W₇₅Re₂₅ thermocouple, and Py denotes pyrophyllite. In addition to MgO-Fe capsules also Ni-NiO capsules were employed in the 10/4 assembly for some of the experiments, similar to the ferropericlasite experiments shown in Fig. 2.8.

Chapter 3

Chemical analysis of diffusion profiles

3.1 Choice of analysis techniques

For determining interdiffusion coefficients using the diffusion couple technique, diffusion profiles have to be measured with an analytical technique with sufficient precision and lateral resolution. For the purpose of profile analysis, after the anneal at high temperatures and pressures, the sample is cut in a plane perpendicular to the interface to obtain access to the diffusion zone. In practice, for multianvil experiments, the octahedron is mounted in epoxy resin and polished until the middle of the diffusion couple is exposed (Figure 3.1).

For measuring the diffusion profiles the samples are first investigated by electron microprobe analysis (EPMA). The lateral resolution for a single point analysis is on the order of $\sim 2 \mu\text{m}$ hence resulting in a minimum profile length of $\sim 6 \mu\text{m}$ (see Section 3.2). For profiles shorter than the resolution limit of EPMA, the transmission electron microscope (TEM) equipped with a Ge solid state energy-dispersive X-ray detector (EDX) is used (Section 3.3). This technique recently became an invaluable tool for studying short diffusion profiles (Meißner et al., 1998). In addition to the high lateral resolution, on the order of 10 nm, microstructural investigations can be performed in conjunction with EDX analysis.

For thin film diffusion experiments, used in studies of tracer diffusion, many other analytical techniques with a very good depth resolution exist, such as secondary ion mass spectrometry (SIMS), photoelectron spectroscopy, Auger electron spectrometry, Rutherford backscattering, or nuclear reaction analysis (an overview of these techniques with respect to diffusion studies can be found in Philibert, 1991). These different methods are difficult to apply for diffusion couple

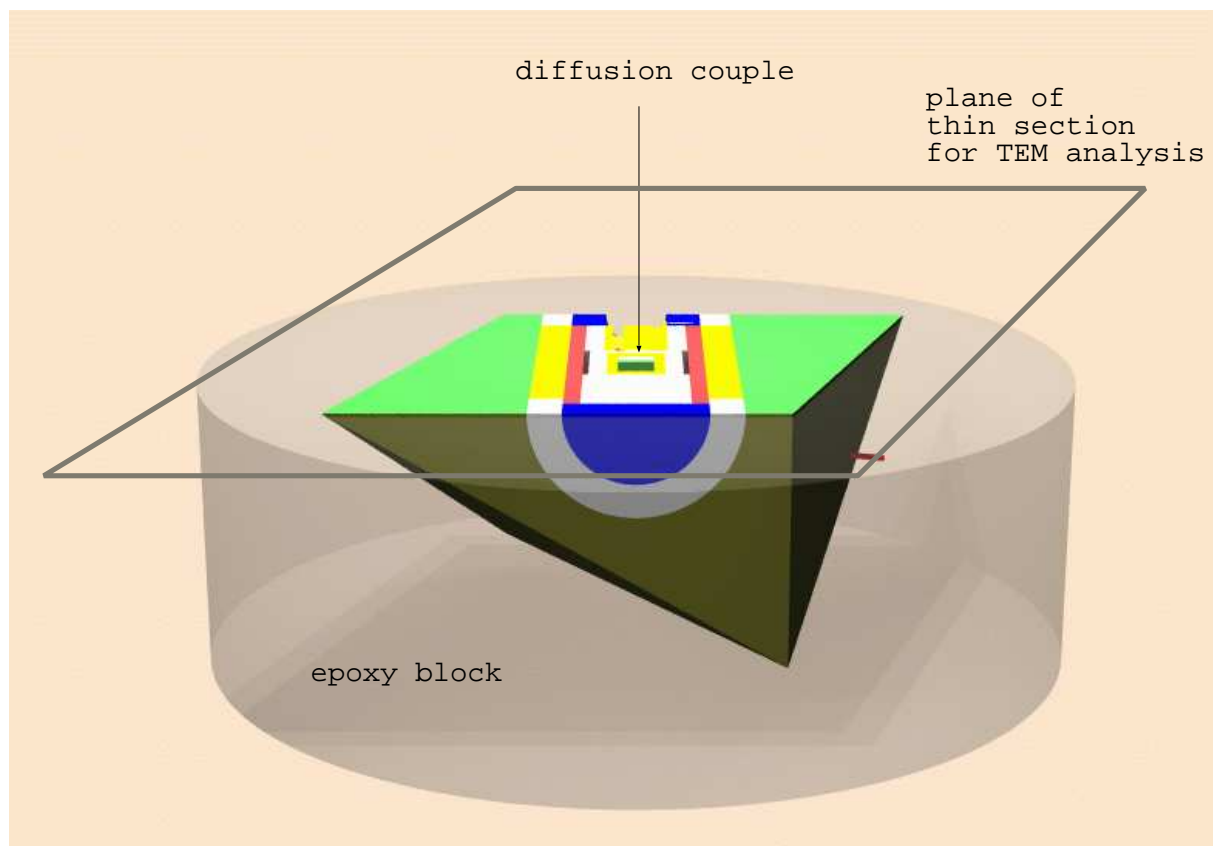


Figure 3.1: After the interdiffusion experiment the octahedron containing the diffusion couple is mounted in epoxy resin and polished down until the diffusion couple is exposed at the surface (a 10/4 assembly is schematically shown as an example, compare with Fig. 2.8 and 2.9). This block is directly used for electron microprobe analysis. For investigations of short diffusion profiles with a transmission electron microscope a glass slide is glued on top and the backside of the sample is polished away such that a thin slide with a thickness of $\sim 30 \mu\text{m}$ remains, which can be further thinned to obtain an electron transparent sample (Section 3.3).

experiments because the diffusion zone can not be investigated in depth mode and the lateral resolution of the aforementioned techniques often makes them unsuitable.

3.2 Electron microprobe analysis (EPMA)

Reviews about the method can be found in Reed (1975), Heinrich and Newbury (1991), Scott et al. (1995), or Newbury et al. (1984). During analysis, the sample is subjected to an incident electron beam. Interactions of the electrons with the atoms in the sample give rise to a number of

secondary signals, among them characteristic X-rays. The X-rays can be detected either with an energy dispersive or a wavelength dispersive system. The latter method has much better energy resolution and lower detection limits and is used for quantitative analysis in the case of EPMA, whereas the TEM used for short profile investigations is equipped with an EDX system (see next Section).

The lateral resolution depends on the diameter of the interaction volume excited in the sample. The shape and size of the interaction volume can be modeled by Monte Carlo simulations (see literature cited in Scott et al., 1995). For operating conditions of 10-20 kV, used in this study, the smallest diameter of the interaction volume is on the order of 2 μm if the beam is carefully focused on the sample. The best focus was achieved by aligning the objective aperture by means of a cathodoluminescence spot on SnO_2 . Resolution was optimized by correcting for astigmatism at high magnifications. With this diameter, profile convolution becomes significant for a profile length of less than 8 μm . The mathematical treatment of deconvolution is evaluated in Ganguly et al. (1988).

In this work, a Cameca SX-50 equipped with 4 wavelength dispersive spectrometers and a Jeol JXA 8900 RL at the Institut für Mineralogie und Geochemie, Universität zu Köln, equipped with 5 wavelength dispersive spectrometers, were employed. Tables 3.1 and 3.2 list standards and measurement conditions for EPMA. Samples were carbon coated (thickness ~ 12 nm) to avoid charging of the surface. Olivine, wadsleyite, ringwoodite and ferropericlasite were studied at acceleration voltages of either 15 or 20 kV and probe currents between 15 and 20 nA. All phases are stable at these conditions. On the contrary $(\text{Mg,Fe})\text{SiO}_3$ perovskite is very unstable under the electron beam. To minimize beam damage the probe current was reduced to 5 nA at 15 kV. The clearly visible cathodoluminescence spot on pure MgSiO_3 perovskite decays within 2 sec at these conditions, implying a very fast amorphization.

The detection limits given in Tables 3.1 and 3.2 are calculated by the Cameca software (Version 2.15). For major elements, normal working conditions at 15-20 kV and 5-20 nA ensure sufficient relative precision below $\sim 1\%$ at measurement times between 5 and 20 sec (Reed, 1996). Only for the trace elements Ni and Mn in olivine, it was critical to extend the counting time to 120 and 150 sec on the peak and 60 and 75 sec on the background, respectively. The

Element	Crystal	St	time, sec		HV, kV	PC, nA	C_{min} , ppm
			P	B			
Si	TAP	en,ol	20	10	15-20	15-20	637-1004
Mg	TAP	MgO,en,ol	20	10	15-20	15-20	635-1217
Fe	LIF	Fe,ol,Fe ₂ O ₃	20-30	10-15	15-20	15-20	520-4094
Ni	LIF	NiO	20	10	15-20	15-20	2194-4014
Ni	LIF	Ol	120	60	15-20	20	58-98
Mn	LIF	Ol	150	75	15-20	20	32-47

Table 3.1: Conditions of EPMA for olivine, wadsleyite and ferroperricite. For the trace elements Ni and Mn longer counting times were necessary than the counting times for major elements. Hence, in olivine counting times of 120 sec on the peak position for Ni was chosen, whereas in experiments in Ni-NiO capsules Ni was measured for only 20 sec on the peak position. Mn was only determined in olivine experiments. Abbreviations: TAP = Thallium acid phthalate (with $2d = 25.75$ Å), LIF = Lithium fluoride (with $2d = 4.028$ Å), en = enstatite, ol = San Carlos olivine, C_{min} = detection limit as calculated with the Cameca software (Version 2.15), P = Peak, B = Background, HV = high voltage, PC = probe current, St = standard.

Element	Crystal	St	time, sec		HV, kV	PC, nA	C_{min} , ppm
			P	B			
Si	TAP	en	5-10	2.5-5	15	5-10	1836-2585
Mg	TAP	en	5-10	2.5-5	15	5-10	1920-2716
Fe	LIF	Fe,ol	5-10	2.5-5	15	5-10	2773-14000

Table 3.2: Conditions of EPMA for silicate perovskite. Abbreviations: see Table 3.1

relative statistical error of the measurement is less than 2% at these conditions (Petry, 1999b). For some elements different standards were tested (Tables 3.1 and 3.2) to optimize analyses with totals closest to 100 %.

3.3 Transmission electron microscopy

The technique and various applications are described in detail in Edington (1976) and Williams and Carter (1996). The principle of the method is based on the fact that very thin specimens become transparent to an electron beam. Typically the acceleration voltage is between 100 and 300 kV (but acceleration voltages as high as 1.4 MeV have been used) and the thickness of the

sample should not be greater than a few hundred nanometers. In favorable instances a resolution on the atomic scale can be achieved (High Resolution Transmission Electron Microscopy, HRTEM), depending on lattice constants and the stability of the structure.

Unlike EPMA, sample preparation is elaborate because the samples have to be thinned to be electron transparent. Diffusion profiles in ferropericlase and wadsleyite samples were long enough to be analyzed by EPMA but some of the olivine experiments resulted in profiles which might be susceptible to convolution effects (see Section 5.2). Silicate perovskite diffusion profiles could only be investigated by TEM-EDX (Section 5.5). Thus, samples consisting of diffusion couples in olivine and silicate perovskite were thinned for TEM analysis.

For thinning, the microprobe blocks (Fig. 3.1) were first prepared into thin sections approximately 30 μm thick. The thin sections were glued to the slide with Lakeside, a glue dissolvable in acetone. Subsequently, grids of Cu or Mo (75 mesh) were mounted with Araldite (Ciba-Geigy) on top of the thin sections such that the region of interest for the analysis is in the center or slightly off-center of a central mesh. After removing the sample from the glass slide by dissolving the Lakeside glue with Acetone, thinning is performed in a Gatan dual ion mill, model 600, at an angle of 14° , 4 kV acceleration voltage and 1 mA beam current of the Ar^+ -ion beam. Samples consisting of silicate perovskite were always cooled with liquid nitrogen to prevent beam damage of the samples by the argon ion beam. The acceleration voltage was reduced to 3.5 kV at the end of the thinning process to further minimize beam damage. For silicate perovskite, normal thinning durations are on the order of 30-40 h, whereas for olivine the time for thinning is significantly shorter, in the range of 15-20 h. The relatively long thinning duration of perovskite is due to the mechanical hardness of the material that contrasts with its structural instability with respect to temperature. Although pure MgSiO_3 perovskite is more sensitive to electron bombardment, it is thinned slower than Fe-bearing silicate perovskite. In samples where the difference in Fe-content is relatively large, it is difficult to avoid a large thickness variation across the interface. As for EPMA, samples have to be coated to avoid charge built-up on the surface. Carbon coating was performed in a BAL-TEC, MED020, coating system. The thickness of the coating is less than 5 nm (Lauterbach, 2000).

In this study a Philips CM20 FEG (field emission gun) TEM, operating at 200 kV, has been

used. The advantage of using a FEG is having a bright and coherent source. Because of the high brightness of a FEG, the detectability limits (smallest amount of an element that can be detected) are on the order of 0.1 % or less (Williams and Carter, 1996). For a comparison of different TEM gun systems see Table 5.1 in Williams and Carter (1996). The instrument is equipped with a scanning unit which was used for beam control during the analysis performed in this study. A Ge solid state detector with a Novar ultrathin film window, enabling the measurement of light elements using for example the oxygen k_{α} line, was employed for EDX analysis.

In a pioneering work, Meißner et al. (1998) and Meißner (2000) studied the measurement of short interdiffusion profiles in olivine, using the same instrument as in this study. The spatial resolution of the instrument is thoroughly discussed in Meißner (2000) and found to be between 10 and 26 nm diameter for spot sizes (on the surface of the sample) between 2 and 5 nm.

EDX spectra were collected for a total counting time of 60 sec at 200 kV. No peak overlap occurs for elements analyzed in olivine or silicate perovskite. Analyses were preferably taken in regions that result in a deadtime of 20-30%. Spectra were collected employing the EDX software Vantage 1.4 (Noran). For the determination of intensities, the Filter-Fit fit method of the Vantage software was used, which employs a digital top hat filter for removing the background. The sample was always tilted at an angle of 15° towards the detector. With aid of the Analysis Manager of the Vantage software, line profile analysis was automatized by specifying the startpoint, the endpoint and the number of measurements.

For quantification of the measured intensities the Cliff-Lorimer ratio technique with absorption correction was used. In the limit of an infinitely thin sample, where absorption or fluorescence can be neglected, the composition can be calculated by (Williams and Carter, 1996):

$$\frac{c_{\alpha}}{c_{\beta}} = k_{\alpha\beta} \frac{i_{\alpha}}{i_{\beta}} \quad (3.1)$$

where c_{α} and c_{β} are the weight percentages of the elements α and β respectively, i_{α} and i_{β} are the intensities and $k_{\alpha\beta}$ is the Cliff-Lorimer factor. This factor has to be determined for each acceleration voltage and each element relative to a reference element by the parameterless correction method of Van Cappellen (1990). Examples are described in Langenhorst (1995) and Meißner (2000). Si was used as the reference element. For each element a series of spectra on a standard is measured at the same conditions as for the sample. The concentration of α , calculated with

$k_{\alpha\beta} = 1$ is plotted against the raw counts per unit time $rcps = (i_{\alpha} + i_{Si})/t$, which is a monotonous function of thickness. A regression of this plot extrapolated to $rcps = 0$ counts sec^{-1} leads to the apparent concentration at zero thickness. The ratio of the correct concentration and the apparent concentration resulting from extrapolation gives the Cliff-Lorimer factor.

Unlike EPMA only the absorption effect has to be corrected for in TEM-EDX. The absorption-corrected k factor $k_{\alpha\beta}^A$ can be derived by:

$$k_{\alpha\beta}^A = k_{\alpha\beta} \cdot k^A \quad (3.2)$$

According to Williams and Carter (1996) the absorption correction factor k^A can be expressed as:

$$k^A = \frac{\left[\frac{\mu}{\rho}\right]_{spl}^{\alpha} \cdot \frac{1 - \exp\left(-\left[\frac{\mu}{\rho}\right]_{spl}^{\beta} \rho t \operatorname{cosec}(\gamma)\right)}{\left[\frac{\mu}{\rho}\right]_{spl}^{\beta}}}{\left[\frac{\mu}{\rho}\right]_{spl}^{\beta} \cdot \frac{1 - \exp\left(-\left[\frac{\mu}{\rho}\right]_{spl}^{\alpha} \rho t \operatorname{cosec}(\gamma)\right)}{\left[\frac{\mu}{\rho}\right]_{spl}^{\alpha}}} \quad (3.3)$$

where the mass absorption coefficient for a specific X-ray of element α in the sample $\left[\frac{\mu}{\rho}\right]_{spl}^{\alpha}$ is calculated by summing the mass absorption coefficients of this X-ray with respect to each element in the sample $\left[\frac{\mu}{\rho}\right]_i^{\alpha}$ times their concentration c_i :

$$\left[\frac{\mu}{\rho}\right]_{spl}^{\alpha} = \sum_i \left(c_i \cdot \left[\frac{\mu}{\rho}\right]_i^{\alpha}\right) \quad (3.4)$$

In Equation 3.3, values for the density, thickness and take off angle have to be known independently for each measurement spot. It is possible to avoid this difficulty for ionic compounds, according to Van Cappellen and Doukhan (1994), using the electroneutrality constraint. Values for the density and take off angle are fixed during the calculation at 4 g/cm^3 and 14° and then the thickness is varied until the absolute sum of all positive charges just equals the absolute sum of all negative charges:

$$\sum_{cation} |(X_{cation} \cdot V_{cation})|_t = \sum_{anion} |(X_{anion} \cdot V_{anion})|_t \quad (3.5)$$

where X is the atomic concentration of the anion or cation, V is the valence state of the cation or anion, and t is thickness.

For quantifying EDX-TEM profile analysis, Equations 3.1-3.5 were incorporated into a self-generated computer program, TEMQuant, that automatically reads the intensities from the datafile generated by the Vantage software. TEMQuant is described in detail in Appendix B.

For silicate perovskite, Mg-loss inevitably occurs during analysis. This effect is especially evident at very thin parts of the sample near the edge of the hole. Mass balance calculations of the analysis results reveal that the species lost is MgO. See Section 5.5.4 for further details.

Chapter 4

Mathematical treatment of diffusion profiles

4.1 General remarks

The mathematical treatment of experimentally-determined diffusion profiles consists of solving the diffusion equation (Eq. 1.2) for the appropriate initial and boundary conditions of the experiments. The diffusion coefficient D is then derived by fitting an analytical solution to the profile or by simulating the profile numerically and refining the diffusion coefficient until a suitable goodness of fit parameter is optimized. Reviews of the theory and solutions for a wide variety of initial and boundary conditions are given in Crank (1979) and Carslaw and Jaeger (1946). For practical reasons the concentration $C(x, t)$ at time t at a position x along the profile are normalized before treatment of the profiles by:

$$C_{norm}(x, t) = \frac{C(x, t) - C_r}{C_l - C_r} \quad (4.1)$$

with C_l and C_r denoting the initial concentrations of the two endmembers of the diffusion couples. The initial conditions at time $t = 0$ of all experiments of this study can be expressed in terms of normalized concentrations (the subscript norm is dropped in subsequent expressions for clarity) as:

$$\begin{aligned} C &= 1, \quad x < 0, \quad t = 0 \\ C &= 0, \quad x > 0, \quad t = 0, \end{aligned} \quad (4.2)$$

where $x = 0$ at the original interface. For all experiments described in this study, at time $t > 0$, the diffusion couple can be regarded as consisting of two semi-infinite media where always a

limiting value x_∞ exists for which:

$$\begin{aligned} C &= 1, \quad x < x_\infty, \quad t > 0, \\ C &= 0, \quad x > x_\infty, \quad t > 0. \end{aligned} \quad (4.3)$$

These boundary conditions imply that the diffusion profile does not reach the end of the diffusion couple at either side of the interface. In Section 4.2, the solution of Equation 1.2 subject to the initial conditions 4.2 and boundary conditions 4.3 for a diffusion coefficient D that does not depend on composition is described. In this case an analytical solution exists that can be directly fitted to the diffusion profile, whereas no analytical solution can be derived if D does significantly depend on composition. The problem of a composition-dependent diffusion coefficient can be treated either with the Boltzmann-Matano analysis (Section 4.3.1) or by employing numerical techniques (Section 4.3.2).

4.2 Two semi-infinite media, D constant

The solution in this case can be derived by considering the solution to the diffusion equation that describes the diffusion of a substance M , initially deposited at time $t = 0$ in the plane $x = 0$ (Crank, 1979):

$$C = \frac{M}{2\sqrt{\pi Dt}} \exp\left(\frac{-x^2}{4Dt}\right). \quad (4.4)$$

The way to proceed is to consider the semi-infinite diffusion couple as an infinite number of line sources and adding the individual contributions.

For performing the superposition of the individual line sources, a useful mathematical function is the error function, defined as:

$$\operatorname{erf}(z) = \frac{2}{\sqrt{\pi}} \int_0^z \exp(-\eta^2) d\eta \quad (4.5)$$

and the complimentary error function erfc , which is given by $\operatorname{erfc}(z) = 1 - \operatorname{erf}(z)$. The solution of Eq. 1.2 for the initial and boundary conditions given in Equations 4.2 and 4.3 than becomes:

$$C = \frac{C(x,t) - C_r}{C_l - C_r} = \frac{1}{2} \operatorname{erfc}\left(\frac{x}{2\sqrt{Dt}}\right). \quad (4.6)$$

Figure 4.1 shows an example profile calculated employing Equation 4.6. The profile is symmet-

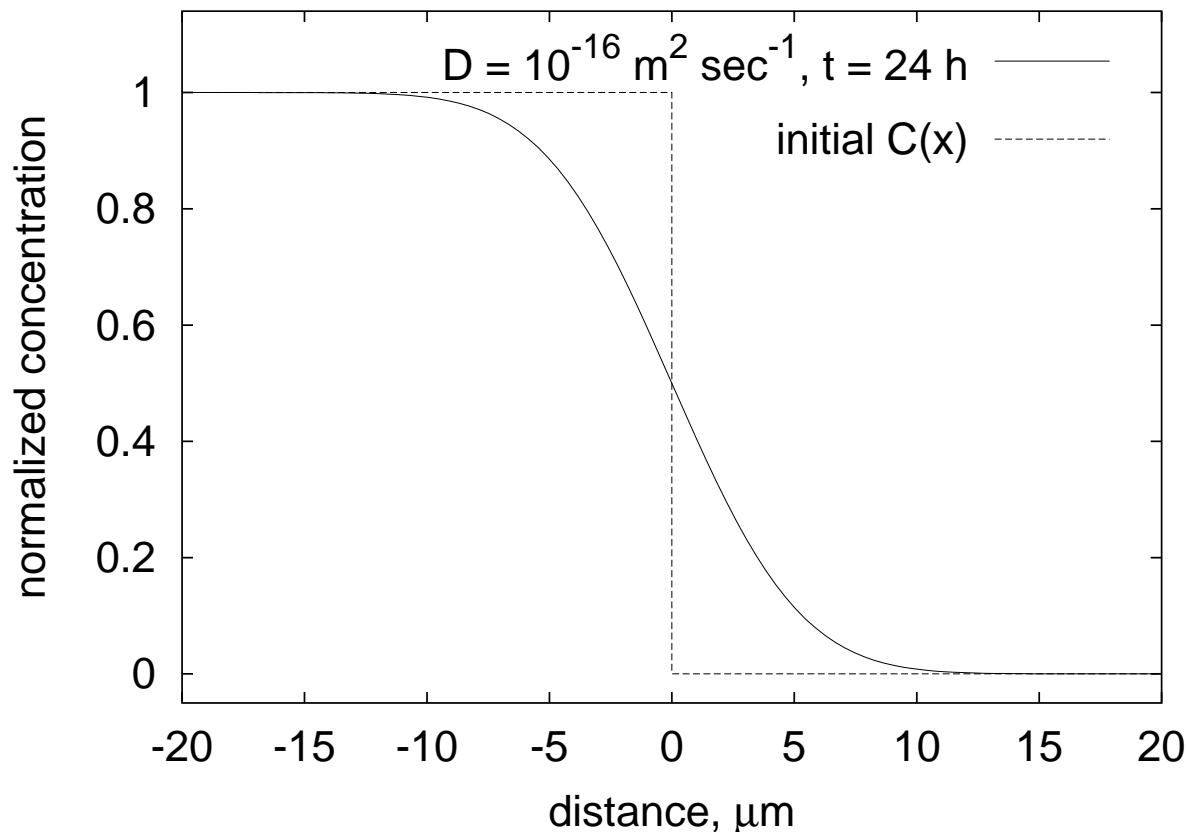


Figure 4.1: Analytical solution, Eq. 4.6, with initial and boundary conditions given in Eq. 4.2 and 4.3 implying a step distribution at $t = 0$ and two semi-infinite media. Because the diffusion coefficient does not depend on concentration, the profile is symmetric around the origin.

ric with respect to the origin of the coordinate system. A common feature of solutions of the diffusion equation (Eq. 1.2) is the linear dependence of x on \sqrt{Dt} . This is further illustrated in Figure 4.2. The diffusional length scale is defined here as the profile length between normalized concentrations $C = 0.01$ and 0.99 . Therefore, the diffusional length scale corresponds to the distance of two concentration boundaries moving along the constant concentration nodes $C = 0.01$ and 0.99 , respectively. In a diffusion experiment, in order to increase the diffusion profile length by a factor of 2 the time of the experiment has to be increased by a factor of 4. The length of a profile can be estimated by the linear relationship between the diffusional length scale x and \sqrt{Dt} derived in Fig. 4.2, $x = 6.6 \times \sqrt{Dt}$, but it has to be kept in mind that the proportionality factor depends on the definition of the limiting concentrations (0.01 and 0.99 in this

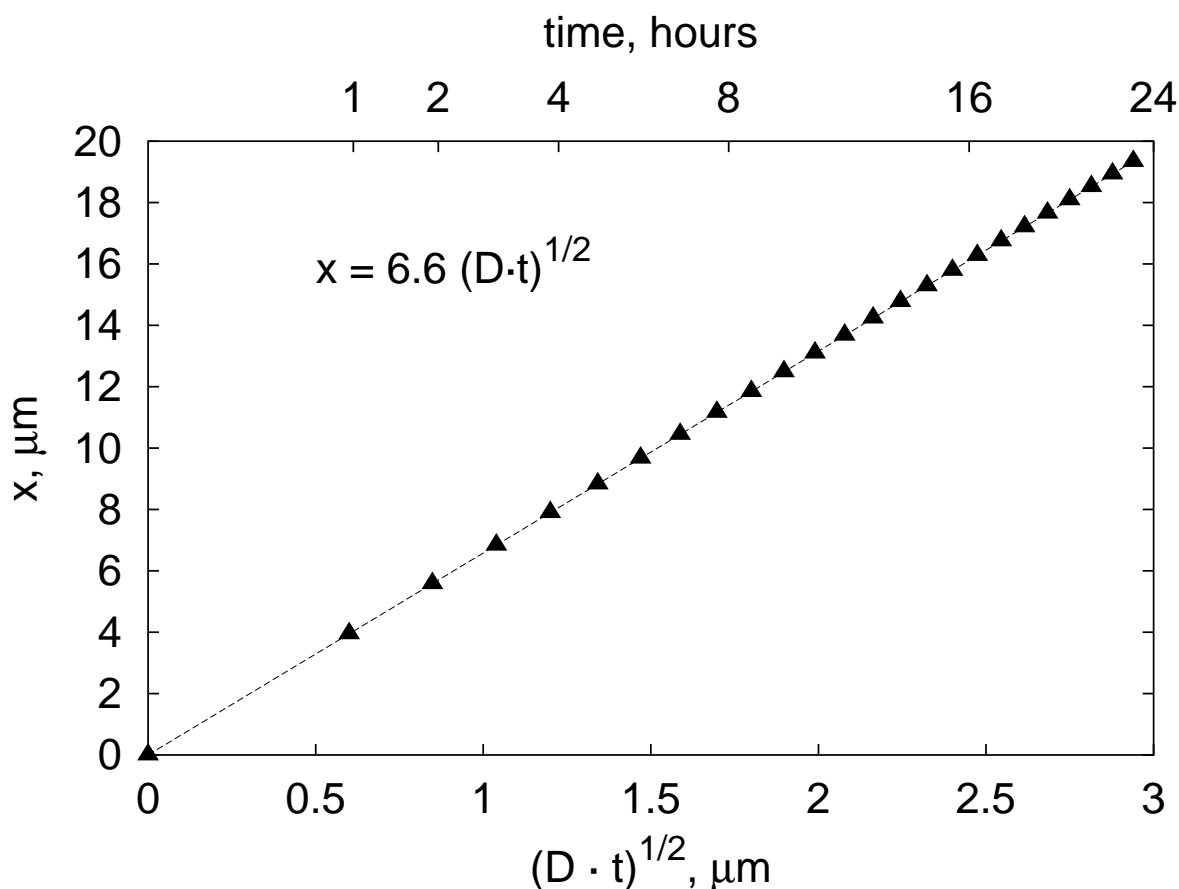


Figure 4.2: The diffusional length scale x (as defined in the text) depends linearly on \sqrt{Dt} ($D = 1 \times 10^{-16} \text{ m}^2 \text{ sec}^{-1}$) in this example. The triangles are spaced at a constant time interval of 1 hour showing that with increasing time the relative increase in diffusion length becomes smaller. The proportionality factor of 6.6 between x and \sqrt{Dt} does not depend on the units chosen or the absolute value of D , but on the definition of the limiting concentrations (see text for details).

case). For a time duration of $t_{exp} = 24$ hour and a profile length of $6 \mu\text{m}$, corresponding to a typical minimum profile length x_{min} of EPMA, the minimum diffusion coefficient D_{min} that can be measured is $\sim 10^{-17} \text{ m}^2 \text{ sec}^{-1}$, whereas in the case of EDX-STEM, with $x_{min} \approx 150 \text{ nm}$, $D_{min} = 6 \times 10^{-21} \text{ m}^2 \text{ sec}^{-1} \approx 10^{-20} \text{ m}^2 \text{ sec}^{-1}$ ($t_{exp} = 24$ hour).

4.3 Semi-infinite media, D concentration-dependent

4.3.1 Boltzmann-Matano analysis

The Boltzmann-Matano analysis is an exact formulation that describes the composition-dependent diffusion coefficient in terms of the derivative and the integral of the concentration-distance function (for example Shewmon, 1989):

$$D(C^*) = -\frac{1}{2t} \left(\frac{dx}{dC} \right)_{C^*} \int_{C=0}^{C^*} x dC \quad (4.7)$$

where $D(C^*)$ is the diffusion coefficient at the concentration C^* , t is the duration of the diffusion anneal, x is the position along the profile, and C is normalized concentration. The zero point of the spatial coordinate x is defined by the Matano interface to satisfy the condition:

$$\int_{C=0}^{C=1} x dC = 0 \quad (4.8)$$

Hence, the Matano interface is the plane through which equal fluxes flowed to the right and left. As a consequence, the area under the profile function $x(C)$ is the same on both sides of $x = 0$. A graphical interpretation is given in Figure 4.3. Equation 4.7 can be derived using the Boltzmann transformation employing the variable substitution $\lambda = x/\sqrt{t}$ in Eq. 1.2 (Philibert, 1991). Thus, it must be possible to express the initial and boundary conditions of the experiments in terms of the transformed variable λ . It is not necessary that the concentration distribution is continuous to apply the Boltzmann-Matano analysis as long as a discontinuous function at $t > 0$, where more than one discontinuity may exist, results from a step distribution at $t = 0$ (Jost and Hauffe, 1972). Therefore, diffusion taking place at the same time with a phase change or a reaction can be treated by Boltzmann-Matano analysis. In the case that the molar volume difference of the diffusion couple is larger than 10% a generalized Boltzmann-Matano formulation is given in Wagner (1969). In this study the difference in molar volume was always below 10% and therefore Equation 4.7 was used.

For computing the derivative in Eq. 4.7 from the experimental data, a smoothing function is required. Different functions, normally used for sigmoidal growth models (Ratkowsky, 1983), were applied :

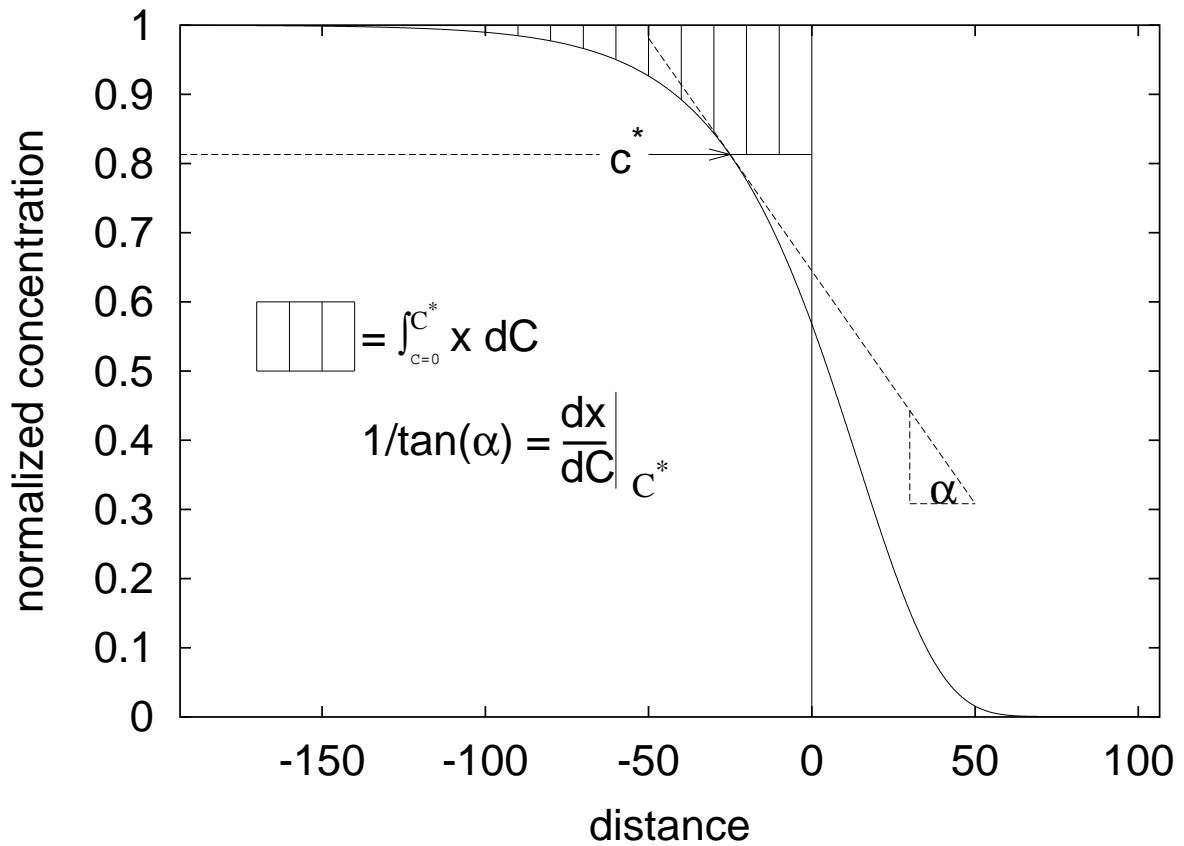


Figure 4.3: Graphical interpretation of Equation 4.7. To calculate the diffusion coefficient at a specific composition C^* one needs the inverse slope and the integral given by the hatched area. Note that the Boltzmann-Matano interface at $x = 0$ and defined by Eq. 4.8 is in general not at $C = 0.5$. This would be only true for a symmetrical profile, when D does not depend on composition.

- Richards type

$$y = \frac{P_1}{[1 + \exp(P_2 - P_3x)]^{1/P_4}} \quad (4.9)$$

This type of equation, with an additional addend P_5 for shifting the curve along the y-axis, was used by Petry (1999b) and subsequently by Mackwell et al. (2004) for analyzing the composition dependence of Ni diffusion in olivine diffusion couples with varying Fe-contents and for ferropericlasite interdiffusion experiments, respectively.

- Morgan-Mercer-Flodin type

$$y = \frac{P_1 P_2 + P_3 x^{P_4}}{P_2 + x^{P_4}} \quad (4.10)$$

- Weibull type

$$y = P_1 - P_2 \exp(-P_3 x^{P_4}) \quad (4.11)$$

The fits of experimental data are not significantly different employing the different fit functions given in Equations 4.9-4.11. Due to the strong nonlinearity of these functions, precise fitting can be problematic as shown in Chapter 5. As an alternative, if fitting a single function over the entire profile length is difficult, a combination of polynomials can be used.

4.3.2 Numerical simulations: Finite difference method

Numerical simulations of phenomena governed by partial differential equations are becoming more and more important for many applications in science and technology such as continuum mechanics, thermal conduction or diffusive mass transport. Different techniques for computation exist, for example the finite element and the finite difference methods. For simulating diffusion profiles numerically in this study a finite difference method was applied. The principle of the technique is the discretization of the composition function $C(x,t)$ in space and time and the approximation of the partial derivatives that arise in the diffusion equation, Eq. 1.2, by a Taylor series expansion between the space and time nodes. Several monographs describing this method in detail exist, e.g. Smith (1985) - a short introduction is also given in Crank (1979) and Ghez (1988). To illustrate the technique, an example with an exponential composition dependence, used for most of the composition-dependent problems in latter sections, is described here. An example program for computation is given in Appendix C.

The diffusion equation, Equation 1.2, with D depending exponentially on composition, can be written as:

$$\frac{\partial C}{\partial t} = \frac{\partial}{\partial x} \left(D_0 \cdot \exp(a \cdot C(x)) \frac{\partial C}{\partial x} \right), \quad (4.12)$$

which after differentiation gives:

$$\frac{\partial C}{\partial t} = a \cdot D_0 \cdot \exp(a \cdot C(x)) \left(\frac{\partial C}{\partial x} \right)^2 + D_0 \cdot \exp(a \cdot C(x)) \cdot \frac{\partial^2 C}{\partial x^2}. \quad (4.13)$$

Several finite difference schemes for solution may be employed. The simplest method for approximation of the partial derivatives is the explicit formulation, also used in this study. An

alternative would be for example an implicit finite difference scheme (Smith, 1985). The advantage of this method is the unconditional stability but the drawback is that a large set of linear equations has to be solved simultaneously. Therefore, the method is far more difficult to implement. Because no significant improvements of computational speed or accuracy are expected for profiles investigated in this study, only the explicit method was implemented and is described in the following paragraphs. The arguments for using the explicit instead of the more efficient implicit method follow the same line of reasoning as in Gaetani and Watson (2002) in their study of diffusive reequilibration of melt inclusions.

For implementation of an explicit finite difference scheme, the space coordinate of a diffusion profile is divided into steps δx and the time coordinate is divided into steps δt (Fig. 4.4). Expanding the concentration in time into a Taylor series gives:

$$C(i, j+1) = c(i, j) + \delta t \left. \frac{\partial C}{\partial t} \right|_{i,j} + \frac{1}{2} (\delta t)^2 \left. \frac{\partial^2 C}{\partial t^2} \right|_{i,j} + \dots \quad (4.14)$$

If higher than linear terms are neglected the time derivative can be written as:

$$\left. \frac{\partial C}{\partial t} \right|_{i,j} = \frac{C(i, j+t) - c(i, j)}{\delta t} \quad (4.15)$$

which according to Smith (1985) is first-order accurate in δt . The first derivative of the concentration with respect to the space coordinate is expressed with a symmetric expression where the Taylor series is used in the negative and positive x-direction:

$$\left. \frac{\partial C}{\partial x} \right|_{i,j} = \frac{C(i+1, j) - C(i-1, j)}{2\delta x} \quad (4.16)$$

This expression has the advantage of being second-order accurate in δx and is therefore preferred to simple backward or forward approximations (Ghez, 1988). A Taylor series expansion in the x-direction truncated after the term containing the second derivative of the concentration with respect to distance leads to an expression of the second derivative of the composition C with respect to x :

$$\left. \frac{\partial^2 C}{\partial x^2} \right|_{i,j} = \frac{C(i+1, j) - 2C(i, j) + C(i-1, j)}{(\delta x)^2} \quad (4.17)$$

where the leading error is on the order of δx^2 (Smith, 1985).

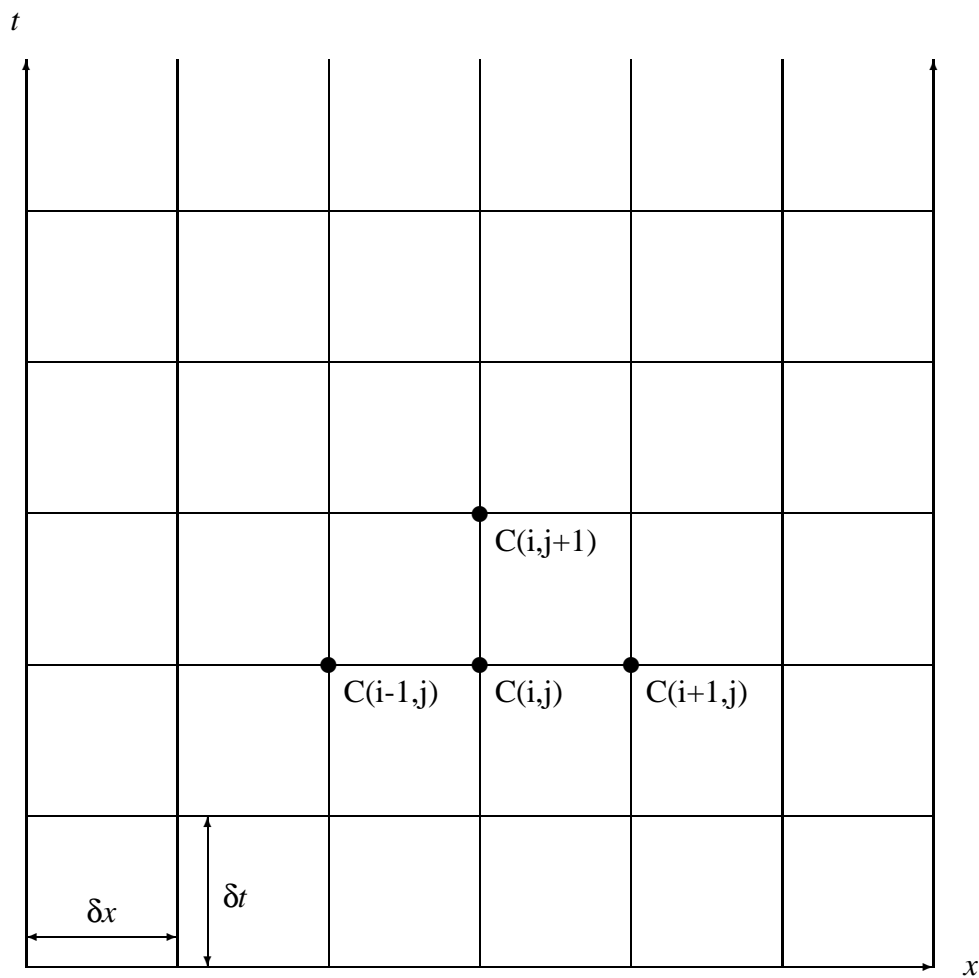


Figure 4.4: Grid for performing the explicit finite difference method. Each node in space x_i and time t_i represents a concentration $C(x_i, t_j)$. The solution is propagated along the time axis by calculating the unknown concentration $c(i, j+1)$ in terms of the known concentrations $C(i-1, j)$, $C(i, j)$, and $C(i+1, j)$ with the aid of Equation 4.18

Inserting these finite difference approximations into the diffusion equation employing an exponential composition dependence, Eq. 4.12, and rearranging finally results in:

$$\begin{aligned}
 C(i, j+1) = & C(i, j) + \dots \\
 & + \frac{1}{4} \kappa \cdot a D(i, j) [C(i+1, j) - C(j-1)]^2 + \dots \\
 & + \kappa \cdot D(i, j) [C(i+1, j) - 2C(i, j) + C(i-1, j)]
 \end{aligned} \tag{4.18}$$

where $D(i, j) = D_0 \exp(a \cdot C(i, j))$ and $\kappa = \delta t / (\delta x^2)$. The condition $\kappa \cdot D(i, j) < 0.5$ has to be fulfilled, otherwise the algorithm becomes instable.

A numerical simulation is performed by applying Equation 4.18 repeatedly for each grid-node of a new timestep until all timesteps add up to the duration of the experiment. As goodness of fit criterion of a simulation, the sum of squared differences between the measured concentration C_m and the simulated concentration C_s at each distance-step $\sum_{\delta x} (C_m - C_s)^2$ is calculated and minimized by iteratively changing D_0 and a .

As a test of accuracy, Figure 4.5 compares simulations for different values of $\kappa \cdot D$ and an analytical solution for composition-independent D (setting a in Eq. 4.12 equal to zero) using a typical average value for ferropericalse diffusion experiments (Section 5.4) and 1200 sec of diffusion. At values of $\kappa \cdot D \geq 0.5$ oscillations of calculated concentrations appear which rapidly increase towards infinity for only slightly increasing values of $\kappa \cdot D$, whereas for all $\kappa \cdot D < 0.5$ the overall deviation from the analytical solution is less than random scatter corresponding to an analytical uncertainty of 0.1%. Hence, within the experimental error for the profile measurements all simulations for $\kappa \cdot D < 0.5$ give accurate results in this example. This is in general true for time scales up to 16 h, which is the longest timescale of experiments resulting in asymmetric profiles investigated by finite difference simulations in this study.

As a second test of accuracy, Figure 4.6 and Table 4.1 compare diffusion coefficients derived by the Boltzmann-Matano method, as a function of composition, performed on profiles first derived by numerical simulations with varying $\kappa \cdot D$ values for a composition dependence of $D = 0.06 \cdot \exp(3.4 \cdot C)$. The numerical simulations generate smooth input profiles without any statistical scatter, hence to avoid inaccuracies due to an empirical fit-function, for Boltzmann-Matano analysis an interpolation function supplied by the computer program Mathematica was used as smoothing function.

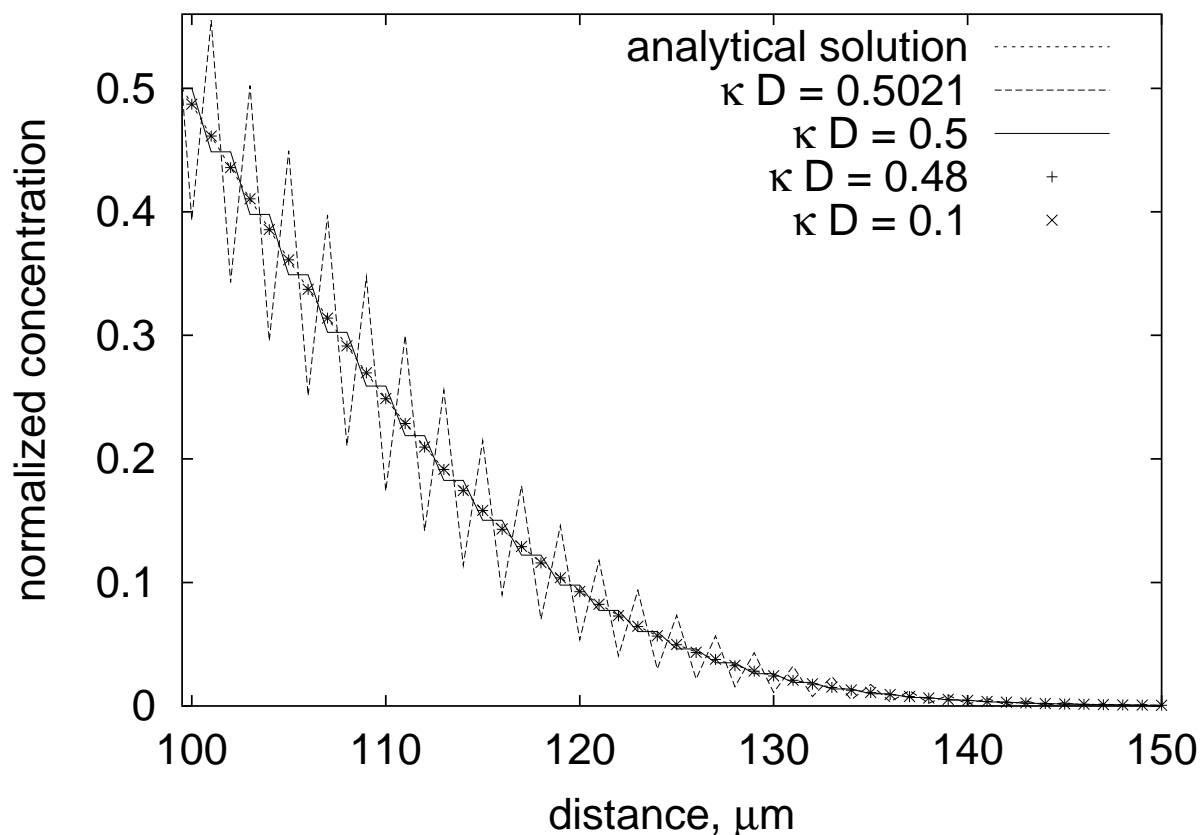


Figure 4.5: Simulation for a diffusion profile with a constant diffusion coefficient D of $0.1 \mu^2 \text{ sec}^{-1}$ and 1200 seconds of diffusion. Only one half of the profile is shown. For values $\kappa \cdot D$ equal or slightly larger than 0.5 the simulations become unstable whereas for all values less than 0.5 the solution agrees well with the analytical solution, Eq. 4.6, keeping in mind the statistical scatter in the profile analysis (see Chapter 3).

In this test, two completely independent methods are used to first generate the profile and second to re-determine the composition-dependent diffusion coefficient. Thus, the consistency between the results and the expected input diffusion coefficients given by $D = 0.06 \cdot \exp^{3.4 \cdot C}$, on the order of 0.3 % (Table 4.1), indicates the accuracy of both methods. If one assumes that the errors arising in the Boltzmann-Matano analysis are much smaller than the deviation of the numerical simulations, because a smooth dataset was employed, than the deviations between calculated diffusion coefficients and input diffusion coefficients solely originate by round-off and discretization error in the numerical algorithm. The difference $(D_{real} - D_{calc})/D_{real}$ in Table 4.1 is slightly larger for larger $\kappa \cdot D$ and compositions in the steeper part of the asymmetric profile. The overall variation of this deviation between 0.17 and 0.46 % is ~ 2 orders of magnitude

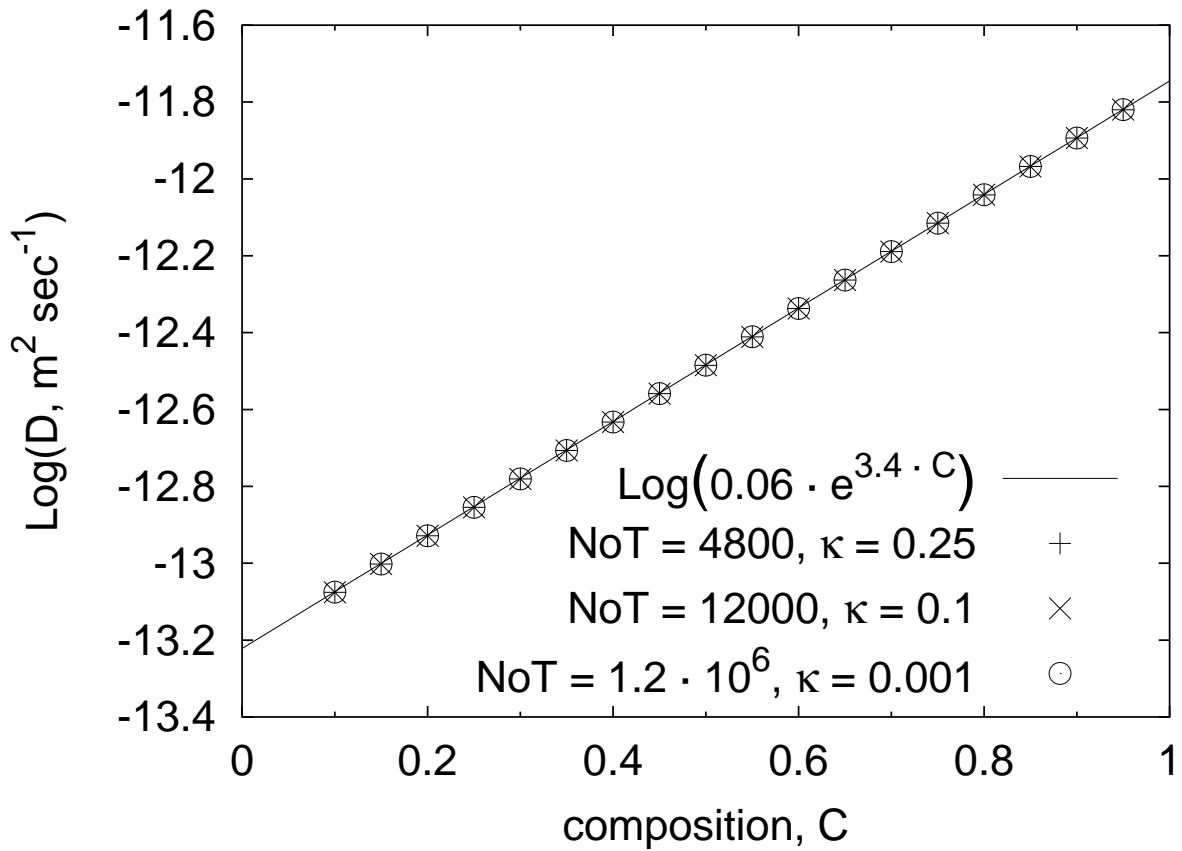


Figure 4.6: Diffusion coefficients calculated by Boltzmann-Matano method using numerical simulations with varying number of timesteps (NoT), κ values corresponding to 1200 sec of diffusion and a composition-dependent diffusion coefficient: $D = 0.06 \cdot \exp(3.4 \cdot C)$.

smaller than the experimental error on D ($\sim 30\%$, see Chapter 5).

Therefore, the two different tests for a constant and a composition-dependent D confirm that as long as $\kappa \cdot D < 0.5$ the numerical simulation is consistent with the diffusion equation, Eq. 4.12, and accurate enough, within experimental error, for the experiments performed in this study.

C_{norm}	$D_{S1}, 10^{13} \frac{m^2}{sec}$	$D_{S2}, 10^{13} \frac{m^2}{sec}$	$D_{S3}, 10^{13} \frac{m^2}{sec}$	$D_{real}, 10^{13} \frac{m^2}{sec}$	$\frac{D_{real}-D_{calc}}{D_{real}}, \%$		
	NoT = 4800 $\kappa = 0.25$	NoT = 12000 $\kappa = 0.1$	NoT = 1200000 $\kappa = 0.001$		S1	S2	S3
0.1	0.84	0.84	0.84	0.84	0.33	0.30	0.28
0.2	1.18	1.18	1.18	1.18	0.46	0.43	0.42
0.3	1.66	1.66	1.66	1.66	0.41	0.39	0.38
0.4	2.33	2.33	2.33	2.34	0.37	0.35	0.34
0.5	3.27	3.27	3.27	3.28	0.31	0.30	0.29
0.6	4.60	4.60	4.60	4.61	0.27	0.25	0.25
0.7	6.47	6.47	6.47	6.48	0.24	0.22	0.23
0.8	9.09	9.09	9.09	9.11	0.22	0.19	0.19
0.9	12.8	12.8	12.8	12.8	0.21	0.17	0.17

Table 4.1: Comparison of diffusion coefficients calculated by Boltzmann-Matano analysis using a finite difference simulation with a composition-dependent diffusion coefficient $D_{real} = 0.06 \times \exp(3.4 C_{norm})$, where C_{norm} is a normalized composition between 0 and 1, as the input-profile. Three simulations were performed, models S1-S3, for a varying number of timesteps (NoT) and corresponding κ values ($\delta x = 1 \mu m$), given in the topline of the table, to test if the resulting diffusion coefficients are consistent with each other.

Chapter 5

Results

5.1 Introduction

In this chapter, the results of the diffusion experiments are described for olivine (Section 5.2), wadsleyite (Section 5.3), ferropericlase (Section 5.4), and silicate perovskite (Section 5.5). The observations include backscatter electron images of the diffusion couples and capsules, profile examples measured by electron microprobe analysis (EPMA) and transmission electron microscopy equipped with an energy dispersive detector (EDX-TEM), and variation of diffusion coefficients with pressure and temperature. Because most of the diffusion experiments have been performed at different P-T conditions in capsules where the oxygen fugacity is buffered by a solid state buffer system (either Ni-NiO or MgO-Fe, see Section 2.4), diffusion coefficients are determined at variable oxygen fugacity conditions. Measurement of diffusion coefficients D along a buffer system at different P and T conditions introduces variability from two sources into the diffusion data: (I) As fO_2 changes along a buffer with temperature, the change in D due to this variation in fO_2 is absorbed into the temperature dependence, resulting in a higher activation energy determined in an Arrhenius plot compared to the true activation energy at constant temperature. (II) The fO_2 -T relation itself shifts with a variation in pressure implying that experiments carried out at the same temperature and fO_2 buffer but at different pressures are not equivalent. Ideally, corrections should be made for both of these effects in order to represent D as a function of the independent variables P, T and fO_2 .

In a review of garnet diffusion data (Chakraborty and Ganguly, 1991), obtained along the graphite- O_2 buffer, it is estimated that at pressures up to 4 GPa the effect of (II) is negligible

implying an insignificant difference either if the activation volume is determined using values along the buffer or at constant fO_2 , whereas the effect of (I) yields an activation energy that is $\sim 10\%$ larger than the value at constant fO_2 . In the studies of Farber et al. (2000) and Holzzapfel et al. (2003), where diffusion coefficients were determined along the Ni-NiO buffer, no attempt was made to normalize the results to a constant oxygen fugacity. In this case, the values derived for the activation energy and the activation volume are only valid at conditions of the buffer system used. The reason not to normalize the results to a constant value of fO_2 in Holzzapfel et al. (2003) was the relatively large uncertainty in calculating the fO_2 at high pressures. In addition, the fact that the absolute fO_2 of a solid buffer system changes with P and T implies that the relative fO_2 scale (fO_2 relative to a buffer system) is a better indicator for the redox state of the system than the absolute fO_2 scale itself. The fO_2 inside the Earth most likely changes subparallel to fO_2 curves equivalent to solid state buffers (Frost, 1991). However, the activation energy and activation volume are physical quantities strictly only defined at a constant oxygen fugacity. Hence, in the present study, the effects of a changing fO_2 of the Ni-NiO buffer as a function of P and T (cases (I) and (II) defined above) is estimated using thermodynamic data of the redox reaction in order to correct diffusion coefficients obtained using Ni-NiO capsules at pressures below 24 GPa.

In Figure 5.1 the variation of the Ni-NiO buffer with pressure and temperature is shown using values of Huebner (1971), Ride (1991), O'Neill and Pownceby (1993), and Pownceby and O'Neill (1994). Ride (1991) lists an expression for the free energy change ΔG^0 of the oxidation reaction of Ni:



The oxygen fugacity of reaction 5.1 can then be calculated at 1 bar by

$$\log(fO_2) = \frac{2 \Delta G^0}{R T \ln(10)}. \quad (5.2)$$

At elevated pressures, Equation 5.2 has to be rewritten as:

$$\log(fO_2) = \frac{2 (\Delta G^0 + \int_{1 \text{ bar}}^P \Delta V^0(P, T) dP)}{R T \ln(10)}, \quad (5.3)$$

where $\Delta V^0(P, T) dP$ is the volume change of Reaction 5.1. In model [1] in Figure 5.1 a constant volume change of reaction 5.1 was assumed using molar volumes of Ni and NiO also given in

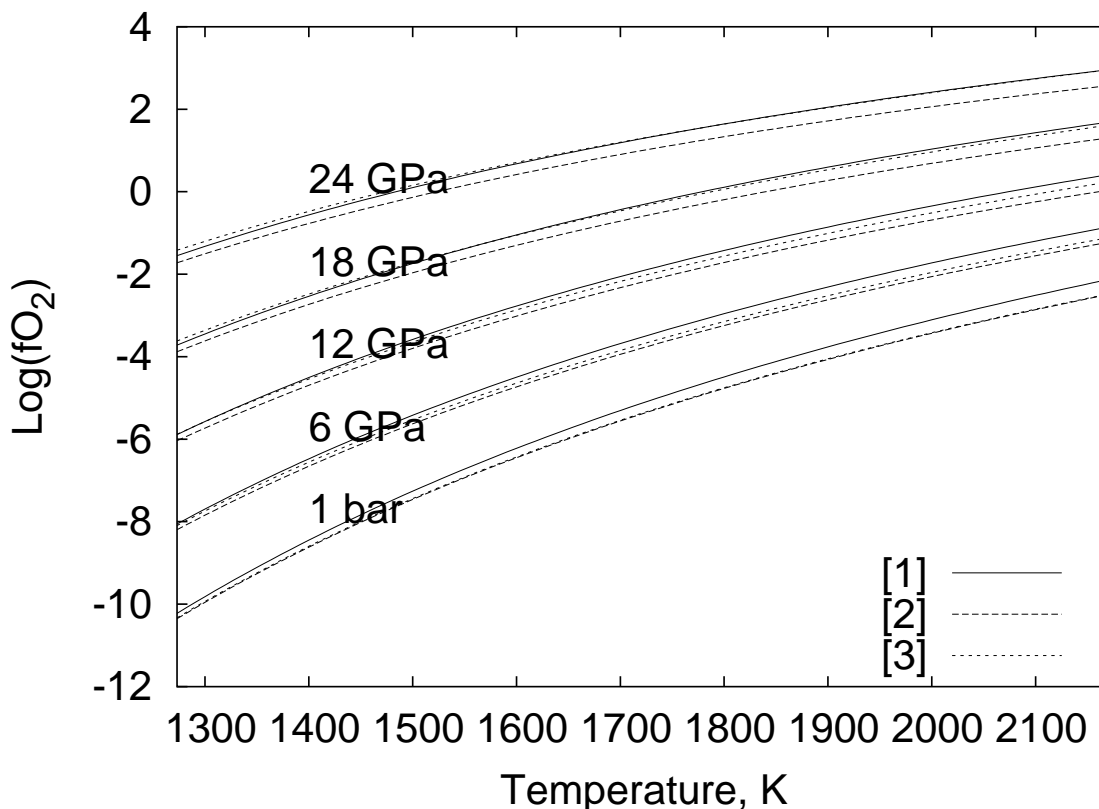


Figure 5.1: Variation of oxygen fugacity as a function of pressure and temperature. References are: [1] Huebner (1971), [2] Ride (1991), [3] 1 bar: O'Neill and Pownceby (1993), $P > 1$ bar: Pownceby and O'Neill (1994). See text for further discussion.

Ride (1991). The equation given in Huebner (1971) also utilized a constant volume change of the oxidation reaction (Equation 5.1), whereas Pownceby and O'Neill (1994) employed results for the thermal expansivity and compressibility of Ni and NiO published in the literature to calculate the integral $\int_{1\text{bar}}^P \Delta V_{T,P}^0 dP$ in Equation 5.3. For the three different models, the oxygen fugacity imposed by the equilibrium of Ni and NiO increases with increasing temperature and pressure. Values calculated by Ride (1991) are approximately 0.2 to 0.3 log-units lower than the results of Huebner (1971). The oxygen fugacity calculated using the full expression of O'Neill and Pownceby (1993) is closer to the results derived using values of Ride (1991) at lower pressures whereas at higher pressures they nearly coincide with the results of Huebner (1971). However, the expressions used by O'Neill and Pownceby (1993) are derived employing experimental results at pressures and temperatures lower than in the present study. In addition, the difference

between the different models seem to be insignificant, only on the order of 0.3 log units for an absolute variation of oxygen fugacity by approximately 4 orders of magnitude between 0 and 24 GPa. Therefore, in subsequent calculations the oxygen fugacity is calculated using the expression derived from Ride (1991).

An overview and comparison of diffusion coefficients as a function of pressure and temperature for the different mineral systems are given in Section 5.6. Establishing absolute diffusivities allows the effect of temperature gradients on the diffusion profiles to be discussed (Section 5.7.2) and the influence of diffusion taking place during the initial heating of the experiments to be characterized (heating effect, Section 5.7.3). Computer programs implementing explicit finite difference schemes for investigations of heating effects might be used for other studies where very rapid diffusion occurs, e.g. diffusion in silicate melts.

5.2 Olivine

5.2.1 Conditions of experiments

The pressure and temperature conditions of all olivine diffusion experiments, together with the capsule types used, are listed in Table 5.1. Both Au and Ni-NiO capsules were employed (Section 2.4). Au capsule experiments are limited to lower pressures by the melting point of Au, about 1673 K at 8 GPa (extrapolated values given in Young, 1991). Two series of experiments were performed employing Au capsules: The first isothermally at 1673 K and pressures between 8 and 12 GPa and the second isobarically at 12 GPa between 1623 K and 1823 K. The Au capsule technique was developed by Chakraborty et al. (1999), whereas the design of the Ni-NiO capsules was developed in this study. The main purpose of using Ni-NiO capsules, in addition of Au-capsules, was to constrain the f_{O_2} conditions prevailing inside the Au capsules to enable a better comparison of results of this work and of Chakraborty et al. (1999) with results of other studies in the literature (see also Section 1.3.2 and 2.4). For all experiments a 14/8 assembly in a 500 t Walker style multianvil press was used (see Section 2.5).

Sample	Capsule	T , K	P , GPa	t , min	$\log(D_{Fe-Mg}/\frac{m^2}{sec})$	$\log(D_{Ni}/\frac{m^2}{sec})$	$\log(D_{Mn}/\frac{m^2}{sec})$
1CS12	Au	1673	12	1440	-16.2(3)	-16.5(4)	-16.1(5)
2CS10	Au	1673	10	1440	-16.4(3)	-15.5(4)	-16.4(5)
3CS8	Au	1673	8	1440	-15.6(3)	-15.7(4)	-15.8(5)
4CS11	Au	1673	11	1440	-15.5(3)	-15.7(4)	-15.4(5)
5CS12	Au	1673	12	1440	-16.3(3)	-16.4(4)	-16.1(5)
6CS10	Au	1673	10	1440	-16.3(3)	-15.5(4)	-16.5(5)
7CS11.5	Au	1673	11.5	1440	-16.1(3)	-15.8(4)	-16.2(5)
8CS10.5	Au	1673	10.5	1440	-16.1(3)	-15.5(4)	-15.9(5)
9CS11	Au	1673	11	1440	-15.3(3)	-15.4(4)	-15.5(5)
10CS11.5	Au	1673	11.5	1440	-16.3(3)	-16.1(4)	-16.3(5)
13CS12	Au	1773	12	1440	-15.9(3)	-16.1(4)	-16.0(5)
14CS12	Au	1723	12	1440	-16.1(3)	-16.3(4)	-16.2(5)
15CS12	Au	1823	12	1440	-15.5(3)	-15.6(4)	-15.6(5)
16CS12	Au	1623	12	4320	-16.8(3)	-16.9(4)	-16.5(5)
17CS12	Ni-NiO	1673	12	1443	-16.7(3)	-16.6(4)	-16.7(5)
18CS6	Ni-NiO	1673	6	1440	-15.7(3)	n.m.	n.m.
20CS6	Ni-NiO	1673	6	1440	-15.4(3)	-15.4(3)	-15.5(5)

Table 5.1: Results and conditions of the olivine high pressure diffusion runs - Diffusion coefficients are given in $\log_{10}(D)$, n.m. denotes not measured (see text for explanation, Section 5.2.3)

5.2.2 Characterization of diffusion couples after the experiments

To detect and exclude irregular artifacts along the diffusion interface due to possible instabilities of the diffusion front, all samples have been studied by high resolution backscattered electron imaging (Figure 5.2) and elemental mapping. Diffusion fronts are usually regular and parallel to the crystal interface. In one experiment, 20CS6, the central part of the diffusion couple sheared between two cracks (formed probably during initial compression) and recrystallized. Grain boundary diffusion is evident in backscatter electron images and elemental maps. For measuring diffusion profiles, undisturbed areas outside the shear zone were investigated, where the original single crystal structure remained intact.

Sometimes, the two crystals of the diffusion couple separated at the interface due to decompression and/or sample preparation. The length scale of this separation is much less than $1 \mu\text{m}$ and therefore insignificant with respect to profile shape and length (normally $\geq 10 \mu\text{m}$, see below).

The thermocouple and the capsule in the 14/8 assemblies (Section 2.5) used for the olivine

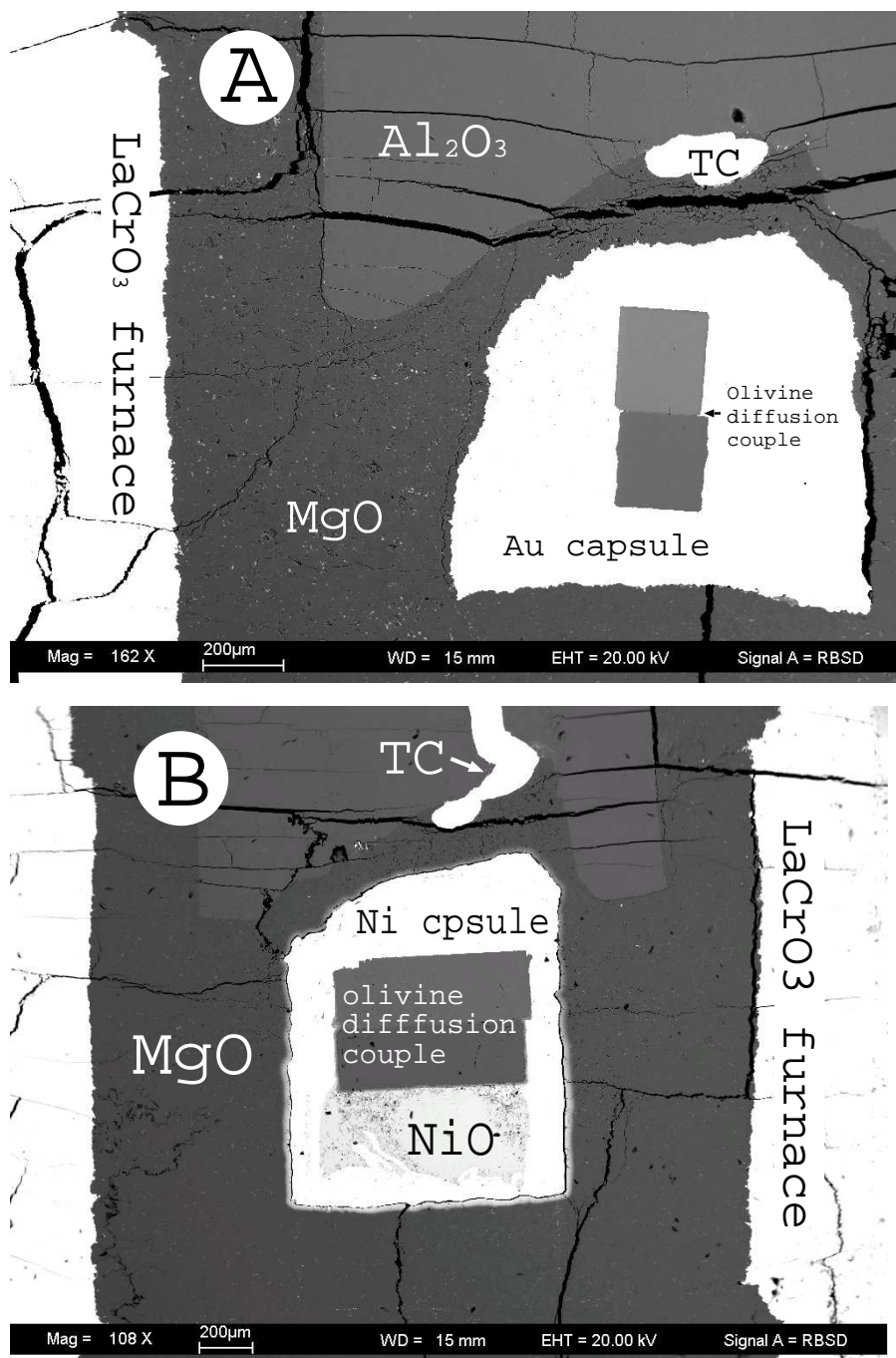


Figure 5.2: Backscattered electron images of the two capsule types used: A gold capsule, B Ni-NiO capsule (see Section 2.4). For all experiments a 14/8 assembly was employed. The step of the inner LaCrO₃ furnace-part is visible in A and B.

experiments were effectively shielded from each other by a MgO disc (Fig. 2.6 and 5.2) and no Ni contamination could be detected in the thermocouple. With Ni-NiO capsules, prevention of

this effect is utterly important because otherwise Ni can diffuse into the thermocouple, seriously influencing the temperature reading. In initial experiments, employing Au capsules, instead of using a lid covering the capsule and the MgO cylinder separating the capsule from the furnace, a MgO plug was used on top of the capsule. In this case, the Au extruded from the capsule between the plug and the inner wall of the MgO cylinder into the bore holes of the Al_2O_3 thermocouple sleeve. Because the Au did not react with the thermocouple, the temperature reading was not significantly effected.

Water potentially influences diffusion rates in olivine as shown in the study of Mei and Kohlstedt (2000) for diffusional creep, which depends on Si diffusion. To characterize the water contents of the crystals, infrared spectra were measured on sample 8CS10.5 employing a Bruker IFS 120 HR high resolution FTIR spectrometer. The synthetic forsterite contained no detectable amounts of water whereas the San Carlos olivine had on the order of 25 ppm by weight water based on the absorption correction of Paterson (1982) after the experiment.

5.2.3 Profiles and diffusion coefficients

Example profiles for Fe, Mg, Ni, and Mn are shown in Figure 5.3. The profiles analyzed by EPMA are symmetrical for the experiments described here, whereas strongly asymmetric profiles were observed by Chakraborty (1997). This apparent discrepancy can be explained by the limited compositional range, Fo₁₀₀-Fo₉₄, used in this study (Section 2.3.2). Hence, the composition dependence of diffusion cannot be resolved in the experiments reported here using profiles determined by EPMA (for analysis employing EDX-STEM see below), and the diffusion coefficient is representative of the average composition of the diffusion couple (Mg# = 0.97). This is the case for the Fe-Mg interdiffusion coefficient and also for Mn and Ni diffusion. The length of the diffusion profiles is approximately 10-20 μm and therefore much smaller than the length of the single crystals forming the diffusion couple. Thus, the profiles were analyzed with Equation 4.6, the analytical solution of the diffusion equation (Equation 1.2) using initial and boundary conditions given by Equations 4.2 and 4.3. For fitting the profiles to Equation 4.6 the nonlinear least square fit routine supplied by the computer program Mathematica (Version 4.2.0.0) was employed for solving for $2\sqrt{Dt}$ and the position of the interface a , with respect to the lab reference frame (x_{lab} , for a discussion of different reference frames see Brady, 1975b):

$$C(x, t) = \frac{1}{2} \cdot \operatorname{erfc} \frac{x_{lab} - a}{2\sqrt{Dt}}. \quad (5.4)$$

The fitted function was always checked by eye and starting values or number of iterations were systematically changed if necessary.

Diffusion coefficients derived by the procedure just outlined are listed in Table 5.1. The error was estimated first by the scatter associated with different profile measurements on the same sample and with profiles measured on samples at the same conditions (experimental reproducibility). This error is on the order of 0.2 log-units for Fe-Mg interdiffusion, corresponding to a relative error of 50%. For Ni and Mn, errors of 0.3 and 0.4 log-units, respectively, were estimated. The increased error of Ni and Mn diffusion coefficients compared to Fe-Mg interdiffusion coefficients is caused by the larger analytical scatter for the two trace elements (see Fig. 5.3). As shown later in Sections 5.2.4, 5.2.5 and in the ferropericlasite system (Section 5.4) the error for high pressure multianvil diffusion experiments is somewhat larger because of errors in pressure and temperature. Hence, the overall error for the high pressure experiments in the olivine system

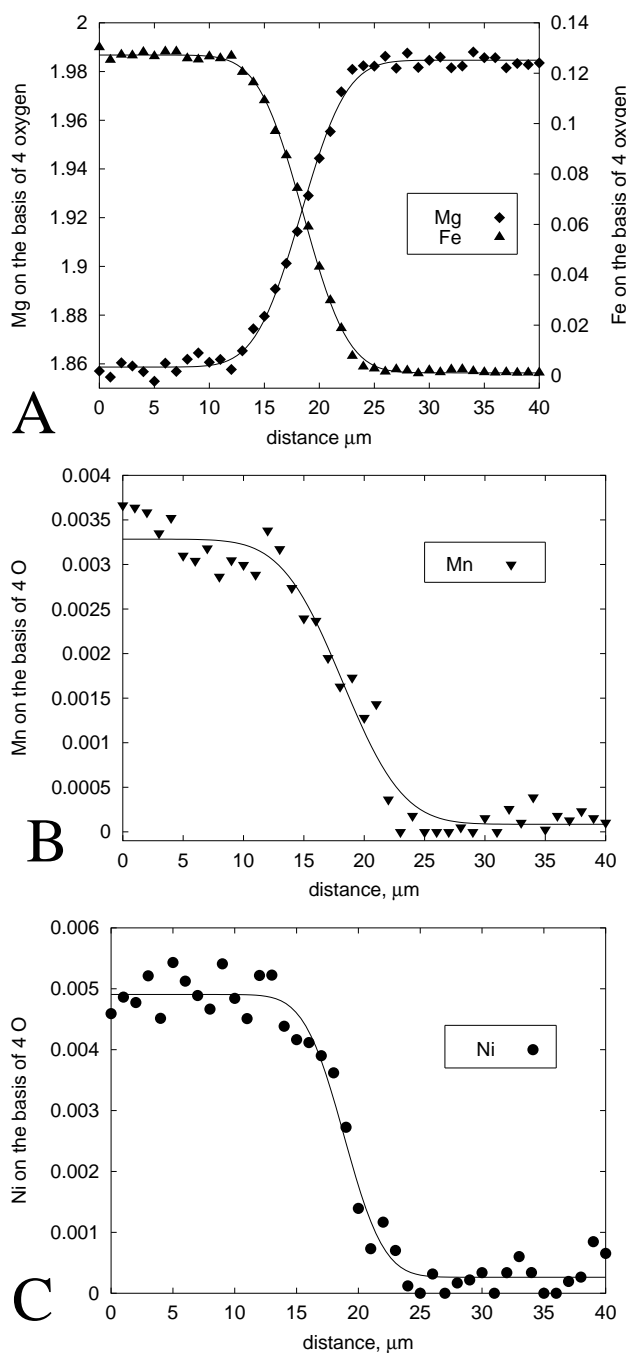


Figure 5.3: Diffusion profile examples for olivine measured by EPMA (electron microprobe). The experiment was performed at 12 GPa, 1623 K and annealed for 72 h (16CS12). In (A) the Fe and the Mg profiles are shown together. The Fe-Mg interdiffusion coefficient can be derived from either of the two profiles (Section 1.2.3). In (B) the Mn profile and in (C) the Ni profile are shown.

X_c	$\frac{D_t}{D_c}$	% error
7	0.96	4
6	0.95	5
5	0.93	8
4	0.89	12
3	0.80	24
2	0.56	79

Table 5.2: Error of the true diffusion coefficient D_t given in % deviation of D_t from the diffusion coefficient D_c determined from a convolved profile. The ratio D_t/D_c was calculated employing Equation (20) given in Ganguly et al. (1988, see also Eq. 5.5). X_c denotes half-length of the profile in microns.

is on the order of 0.3 log-units for Fe-Mg interdiffusion, 0.4 log-units for Ni and 0.5 log-units for Mn diffusion.

Because some of the profiles are only $\sim 8 - 10 \mu\text{m}$ long, they may be susceptible to convolution effects. The possible effect of profile broadening, due to the finite excitation volume of the X-rays (Section 3.2), was estimated using the algorithm developed by Ganguly et al. (1988). The standard deviation ε of the X-ray excitation volume, assuming a Gaussian intensity distribution, was determined to be better than $0.46 \mu\text{m}$. This value was derived by scanning across the Al_2O_3 -MgO boundary between the thermocouple sleeve and the MgO cylinder (compare with Figure 2.7) in the low-temperature part of the assembly. The effect of convolution can be estimated employing Equation (20) of Ganguly et al. (1988):

$$\frac{D_t}{D_c} = 1 - 8 \left(\frac{\varepsilon}{X_c} \right)^2 \quad (5.5)$$

where D_t is the true diffusion coefficient, D_c denotes the apparent diffusion coefficient determined from the profile subject to convolution broadening and X_c is the half width of the profile. This equation is only valid for a composition-independent diffusion coefficient. Table 5.2 shows errors as percent deviation from the true diffusion coefficient D_t for profile half widths between 2 and $7 \mu\text{m}$. If an error of 12% is considered as acceptable, keeping the experimental uncertainties in mind (see above), profiles as short as $8 \mu\text{m}$ still give reliable diffusion coefficients.

To verify these calculations, two samples, 6CS10 and 17CS12 (Table 5.1), with diffusion profile lengths of 10 and $8 \mu\text{m}$, respectively, were analyzed by EDX-STEM following the experimental procedure developed by Meißner et al. (1998) and described in Section 3.3. Figure

5.4 shows the profiles for both samples. In both cases the difference for diffusion coefficients determined by fitting a composition-independent diffusion coefficient is on the order of 30%, somewhat larger than estimated in Table 5.2. As outlined above the difference in D for different profiles determined on the same sample is as large as 0.2 log-units corresponding to a relative error of $\sim 50\%$. Therefore, profiles measured by EPMA, show no significant convolution effects with respect to the average diffusion coefficient of the profile.

However, Figure 5.4 shows also that the composition-dependence of diffusion can be resolved by EDX-STEM, whereas the subtle asymmetry of the profiles is not detectable by EPMA. For both samples shown in Figure 5.4, 6CS10 and 17CS12, an asymmetric fit employing a composition factor of $\exp(6.9 X_{\text{Fe}_2\text{SiO}_4})$, observed at 1 bar (Chakraborty, 1997, Dohmen, pers. com.), is fully compatible with the TEM profiles. Hence, to correct Fe-Mg interdiffusion coefficients at $X_{\text{Fe}_2\text{SiO}_4} = 0.97$, as determined in this study, to $X_{\text{Fe}_2\text{SiO}_4} = 0.90$, the average olivine composition in the upper mantle, requires the addition of 0.2-0.3 log-units.

Sample 18CS6 at 6 GPa and 1673 K (Table 5.1) employed a slightly different Ni-NiO capsule than originally developed in this study (Section 2.4). Instead of using Ni-foil, a Ni-wire was drilled similar to the Au capsule design. After the diffusion experiment the olivine diffusion couple showed Mn contamination along the rim of the crystals and across the diffusion zone. Hence, a peak-shaped Mn distribution developed across the interface (up to 3.7 wt% MnO). This phenomenon can only be explained by Mn or MnO contamination from the capsule. Because the capsule was produced from high-purity Ni-wire, the Mn contamination of the capsule presumably occurred during drilling (e.g. by a Mn-bearing drill bit). Therefore, only the Fe-profile was analyzed in this sample, because 3.7 wt% MnO does not alter the thermodynamic factor for Fe-Mg interdiffusion significantly, implying no change of the Fe-Mg interdiffusion coefficient as compared to the Mn-free system. This is not clear for Ni diffusion. Therefore, Ni profiles were omitted for sample 18CS6 when deriving diffusion coefficients.

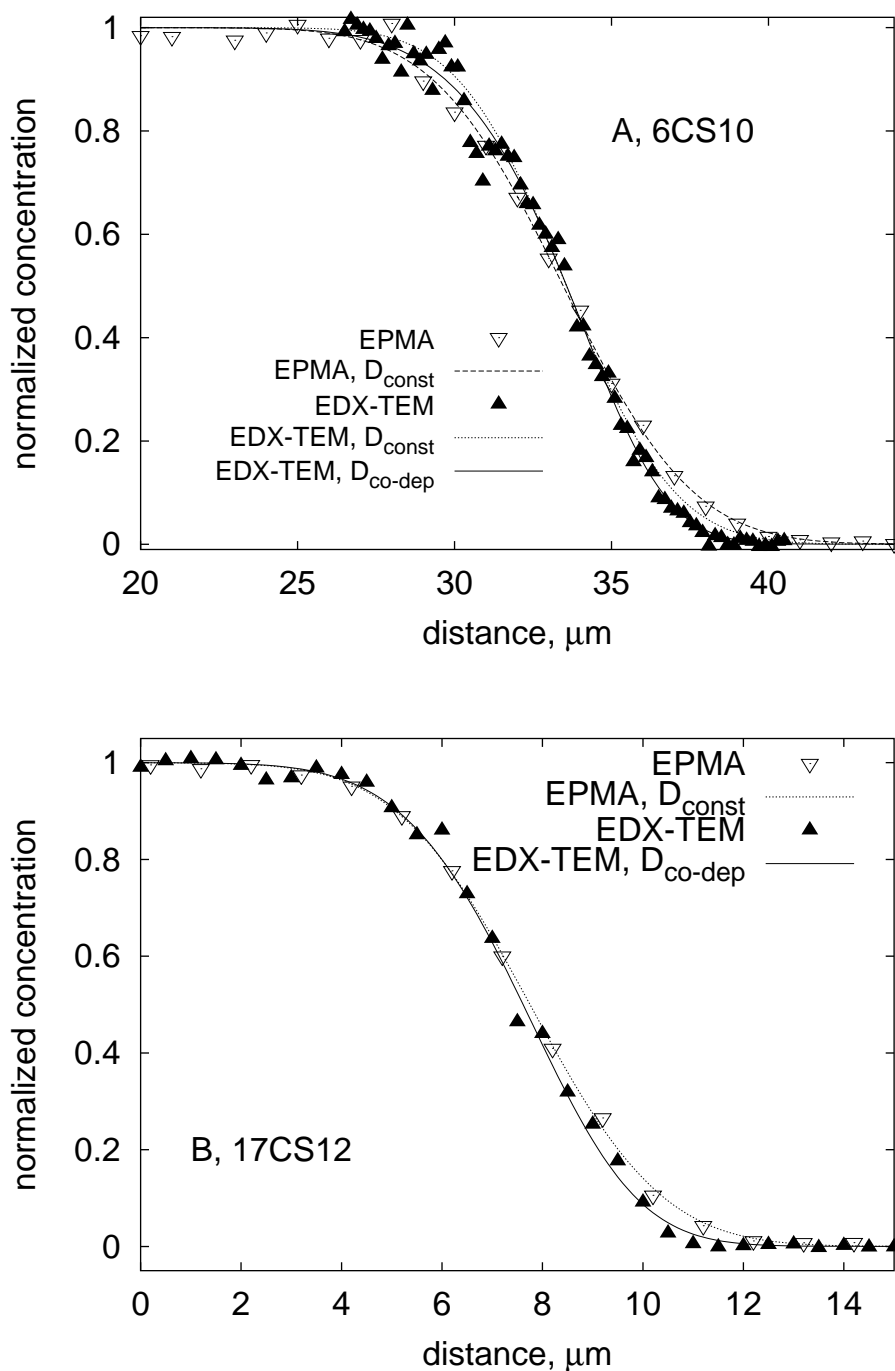


Figure 5.4: Comparison of Fe-profiles (normalized concentration) measured by EPMA and EDX-TEM for samples 6CS10 (A) and 17CS12 (B, see Table 5.1). For fitting the data an analytical solution (Eq. 5.4) was used (D_{const}) or a simulation employing an exponential composition dependence ($D_{\text{co-dep}}$), as discussed in the text.

5.2.4 Pressure dependence at constant temperature (1673 K)

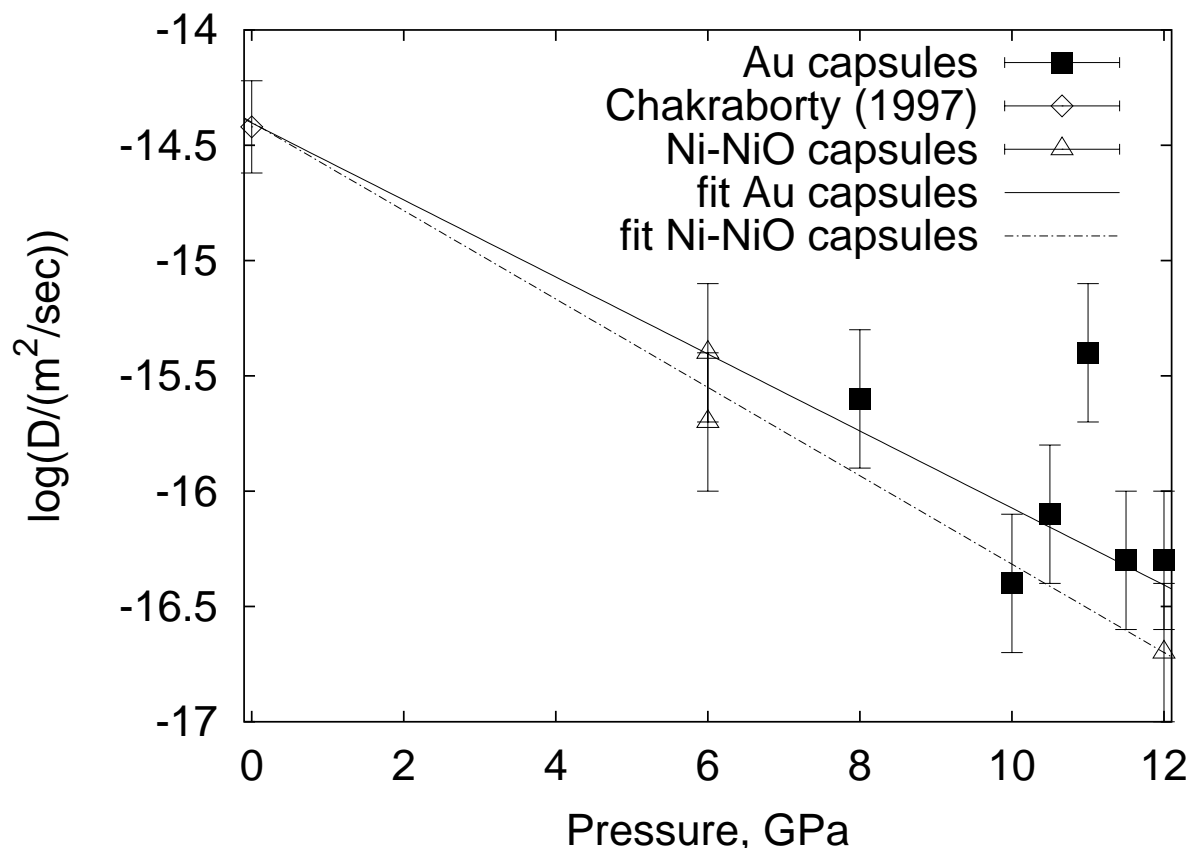


Figure 5.5: Diffusion coefficients as function of pressure for Fe-Mg exchange at 1673 K. In addition, a linear fit using results of experiments employing Ni-NiO capsules and a linear fit of results obtained from Au capsule experiments are shown. For the latter, the datapoint at 11 GPa was excluded as discussed in the text.

Diffusion coefficients listed in Table 5.1 at 1673 K and pressures between 6 and 12 GPa are plotted together with literature values at 1 bar (Chakraborty, 1997; Petry, 1999b) as function of P in Figures 5.5-5.7. Considering the experimental error, as outlined above, values determined using Ni-NiO capsules and therefore buffered close to the Ni-NiO buffer, are close to the values determined from Au capsule experiments, implying that the oxygen fugacity conditions in the Au capsules are close to the oxygen fugacity imposed by the Ni-NiO buffer. Nevertheless, the deviation seems to be systematically to slightly lower values although this conclusion is mainly based on the outcome of experiment 17CS12 at 12 GPa (Table 5.1). Hence activation volumes are

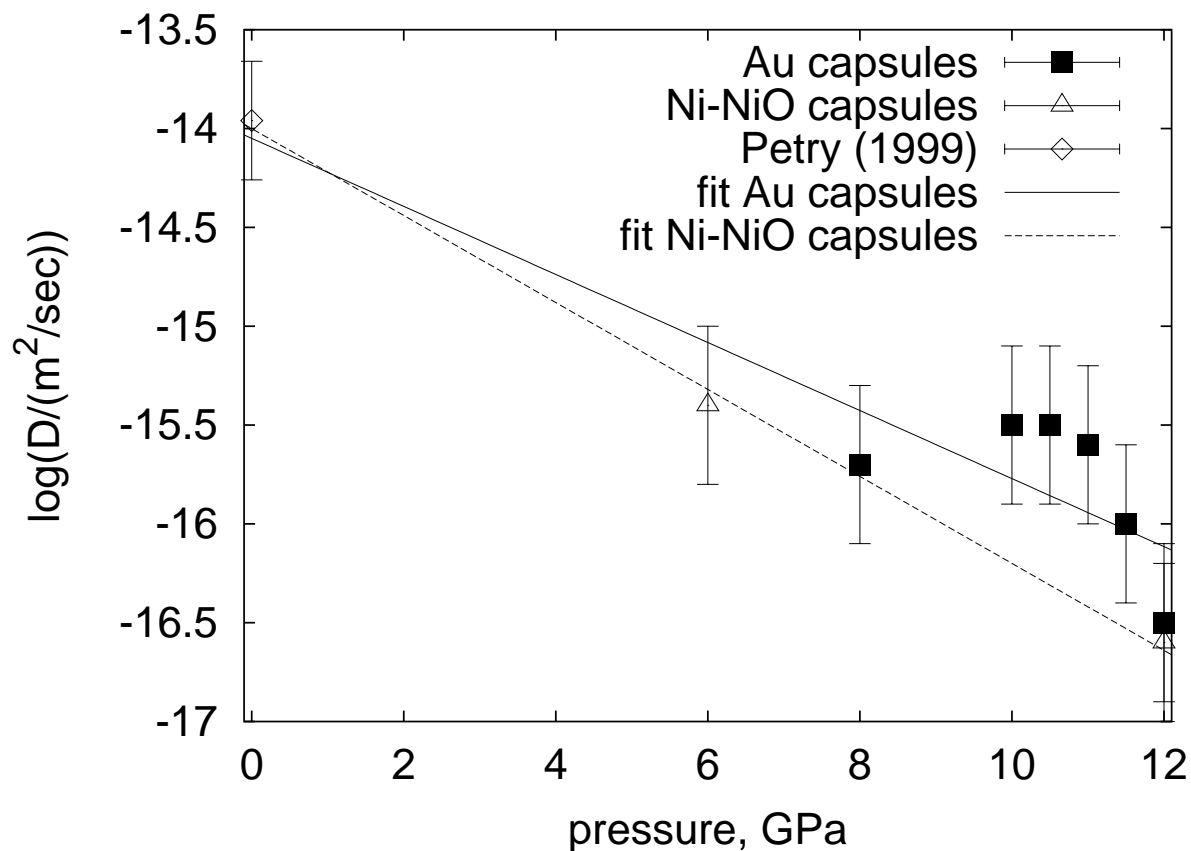


Figure 5.6: Diffusion coefficients as function of pressure for Ni at 1673 K. In addition, a linear fit using results of experiments employing Ni-NiO capsules and a linear fit of results obtained from Au capsule experiments are shown. For the latter, the datapoint at 11 GPa was excluded as discussed in the text.

calculated for both the complete dataset and for the experiments performed in Ni-NiO capsules alone to be able to judge if a statistically-significant difference exists.

For comparison, diffusion data for Fe-Mg exchange at 1 bar are taken from Chakraborty (1997), where an Arrhenius plot is given for Fo_{86} and Fo_{92} compositions at an oxygen fugacity of 10^{-12} bar (Fig. 5 in Chakraborty, 1997). The logarithm of the Fe-Mg interdiffusion coefficient at 1673 K and $X_{Fe_2SiO_4} = 0.08$ is $\log(D_{Fe-Mg}) = -15.36$. Taking the compositional dependence, as discussed in the previous section (Section 5.2.3), into account, the corresponding value for Fo_{97} is approximately 0.3 log-units smaller. The fO_2 effect is corrected with an oxygen fugacity exponent of 1/5, consistent with recent experimental results of Dohmen (pers. communication). Hence, the logarithm of the Fe-Mg interdiffusion coefficient at 1 bar, 1673

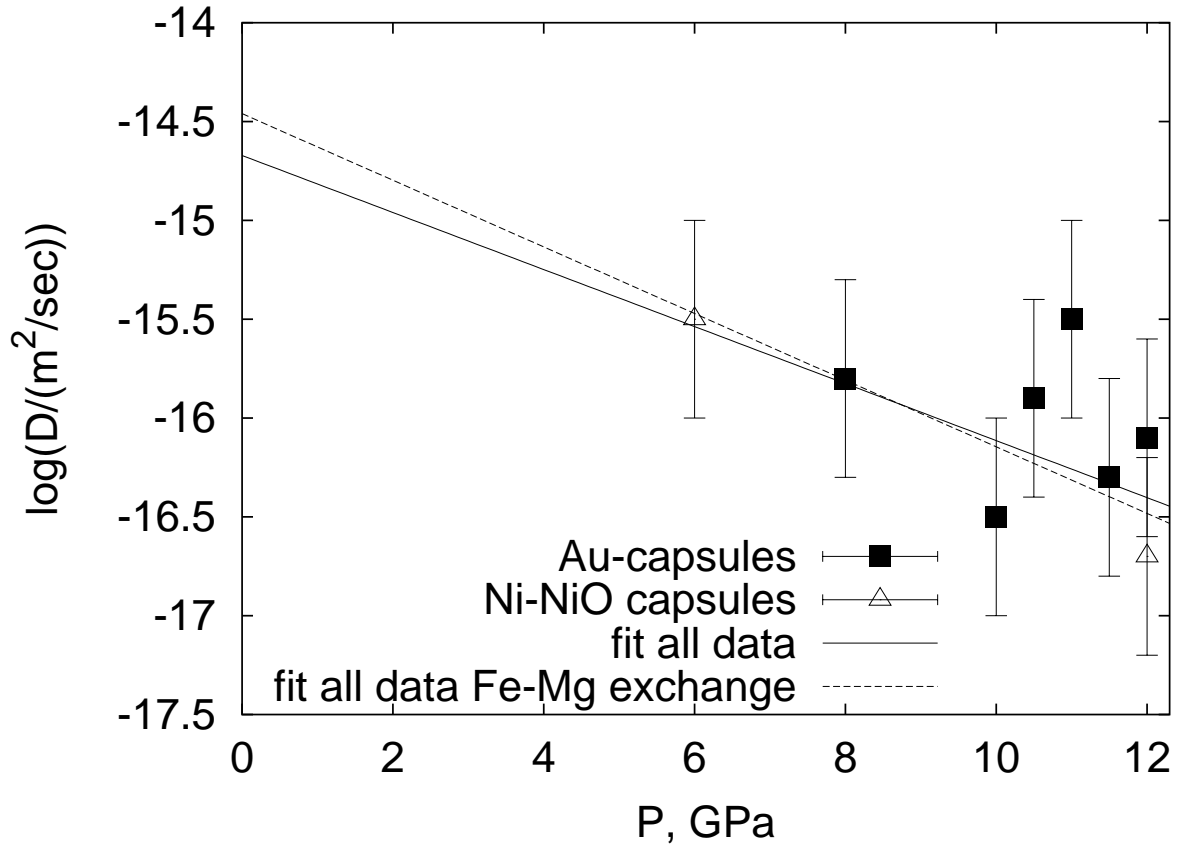


Figure 5.7: Diffusion coefficients as function of pressure for Mn diffusion at 1673 K.

K and $\log(fO_2) = 5.79$, equivalent to the Ni-NiO buffer at these conditions (calculated with data from Ride, 1991), becomes $\log D_{Fe-Mg}^{Fo_{97}} = -14.42$. For Ni diffusion, values derived from olivine diffusion couple experiments at 1 bar from Petry (1999b) and Petry et al. (2003) were chosen, employing a similar correction procedure. At 1673 K and $\log(fO_2) = -11$ the logarithm of D_{Ni} is -15.2 (Fig. 38 in Petry, 1999b, see also Petry et al., 2003). The compositional dependence is slightly less pronounced and a correction of 0.1 log-units was employed, whereas the fO_2 exponent is equal to 1/4.25, somewhat larger than for Fe-Mg interdiffusion, leading to $\log(D_{Ni}^{Fo_{97}}) = -14.0$. For Mn diffusion no rigorous correction scheme for the fO_2 and composition dependence can be employed for 1 bar data. Hence, only the high pressure data were fitted for retrieving the activation volume.

In Figures 5.5-5.7 it is evident that diffusivities at 11 GPa are significantly faster than a linear relationship between $\log(D)$ versus pressure would imply, especially for Fe-Mg interdiffusion.

Exp	$\Delta V_a(\text{Fe} - \text{Mg})$	Error	$\Delta V_a(\text{Ni})$	Error	$\Delta V_a(\text{Mn})$	Error
Ni-NiO (ex 1 bar)	6.1	1.4	6.4	n.d.	6.4	n.d.
Ni-NiO (in 1 bar)	6.1	0.6	7.0	0.4	-	-
Au (ex 1 bar)	5.3	2.2	5.5	4.0	2.5	3.1
all (ex 1 bar)	5.1	1.0	5.2	2.1	4.6	1.7
all (in 1 bar)	5.4	0.6	5.9	1.0	-	-

Table 5.3: Activation volumes ΔV_a for Fe-Mg interdiffusion, Ni diffusion, and Mn diffusion in olivine using linear fits for the data shown in Figures 5.5-5.7. Ni-NiO denotes results obtained in Ni-NiO capsules (including, in, or excluding, ex, data at 1 bar), Au denotes results obtained in Au capsules and all denotes the complete dataset.

This effect is also evident in the preliminary results of Chakraborty et al. (1999) as shown later in Fig. 5.14. The cause for this “spike” is uncertain, but the value at 11 GPa is derived from more than one experiment and thus cannot be regarded simply as a single outlier of the data. Careful electron imaging reveals a separation of both crystals after the diffusion experiments in this study, but the gap is smaller than 1 μm and any correction would only shift the datapoints slightly towards lower diffusivities ($\ll 0.1$ log-unit). Because no physical explanation for a real peak at this pressure is evident, the data at 11 GPa were excluded in the linear fit to calculate the activation volume. The linear fit is therefore designed to reproduce the remaining values as a function of pressure using the most simple model and including the results at 11 GPa would artificially shift the fit line. Hence the activation volumes derived in the following text gives a constant, average apparent activation volume that can be used to calculate data at higher pressures empirically, irrespective of its microscopic significance.

Table 5.3 lists the results for the activation volume of Fe-Mg interdiffusion, Ni diffusion and Mn diffusion employing Ni-NiO capsules only, Au capsules only, and the whole dataset determined using a linear fit according to Fig. 1.1. Depending on the data chosen, the activation volume lies in the range of 5.1 - 6.1 $\text{cm}^3 \text{mol}^{-1}$. The quoted errors in Table 5.3 are the asymptotic standard deviations of the fits given by the computer program gnuplot employing a Levenberg-Marquardt algorithm. Although this technique is a nonlinear least-square regression, the results are the same as obtained by simple linear regression and the asymptotic standard deviation becomes equal to the normal standard deviation for the regression parameters as calculated by for example formulas 5.60-5.61 in Sachs (1997). Considering the magnitude of the errors, the

difference between the activation volumes derived in Table 5.3 is not statistically significant. In addition, the difference in absolute diffusivities and the extrapolation towards a pressure of 1 bar implies that the values derived from Au capsule experiments are representative for diffusivities at an oxygen fugacity close or slightly higher than the Ni-NiO buffer.

For Ni-diffusion the data for the activation volumes are in the range of $5.5 \pm 1.0 \text{ cm}^3 \text{ mol}^{-1}$ to $7.0 \pm 0.4 \text{ cm}^3 \text{ mol}^{-1}$, for a fit of results employing Au capsules and a fit for Ni-NiO buffered data (including the 1 bar value of Petry et al., 2003), respectively. The uncertainty of the results obtained for Ni diffusion is much larger than for Fe-Mg interdiffusion. Hence, the activation volumes determined for Fe-Mg interdiffusion and for Ni diffusion are very close to each other within error (Table 5.3). The same statistical arguments as used for Fe-Mg exchange with respect to the $f\text{O}_2$ conditions prevailing inside the Au capsules experiments apply for Ni diffusion as well. Thus, diffusivities determined using Ni-NiO capsules and Au capsules are very close to each other.

For Mn diffusion, the activation volume using results of experiments performed in Au capsules is $2.5 \pm 3.1 \text{ cm}^3 \text{ mol}^{-1}$. The large analytical scatter of the Mn results, is the reason for the large uncertainty. Only a fit using all data results in a statistically significant activation volume of $4.6 \pm 1.7 \text{ cm}^3 \text{ mol}^{-1}$, fully compatible with values derived for Fe-Mg interdiffusion (Table 5.3). Therefore, in Figure 5.7, the fit for Fe-Mg interdiffusion is shown in addition to the fit for the Mn diffusion coefficients. Within the scatter of the data, the regression of Fe-Mg interdiffusion coefficients is fully compatible with the results for Mn. The extrapolated diffusivity at 1 bar is $\log(D_{\text{Mn}}) = -14.7$, which is close to the value of Fe-Mg interdiffusion ($\log(D_{\text{Fe-Mg}}) = -14.4$).

Based on the results presented in this section it can be concluded that the diffusion coefficients determined for divalent cations in olivine are close to each other, as already observed in studies at 1 bar (e.g. Petry et al., 2003). This is also true for the activation volume of diffusion which, for all three diffusion processes, lies in the range $4.0 - 7.0 \text{ cm}^3 \text{ mol}^{-1}$. Because no statistical significant difference between diffusion coefficients determined from experiments employing Au capsules and from those employing Ni-NiO capsules was found, the activation volume derived by a fit of all diffusion data in one system is regarded as the best estimate of the true activation volume at 1673 K and an $f\text{O}_2$ close to the corresponding value of the Ni-NiO buffer. Hence the most likely

value for Fe-Mg interdiffusion is $5.6 \pm 1.0 \text{ cm}^3 \text{ mol}^{-1}$. This would be the recommended value to use for the other elements as well, although consideration of formal errors suggests $4\text{-}7 \text{ cm}^3 \text{ mol}^{-1}$ based on data from various trace elements. This best fit value is also essentially the same as found for Fe-Mg interdiffusion by Misener (1974).

As discussed above, the values for the activation volume of Fe-Mg interdiffusion, Ni diffusion and Mn diffusion so far derived are valid along the Ni-NiO buffer. Therefore, the values of V_a include the variation of $f\text{O}_2$ representative of the Ni-NiO buffer. Strictly, the activation volume is defined for a constant oxygen fugacity. This is only possible if the oxygen fugacity variation of the Ni-NiO buffer can be calculated as a function of pressure and temperature. Literature values published so far can only be used as an approximation because of difficulties of measuring the oxygen potential at high pressures. Using values given in Ride (1991), the variation of $f\text{O}_2$ at 1673 K is between $\log f\text{O}_2 = -5.8$ at 1 bar to $\log f\text{O}_2 = -2.5$ at 12 GPa, assuming a constant volume of the oxidation reaction of Ni (see Section 5.1 for further explanations). This change in $f\text{O}_2$ corresponds to a change of 0.7 log units of diffusivity. Therefore an activation volume of $5.6 \text{ cm}^3 \text{ mol}^{-1}$ along the Ni-NiO buffer corresponds to a value of $7.4 \text{ cm}^3 \text{ mol}^{-1}$ at constant oxygen fugacity.

5.2.5 Temperature dependence at constant pressure (12 GPa)

To constrain the temperature dependence at elevated pressures, experiments at variable temperatures between 1623 K and 1823 K have been performed employing Au capsules. Diffusion coefficients for Fe-Mg interdiffusion, Ni diffusion and Mn diffusion are given in Table 5.1 and are displayed in Arrhenius plots in Figures 5.8-5.10. In all cases a linear trend without any significant kink is observed indicating that the diffusion mechanism does not change for divalent cations at 12 GPa in the temperature range 1623-1823 K. The slope over this temperature range is interpreted to be representative for the transition metal-extrinsic (TaMED) regime (Section 1.2.3). Hence, the activation energy is close to, but not exactly, the migration energy.

The activation energy at high pressure, E_a^P , calculated from the slope of the regression lines in Figures 5.8-5.10 is related to the activation energy at 1 bar, E_a^1 , by:

$$\left(\frac{\partial \ln D}{\partial \frac{1}{T}} \right)_P = -\frac{E_a^P}{R} = -\frac{E_a^1 + P \cdot \Delta V_a}{R} \quad (5.6)$$

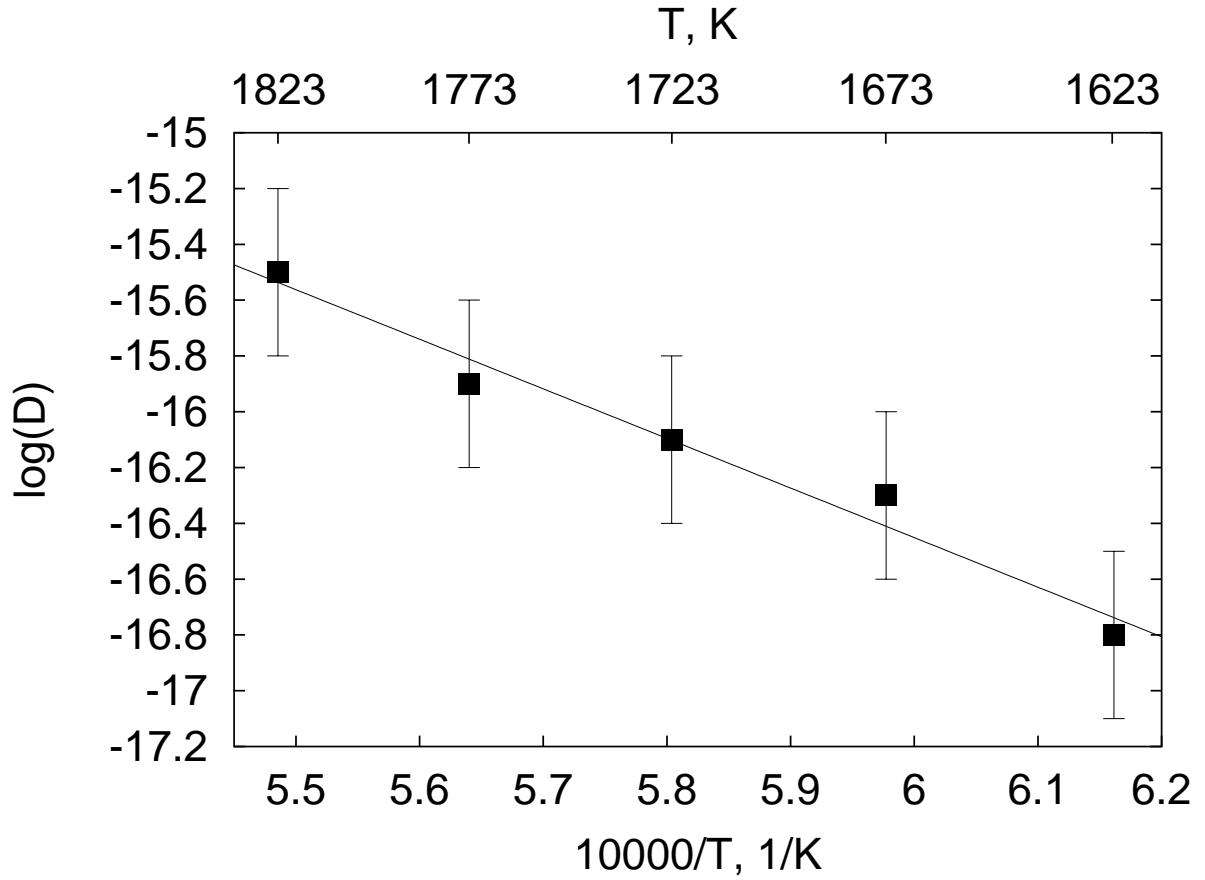


Figure 5.8: Diffusion coefficients as a function of inverse temperature for Fe-Mg exchange at 12 GPa using Au capsules.

as shown in Section 1.2.6 and Figure 1.1, assuming that the preexponential factor is pressure independent. In addition, as shown in the last section, the diffusion coefficients obtained using Au capsules follow a trend compatible with a change in fO_2 consistent with the Ni-NiO buffer, rather than representing values at constant fO_2 . Therefore the slope determined from a plot of $\log D$ versus inverse temperature must also consist of a fO_2 contribution. Formally this contribution can be derived by considering the total differential of $\log(D)$ with respect to inverse temperature and fO_2 at constant pressure:

$$(d\ln D)_P = \left(\frac{\partial \ln D}{\partial \frac{1}{T}} \right)_{fO_2, P} \left(\frac{\partial \frac{1}{T}}{\partial T} \right)_P + \left(\frac{\partial \ln D}{\partial \ln fO_2} \right)_{P, \frac{1}{T}} (d\ln fO_2)_P. \quad (5.7)$$

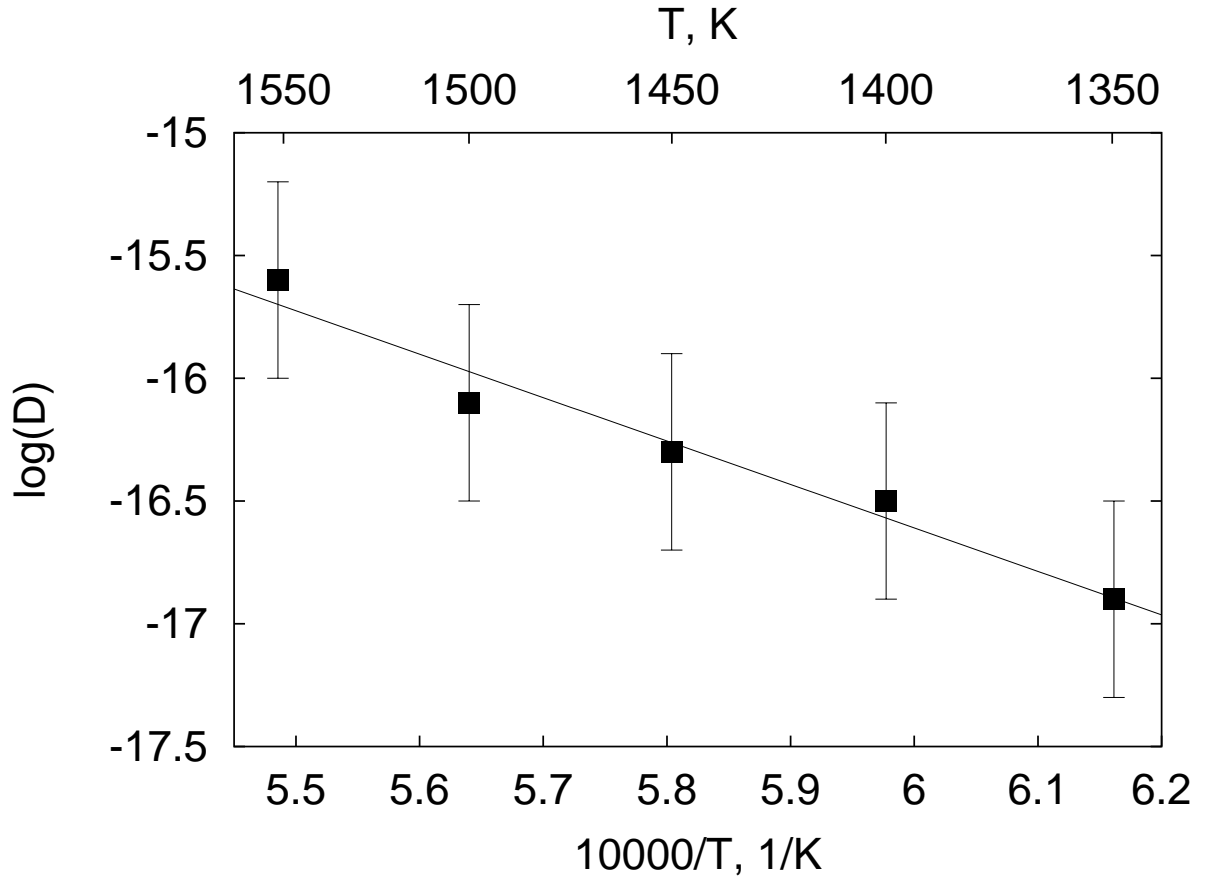


Figure 5.9: Diffusion coefficients as a function of inverse temperature for Ni at 12 GPa using Au capsules.

Equation 5.7 can be rewritten as:

$$(d\ln D)_P = -\frac{E_a}{R} \left(\frac{\partial \frac{1}{T}}{\partial T} \right)_P + \left(\frac{\partial \ln D}{\partial \ln f_{O_2}} \right)_{P, \frac{1}{T}} \left(\frac{\partial \ln f_{O_2}}{\partial \frac{1}{T}} \right)_{NNO, P} \left(\frac{\partial \frac{1}{T}}{\partial T} \right)_P. \quad (5.8)$$

Hence, the activation energy at high pressure including the effect of f_{O_2} , E_a^* , is:

$$E_a^* = E_a^{P,c} - R \left(\frac{\partial \ln D}{\partial \ln f_{O_2}} \right)_{P, \frac{1}{T}} \left(\frac{\partial \ln f_{O_2}}{\partial \frac{1}{T}} \right)_{NNO, P}, \quad (5.9)$$

where $H_a^{P,c}$ is the activation energy at high pressure and constant f_{O_2} . From recent experimental results, the dependence of the Fe-Mg interdiffusion coefficient on oxygen fugacity can be described with an exponent of 1/4.5 - 1/5.5 (Petry et al., 2003). Hence, an average value of 1/5 is assumed in this study. The temperature dependence of oxygen fugacity corresponding to the Ni-NiO buffer (NNO) at 12 GPa is much less well constrained. If a constant volume change,

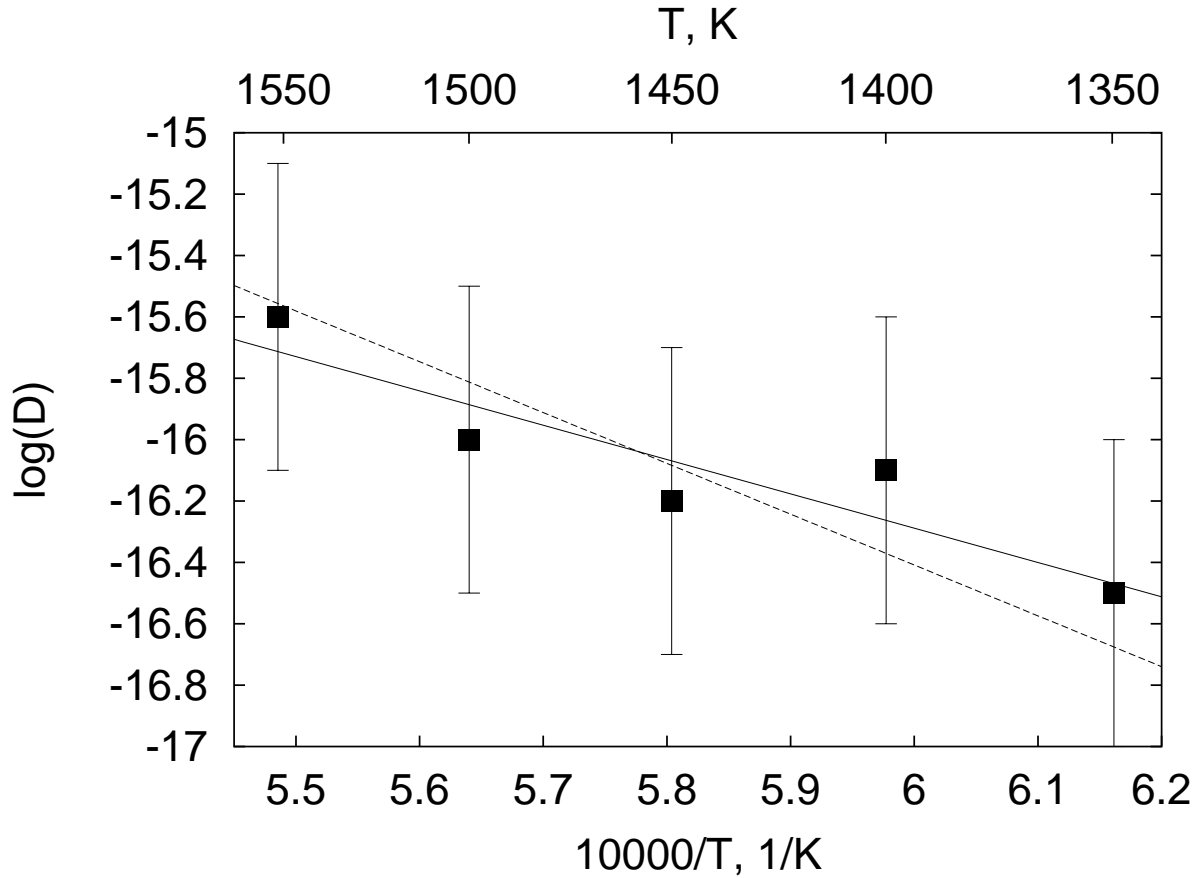


Figure 5.10: Diffusion coefficients as a function of inverse temperature for Mn at 12 GPa using Au capsules. The solid line is a linear fit of the Mn data. For comparison the dashed line shows the fit of the Fe-Mg interdiffusion data (Figure 5.8).

independent of pressure, of the Ni oxidation reaction is assumed, the apparent activation energy at 12 GPa $E_a^{*,12}$ including the change in fO_2 can be described according to Equation 5.8 using values of Ride (1991) as:

$$E_a^{*,12} = E_a + 72 \text{ kJ mol}^{-1}. \quad (5.10)$$

In the following paragraphs it will be tested if the activation energy including an fO_2 correction according to Equation 5.10, and considering the activation volume due to the pressure effect (Section 5.2.4), can describe the results of diffusion coefficients at variable temperatures at 12 GPa employing Au capsules.

For Fe-Mg interdiffusion, the slope of a linear fit of the results shown in Figure 5.8 leads to an activation energy E_a^* at 12 GPa of $317 \pm 23 \text{ kJ mol}^{-1}$. The activation energy E_a^* of Ni

diffusion is $339 \pm 37 \text{ kJ mol}^{-1}$ (determined using Figure 5.9) and for Mn diffusion a value of $214 \pm 55 \text{ kJ mol}^{-1}$ (Figure 5.10) is derived. The errors correspond to the $1-\sigma$ standard deviation of the linear fits. Considering the relatively small temperature range investigated, this error slightly underestimates the true experimental error, as is evident by the fact that a change of 0.1 log units of the datapoint for Fe-Mg interdiffusion at 1623 K changes the value of H_a^* from 317 to 340 kJ mol^{-1} . In addition, the fit of the Fe-Mg interdiffusion coefficients can relatively well describe the Mn data within the error of the measurements (Figure 5.10), although the difference in the best fit value of E_a^* between Fe-Mg interdiffusion and Mn diffusion is 100 kJ mol^{-1} .

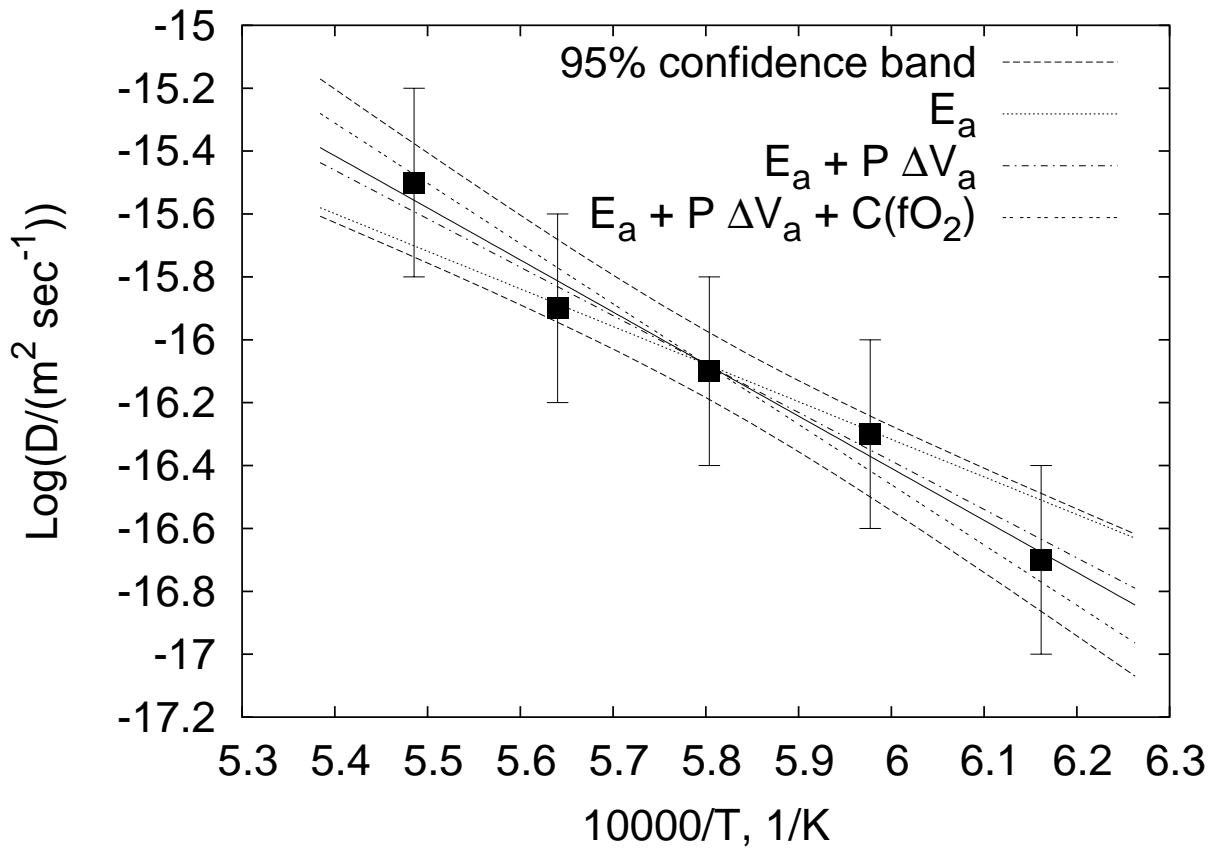


Figure 5.11: 95% confidence bands for Fe-Mg interdiffusion (dashed lines). The solid line is the linear fit of the data as described earlier in this section (page 101). The line labelled E_a has a slope consistent with the 1 bar pressure activation energy. The other lines take the variation of fO_2 with pressure at constant temperature ($E_a + P V_a$) and the variation of fO_2 with temperature at 12 GPa ($E_a + P \Delta V_a + C(fO_2)$) into account.

Figure 5.11 shows results of Fe-Mg interdiffusion coefficients at 12 GPa obtained using Au

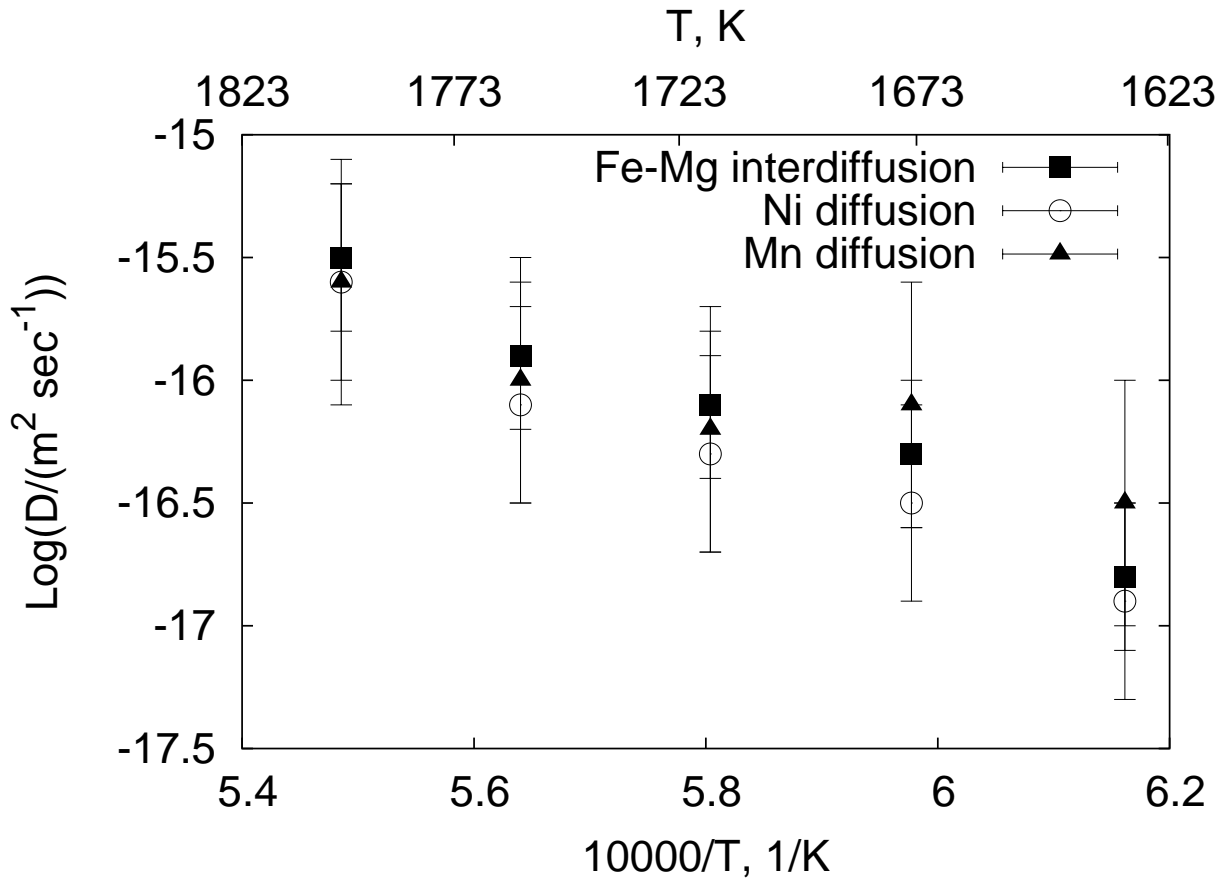


Figure 5.12: Superposition of results for Fe-Mg interdiffusion, Ni diffusion and Mn diffusion.

capsules together with the 95% lower and upper confidence bounds of a linear fit calculated with the computer program MicrocalTMOriginTM (see also Sachs, 1997) superimposed. The solid line is the linear fit obtained earlier (Figure 5.8). The line labelled E_a has a slope corresponding to the 1 bar value of 229 kJ mol^{-1} (Chakraborty, 1997). Considering the confidence bounds, the deviation of this line from the best linear fit can still be interpreted by the error of the measurements although the slope appears to underestimate the observed temperature dependence. To account for the pressure effect, a term $P \times \Delta V_a$ is added to the low pressure value (line $E_a + P \Delta V_a$ in Figure 5.11), using the activation volume along the Ni-NiO buffer of $\sim 5.5 \text{ cm}^3 \text{ mol}^{-1}$ determined in Section 5.2.4, hence including the variation in fO_2 due to pressure at constant temperature. This line is very close to the variation of $\log(D)$ versus inverse temperature observed in Figure 5.11. If the oxygen fugacity inside the Au capsules would vary in the same way as the Ni-NiO buffer then the contribution due to a change of fO_2 with temperature at 12 GPa has to be included in the

activation energy (Equation 5.10, line termed $E_a + P \Delta V_a + C(fO_2)$ in Figure 5.11). The slope of this line is slightly higher than the linear best fit but still describes the experimental results very well considering the limits of the confidence bounds. This implies that within the error of the experimental results, Fe-Mg interdiffusion coefficients determined using Au capsules, are very close to conditions imposed by the Ni-NiO buffer in the experimental range of 1623 K to 1823 K at pressures between 6 and 12 GPa.

Figure 5.12 shows a superposition of results obtained for Fe-Mg interdiffusion, Ni diffusion and Mn diffusion in order to compare the diffusivities of the different components to each other. The data plotted in Figure 5.12 are overlapping to a large extent implying that within the temperature interval investigated, diffusivities of divalent cations are very similar to each other as already observed at 1 bar (Petry et al., 2003). Therefore, Fe-Mg interdiffusion coefficients can be used as a proxy for divalent cation diffusion at high pressure in olivine.

5.2.6 Model of diffusion in olivine

In Section 5.2.4 the activation volume for Fe-Mg interdiffusion along the Ni-NiO buffer was constrained to lie in the range of 5.1 to 6.1 cm³ mol⁻¹. Therefore, a value of 5.6 ± 0.5 cm³ mol⁻¹ is taken as the best fit value for the activation volume of Fe-Mg interdiffusion along the Ni-NiO buffer. This value corresponds to a true activation volume of 7.4 ± 1.0 cm³ mol⁻¹ at constant oxygen fugacity (Section 5.2.4), estimated using a model for fO_2 as a function of pressure with a constant volume change of the oxidation reaction of Ni. Combining these values with existing results at 1 bar (Chakraborty, 1997, Dohmen, personal communication), allows to formulate an Equation for Fe-Mg interdiffusion coefficients as function of pressure, temperature, composition and oxygen fugacity in olivine along the c-axis :

$$D_{\text{Fe-Mg}} = 9.48 \times 10^{-7} \frac{\text{m}^2}{\text{sec}} (fO_2)^{\frac{1}{5}} \exp\left(-\frac{229000 + 0.74 P(\text{bar})}{8.31441 T(\text{K})}\right) \exp(7 X_{\text{Fe}_2\text{SiO}_4}). \quad (5.11)$$

In Figure 5.13, Equation 5.11 is compared to Fe-Mg interdiffusion coefficients determined at temperatures between 1623 K and 1823 K employing diffusion couples contained in Au capsules at a pressure of 12 GPa. Within the error of the experiments a good consistency is observed. Diffusion coefficients derived for Ni and Mn are very similar to values derived for Fe-Mg interdiffusion (Section 5.2.4, 5.2.5). Therefore, diffusion coefficients calculated using Equation 5.11

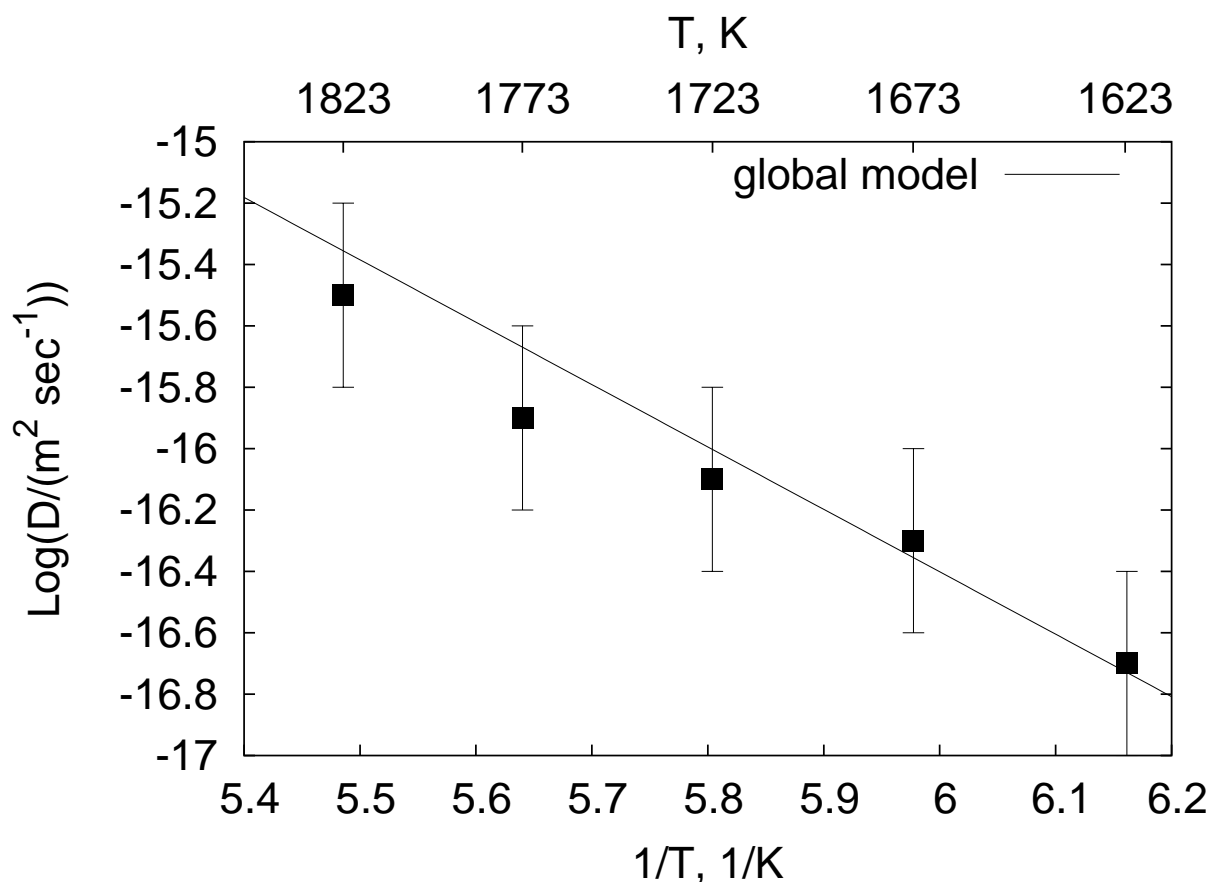


Figure 5.13: *Fe-Mg interdiffusion coefficients are consistent with a model combining the activation volume determined in this study with results at 1 bar (Equation 5.11). See text for further details.*

are very close to the diffusion coefficients of Ni and Mn at the same conditions.

5.2.7 Comparison with previous results

The results for Fe-Mg interdiffusion obtained in this study are shown together with literature values of Misener (1974), Farber et al. (2000), and Chakraborty et al. (1999) in Figure 5.14.

Misener (1974) performed high pressure experiments up to 3.5 GPa in a piston cylinder apparatus. Fe-Mg interdiffusion data at 1373 K and $X_{\text{Fe}_2\text{SiO}_4} = 0.4$ were taken from Fig. 6 in Misener (1974). A temperature correction to 1673 K employing an activation energy of 229 kJ mol⁻¹ (Chakraborty, 1997) was performed. The composition dependence was taken into account with a correction of -1.0 log-units consistent with the correlation of diffusivity and composition

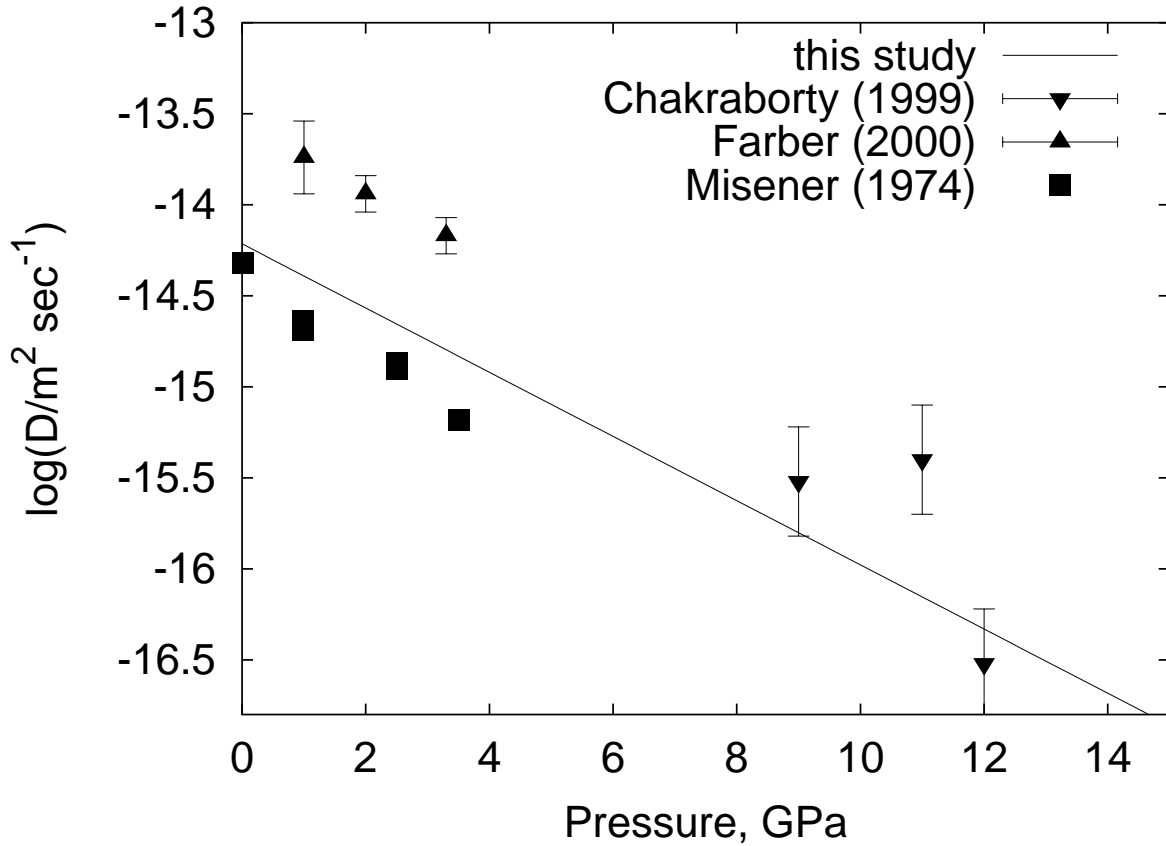


Figure 5.14: Comparison of the results obtained in this study for Fe-Mg interdiffusion (Equation 5.11) with results of other high pressure studies in the literature. All values are normalized to $X_{\text{Fe}_2\text{SiO}_4} = 0.03$, 1673 K at an fO_2 corresponding to the Ni-NiO buffer.

shown in Fig. 4a of Chakraborty (1997). The oxygen fugacity was not corrected because the experiments of Misener (1974) were performed in silica tubes where the oxygen fugacity most likely is close to the quartz-fayalite-magnetite buffer (QFM) which is within one order of magnitude of the fO_2 imposed by the Ni-NiO buffer at 1 bar (Frost, 1991). The data are in very good agreement with the correlation found in this study for both the absolute value of the diffusion coefficients and the pressure trend. The activation volume of $5.5 \text{ cm}^3 \text{ mol}^{-1}$ originally derived by Misener (1974) is identical within error to the value derived in this study ($5.6(1.0) \text{ cm}^3 \text{ mol}^{-1}$, along the Ni-NiO buffer).

In contrast, the values of Farber et al. (2000) are approximately 0.8 log-units higher. Farber et al. (2000) give no explanation for the difference but it is interesting to note that in their dis-

cussion they conclude that the results of Buening and Buseck (1973) are consistent with their results although the diffusion coefficients of Buening and Buseck (1973) are almost an order of magnitude faster. Hence, the establishment of consistency used in Farber et al. (2000) seems to be rather ambiguous. In addition, the fact that the redox conditions prevailing in the experiments of Misener (1974) are different than in Farber et al. (2000) is completely ignored in the discussion of Farber et al. (2000). The water content of the diffusion couples of Farber et al. (2000) was only established for the single crystals of olivine. More important would have been at least a qualitative estimate of the water content of the polycrystalline parts of the experiments because of possible water enrichment on the particle surfaces.

Partly, the difference between the results of this study and Farber et al. (2000), could be due to grain boundary diffusion in the experiments of the latter which utilized a single crystal of forsterite and polycrystalline fayalite as the diffusion couple. Based on estimates of the grain boundary width in olivine and grain size, Farber et al. (2000) calculate that effective diffusion coefficients (representing a combination of grain boundary and bulk diffusion) might be up to 5 times greater than the true volume diffusion coefficient for their experiments. In addition, the composition space investigated by Farber et al. (2000) comprises the whole compositional range of $X_{\text{Fe}_2\text{SiO}_4}$ between 0 and 1. This might lead to some inaccuracies when calculating diffusivities at the more extreme ends of the diffusion couple. Because their values are all normalized to $X_{\text{Fe}_2\text{SiO}_4} = 0.15$, the diffusion coefficients were adjusted to $X_{\text{Fe}_2\text{SiO}_4} = 0.03$ by subtracting 0.5 log-units. The oxygen fugacity was close to the Ni-NiO buffer as in this study because Ni containers with NiO were used. The experiments performed by Farber et al. (2000) for Fe-Mg interdiffusion in olivine only span the pressure range up to 3.3 GPa. The pressure dependence of Fe-Mg interdiffusion given in Farber et al. (2000) with an activation volume of $5.4(4.0) \text{ cm}^3 \text{ mol}^{-1}$ along the Ni-NiO buffer is in good agreement with the results presented in this work ($5.6(1.0) \text{ cm}^3 \text{ mol}^{-1}$).

In Chakraborty et al. (1999) three experiments performed in Au capsules using a similar assembly to that employed in this study were reported. These experiments were performed at the Bayerisches Geoinstitut using 1200 t multianvil press rather than the 500 t press used in this study (see Section 2.2). The profile in Fig. 2A for olivine in Chakraborty et al. (1999) leads to

a composition-dependent diffusion coefficient of $D = 2.2 \times 10^{-16} \exp(14.2 X_{\text{Fe}_2\text{SiO}_4})$, reinvestigated with the numerical algorithm developed in Section 4.3.2. The composition dependence is significantly stronger than observed at 1 bar as already noted in Chakraborty et al. (1999). A closer investigation of one of their samples by EBSD revealed that only the Fe-rich olivine was oriented along the *c* direction whereas the forsterite was oriented along the *a* axis generally showing slower diffusion coefficients. From EBSD-mapping the change in orientation occurs on a length scale below 1 μm , implying no long range misorientation profiles. This explains the strong asymmetry observed in the profiles of Chakraborty et al. (1999), although no kink in the profile is observed. The comparison of data at 9, 11 and 12 GPa for Fe-Mg interdiffusion given in Chakraborty et al. (1999) shows a good agreement with results of the present study although interestingly the value at 11 GPa is again much faster than expected by a simple linear relationship between $\log D$ and pressure P . The error bars were taken as large as in the present study because the experimental procedure was the same in both sets of experiments.

It is difficult to compare the values of Jaoul et al. (1995), obtained between 0.5 and 9 GPa, with the results reported here. In the present study, diffusion was determined in the *c* direction whereas Jaoul et al. (1995) investigated diffusion along the *b* axis. The activation energy derived is only 147 or 62 kJ mol^{-1} , depending on the model describing the diffusion regime of the experiments. It was claimed that these low activation energies are due to the experiments being performed at low temperatures (873 K - 1173 K) in an extrinsic regime, whereas other experiments at higher temperature would be in an intrinsic regime. The experiments of Buening and Buseck (1973), from which a kink in the Arrhenius plot at 1373 K is observed, are taken as evidence of this transition. This conclusion is contradicted by the conclusions of Chakraborty (1997). According to his study, diffusion in Fe-bearing olivine occurs in laboratory experiments always in a transition metal-extrinsic (TaMED) regime because diffusion rates depend on oxygen fugacity (Section 1.2.3). The kink observed by Buening and Buseck (1973) is thus attributed to the transition from a bulk to a grain boundary diffusion dominated regime. Hence, it is not clear how to correct the data from Jaoul et al. (1995) to the high temperature conditions of this study and they are thus omitted in Figure 5.14.

5.3 Wadsleyite

5.3.1 Conditions of experiments

The conditions of the wadsleyite diffusion experiments are presented in Table 5.4. They were conducted at temperatures higher than in the previous studies of Chakraborty et al. (1999) and Farber et al. (2000) in order to extend the currently available dataset on Fe-Mg interdiffusion coefficients to better estimate the activation energy. For diffusion experiments, Ni-NiO capsules have been used, buffering fO_2 close to the Ni-NiO buffer. As shown in the previous section on olivine, diffusion coefficients determined using Au capsules (this study and Chakraborty et al., 1999) are similar to results for experiments performed with Ni-NiO capsules. In addition, the agreement between Fe-Mg interdiffusion coefficients of wadsleyite derived by Chakraborty et al. (1999), employing Au capsules, and by Farber et al. (2000), using Ni-NiO capsules, show that experiments using both types of capsules are directly comparable to each other without any fO_2 correction.

Due to the restricted pressure and temperature stability field of wadsleyite (Akaogi et al., 1989), experiments in this study were conducted at a constant pressure of 15 GPa, which is the same pressure used by Chakraborty et al. (1999). The composition of the diffusion couples ranges from $X_{Fe_2SiO_4} = 0$ to 0.16 as shown in Section 2.3.3, where $X_{Fe_2SiO_4}$ is mole fraction of Fe_2SiO_4 in the $(Mg,Fe)_2SiO_4$ solid solution.

Sample	Capsule	T , K	P , GPa	t , min	D_{Fe-Mg}	
					D_0 , $\frac{\mu m^2}{sec}$	a
C45	Ni-NiO	1773	15	16	0.047	11.79
C49	Ni-NiO	1673	15	20	0.049	13.89

Table 5.4: Results and conditions of the wadsleyite high pressure diffusion runs. Composition-dependent Fe-Mg interdiffusion coefficients are given as $D_{Fe-Mg} = D_0 \exp(a X_{Fe_2SiO_4})$ resulting from numerical simulations of the diffusion coefficient as described in Section 4.3.2.

5.3.2 Backscatter images and sample characterization

Backscatter images of Fe-Mg interdiffusion experiments employing presynthesized polycrystalline wadsleyite samples (Section 2.3.3) are shown in Figures 5.15 and 5.16. Careful ob-

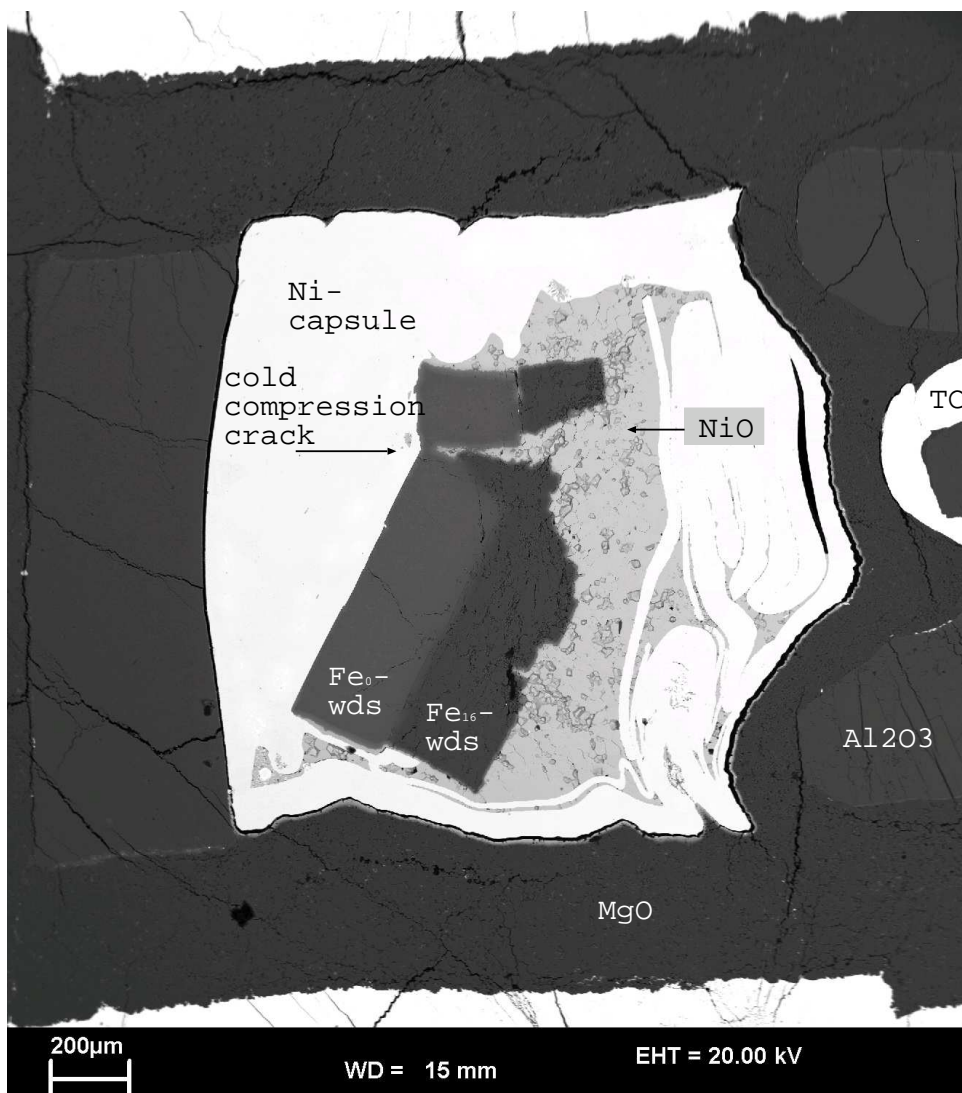


Figure 5.15: Backscatter image of sample C45, performed at 1773 K, 15 GPa for 16 minutes in a 14/8 assembly. Presumably during initial compression, the diffusion couple broke into two parts. Profiles were investigated, where the diffusion front is regular, away from the cracked zone.

servations of the diffusion zone by backscatter imaging and elemental mapping does not reveal any significant disturbances of the diffusion front, which would be expected if grain boundary diffusion plays an important role. Orientation contrast imaging reveals that grain sizes on the

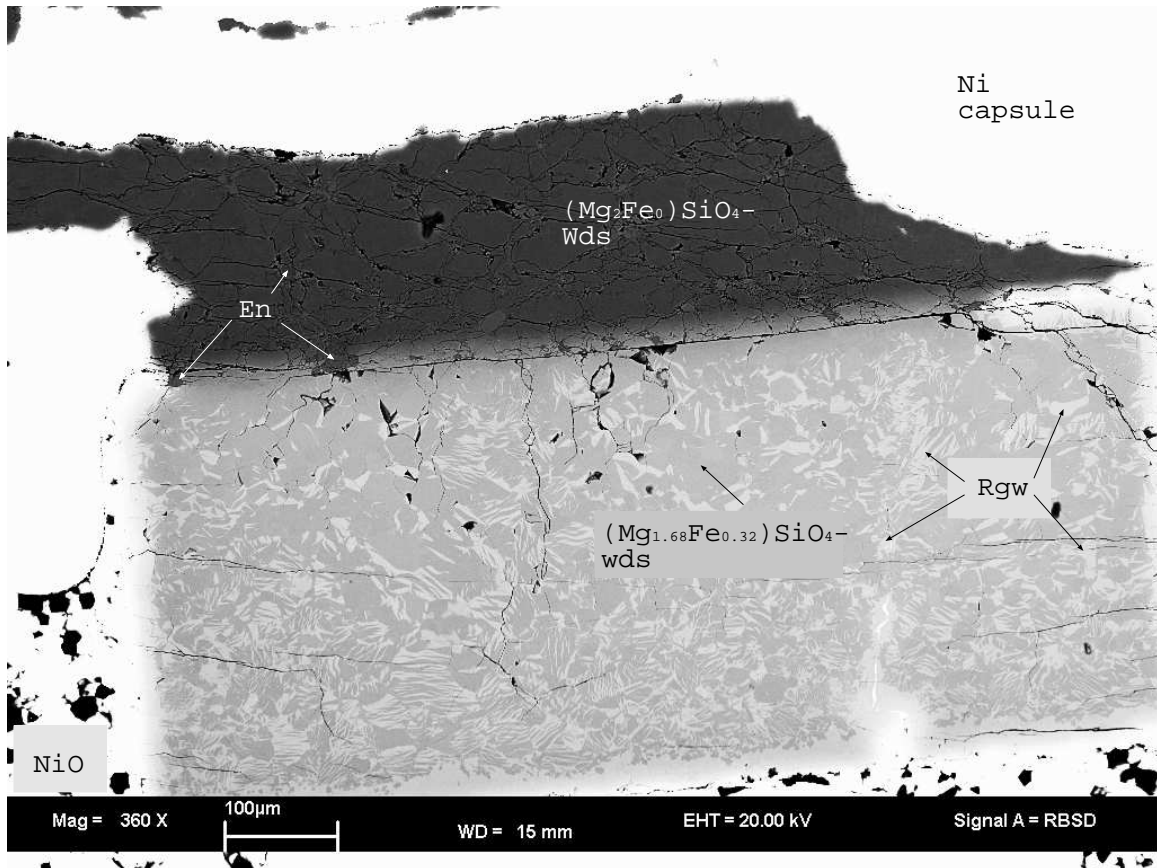


Figure 5.16: Backscatter image of sample C49, performed at 1673 K, 15 GPa for 10 minutes in a 14/8 assembly. Wds denotes wadsleyite, Rgw denotes ringwoodite, and En denotes enstatite.

Fe-rich side are on the order of $25\ \mu\text{m}$. On the Mg-rich side, grains of approximately $60\ \mu\text{m}$ are found which show a pervasive deformation microstructure. The large grains are recrystallized into subgrains of $\sim 1\ \mu\text{m}$ during the high-pressure, high-temperature anneal. Potentially this could lead to enhanced diffusion as was shown for the feldspar system by Yund and Tullis (1991). Sometimes, diffusion along subgrain boundaries effects very short profiles ($< 500\ \text{nm}$) in perovskite diffusion experiments (see Section 5.5.3), but is probably not significant in the wadsleyite experiments discussed here, as no effect is detected from element mapping.

The backscatter image of samples C45 and C49 (Figures 5.15 and 5.16), together with element mapping, reveal the presence of a silica-rich phase with enstatite stoichiometry (hereafter called enstatite), in addition to wadsleyite, on the Fe-free side of the interface. In this case this phase is interpreted to result from the synthesis where the stoichiometry of the starting mixture

was not in the exact proportions.

On the Fe-rich side of the diffusion couples, the presence of a Fe-rich phase is observed in sample C49 and also in minor quantities in sample C45. This phase was identified as ringwoodite by Raman spectroscopy (Fig. 5.17). The amount of ringwoodite depends on the temperature

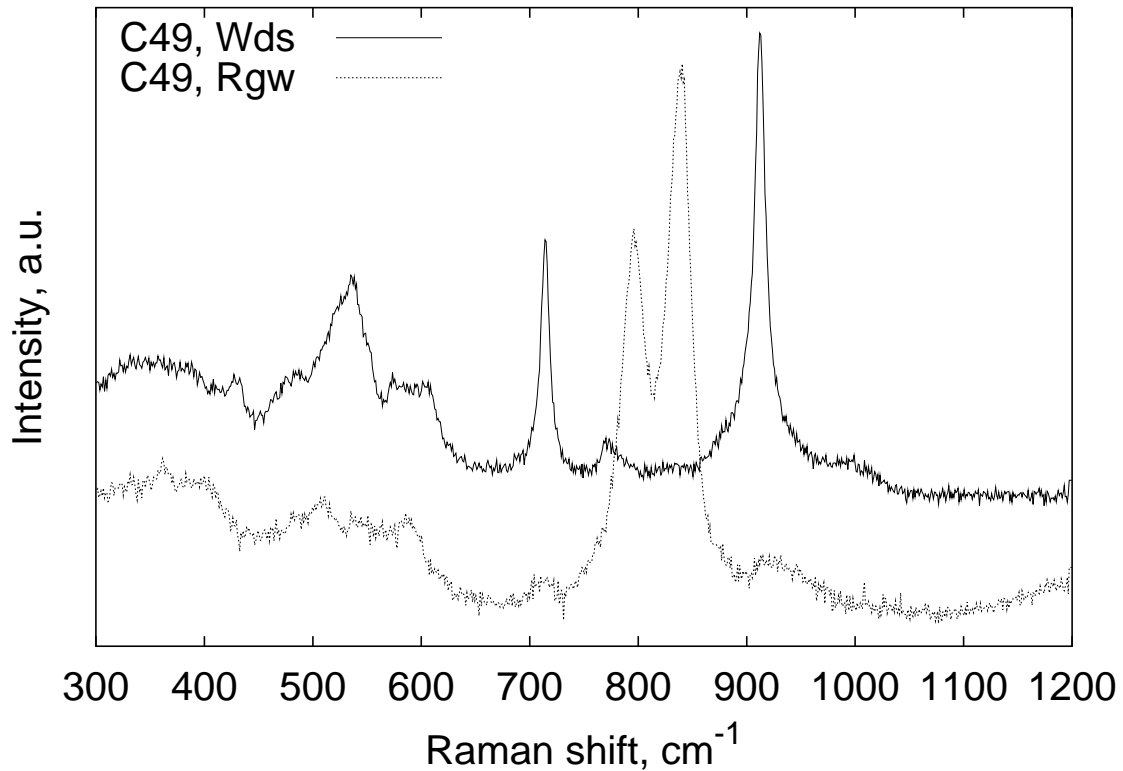


Figure 5.17: Raman spectra for the Fe-rich side of sample C49: The host phase is wadsleyite (C49, Wds) with newly formed inclusions of ringwoodite (C49, Rgw).

of the experiment with less ringwoodite occurring at higher temperature, consistent with the wadsleyite stability field in the $\text{Mg}_2\text{SiO}_4\text{-Fe}_2\text{SiO}_4$ phase diagram (Akaogi et al., 1989). The composition of the wadsleyite matrix in sample C49 is $X_{\text{Fe}_2\text{SiO}_4} = 0.15$ and that of the ringwoodite inclusions is $X_{\text{Fe}_2\text{SiO}_4} = 0.22$, placing an additional constraint on the pressure during the experiment. Employing the compositions of coexisting wadsleyite and ringwoodite and using Fig. 8 in Akaogi et al. (1989) and a linear temperature interpolation of the phase boundaries between 1473 and 1873 K, the estimated pressure for $T = 1673$ K is 15.5 ± 0.5 GPa. This value is slightly higher than but within error of the nominal pressure of 15 GPa. The volume decrease during transformation and corresponding pressure drop in the synthesis experiments explains

why ringwoodite inclusions are not evident in the synthesized samples prior to the diffusion experiments.

Because wadsleyite can potentially accommodate several thousand ppm of water (Kohlstedt et al., 1996; Bolfan-Casanova et al., 2000; Litasov and Ohtani, 2003), IR-spectroscopy was performed on sample C45, resulting in water concentrations of around 35 ppm for both endmembers (employing the absorption correction procedure of Paterson, 1982). This is an extremely low water content for wadsleyite showing that the results presented here are representative of dry wadsleyite. Preliminary results of Shimojuku et al. (2002) suggest that there may be a strong influence of water on Fe-Mg interdiffusion in wadsleyite.

5.3.3 Profiles

Figures 5.18 and 5.19 show representative Fe and Mg concentration profiles for samples C45

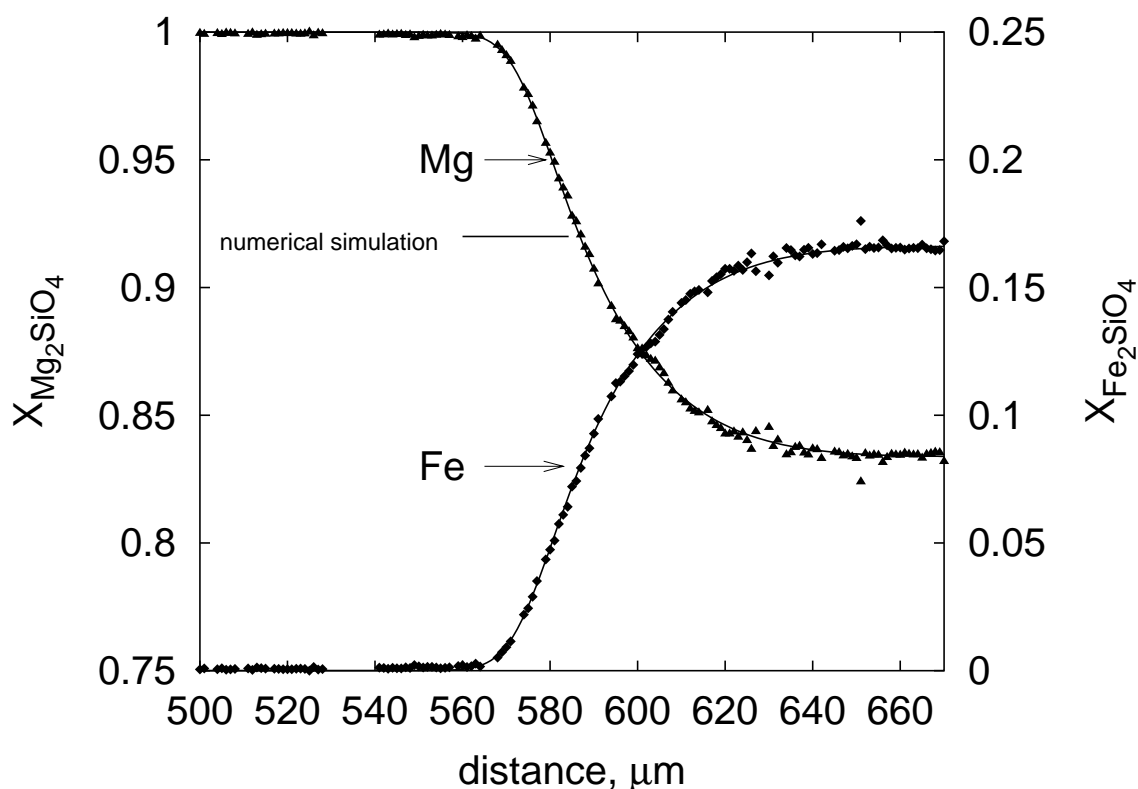


Figure 5.18: Representative Fe and Mg profiles measured by EPMA on sample C45, performed at 15 GPa, 1773 K for 16 minutes.

and C49 (Table 5.4). Both profiles show a marked asymmetry, implying that the Fe-Mg interdif-

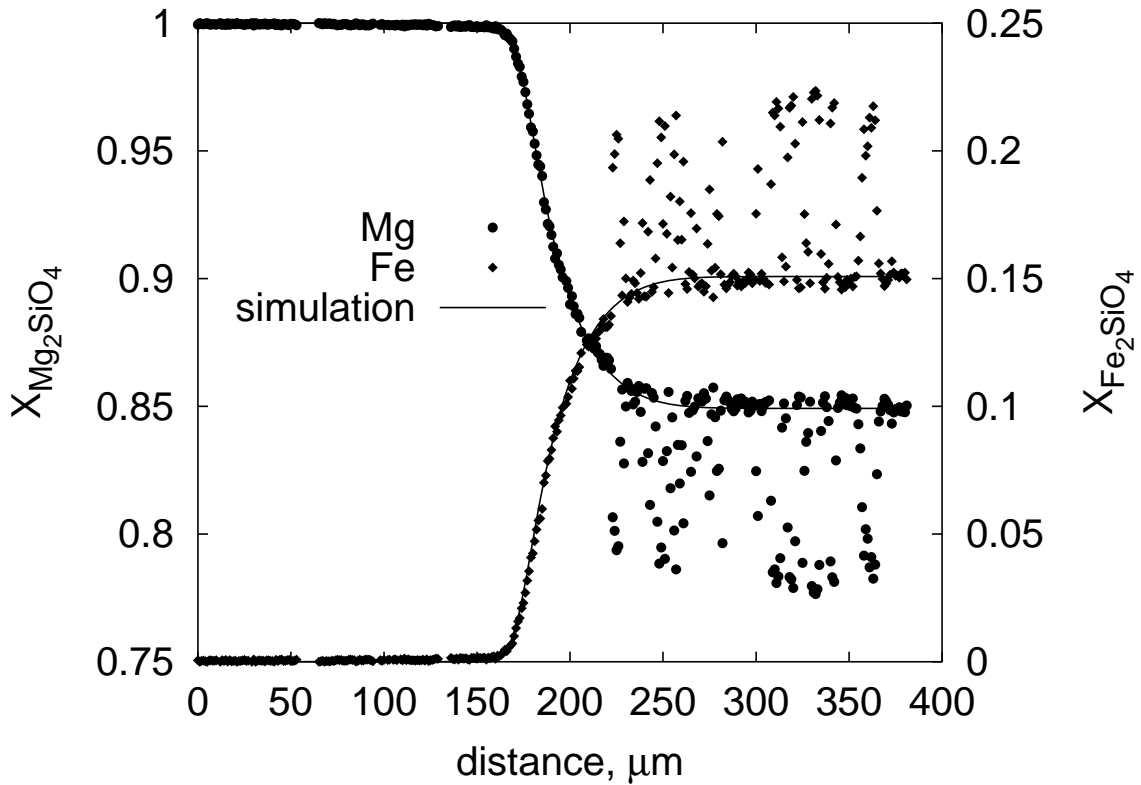


Figure 5.19: Representative Fe and Mg profiles measured by EPMA on sample C49, performed at 15 GPa, 1673 K for 20 minutes. The large analytical scatter on the Fe-rich side of the profile results from the presence of inclusions of ringwoodite (see text), which are smaller than the resolution limit of the profile analysis.

fusion coefficient is strongly composition-dependent. Hence, for retrieving diffusion coefficients numerical simulations had to be performed, also shown in Fig. 5.18 and 5.19. It was found that an exponential composition dependence, qualitatively valid also for olivine (Chakraborty, 1997), well reproduces the observed asymmetry of the profiles.

On the Fe-rich side of the profile shown in Figure 5.19 for experiment C49, performed at 15 GPa and 1673 K, the crystallization of ringwoodite, as described in the previous section, causes the analytical scatter. For the simulation of the profile the composition of the wadsleyite is taken for profile normalization (Section 4.1) and the ringwoodite is assumed to have formed immediately after heating the experiment. This assumption is justified because the wavelength of the inclusions is roughly a factor of 10 smaller than the diffusion profile. Therefore, the time of equilibration of the ringwoodite in the wadsleyite matrix should be approximately a factor of 100 faster than the establishment of the diffusion profile (estimated from $x \propto \sqrt{Dt}$, see Section

4.2). In addition, because the crystallization of ringwoodite only occurred on the most Fe-rich side of the diffusion couple, most of the profile length is not affected. Hence, the role of ringwoodite crystallization for the determination of diffusion coefficients should be negligible. Even if the composition of the wadsleyite on the Fe-rich side changes during the diffusion experiment, from $X_{\text{Fe}_2\text{SiO}_4} = 0.165$, the average composition of the wadsleyite of sample C45 which is almost unaffected by ringwoodite crystallization, to $X_{\text{Fe}_2\text{SiO}_4} = 0.153$, the average wadsleyite composition of C49, the composition-dependent Fe-Mg interdiffusion coefficient would be between $4.9 \times 10^{-14} \exp(12.96 X_{\text{Fe}_2\text{SiO}_4}) \text{ m}^2 \text{ sec}^{-1}$ and $4.9 \times 10^{-14} \exp(13.89 X_{\text{Fe}_2\text{SiO}_4}) \text{ m}^2 \text{ sec}^{-1}$, resulting in a change of $\log D_{\text{Fe-Mg}}$ from -12.47 to -12.41 (for $X_{\text{Fe}_2\text{SiO}_4} = 0.15$) at most. This is well below the overall uncertainty of diffusion experiments in the multianvil apparatus, established for the olivine experiments in Section 5.2.3. Therefore, absolute diffusivities determined for sample C49 were included for the determination of the activation energy (see Section 5.3.4). More critical is the value in the exponent of the composition dependence. Because of a possible change in the composition of the wadsleyite during the experiment (see above) and a higher dislocation density in grains affected by ringwoodite crystallization (only for grains with $X_{\text{Fe}_2\text{SiO}_4} > 0.14$) this value might be slightly higher than the true value. Therefore, the composition dependence determined for sample C45, is regarded as the best fit value for the composition dependence of Fe-Mg interdiffusion in wadsleyite.

The relatively strong asymmetry of profiles observed in Fig. 5.18 and 5.19 contrasts with the symmetric profile shown for wadsleyite interdiffusion experiments in Fig. 2A of Chakraborty et al. (1999). This difference results from the much smaller compositional range investigated by Chakraborty et al. (1999) and is further investigated in the next section, after establishing the activation energy for Fe-Mg interdiffusion in wadsleyite.

5.3.4 Temperature dependence at 15 GPa

An Arrhenius plot showing the logarithm of the Fe-Mg interdiffusion coefficients $\log D_{\text{Fe-Mg}}$ versus the inverse temperature, is given in Figure 5.20 with results performed in this study and Chakraborty et al. (1999). The experiments of Chakraborty et al. (1999), performed in Au capsules, are believed to be at an oxygen fugacity close to the Ni-NiO buffer as the experiments

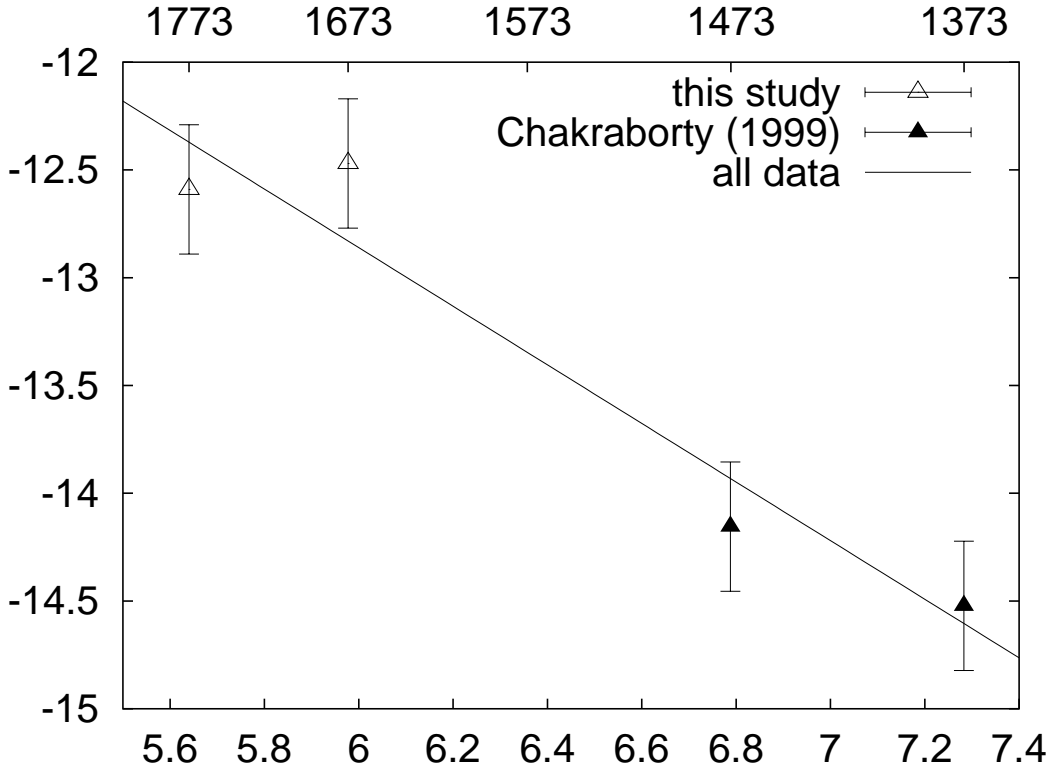


Figure 5.20: Logarithm of the Fe-Mg interdiffusion coefficient for wadsleyite at 15 GPa as a function of inverse temperature obtained in this study and by Chakraborty et al. (1999). The data of this study are recalculated to $X_{\text{Fe}_2\text{SiO}_4} = 0.14$, the average composition of the earlier study of Chakraborty et al. (1999). As described in the text, the activation energy is derived by fitting all data simultaneously.

in this study employing Ni capsules as discussed in Section 5.3.1. The diffusivities given in Chakraborty et al. (1999), employing a composition-independent analytical solution to the diffusion equation, Eq. 1.2, are representative of $X_{\text{Fe}_2\text{SiO}_4} = 0.14$, the average composition of their diffusion couples. Thus values of this study were recalculated to $X_{\text{Fe}_2\text{SiO}_4} = 0.14$ employing the composition dependence given in Table 5.4 for the comparison shown in Figure 5.20.

The activation energy at 15 GPa, $E_a^{15} = E_a + P \times \Delta V_a$, where ΔV_a is the activation volume along the Ni-NiO buffer, and E_a is the activation energy at 1 bar, calculated from a linear regression using the combined dataset of this study and Chakraborty et al. (1999) is $E_a^{15} = 260 \pm 50 \text{ kJ mol}^{-1}$, significantly larger than the preliminary estimate of 145 kJ mol^{-1} derived by Chakraborty et al. (1999). It should be emphasized that this activation energy was determined along the Ni-NiO buffer and therefore also contains a contribution due to a change

of fO_2 with temperature at 15 GPa. The combined results of this study and of Chakraborty et al. (1999) are in agreement with Farber et al. (2000) with respect to absolute diffusivities as shown in Fig. 8 of Farber et al. (2000). It should be noted, that it is difficult to understand the data reduction scheme employed by Farber et al. (2000), because all data of Farber et al. (2000) are recalculated to $X_{Mg} = 0.85$ as stated in the text, but at 10 GPa, and 1473 K ringwoodite is not stable but a spinel datapoint is listed in Table 1 of Farber et al. (2000) and plotted in their Figure 8. Presumably diffusion coefficients were extrapolated across the phase boundary. A combined activation volume is given for wadsleyite and ringwoodite together, employing only 1 datapoint for wadsleyite. Hence, the determination of the activation volume in Farber et al. (2000) is questionable. Therefore, for wadsleyite itself, no precise activation volume is available, and no pressure correction of the activation energy was performed and the value of 260 kJ mol^{-1} is strictly only valid at pressures of 15 GPa for oxygen fugacity conditions close to the Ni-NiO buffer.

In Section 5.3.2 it was reported that element mappings and backscattered electron images do not reveal any grain boundary component. This is in agreement with the results of Chakraborty et al. (1999) where a significant grain boundary contribution was observed at 1373 K, but not at 1473 K because the contribution of grain boundary diffusion becomes smaller with increasing temperature¹.

The results obtained in this study for Fe-Mg interdiffusion in wadsleyite show an exponential composition dependence which is stronger than observed for olivine (Table 5.4, Equation 5.11). In order to test if the composition dependence observed in this study is compatible with the profiles measured by Chakraborty et al. (1999), simulations taking the value of the exponent of the composition dependence of sample C45 (Table 5.4) and an preexponential factor consistent with the average diffusion coefficient of $7 \times 10^{-15} \text{ m}^2 \text{ sec}^{-1}$ observed at 1473 K in Chakraborty et al. (1999) were performed and compared to an example profile of sample H654, kindly provided by S. Chakraborty in Figure 5.21. The simulated and measured profiles agree very well with each other, implying that the composition dependence observed for a wider range of compositions in this study is consistent with the results of Chakraborty et al. (1999), using a much smaller

¹As evident in Figure 2 A of Chakraborty et al. (1999) the samples were switched in the original discussion. Sample H696, performed at 1373 K showed a significant contribution of grain boundary diffusion, whereas the profiles of sample H654, performed at the higher temperature of 1473 K result from lattice diffusion only.

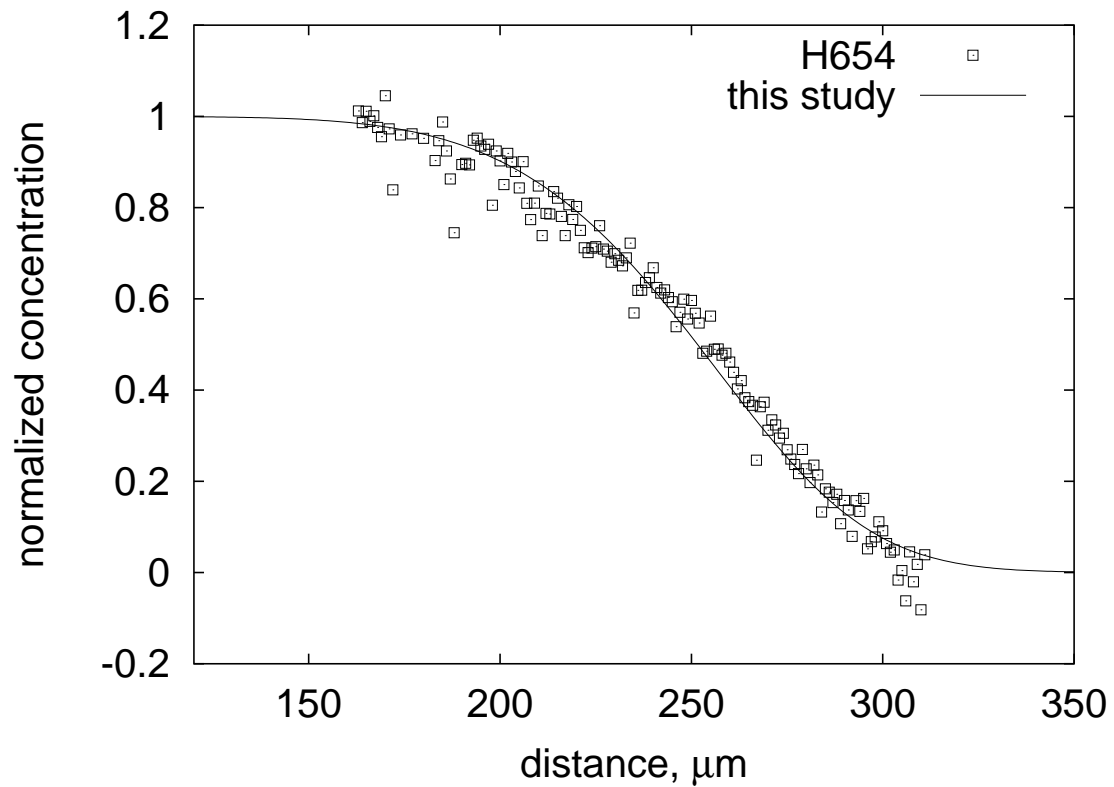


Figure 5.21: Comparison of a numerical profile simulation using values for the composition dependence obtained at high temperature in this study, as described in the text, and an example profile of sample H654 of the study of Chakraborty *et al.* (1999), kindly provided by S. Chakraborty.

compositional range.

5.3.5 Summary: Fe-Mg interdiffusion in wadsleyite

The preferred model for the Fe-Mg interdiffusion coefficient $D_{\text{Fe-Mg}}$ in wadsleyite at 15 GPa, along the Ni-NiO oxygen fugacity buffer, determined from the fit of all data shown in Fig. 5.20, combined with the composition dependence obtained for sample C45, is:

$$D_{\text{Fe-Mg}} = (3.6 \pm 1.3) \times 10^{-6} \exp((11.8 \pm 1.5) X_{\text{Fe}_2\text{SiO}_4}) \exp\left(-\frac{260000 \pm 50000}{RT(\text{K})}\right) \frac{\text{m}^2}{\text{sec}}. \quad (5.12)$$

Hence, the activation energy along the Ni-NiO oxygen fugacity buffer at 15 GPa for wadsleyite has been shown to be 260 kJ mol⁻¹ combining the data of this study and of Chakraborty et al. (1999). This value is in much closer agreement with activation energies of “normal” silicates, as the preliminary estimate of 145 kJ mol⁻¹ determined earlier in Chakraborty et al. (1999). If the activation energy is calculated on either dataset alone, the value is much different, showing that for the determination of diffusional properties the range of conditions should be as large as possible due to the relatively large uncertainties of high pressure diffusion experiments.

Figure 5.22 shows the difference in the Fe-Mg interdiffusions coefficient for olivine and wadsleyite at the same temperature of 1673 K using Equations 5.11 and 5.12. The difference is roughly 4 orders of magnitude. This value is in agreement with Farber et al. (2000) and larger than estimated in Chakraborty et al. (1999), because of the higher activation energy determined in this study compared to the preliminary estimate of Chakraborty et al. (1999). This large change in diffusivity across the olivine-wadsleyite phase boundary re-emphasizes the conclusions that reequilibration becomes much faster in the transition zone than in the upper mantle, originally drawn by Chakraborty et al. (1999, see also Chapter 6).

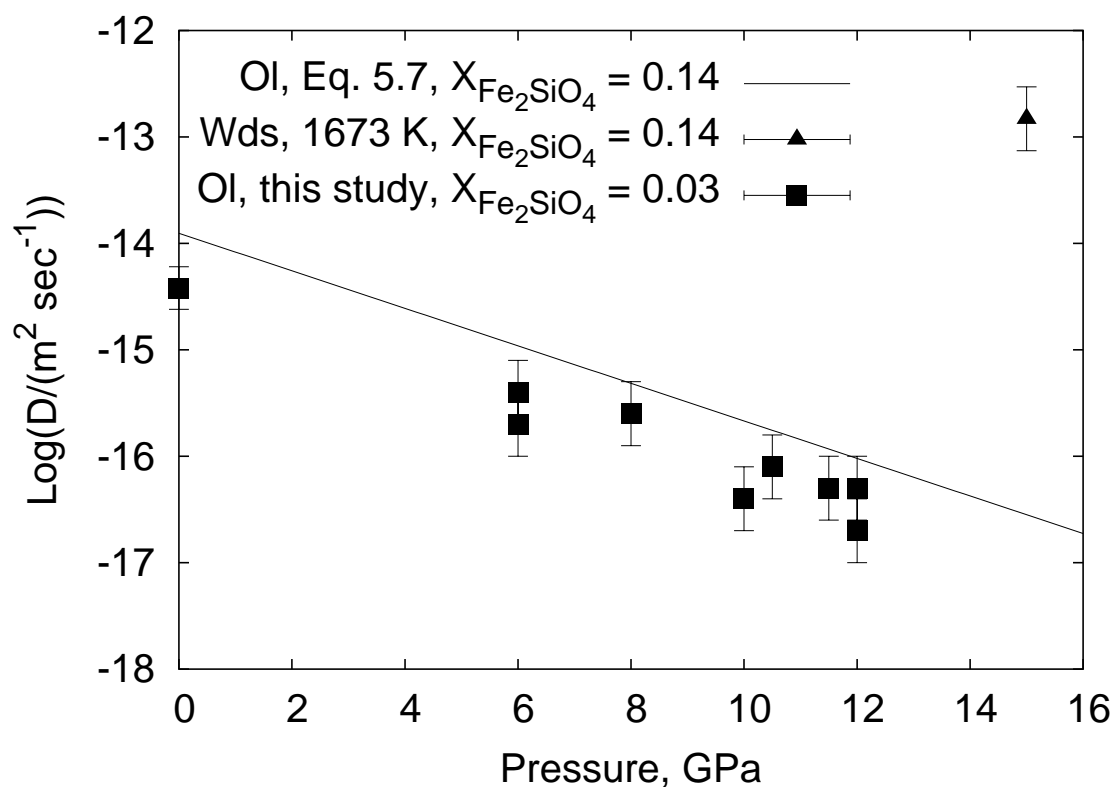


Figure 5.22: Comparison of results of Fe-Mg interdiffusion experiments employing $(\text{Mg,Fe})_2\text{SiO}_4$ olivine and wadsleyite solid solutions. Ol denotes olivine and Wds denotes wadsleyite. The value for olivine diffusion at 1 bar is taken from Chakraborty (1997).

5.4 Ferropericlasite

5.4.1 Conditions of experiments

The initial compositions of the crystals and the experimental conditions are listed in Table 5.5. The experiments were performed at temperatures between 1656 and 2073 K, at pressures between 8 and 23 GPa, and compositions of X_{FeO} between 0.07 and 0.37, where X_{FeO} denotes mole fraction of FeO in (Mg,Fe)O. In addition, one experiment was performed where pure MgO ($X_{\text{FeO}} = 0$) was one endmember of the diffusion couple. This crystal had not been oriented previously but otherwise prepared in a similar fashion to the Fe-bearing single crystals. For a characterization of the crystals forming the diffusion couple see Section 2.3.4. All diffusion couples were enclosed in Ni-NiO capsules for buffering the $f\text{O}_2$ close to the Ni-NiO buffer (Section 2.4). At pressures below 15 GPa a 14/8 assembly was used, whereas above 15 GPa a 10/4 assembly was employed. For a description of the assemblies see Section 2.5.

The experiments were performed in the 1000 t or 1200 t press (Sections 2.2 and Appendix A). For the short duration experiments (< 10 minutes annealing time), heating was performed automatically with PID parameters of the Eurotherm temperature controller optimized in earlier experiments. The proportionality band (P) was usually set to 2000%, the integral time (I) to

Table 5.5: *Experimental conditions, initial compositions of diffusion couples, parameters D_0 , D_1 and a for the equation $D = (D_0 + D_1 \cdot (X_{\text{FeO}})^{1.17}) \cdot \exp(a \cdot X_{\text{FeO}})$ (c.f. Eq. 1.16), and Fe-Mg interdiffusion coefficients for $X_{\text{FeO}} = 0.2$. D_1 was only fitted for sample C64 in which pure MgO was one end member. For all other results the power law contribution of the compositional dependence is not significant; D_1 was therefore set to 0 (Eq. 1.17). All values are averages of simulations of at least two profiles measured on each sample. As an example Fe-Mg interdiffusion coefficients for $X_{\text{FeO}} = 0.2$ are given in the last column.*

Sample	P, GPa	T, K	Assembly	time, min	X_{FeO} crystal 1	X_{FeO} crystal 2	$D_0, \frac{\mu\text{m}^2}{\text{sec}}$	$D_1, \frac{\mu\text{m}^2}{\text{sec}}$	a	$\log(D/(\text{m}^2 \text{sec}^{-1}))$ $X_{\text{FeO}} = 0.2$
C48	23	2063	10/4	40	0.079	0.363	0.037	0	7.23	-12.80
C51	23	1851	10/4	183	0.080	0.370	0.0048	0	7.49	-13.67
C53	23	1656	10/4	961	0.077	0.359	0.000454	0	6.82	-14.75
C55	23	2073	10/4	21	0.079	0.362	0.035	0	7.38	-12.81
C62	16	1873	10/4	45	0.082	0.356	0.053	0	7.54	-12.62
C64	8	1873	14/8	20	0.00	0.354	0.0168	1.20	4.00	-12.35
C67	8	1873	14/8	5	0.087	0.350	0.12	0	8.92	-12.15
C68	12	1673	14/8	48	0.085	0.354	0.0063	0	10.66	-13.27
C72	12	1873	14/8	20	0.077	0.335	0.042	0	8.87	-12.60
C73	23	1923	10/4	46	0.082	0.340	0.028	0	7.41	-12.91
C81	8	1873	14/8	15	0.086	0.363	0.132	0	8.66	-12.13

4 sec, and the derivative time (D) to 1 sec. Consequently, no overshoot in temperature larger than 2 K occurred at any heating rate. At the same time automatic recording of temperature and pressure was employed for a precise determination of the experimental duration. Heating rates ranged from 2.5 K sec^{-1} for long duration experiments to 40 K sec^{-1} for experiment C67, run for only 5 minutes (Table 5.5). From the knowledge of the heating rates, time durations of the experiments, diffusion parameters such as activation energy and activation volume (determined in Section 5.4.4 and 5.4.5), a computer code was developed (described in Section 5.7.3) to predict the amount of diffusion taking place during initial heating.

5.4.2 Sample characterization

Figure 5.23 shows a backscattered electron image of an Fe-Mg interdiffusion experiment performed at 16 GPa, 1873 K for 45 min in a 10/4 assembly (C62, Table 5.5). The diffusion interface is regular and no serious crack formation is visible. This observation holds true for all of the interdiffusion experiments. Nevertheless, orientation contrast imaging of the samples reveal that experiments performed in 14/8 assemblies show no recrystallization, whereas experiments employing a 10/4 assembly usually reveal recrystallization with grain sizes of 50-100 μm on the Fe-rich side and formation of a subgrain microstructure on the Mg-rich side. However, the straight and regular diffusion interfaces observed in all samples (Figure 5.23) and the smooth correlation of diffusion coefficients with pressure (see below) rule out any significant variation of the diffusion coefficients due to deformation.

To determine the Fe^{3+} content of the samples, Mössbauer analysis was performed on sample C55, annealed at 2073 K and 23 GPa for 21 minutes, using a thin section 100 μm thick. The Fe^{3+} content was approximately 2-3 atomic% of the total Fe content. The same sample was also used for Fourier transform infrared spectroscopy. Only the crystal with a low Fe content could be examined because of severe absorption on the Fe-rich side. Most analysis points gave a water content of around 12 ppm by weight employing the absorption correction of Paterson (1982); only one measurement point near the edge of the sample showed 60 ppm of water. The total water content is therefore low and consistent with previous water solubility measurements (Bolfan-Casanova et al., 2002).

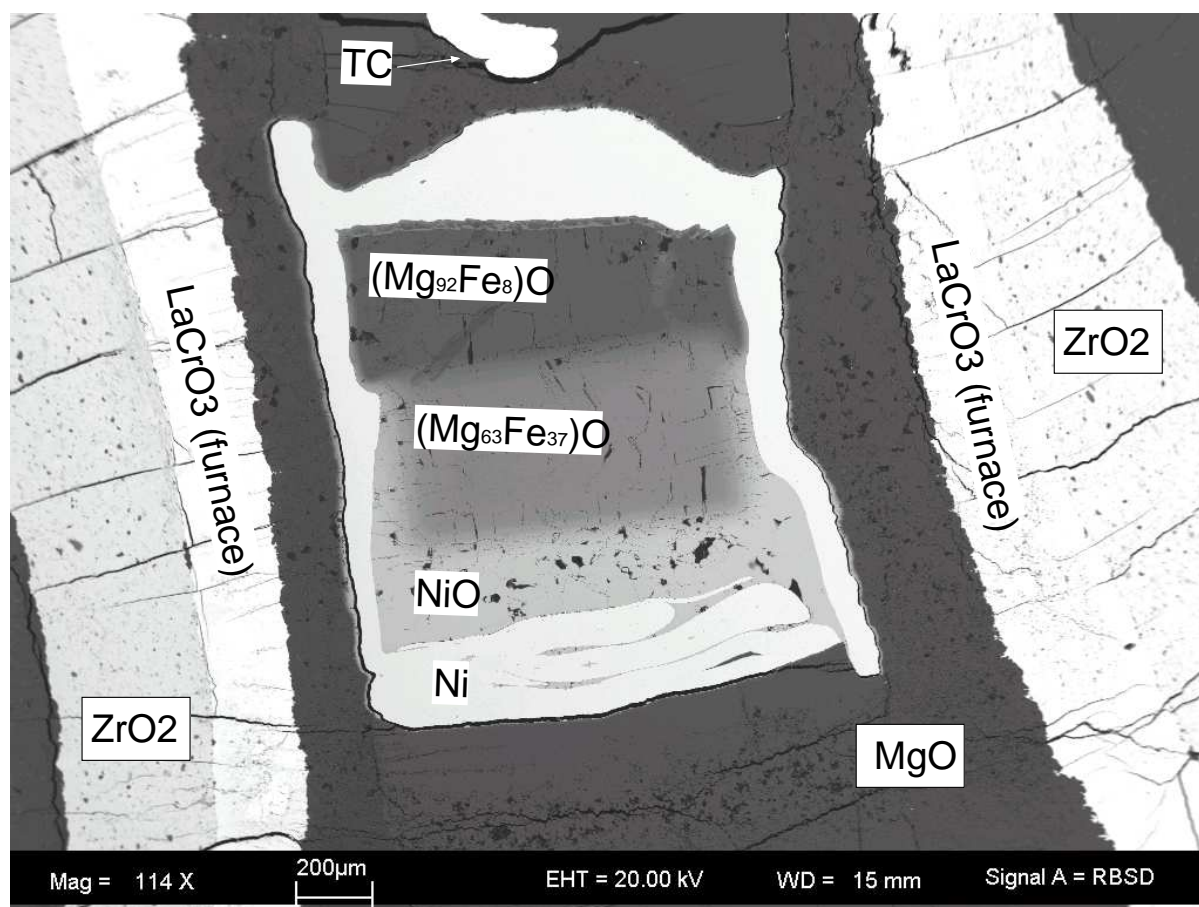


Figure 5.23: Backscattered electron image of the pressure assembly after a ferropericlasite diffusion experiment. Conditions of the experiment were 16 GPa and 1873 K with an annealing time of 45 min. The diffusion couple is seen surrounded by the Ni capsule. The NiO used for buffering fO_2 also interacted chemically with the end of the diffusion couple over a distance of $\sim 150 \mu\text{m}$

5.4.3 Profiles and diffusion coefficients

Profiles of Fe and Mg in ferropericlasite are strongly asymmetric as shown by an example of an experiment performed at 8 GPa, 1873 K for 15 minutes in a 14/8 assembly in Figure 5.24. The lengths of the profiles, measured on different samples, range between 80 and 230 μm . Hence, diffusion profiles can be easily investigated by EPMA. For deriving the composition-dependent diffusion coefficient, both methods described in Section 4.3, Boltzmann-Matano analysis (BMA) and the numerical finite difference method (FDM), were applied. A comparison of diffusion coefficients derived using both methods is given in Figure 5.25. The numerical simulation very precisely reproduces the asymmetry of the profile whereas the fitting function fails to adequately

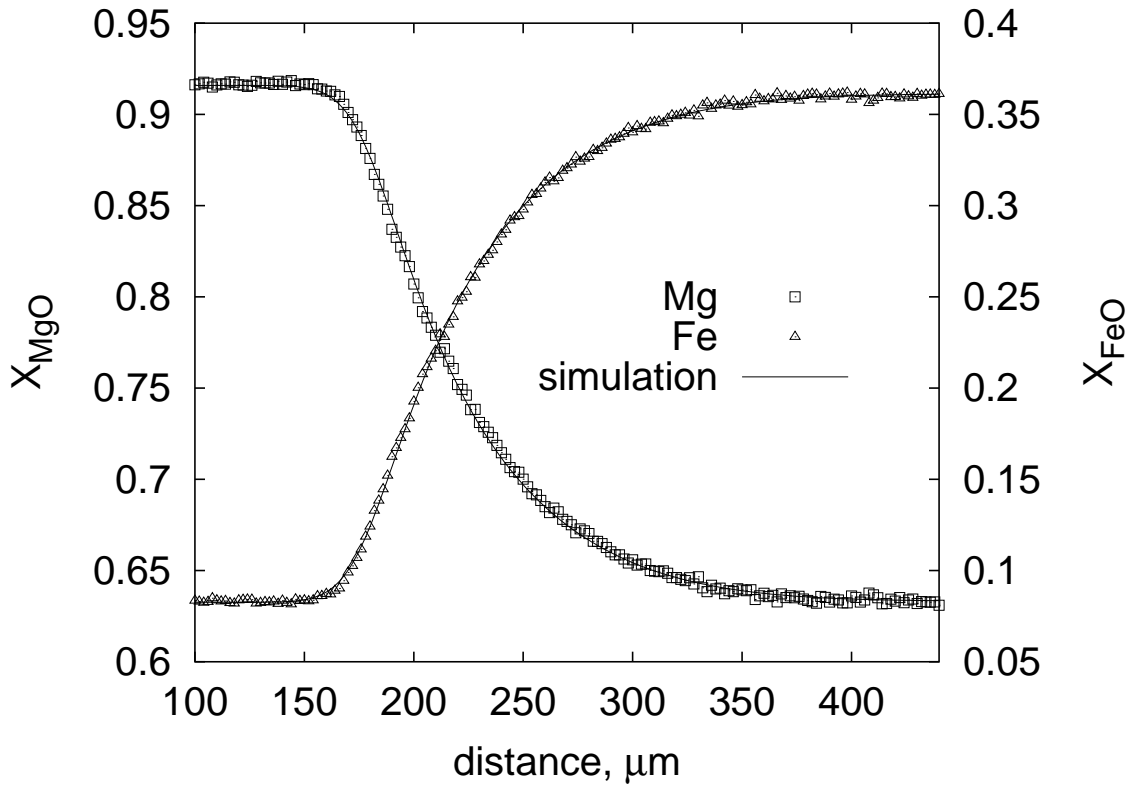


Figure 5.24: *Fe and Mg profiles for sample C81, performed at 8 GPa, 1873 K for 15 min. $X_{\text{MgO,FeO}}$ denotes mole fraction of FeO or MgO. Also shown is a profile simulation employing a finite difference algorithm (see text and Section 4.3.2)*

describe the profile at very low and very high Fe contents. Presumably this happens because the middle part of the profiles contributes more to the sum of squared deviations minimized during the least square nonlinear fit of the fitting function. This holds true for all fitting function types described in Section 4.3.1. The fitting might be also problematic because of the high nonlinearity of the fitting functions. Hence, the detection of the global minimum becomes difficult. As a consequence diffusion coefficients derived by BMA and by FDM agree very well at intermediate compositions whereas at the extreme ends of the profile a systematic deviation of ~ 0.1 log-unit was observed (inset of Figure 5.25). Based on these comparisons, all diffusion coefficients reported for ferropicrclase were derived by FDM and fitted parameters for the constants D_0 and a in Eq. 1.17 are also listed in Table 5.5.

For sample C64, in which an MgO single crystal was used as one end member, the numerical model, using only an exponential composition dependence (Equation 1.17), slightly

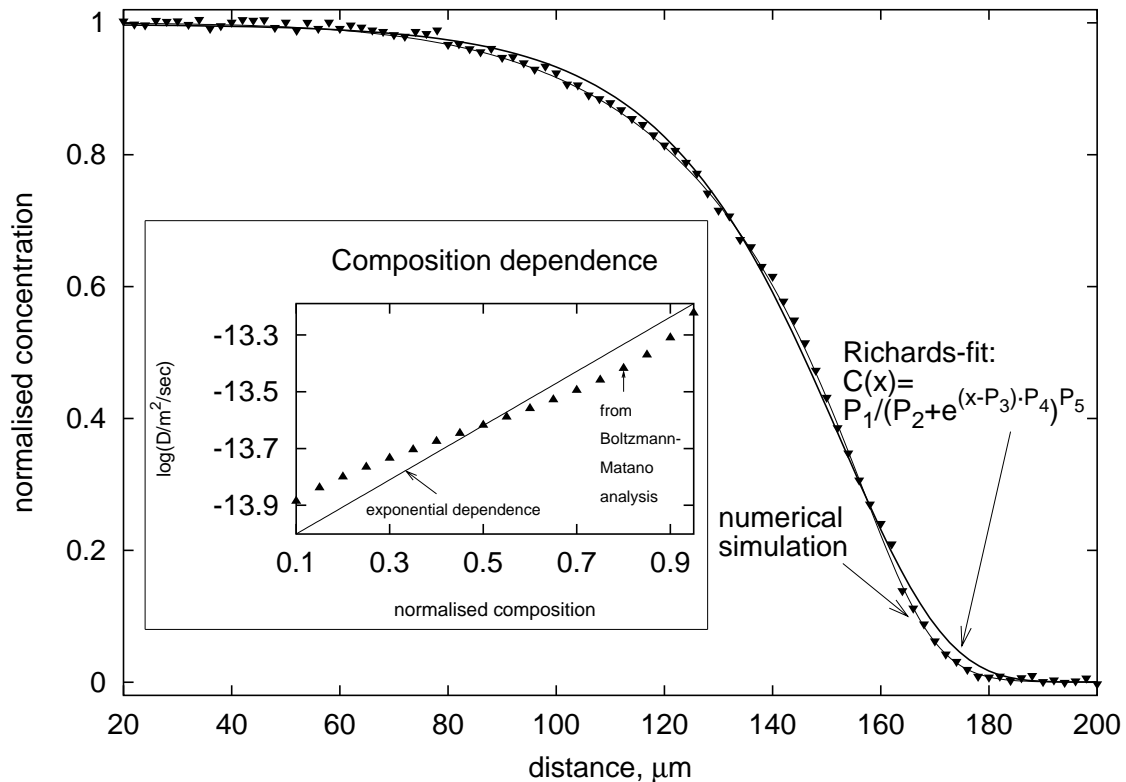


Figure 5.25: Comparison of diffusion coefficients derived by Boltzmann-Matano analysis and finite difference simulations for sample C51 (Table 5.5). The profile is shown onto which the fitting function for the Boltzmann-Matano analysis and the results of the numerical simulation are superimposed. The inset shows the logarithm of the diffusion coefficient as a function of normalized Fe-content.

overestimates diffusivities at the MgO-rich end of the profile (Figure 5.26). In this region the composition power law dependence contributes significantly to the diffusivity (see Eq. 1.16 and Mackwell et al., 2004). This implies a change in the charge neutrality condition for point defects when approaching the MgO rich end of the solid solution. Therefore the profiles for this sample were reanalyzed with a composition dependence of $D = (D_0 + D_1 \cdot (X_{FeO})^{1.17}) \cdot \exp(a \cdot X_{FeO})$ (cf. Eq. 1.16), where the constant a was fixed at a constant value of 4, consistent with the results at 1 bar (Mackwell et al., 2004), and the constants D_0 and D_1 were allowed to vary. The result of this simulation is also given in Table 5.5. The details of this simulation are further described in Appendix C.

To test the inter-experiment reproducibility a time series of experiments was performed at constant temperature of 1873 K and constant pressure of 8 GPa (Fig. 5.27). The three experi-

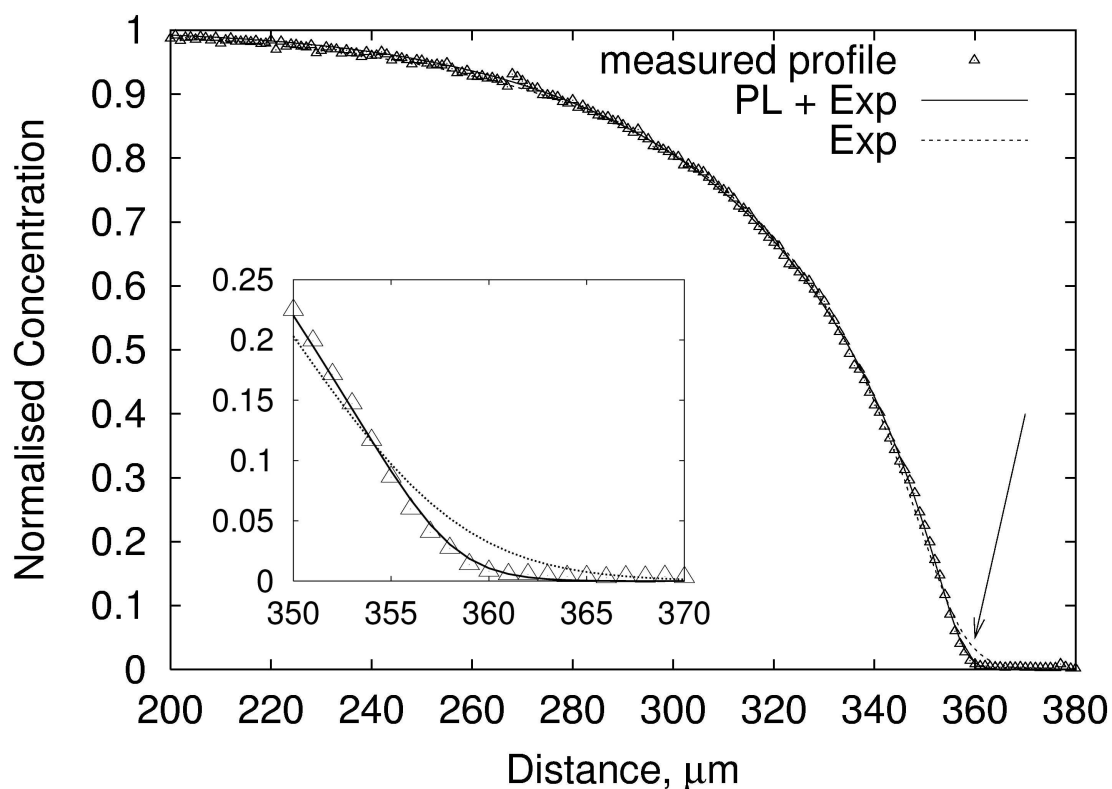


Figure 5.26: *Fe profile measured on sample C64, performed at 8 GPa, 1873 K, for 20 minutes employing a diffusion couple of $0 < X_{\text{FeO}} < 0.35$ (see Table 5.5). The inset shows the region of low Fe concentrations, where a simulation with a pure exponential composition dependence of the diffusion coefficient (Exp) does not adequately reproduce the profile and a simulation with a power law dependence in the preexponential factor (PL + Exp) had to be employed (see Equations 1.16 and 1.17 and text for further explanations).*

ments were performed for 5, 15 and 20 minutes using different heating rates, multianvil presses and types of diffusion couples as indicated in Figure 5.27. No systematic variation of diffusivity as a function of time was observed and the overall scatter of the data was found to be better than ± 0.3 log-units. Therefore, at these conditions no zero-time effect due to heating was observed experimentally.

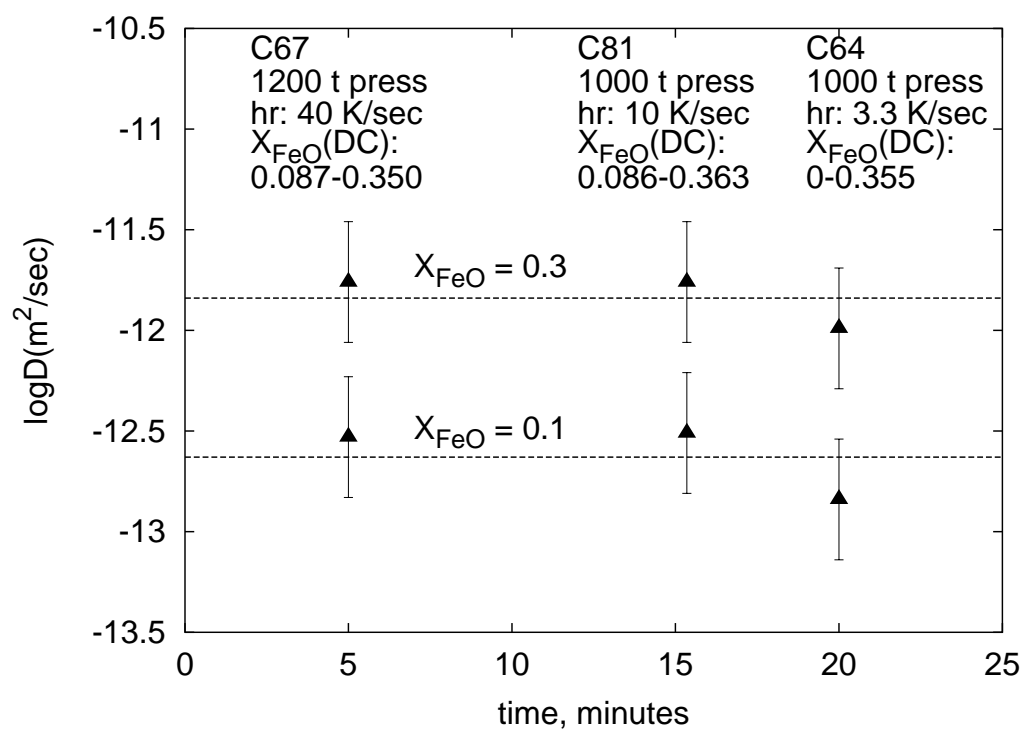


Figure 5.27: Logarithm of the diffusion coefficient at constant temperature of 1873 K and constant pressure of 8 GPa. The dashed lines show the average values of diffusivity, recalculated for $X_{\text{FeO}} = 0.1$ and 0.3 . The time series shows that the effects of the variation of heating rate (hr), multianvil press (1000 t or 1200 t), and compositions of the diffusion couples (DC) on the results are negligible.

5.4.4 Pressure dependence at constant temperature

The composition-dependent Fe-Mg interdiffusion coefficient D at high pressure can be described by:

$$D = D_0 \cdot \exp\left(\frac{A \cdot X_{FeO}}{R \cdot T}\right) \cdot \exp\left(-\frac{E_a + (P - P_{ref}) \cdot \Delta V_a}{R \cdot T}\right) \quad (5.13)$$

where the constant A describes the compositional dependence, X_{FeO} is the mole fraction of FeO, ΔV_a is the activation volume, E_a is the activation energy, P is the pressure, P_{ref} is the reference pressure (= 1bar), and T is absolute temperature (compare with Equations 1.14 and 1.16). As discussed by Poirier (2000) the pressure dependence of the entropic term is neglected in this formulation. Equation 5.13 is consistent with Eq. 1.16, derived from point defect considerations, as long as $X_{FeO} > 0.07$ (see Section 1.3.2). Strictly, Equation 5.13 is only valid at constant oxygen fugacity. Because the experiments of this study were performed at oxygen fugacity conditions close to the Ni-NiO buffer, values derived later for the activation energy and the activation volume will also include a contribution due to change in fO_2 .

Figures 5.28 and 5.29 show the pressure dependence of diffusion from which the value of the activation volume ΔV_A (Eq. 5.13) has been determined using the slope of a linear regression. Diffusivities at different compositions were calculated for each experiment by using the constants a and D_0 in Eq. 1.17 listed in Table 5.5. The constant a in Eq. 1.17 corresponds to $A/(R \cdot T)$ in Eq. 5.13. At 23 GPa, Fe-Mg interdiffusion coefficients were recalculated to 1673 K and 1873 K using the temperature dependence given in Fig. 5.30. At 8 GPa and 1873 K three experiments have been performed, one of them using a diffusion couple of a pure MgO single crystal as one endmember (C64 - Table 5.5) and two employing a diffusion couple with $X_{FeO} = 0.09$ and $X_{FeO} = 0.35$ (C67, C81). No significant differences in the diffusion coefficients derived using the different kinds of diffusion couples are observed (Fig. 5.27). Hence the result from C64 was included in all calculations presented below. From Fig. 5.28 values for the activation volume of 3.4 ± 0.5 and $3.3 \pm 0.5 \text{ cm}^3 \text{ mol}^{-1}$ at 1673 and 1873 K respectively are evaluated from the slopes of the regression lines. Figure 5.29 shows that at 1873 K the activation volume is $3.0 \pm 0.5 \text{ cm}^3 \text{ mol}^{-1}$ at $X_{FeO} = 0.1$, $3.3 \pm 0.5 \text{ cm}^3 \text{ mol}^{-1}$ at $X_{FeO} = 0.2$, and $3.5 \pm 0.5 \text{ cm}^3 \text{ mol}^{-1}$ at $X_{FeO} = 0.1$. The error on the activation volume was estimated from the 1 sigma standard deviation of the fit of $\log D$ versus pressure at a fixed temperature and composition. Because the

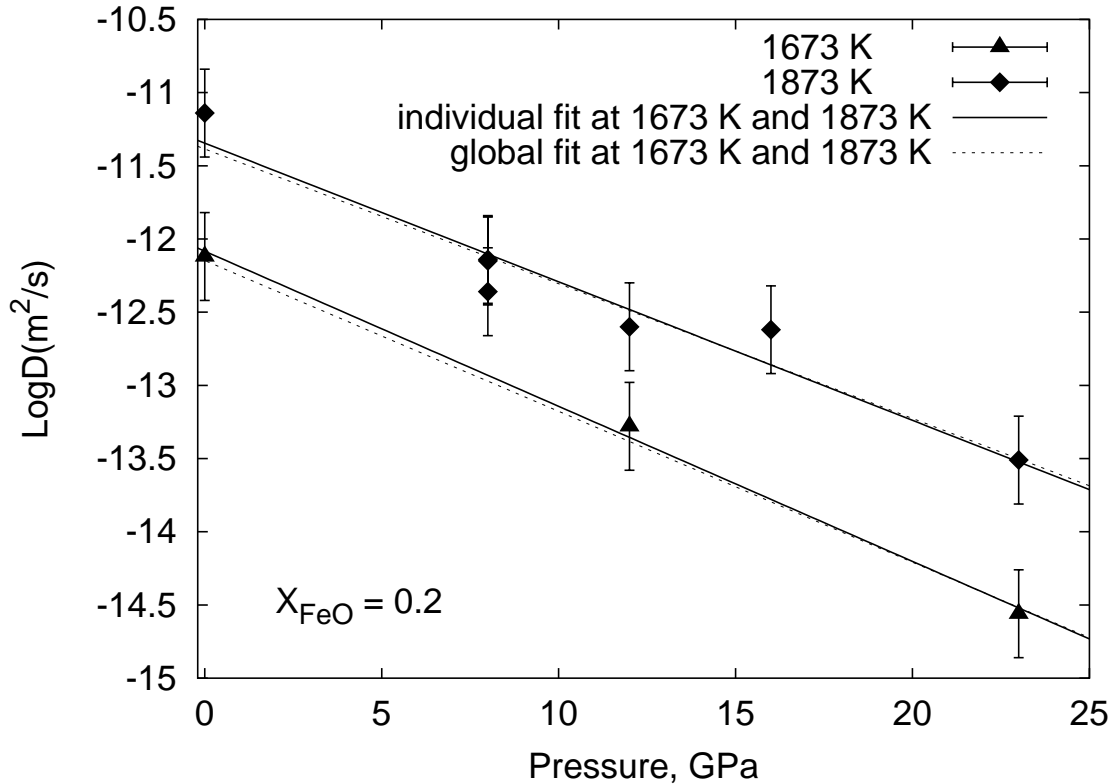


Figure 5.28: Pressure dependence of diffusivity at 1673 K and 1873 K and a constant composition of $X_{\text{FeO}} = 0.2$ (using data from Table 5.5). Data at 1 bar are from Mackwell et al. (2004). At 23 GPa, data-points are recalculated to 1673 K and 1873 K from the correlation shown in Figure 5.30. Individual fits to the datapoints at each temperature, calculated using values from Table 5.5, are shown by the solid lines. The dotted lines show a global fit of Eq. 5.13 with the parameter values detailed in the text.

total variation is not larger than the 1 sigma standard deviation, it is concluded that at the experimental conditions the activation volume does not depend significantly on either temperature or composition.

5.4.5 Temperature dependence at constant pressure

Figure 5.30 shows an Arrhenius diagram for ferropericlasite diffusion coefficients at 23 GPa. In the case of ferropericlasite, where the diffusion coefficient depends on concentration as given in Equation 5.13, the slope in the Arrhenius diagram is $-(E_a - A X_{\text{FeO}} + \Delta V_a (P - P_{\text{ref}}))/(2.3026 R)$ (see also Figure 1.1). The activation energy E_a at 23 GPa can be determined using the calculated activation volume V_a and the average constant A determined using Table 5.5 where A (Eq. 5.13) = $a(\text{Tbl. 5.5, Eq. 1.17}) \times RT$, which at 23 GPa is $1.16 \times 10^5 \text{ J mol}^{-1}$, from a plot of $\log D$ against

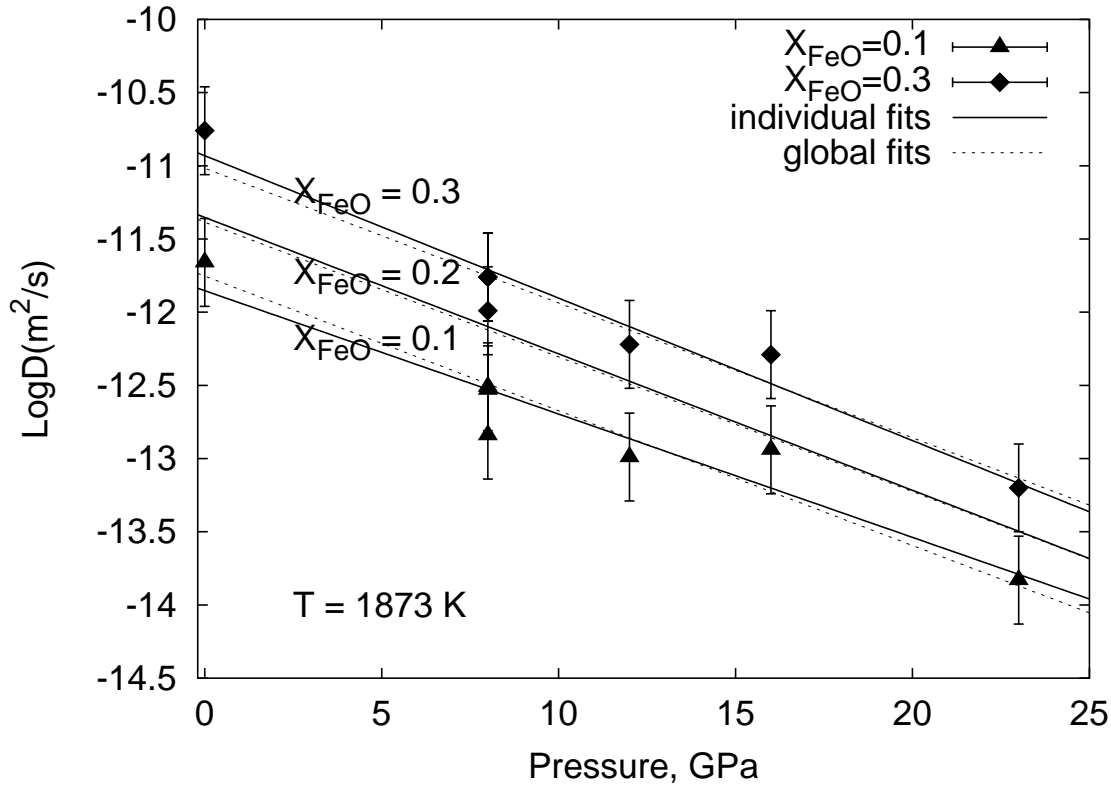


Figure 5.29: Logarithm of the Fe-Mg interdiffusion coefficient as a function of pressure at a constant temperature of 1873 K recalculated for the compositions $X_{FeO} = 0.1$, 0.2, and 0.3 (Table 5.5). Data at 1 bar are from the study of Mackwell et al. (2004). At 23 GPa data-points are recalculated to 1873 K from the correlation shown in Figure 5.30. Individual datapoints are shown for $X_{FeO} = 0.1$ and 0.3. The solid lines are fits to the individual datapoints at $X_{FeO} = 0.1$, 0.2, and 0.3 calculated from the values in Table 5.5. The dotted lines show the global fit of Eq. 5.13.

$10^4/T$ (Fig. 5.30). At 23 GPa, the activation energy is $253 \pm 50 \text{ kJ mol}^{-1}$ for $X_{FeO} = 0.1$, $260 \pm 53 \text{ kJ mol}^{-1}$ for $X_{FeO} = 0.2$, and $271 \pm 55 \text{ kJ mol}^{-1}$ for $X_{FeO} = 0.3$.

As stated in the analytical section the crystal with $X_{FeO} = 0.07$ had some CaO-SiO₂ contamination on one surface. This surface was always on the opposite side of the crystal to the diffusion interface. Results obtained from sample C64, which did not employ this crystal, and from samples C72 and C73, where the contamination layer was removed prior to the diffusion anneal are consistent with the other experiments. Therefore the contamination has no effect on the determined diffusion coefficients.

Using data recalculated to $X_{FeO} = 0.1$, 0.2 and 0.3 (Table 5.5) and including 1 bar data at 1673 K and 1873 K from Mackwell et al. (2004), a global fit of Eq. 5.13 was performed, lead-

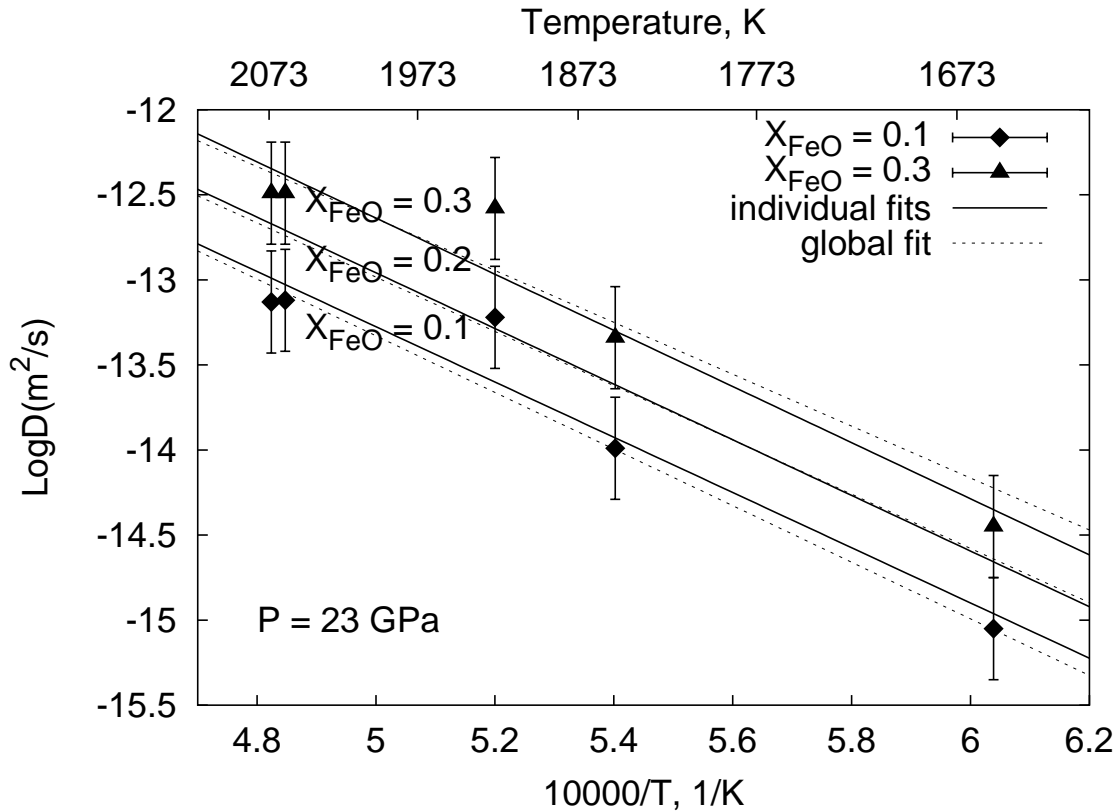


Figure 5.30: *Logarithm of the diffusion coefficient as a function of inverse temperature. Individual datapoints, recalculated for $X_{\text{FeO}} = 0.1$ and 0.3 using parameters listed in Table 5.5, are shown for experiments performed at 23 GPa and 1656 - 2073 K. In addition, for $X_{\text{FeO}} = 0.1, 0.2,$ and 0.3 , individual fits of the datapoints at these conditions are shown by the solid lines. At the same conditions the results of the global fit (Eq. 5.13) are shown by the dotted lines.*

ing to $A = 132 \pm 13 \text{ kJ mol}^{-1}$, activation energy $E_a = 255 \pm 16 \text{ kJ mol}^{-1}$, activation volume $\Delta V_a = 3.3 \pm 0.1 \text{ cm}^3 \text{ mol}^{-1}$, and the preexponential factor $D_0 = (9.8 \pm 0.7) \times 10^{-6} \text{ m}^2 \text{ sec}^{-1}$. The quoted errors are standard errors from the Mathematica (Version 4.1.0.0, Wolfram Research) package LinearRegression. From the deviation of the calculated and experimentally determined values the overall error is estimated to be 0.3 log-units. These values for Eq. 5.13 are valid for an oxygen fugacity corresponding to the Ni-NiO-buffer as discussed in Section 5.1. The experimental conditions for deriving these parameters were pressures of 0 - 23 GPa and temperatures of 1656 - 2073 K.

The value of $3.3 \text{ cm}^3 \text{ mol}^{-1}$ is in good agreement with the activation volume of $3.0 \text{ cm}^3 \text{ mol}^{-1}$ determined for Mg tracer diffusion in the experiments of Van Orman et al. (2003).

5.4.6 Oxygen fugacity

All experiments reported here have been performed in Ni capsules in contact with NiO powder (Fig. 5.23). Therefore Eq. 5.13 is only valid at oxygen fugacities corresponding to the Ni-NiO buffer. Because fO_2 at the Ni-NiO buffer varies with temperature and pressure, this dependence is implicitly built into Eq. 5.13 (Section 5.1).

According to Mackwell et al. (2004), Fe-Mg interdiffusion in ferropericlase varies with fO_2 by the factor of $(fO_2)^{0.22}$. To test if the high-pressure, high-temperature dependence of Fe-Mg interdiffusion is independently consistent with the 1 bar data from Mackwell et al. (2004), Eq. 5.13 was refitted without including the 1 bar data. The difference between diffusivities calculated at 1 bar using the back extrapolation of the high pressure data, and those calculated from the results of Mackwell et al. (2004) at an fO_2 corresponding to the Ni-NiO buffer, ranges from 0.01 log units at 1673 K and $X_{FeO} = 0.1$ to 0.58 log units at 2073 K for $X_{FeO} = 0.3$. Considering the experimental error of 0.3 log-units and the fact that the experimental data are extrapolated over a pressure range of 8 GPa, these differences indicate good consistency between the high pressure results and data obtained at 1 bar.

The results of a similar fit as in the previous section but including fO_2 values calculated using data of Ride (1991) is presented in the next section.

5.4.7 Summary: Ferropericlase

Fe-Mg interdiffusion in ferropericlase has been studied at pressures between 8 and 23 GPa and temperatures between 1653 K and 2073 K, using a multianvil apparatus. The compositions of the single crystal diffusion couples were $X_{FeO} = 0.07$ for one crystal and $X_{FeO} = 0.37$ for the other, although in one case pure MgO was used instead of $X_{FeO} = 0.07$. Fe-Mg interdiffusion at oxygen fugacities buffered by Ni-NiO, including 1 bar data at 1673 K and 1873 K of Mackwell et al. (2004), can be described for $0.07 < X_{FeO} < 0.37$ by:

$$D_{Fe-Mg} = 9.9(\pm 0.7) \times 10^{-6} \exp\left(\frac{132000(\pm 13000) X_{FeO}}{8.31441 T(K)}\right) \cdot \exp\left(-\frac{255000(\pm 16000) + 0.33(\pm 0.01) P(\text{bar})}{8.31441 T(K)}\right) \frac{\text{m}^2}{\text{sec}}. \quad (5.14)$$

These results will be used in Section 6.2.1 to constrain Fe-Mg interdiffusion coefficients of ferropericlase in the Earth's lower mantle.

In addition to the fit of results corresponding to an oxygen fugacity of the Ni-NiO buffer, values for the activation energy and the activation volume were also derived for constant f_{O_2} . For this purpose, the absolute oxygen fugacity of the experiments was calculated using values given in Ride (1991), as discussed in Section 5.1. The results of this recalculation depend on the f_{O_2} exponent of the oxygen fugacity dependence of the Fe-Mg interdiffusion coefficient (e.g. Equation 1.6). In Section 1.2.4 an exponent of 1/6 was derived for a vacancy mechanism of diffusion. In this case the activation volume is $4.8 \text{ cm}^3 \text{ mol}^{-1}$ and the activation energy becomes 178 kJ mol^{-1} . Mackwell et al. (2004) derived an experimental value of 1/4.5 for the f_{O_2} exponent (Equation 1.16) leading to an activation volume of $5.2 \text{ cm}^3 \text{ mol}^{-1}$ and an activation energy of 153 kJ mol^{-1} at constant oxygen fugacity. In both cases, the value of the activation energy is significantly smaller than the 1 bar value of $206500 \text{ J mol}^{-1}$ (Mackwell et al., 2004). Therefore, it is concluded that the temperature dependence of the oxygen fugacity of the Ni-NiO buffer is not accurately predicted at pressures up to 23 GPa using existing data for the Ni-NiO buffer obtained at 1 bar and pressures below 4.5 GPa.

In a recent paper by Yamazaki and Irifune (2003) Fe-Mg interdiffusion in ferropericlase was studied between 7 and 35 GPa. These authors found absolute diffusivities similar to the values observed in this study but the pressure trend was much weaker resulting in an activation volume of $1.8 \text{ cm}^3 \text{ mol}^{-1}$. For experiments up to 28 GPa Yamazaki and Irifune (2003) used Re capsules and assumed that the oxygen fugacity is close to the Re-ReO₂ buffer. Although it was shown by Frost and Langenhorst (2002) that this is a reasonable assumption at pressure of approximately 24 GPa, the data of Yamazaki and Irifune (2003) indicate that this assumption does not hold true at lower pressures. The Fe-Mg interdiffusion coefficient at 1 bar consistent with an oxygen fugacity of the Re-ReO₂ buffer is $5.3 \times 10^{-12} \text{ m}^2 \text{ sec}^{-1}$ using values of Mackwell et al. (2004, see also Section 1.3.2), which is more than a factor of 10 larger than calculated using the model of Yamazaki and Irifune (2003). Hence, the oxygen fugacity inside the Re capsules used by Yamazaki and Irifune (2003) changes from reducing conditions well below the Ni-NiO buffer at 1 bar to oxidizing conditions consistent with the Re-ReO₂ buffer at pressures of ~ 25 GPa.

Therefore, a completely different variation in diffusivity due to a change in fO_2 with pressure is built into the apparent activation volume determined by Yamazaki and Irifune (2003) compared to the results of this study and consequently the activation volumes determined in both studies cannot be compared directly to each other.

5.5 $(\text{Fe}_x\text{Mg}_{1-x})\text{SiO}_3$ Perovskite

5.5.1 Introduction, conditions of experiments

The conditions of all experiments are summarized in Table 5.6. Experiments were performed at temperatures between 1973 K and 2273 K at pressures in the range of 22 to 26 GPa, employing diffusion couples in MgO-Fe and Ni-NiO capsules (Section 2.4). High temperature runs (> 2173 K) were performed in the 5000 t press using an 18/8 assembly in order to achieve a better temperature stability. However, the absolute pressure in this assembly is smaller compared to the 10/4 assembly, as revealed by partial back-transformation of perovskite to majorite (Section 5.5.2). Because of the higher pressures in the 10/4 assembly employed in the 1000 t and 1200 t presses, the pressure of the experiments varies slightly between 22-26 GPa (Table 5.6), depending on the press and assembly used. When comparing diffusivities of perovskite determined using different presses and assemblies in latter sections no pressure normalization was employed because the activation volume of Fe-Mg interdiffusion in silicate perovskite is unknown. The resulting difference in diffusivity due to a pressure variation of 4 GPa would be on the order of 0.5 log-units, assuming a typical activation volume for silicates of $5 \text{ cm}^3 \text{ mol}^{-1}$ (e.g. in olivine).

The diffusion couples used for the perovskite diffusion experiments consisted of pure presynthesized MgSiO_3 perovskite and Fe bearing samples synthesized prior the diffusion experiments employing either synthetic polycrystalline enstatite or a natural single crystal bronzite as discussed in Section 2.3.5. For the high pressure diffusion anneal, the diffusion couples were enclosed either by MgO-Fe capsules (Section 2.4) for buffering the oxygen fugacity at reducing conditions or by Ni-NiO capsules (Section 2.4) for attaining more oxidizing conditions.

5.5.2 SEM and EPMA investigations of perovskite diffusion experiments

After the high pressure experiments, samples were mounted in epoxy and polished until the middle of the diffusion couple was exposed (Figure 3.1). Phases were identified using Raman spectroscopy. For all experiments performed in the 10/4 assembly the perovskite was well preserved. In the 18/8 assembly, employing only MgO-Fe capsules, the perovskite adjacent to the metal was transformed to majorite consuming half of the original perovskite in sample C30 (Table 5.6).

Figure 5.31 shows backscatter electron images of diffusion experiments performed in MgO-

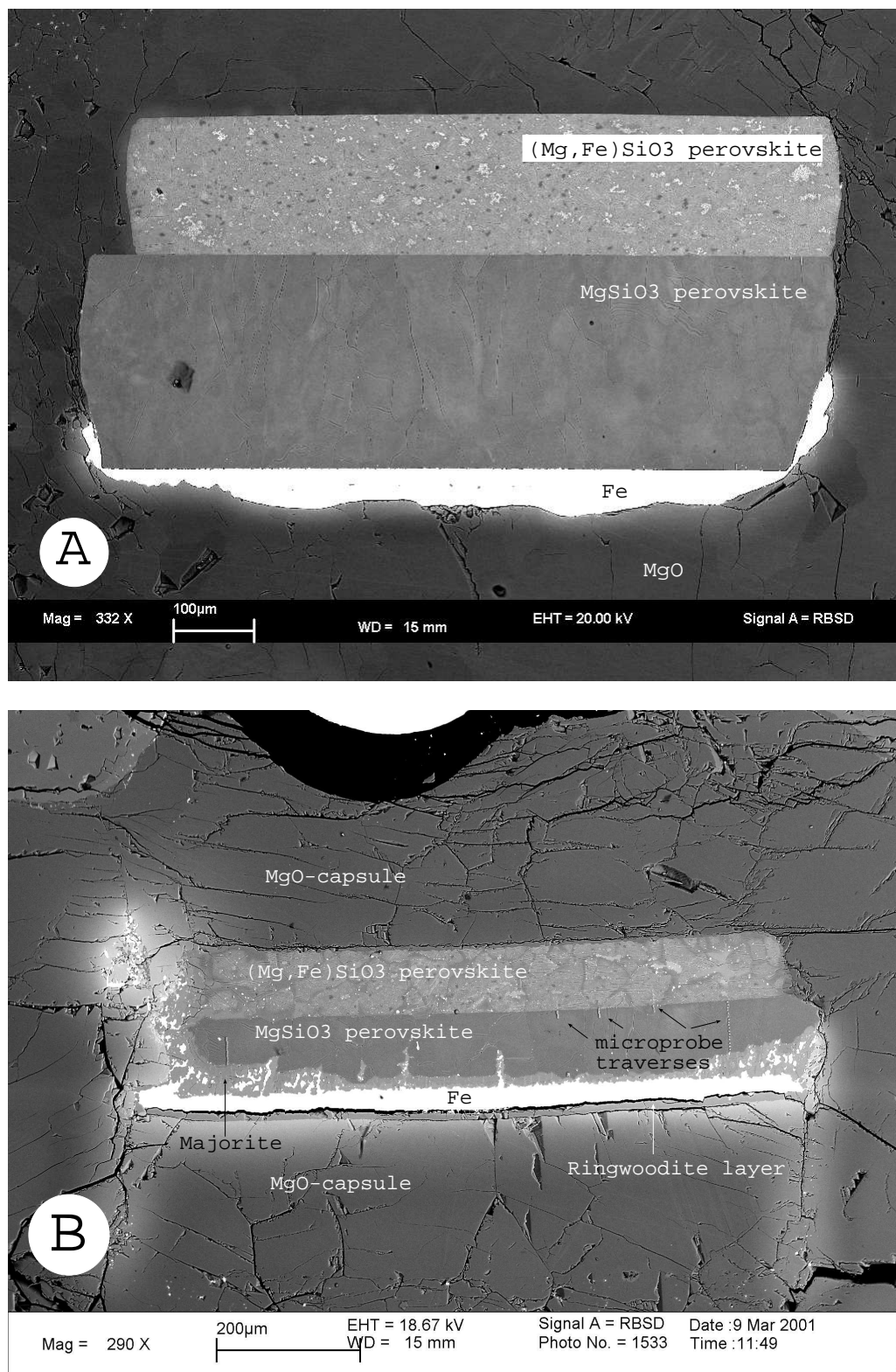


Figure 5.31: Backscattered electron images of perovskite diffusion couples performed in MgO-Fe capsules. The experiment in A was run at 25 GPa, 2073 K for 240 min employing a 10/4 assembly, the experiment in B was run at 22 GPa, 2273 K for 373 min using an 18/8 assembly.

Table 5.6: Conditions of the perovskite diffusion experiments. P is sample pressure, T is sample temperature as indicated by the thermocouple or estimated by the power reading (only C76), t is the duration of the experiment at high temperature, capsule is the capsule type (Section 2.4), X_{FeO} is the mole fraction of FeO in the rim of the MgO capsule for experiments performed in MgO-Fe capsules, and Δf_{O_2} is the oxygen fugacity relative to the iron-wüstite buffer defined in Eq. 5.19 and calculated by assuming ideality in Eq. 5.20 (only for experiments performed in MgO-Fe capsules).

Sample	press	P , GPa	T , K	t , min	capsule	X_{FeO}	Δf_{O_2}
C13	Sumitomo	24	2043	240	MgO-Fe	0.069	-2.33
C19	Hymag	24	2023	483	MgO-Fe	0.027	-3.14
C22	Hymag	24	2073	900	MgO-Fe	0.035	-2.91
C23	Hymag	24	2123	720	MgO-Fe	0.022	-3.33
C28	Hymag	24	2133	1430	MgO-Fe	0.048	-2.64
C30	Zwick	22	2273	373	MgO-Fe	0.116	-1.87
C61	Hymag	26	2073	10	Ni-NiO		
C70	Hymag	26	2173	60	Ni-NiO		
C76	Hymag	26	1973	570	Ni-NiO		

Fe capsules. Fig. 5.31-A shows a cross section of an experiment at 25 GPa, 2073 K run for 240 min in the 1000 t (Hymag) press employing a 10/4 assembly, whereas in Fig. 5.31-B a cross section of a sample at 22 GPa, 2273 K run for 373 min in the 5000 t (Zwick) press employing an 18/8 assembly is shown. In most cases the iron shows structures indicative of melting like intrusion along grain boundaries of the capsule and between capsule and sample but not in the polycrystalline perovskite diffusion couple (Figure 5.31-B). Stishovite crystals and iron oxides are often found in the metal. In the 10/4 assembly in most experiments a perovskite reaction rim is observed adjacent to the MgO of the capsule which is interpreted as reaction of SiO_2 dissolved in the metal with the MgO during quench. Because pressures in the 18/8 assembly are significantly lower, reaction rims observed adjacent to the MgO consists of ringwoodite in this case (Figure 5.31-B). At the same time, for experiment C30 (Table 5.6) performed in an 18/8 assembly, the perovskite is partially consumed and majorite formed (Figure 5.31). Although simultaneous solution of Si and O in metallic iron is limited (O'Neill and Palme, 1998) it seems to be sufficient to precipitate stishovite and a silicate reaction layer on MgO during quench.

Inclusions in the $(\text{Mg,Fe})\text{SiO}_3$ perovskite can be identified in all samples. The inclusion

phases are stishovite, ferropericlase and, in the case of experiments performed in MgO-Fe capsules at low oxygen fugacities (see below), metallic iron. The presence of metallic iron inclusions in perovskite at low oxygen fugacities is consistent with the results of Liebske et al. (2003).

Because silicate perovskite is unstable with respect to electron bombardment, traces of circular spots due to electron microprobe analyses (EPMA) can be identified in Fig. 5.31-B. These traces are amorphous regions within perovskite. The MgSiO_3 perovskite is more susceptible to this effect than the Fe-bearing endmember of the diffusion couples. To minimize beam damage, EPMA was performed at 15 kV and 5 nA beam current. Although amorphization always occurs during EPMA measurements, even at very low beam currents, the stoichiometry of the analyses is consistent with the ideal formula $(\text{Mg,Fe})\text{SiO}_3$. Hence, there is no significant Mg loss during microprobe analysis. The electron microprobe profiles show that diffusion profiles are shorter than $5 \mu\text{m}$ (resolution limit of the technique, see Section 3.2) which is also evident in the backscattered electron images (Fig. 5.31) which shows a sharp contrast change at the interface.

Samples from experiments performed in Ni-NiO capsules generally show the same sharp contrast across the diffusion interface at grain-grain contacts but a light component on the Mg-rich side of the diffusion couple is observed along grain-boundaries (Fig. 5.32). This effect might be explained by grain boundary diffusion. If this is true, the following condition is fulfilled:

$$\delta \ll \sqrt{Dt_{exp}} \ll d_g \quad (5.15)$$

where δ is the width of the grain boundary, t_{exp} is the annealing time of the experiment and d_g is the grain diameter, consistent with B type kinetics according to the classification of Harrison (1961). Also, in $(\text{Mg,Fe})\text{O}$ inclusions at a distance of up to $50 \mu\text{m}$ away from the surface, a NiO component is observed, which is also attributed to a grain boundary transport process. It cannot be excluded that this fast grain-boundary diffusion process might also be due to amorphization during sample preparation, localized to the grain boundaries, and rapid diffusion along these amorphized regions during initial heating. However, in this case it is not clear why this process does not operate in the diffusion couples employing MgO-Fe capsules. Transport along such amorphized regions would immediately stop when they recrystallize at high-pressure and temperature. Figure 5.32 also shows a reaction layer between perovskite and the Ni-NiO capsule but the resulting phases are too small to be identified by EPMA (for further discussion see Section

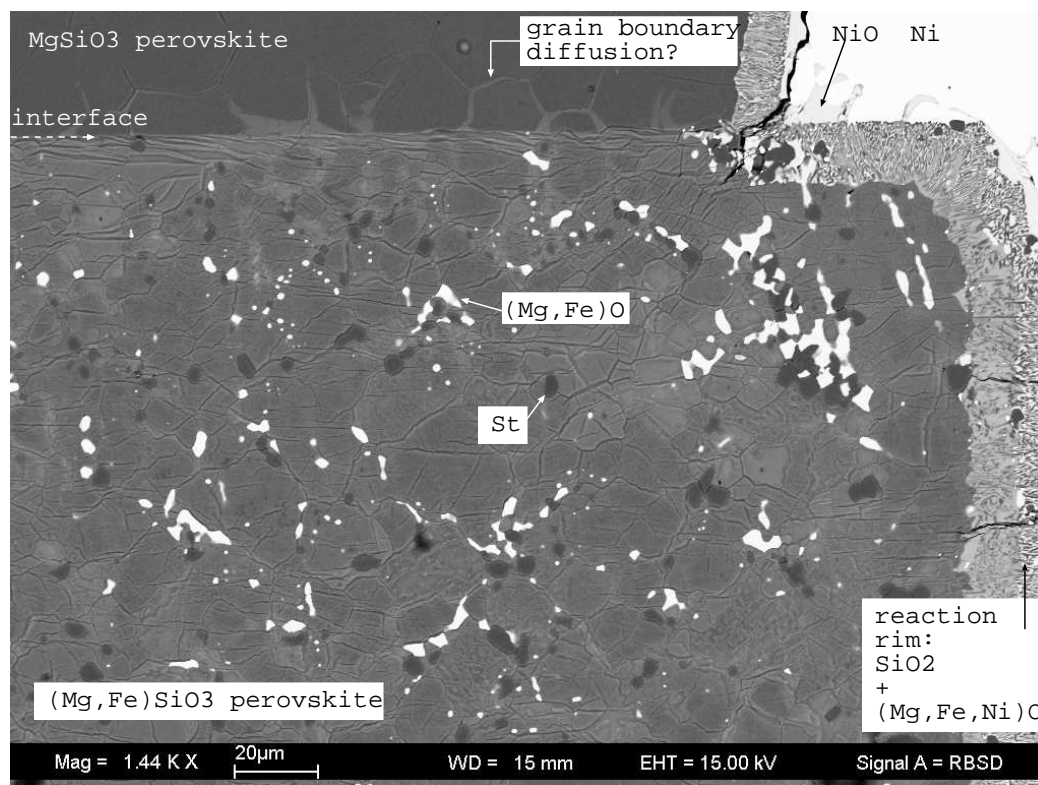


Figure 5.32: Backscattered electron images of a perovskite diffusion couple performed in a Ni-NiO capsule. The experiment was conducted at 25 GPa, 1973 K for 570 min.

5.5.3).

Figure 5.33 shows an orientation contrast image of the MgSiO_3 perovskite endmember of sample C13. The grain size is on the order of 50 - 100 μm , whereas on the Fe-rich side the grain size is smaller, between 5 and 15 μm . Similar dimensions were found in all other experiments. The large grains of the MgSiO_3 perovskite show an elongation perpendicular to the diffusion interface, parallel to the furnace axis (Fig. 5.33). Many of the crystals are twinned with varying thicknesses of the twin lamellae. Sometimes multiple twinning can be observed. Twin lamellae are also visible by optical microscopy. It is not fully understood whether the twinning is due to a phase transformation on quenching (a ferroelastic phase transition) or if the twins originate during the primary crystal growth (see also Section 1.3.1). Most of the twins, run through the whole crystal and terminate at the grain boundaries. Characteristic arrays of needle shaped twins

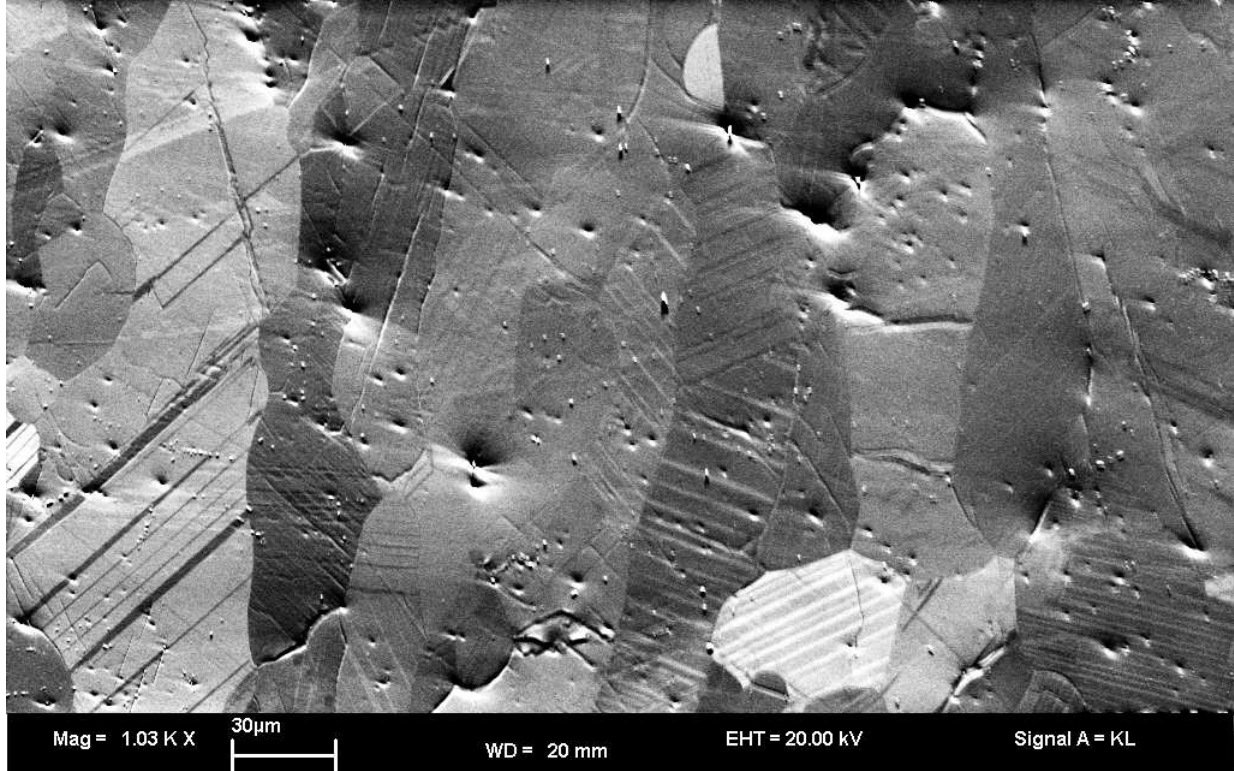


Figure 5.33: Orientation contrast image of sample C13 run at 25 GPa, 2043 K for 240 min. The image shows the MgSiO_3 perovskite. The cylinder axis of the furnace was in a vertical direction.

in more than one orientation, which are normally present in the case of a ferroelastic phase transition (Salje, 1990), are not observed. This would favor an origin by growth.

The $f\text{O}_2$ conditions prevailing during the experiments performed in MgO-Fe capsules can be estimated from the FeO-content of (Mg,Fe)O adjacent to the Fe (compare with Figure 2.6), assuming that the layer of perovskite (10/4 assemblies) or ringwoodite (18/8 assemblies) formed during quenching. In general the oxygen fugacity is governed by the distribution of iron between a metal (me) and an oxide (ox) by the equilibrium (e.g. Holzheid (1996)):



The equilibrium constant $K_{5.16}$ of Equation 5.16 is:

$$K_{5.16} = \frac{a_{FeO,ox}}{a_{Fe,me} \cdot fO_2^{1/2}}, \quad (5.17)$$

where a_c is the activity of the component c. For the iron-wüstite buffer the activities of Fe and FeO are equal to 1 and the equilibrium constant $K_{5.16}$ becomes:

$$K_{5.16} = fO_2(IW)^{-1/2}, \quad (5.18)$$

where $fO_2(IW)$ is the oxygen fugacity of the iron-wüstite buffer. Therefore, the oxygen fugacity relative to the oxygen fugacity of the iron-wüstite buffer, defined as:

$$\Delta_{fO_2} = \log(fO_2) - \log(fO_2(IW)), \quad (5.19)$$

which is characteristic for the equilibrium in Equation 5.16, is given by:

$$\Delta_{fO_2} = -2 \log \frac{a_{FeO,ox}}{a_{Fe,me}}. \quad (5.20)$$

Only in the case of an ideal mixture do the activities equal mole fractions. Calculated values for Δ_{fO_2} assuming ideal mixing behavior in the metal and the oxide are given in Table 5.6. Values for Δ_{fO_2} range from -3.3 in experiment C23 to -1.8 in experiment C31. Hence, oxygen fugacity is on average slightly smaller than but within 1 log-unit of the oxygen fugacity characteristic of the present day core-mantle boundary, which is estimated to be at $\Delta_{fO_2} = -2.3$ (Holzheid, 1996), taking Fe abundances for the mantle and the core given in McDonough and Sun (1995) into account.

The oxygen fugacity in the Ni-NiO capsules is close to the Ni-NiO buffer (Section 5.1). Due to the pressure effect, the difference in oxygen fugacity between the iron-wüstite and the Ni-NiO buffers at high pressure (25 GPa) and temperature (2073 K) is ~ 1.5 log-units compared to 4 log units at room pressure. These values were calculated using Gibbs energies of formation of metal oxides and molar volumes from Ride (1991), assuming a constant reaction volume. If this assumption is correct, the difference in fO_2 between experiments performed in MgO-Fe capsules and experiments performed in Ni-NiO capsules is on the order of 4 log-units.

The difference between Fe-Mg interdiffusivities in perovskite and ferropericlase can be established by comparing the relative diffusion length of Fe-Mg profiles in the same sample. In

all samples the diffusion length of Fe-Mg exchange in the MgO of the capsule material resulting from reaction with the metallic Fe is on the order of 35-120 μm (see contrast in Figure 5.31), whereas the diffusion length of Fe-Mg exchange in silicate perovskite for experiments performed in MgO-Fe capsules is on the order of a few 100 nm (as shown in Section 5.5.4). Hence, because the length of a diffusion profile scales with the diffusion coefficient by $x \propto \sqrt{D t}$, the Fe-Mg interdiffusion coefficient of ferropericlase compared to silicate perovskite is approximately 4 orders of magnitude faster at the same oxygen fugacity.

5.5.3 TEM characterization of the samples

As discussed earlier (section 5.5.2), concentration profiles are shorter than the resolution limit of the electron microprobe. In addition, the existence of inhomogeneities on the Fe-rich side of the diffusion couples leads to an increased scatter in Fe-content, measured by EPMA, because inclusions are often smaller than the interaction volume in the electron microprobe (Section 3.2). Thus, diffusion couples were prepared for analytical TEM measurements following the procedure described in Section 3.3.

Samples with a large difference in Fe-content preserved a large residual differential stress between the two perovskites. Therefore, like a bimetal, the diffusion couple bent upward during thinning, losing coherence with the surrounding material. Thus, after accomplishing approximately 2/3 of the thinning, the diffusion couple was removed from the surrounding material and remounted on a new grid.

As already observed in backscattered electron images, experiments performed in MgO-Fe capsules contain metallic Fe-inclusions on the Fe-rich side (consistent with Liebske et al., 2003). Twinning is also an ubiquitous feature on the TEM scale (Fig. 5.34). No attempts were made to characterize the twin laws in the samples of this study because a detailed study of twin laws for silicate perovskite already exists (Wang et al., 1992). Profiles across twin lamellae and compositional mapping did not reveal any significant disturbances of the diffusion profiles caused by the twin lamellae. In some of the samples, subgrain boundaries formed by dislocations are visible, affecting the diffusion profile (Fig. 5.34). The profile shown in Fig. 5.34 crosses three subgrain boundaries. There are two asymmetric maxima visible along a profile that crosses the two sub-

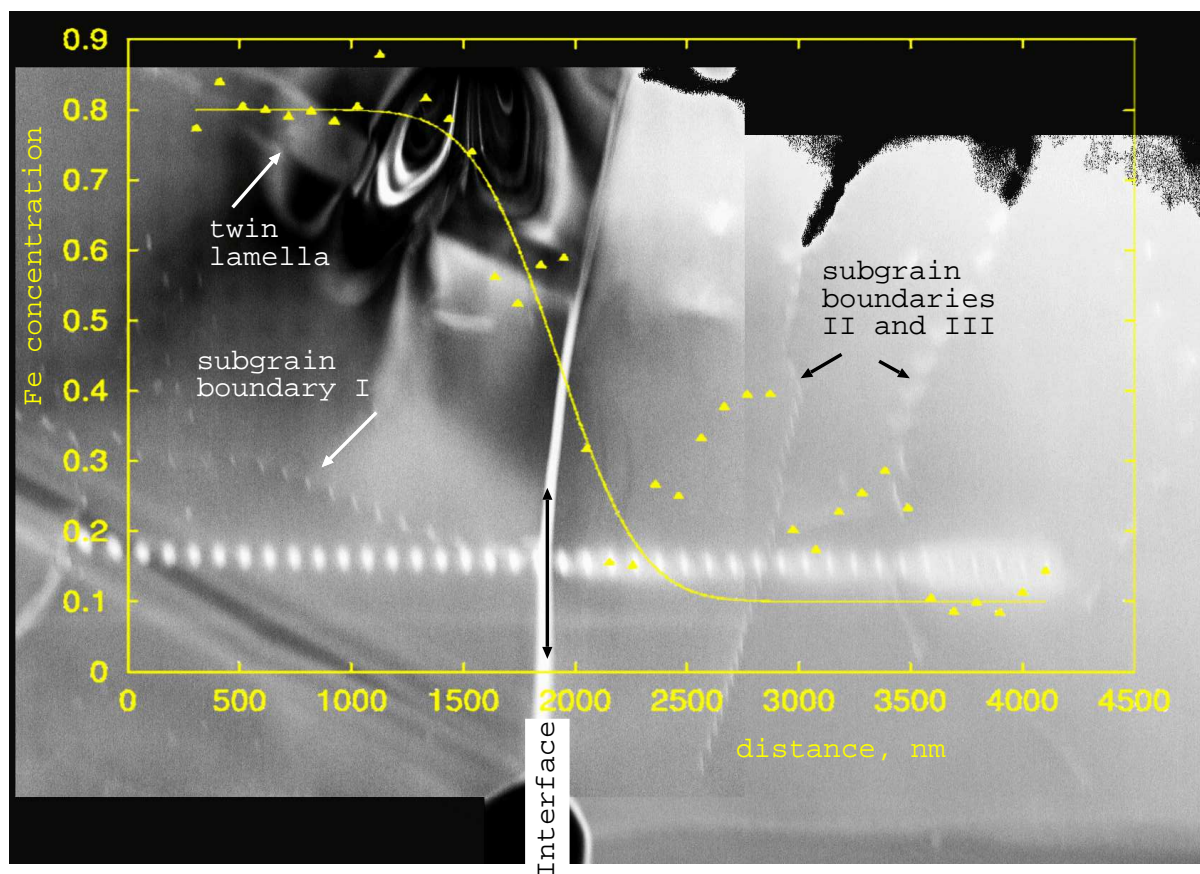


Figure 5.34: EDX-TEM profile on sample C22, annealed at 24 GPa, 2073 K for 900 min. Individual measurement points are clearly visible due to carbon contamination and amorphization. The microstructure consists of three subgrain boundaries and one twin lamella terminating at the diffusion interface.

grain boundaries subparallel to the diffusion interface. The long tail of the asymmetric profile is directed towards the interface implying that the subgrain boundaries originated at the interface and were mobile during the diffusion experiment. Because Fe is preferentially incorporated in the subgrain boundary, the tails are left behind. In Shewmon (1989) a similar effect is described for diffusive enrichment along a moving grain boundary during zincification of iron. In this case the diffusing component is constantly replenished along the grain boundary that was oriented perpendicular to the surface.

The influence of the subgrain boundaries on the shape of the diffusion profiles, as demonstrated in Figure 5.34, stresses the fact that observations of the microstructure are of great importance when measuring short concentration profiles. Such phenomena might be easily overlooked when using methods such as the ion microprobe which averages over a certain area. When, in

addition, grain boundary diffusion plays an important role it might become especially difficult to distinguish between subgrain boundary, grain boundary and bulk diffusion.

$\text{Fe}^{3+}/\Sigma\text{Fe}$ ratios were determined by EELS spectroscopy using the Fe $L_{2,3}$ edges and the universal curve of van Aken et al. (1998). On sample C28, performed in a MgO-Fe capsule, at 24 GPa and 2133 K for 1430 minutes $18 \pm 7 \%$ Fe^{3+} was found, whereas for experiment C70, performed in a Ni-NiO capsule, at 26 GPa and 2173 K for 60 minutes the $\text{Fe}^{3+}/\Sigma\text{Fe}$ ratio is slightly higher with $20 \pm 6 \%$. These values are within error consistent with the Fe^{3+} content determined in Lauterbach et al. (2000) and Frost and Langenhorst (2002) for Al free perovskite performed in Re and Fe capsules.

The reaction rim visible in Fig 5.32 has been identified by EDX-TEM as stishovite finely intergrown with an oxide with $(\text{Ni}_x\text{Mg}_y\text{Fe}_z)\text{O}$ composition. The symplectitic rim can be understood in terms of the binary phase diagram of perovskite, where perovskite becomes unstable at high Fe contents and forms stishovite and ferropericlasite (Jeanloz and Thompson, 1983). The recent experiments show that in the corresponding ternary system $\text{MgSiO}_3\text{-FeSiO}_3\text{-NiSiO}_3$ a similar disproportionation reaction occurs at high Ni contents.

5.5.4 Profiles and diffusion coefficients

Profile measurements were carried out in the TEM using a Gatan 636 double tilt specimen holder cooled by liquid nitrogen following the analytical procedure described in chapter 3.3. The temperature indicated by the thermocouple of the holder was 104 ± 1 K. Selected EDX-spectra are shown in Appendix E. In practice, profiles were automatically measured in the STEM (Scanning Transmission Electron Microscopy) mode making use of the Analysis Manager software module supplied with the Vantage software.

Due to the convergent beam used for obtaining a high spatial resolution, Mg loss occurred during the analysis. This effect is most severe if the sample is very thin. Hence, the measurement spots are clearly visible after the analysis due to the amorphization effect and contamination by deposition of cracked hydrocarbons on the locally heated sample, as is evident in Figure 5.34.

The degree of Mg loss was further investigated with time series analysis on a single measurement point. Figure 5.35 shows a series of spectra obtained by counting repeatedly for a lifetime of

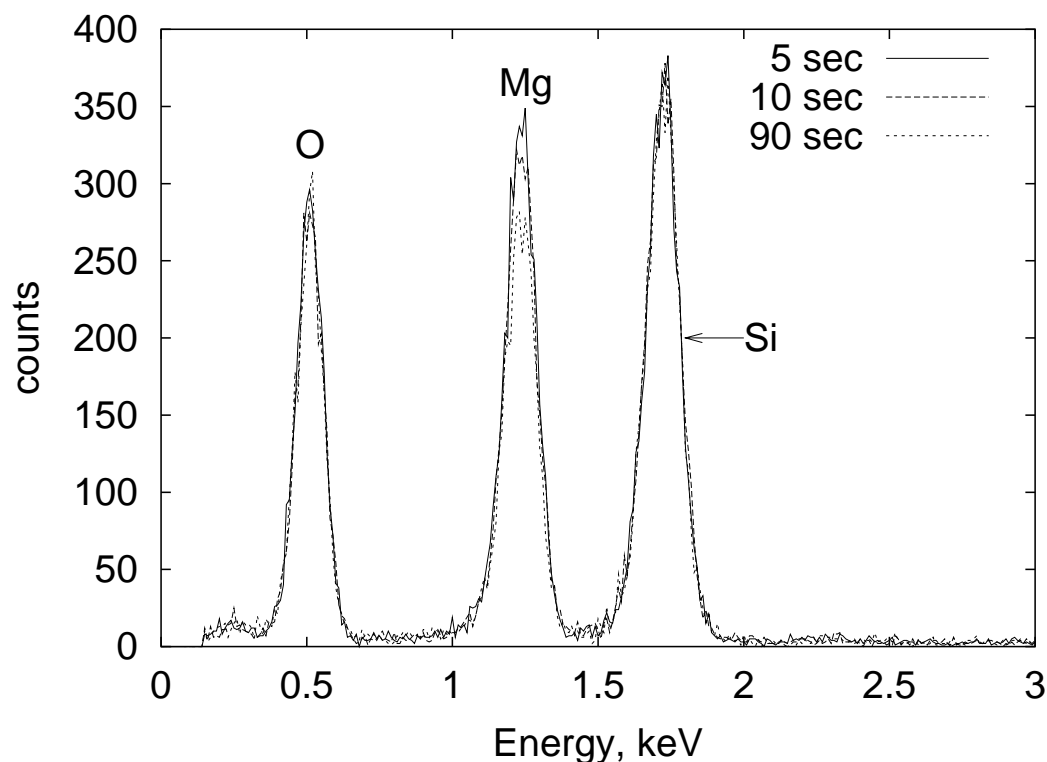


Figure 5.35: Mg loss, investigated by EDX-STEM time series analysis on a single point of sample C23, performed in a MgO-Fe capsule at 24 GPa and 2123 K for 720 minutes. Spectra were measured repeatedly for a lifetime of 5 sec (deadtime was approximately 30%). Three spectra are shown after 5, 10, and 90 seconds of lifetime, clearly revealing the loss in intensity of the Mg peak.

5 sec at the same point of the MgSiO_3 perovskite of sample C23, performed at 24 GPa and 2123 K for 720 minutes. Clearly, a decrease in intensity of Mg is observed for lifetimes between 0 and 90 sec. Mass balance calculations using the analyses suggest that the component lost during electron bombardment is MgO. Hence, to obtain the correct mole fraction of the Fe component in perovskite, X_{FeSiO_3} , the amount of MgO necessary to get a stoichiometric analysis was added to the raw data. The results of this correction show that the absolute Fe concentrations are essentially unaffected, no matter if the MgO loss correction is performed or not, whereas meaningful profiles for Mg can only be obtained by using the correction. Thus, only Fe concentrations were used in subsequent profile investigations for diffusion coefficient determination. The $\text{Fe}^{3+}/\Sigma\text{Fe}$ ratio, determined in Section 5.5.3 was not taken into account because the effect is negligible for

the total Fe concentrations involved.

Figures 5.36 and 5.37 show representative profiles measured on samples from Fe-Mg in-

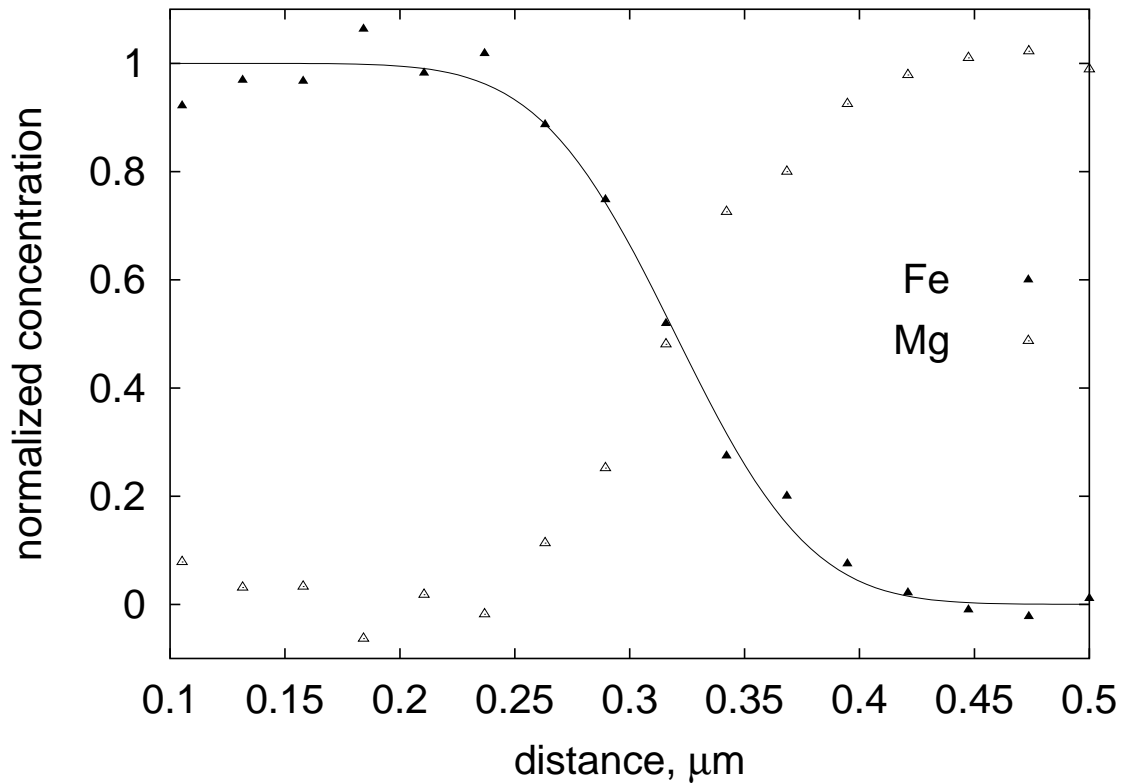


Figure 5.36: Fe and Mg profiles measured by EDX-STEM analysis on sample C19 run at 25 GPa and 2023 K for 483 min. Mg loss was corrected as discussed in the text. The lengths of the profiles of this sample range from 150 - 300 nm. These are the shortest profile lengths measured in this study. The curves drawn in the figure are fitted diffusion profiles with $\log D = -19.43$. Due to variation in the lengths of the profiles, the average diffusion coefficient of this sample is -19.1 (Table 5.7).

terdiffusion experiments employing MgO-Fe capsules. The profiles are symmetrical and were therefore fitted with a composition-independent diffusion coefficient (Eq. 4.6). The composition of the Fe-bearing perovskite, synthesized using synthetic pyroxene as starting material, is not always homogeneous over a scale larger than 5 μm for diffusion experiments performed in MgO-Fe capsules. This problem arises because of the generally small diffusion coefficients in silicate perovskite as revealed by the short diffusion profiles. Hence, inhomogeneities in the starting material could not be completely homogenized during the synthesis and the diffusion experiments. However, it is assumed that local equilibrium, consistent with the initial and boundary

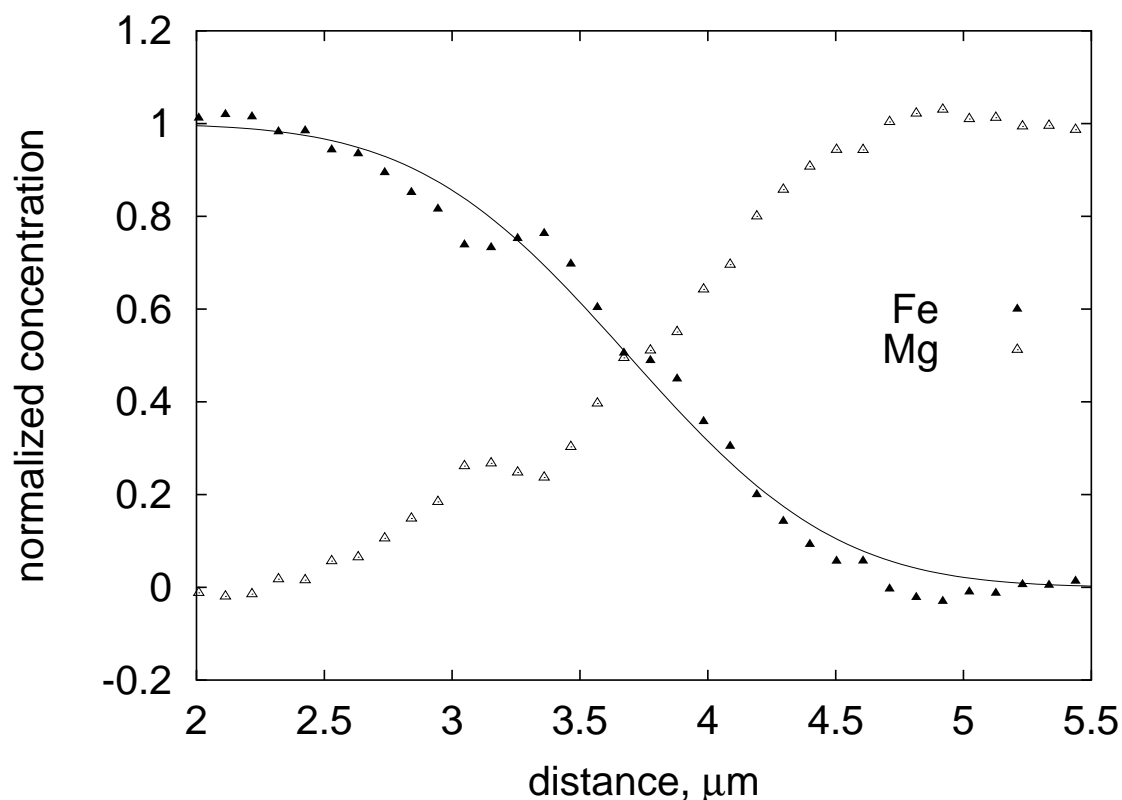


Figure 5.37: Fe and Mg profiles obtained by EDX-STEM analysis on sample C28 run at 24 GPa and 2133 K for 1430 min. Mg loss was corrected as discussed in the text. The length of the profiles of this sample are the longest measured for silicate perovskite in this study. The fit is drawn for a constant diffusion coefficient with $\log(D) = -17.62$.

conditions given in Equations 4.2 and 4.3, exists at the points of the profile analysis. The compositions on both sides of the profiles and the diffusion coefficients, derived by fitting Equation 4.6, are listed in Table 5.7. Profiles of sample C22 are always disturbed by subgrain boundaries, as shown in Figure 5.34. Therefore the diffusivity of C22, obtained by excluding points influenced by subgrain boundary migration, is shown in subsequent figures of diffusion coefficients versus inverse temperature, but is rejected in the determination of the activation energy. The error of a single measurement in log-space is estimated as half the absolute difference in the logarithm of the Fe-Mg interdiffusion coefficient of samples C23 and C28, performed at nearly the same conditions (10 K difference in temperature) and is found to be on the order of 0.4 log-units.

Samples run in Ni-NiO capsules generally show evidence of grain boundary diffusion, as seen in Figure 5.32. The EDX-TEM profiles on sample C61, annealed for only 10 minutes at 26 GPa and 2073 K, show diffusion tails on both sides of the interface of varying extent with

Table 5.7: Results of the different perovskite diffusion experiments. X_{FeSiO_3} is the composition of the Fe-bearing endmember of the diffusion couple, for the Mg endmember no Fe is present at begin of the diffusion experiment, *dur* denotes duration, and *unc* is the uncertainty of the Fe-Mg interdiffusion coefficient $D_{\text{Fe-Mg}}$ in log-units.

Sample	P, GPa	T, K	dur, min	capsule	X_{FeSiO_3}	$D_{\text{Fe-Mg}}$	unc
C13	24	2043	240	MgO-Fe	0.06	-18.8	0.4
C19	24	2023	483	MgO-Fe	0.02-0.05	-19.1	0.4
C22	24	2073	900	MgO-Fe	0.04	-18.2 ¹	0.4
C23	24	2123	720	MgO-Fe	0.02-0.03	-18.4	0.4
C28	24	2133	1430	MgO-Fe	0.06	-17.6	0.4
C30	22	2273	373	MgO-Fe	0.05-0.07	-18.2	0.4
C61	26	1800	10	Ni-NiO	0.10-0.12	n.d. ³	
C70	26	2173	60	Ni-NiO	0.09	-17.0	0.4
C76	26	1973 ²	570	Ni-NiO	0.11	-18.2	0.4

¹ not included in calculations, as discussed in the text

² thermocouple break, temperature estimated from the heating power

³ not determined, because no measurable profile developed (Fig. 5.38)

respect to distance (Fig. 5.38). This observation is interpreted as a grain boundary diffusion component and its varying extent is due to the distance of the diffusion profile from the next grain boundary. A sharp step in composition is observed at the center of the diffusion profile, which is representative of the true bulk diffusion coefficient. Because diffusion coefficients of silicate perovskite are very small (Table 5.7), virtually no diffusion profile due to bulk diffusion developed during the annealing time of 10 minutes. Therefore, sample C61 can be regarded as a zero time test.

Sample C76, performed at 26 GPa and 1973 K for 570 min, also shows tail contributions but the profile due to bulk diffusion can be clearly resolved (Fig. 5.39). Most profile analyses of sample C70 also show evidence of grain boundary diffusion. For this sample, the shortest profile was regarded to represent the true lattice diffusion coefficient. However, this still might be an overestimation, because only one profile was taken into account for deriving the diffusion coefficient. Hence, it is not unequivocally demonstrated that this diffusivity does not include a grain boundary diffusion contribution.

From this discussion, it becomes clear that in polycrystalline silicate perovskite diffusion

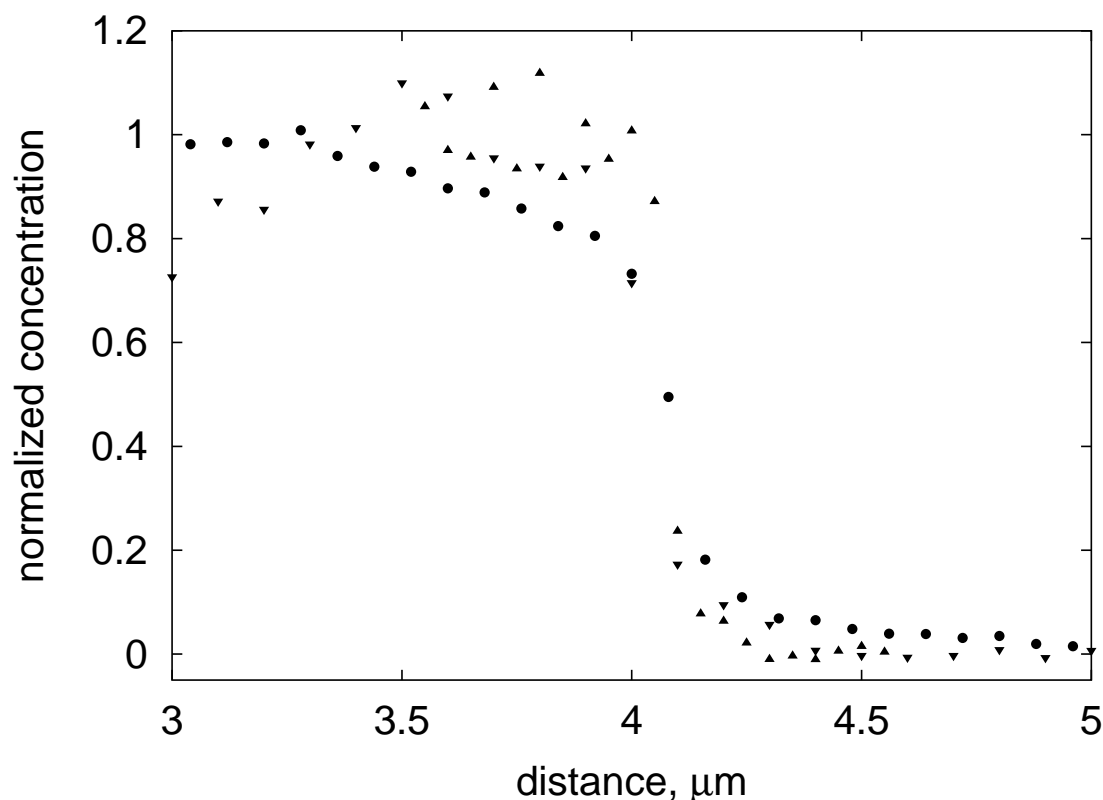


Figure 5.38: Profiles measured on sample C61, run at 26 GPa, 2073 K for 10 min. The profiles are superimposed on each other to show the varying extents of the diffusion tails on each side of the diffusion interface. Note the sharp step in composition at the diffusion interface.

couples, various factors influencing the measured diffusion coefficients, such as grain boundaries or subgrain boundaries, play an important role. Unlike wadsleyite (Section 5.3), bulk diffusion in perovskite is so slow that the experiments were performed in a regime where all these different processes operate at the same time to a similar extent. In addition, problems due to inhomogeneities and exsolution of other phases exist. Therefore, physical quantities, such as for example the activation energy, derived by fitting the diffusion coefficient as function of intensive thermodynamic variables such as temperature (see next section) are associated with larger errors than for the other, in terms of microstructure and chemistry, less complicated systems (olivine, wadsleyite, ferropiclase).

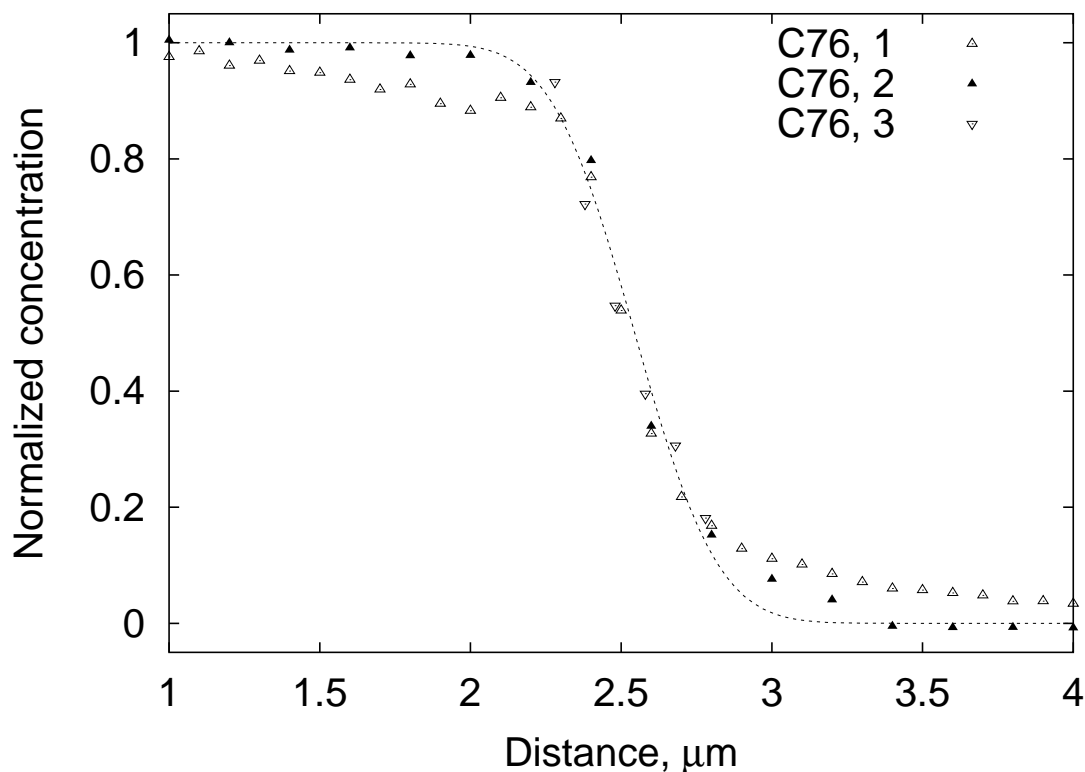


Figure 5.39: Three different profiles measured on sample C76, annealed at 26 GPa, 1973 K for 570 minutes, superimposed onto each other. Note the consistency of the profile at intermediate concentrations and the tails on both sides of the interface. The dashed line is a fit of Equation 4.6 with $\log(D) = -18.16$.

5.5.5 Temperature dependence of Fe-Mg interdiffusion at 24 GPa

Figure 5.40 shows Fe-Mg interdiffusion coefficients of $(\text{Mg,Fe})\text{SiO}_3$ perovskite as a function of inverse temperature (Arrhenius diagram). Most of the experiments were performed at 24 GPa (Table 5.7). Only experiment C30 was at slightly lower pressure (22 GPa), employing an 18/8 assembly, whereas experiments employing Ni-NiO capsules were performed at 26 GPa in order to stabilize the Fe-containing perovskite. As discussed in Section 5.5.1, the difference in diffusivity due to the pressure effect should be negligible, much smaller than the analytical error. Thus, no attempt was made to correct for the effect of pressure. All evidence presented in

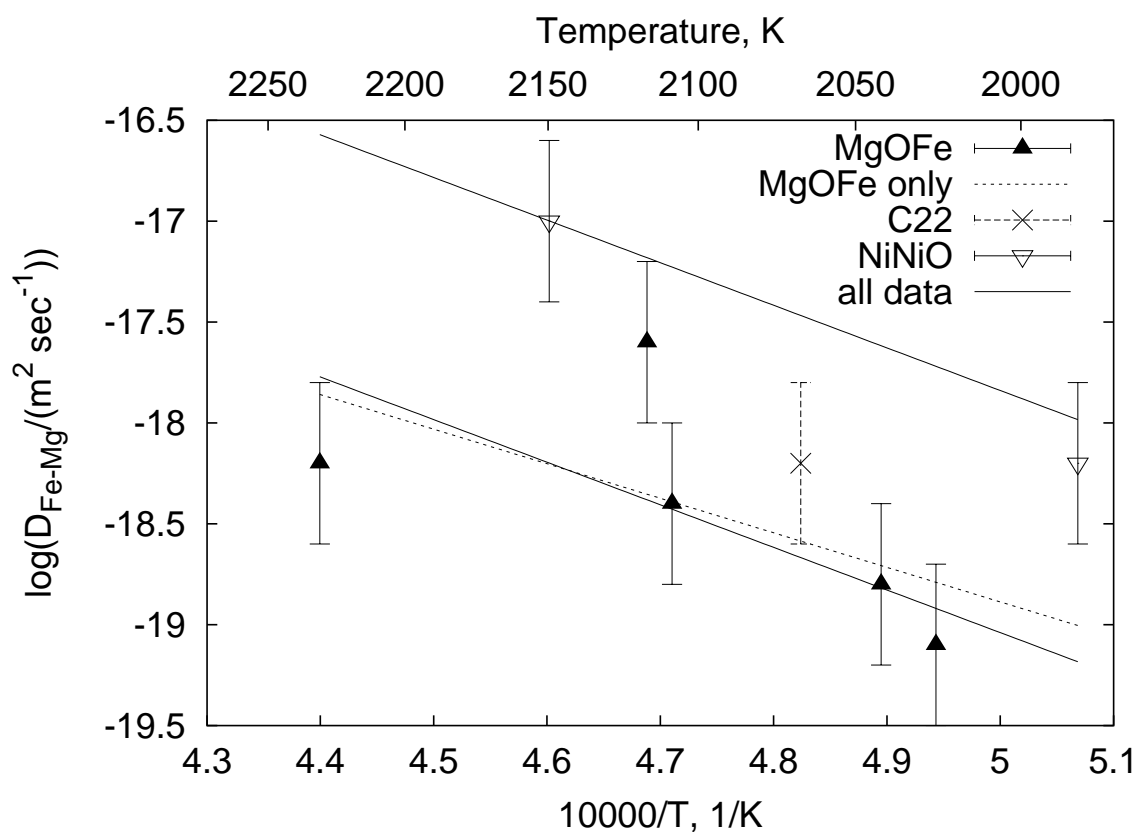


Figure 5.40: *Fe-Mg interdiffusion coefficients (Table 5.7) as function of the inverse temperature of the experiments. The fits for elucidating the activation energy at high pressure ($E_a + P V_a$) are explained in the text.*

Section 5.5.4 points to the conclusion that the compositional effect, at least for $0 < X_{\text{FeSiO}_3} < 0.11$ (range of compositions studied here, see Table 5.7), is insignificant, because profiles due to bulk diffusion were always found to be symmetrical within the analytical uncertainty (Figures 5.36, 5.37, and 5.39).

The activation energy at high pressure was determined using two procedures. A fit of the results of those experiments employing MgO-Fe capsules leads to a value of $E_a + P \Delta V_a = 328 \pm 230 \text{ kJ mol}^{-1}$ (dashed line in Figure 5.40), where E_a is the activation energy at 1 bar and ΔV_a is the activation volume. As discussed in Section 5.1 the activation energy at high pressure also contains a contribution due to a change of f_{O_2} of the buffer systems used. To include the results of experiments performed in Ni-NiO capsules, it was assumed that the activation energy is independent of the absolute value of the oxygen fugacity of the buffer systems. This should

be the case because fO_2 determines the abundance of point defects but not their energies of formation or migration (see Equation 1.6 and Section 1.2.4). Hence, the diffusivities of C70 and C76 (Table 5.7, open triangles in Figure 5.40) were shifted systematically towards lower diffusivity until the error of a linear fit of all data is simultaneously minimized. Determined by this procedure, the overall activation energy at 24 GPa is $404 \pm 144 \text{ kJ mol}^{-1}$ (for a shift of 1.2 log-units, solid lines in Figure 5.40). This value is valid for buffer systems with an fO_2 variation parallel to the Ni-NiO or Fe-FeO buffer, respectively. The shift of 1.2 log units corresponds to an fO_2 exponent of 1/3.3 if the absolute values of fO_2 differ by 4 log-units (Section 5.5.2). It has to be emphasized that this value is subject to much uncertainty due to the extrapolation of the fO_2 values for the solid state buffers. Therefore, no attempt was made to interpret the oxygen fugacity exponent in terms of point defects (see the derivation presented in Section 1.2.4).

The preferred model for Fe-Mg interdiffusion coefficients D_{Fe-Mg} of (Mg,Fe)SiO₃ perovskite at 24 GPa and reducing conditions ($\Delta_{fO_2} \approx -2.7$, Table 5.6) is:

$$D_{Fe-Mg} = 3.3(1.2) \times 10^{-9} \exp\left(-\frac{404000(144000)}{8.31441 T(\text{K})}\right) \frac{\text{m}^2}{\text{sec}}, \quad (5.21)$$

and at an oxygen fugacity corresponding to the Ni-NiO buffer:

$$D_{Fe-Mg} = 5.1(2.0) \times 10^{-8} \exp\left(-\frac{404000(144000)}{8.31441 T(\text{K})}\right) \frac{\text{m}^2}{\text{sec}}. \quad (5.22)$$

The preexponential factor was derived by fixing the activation energy at 404 kJ mol^{-1} . If D_{Fe-Mg} has to be calculated at other oxygen fugacity conditions, a $fO_2^{1/3.3}$ correction might be employed but it has to be kept in mind that this correction relies on the accuracy of the extrapolations of the oxygen fugacities of the Ni-NiO and Fe-FeO buffers, which are poorly constrained at present.

Equations 5.21 and 5.22 do not take any directional dependence into account because from a structural point of view the directional dependence should be relatively weak (Section 1.3.1). However, some of the scatter observed in Figure 5.40 might arise from variations in crystallographic orientation.

At 1973 K and 24 GPa, for oxygen fugacities close to the Ni-NiO buffer, the Fe-Mg interdiffusion coefficient of (Mg,Fe)SiO₃ perovskite D_{Fe-Mg}^{pvsk} is $1.0 \times 10^{-18} \text{ m}^2 \text{ sec}^{-1}$ (Equation 5.22). At the same conditions the Fe-Mg interdiffusion coefficient for ferropericlaase D_{Fe-Mg}^{fp} is $2.1 \times 10^{-14} \text{ m}^2 \text{ sec}^{-1}$ for $X_{FeO} = 0.05$ (Equation 5.14). Hence, the ratio $D_{Fe-Mg}^{fp}/D_{Fe-Mg}^{pvsk}$ is

2×10^4 , nearly the same value that was estimated in Section 5.5.2. The silicon self-diffusion coefficient of silicate perovskite at 1973 K and 24 GPa is $3.5 \times 10^{-19} \text{ m}^2 \text{ sec}^{-1}$ using data of Yamazaki et al. (2000). Hence, silicon self-diffusion at these conditions is only approximately a factor of 3 slower than Fe-Mg interdiffusion estimated employing Equation 5.22. If the Si self-diffusion coefficient is compared to Fe-Mg interdiffusion at reducing conditions (Equation 5.21, $6.7 \times 10^{-20} \text{ m}^2 \text{ sec}^{-1}$) it is found that Si self-diffusion is faster than Fe-Mg interdiffusion. This has important implications for the rheology of the lower mantle which in a diffusional creep regime is determined by the slowest diffusing species. At reducing conditions the slowest diffusing species might be diffusion of the divalent cations rather than Si diffusion. This situation is totally different from relative diffusion rates at conditions of the upper mantle, because for minerals such as olivine, Si diffusion is much slower than Fe-Mg interdiffusion (Béjina, 1999).

5.6 Overview

In Figure 5.41 a comparison of Fe-Mg interdiffusion coefficients for olivine, wadsleyite, fer-

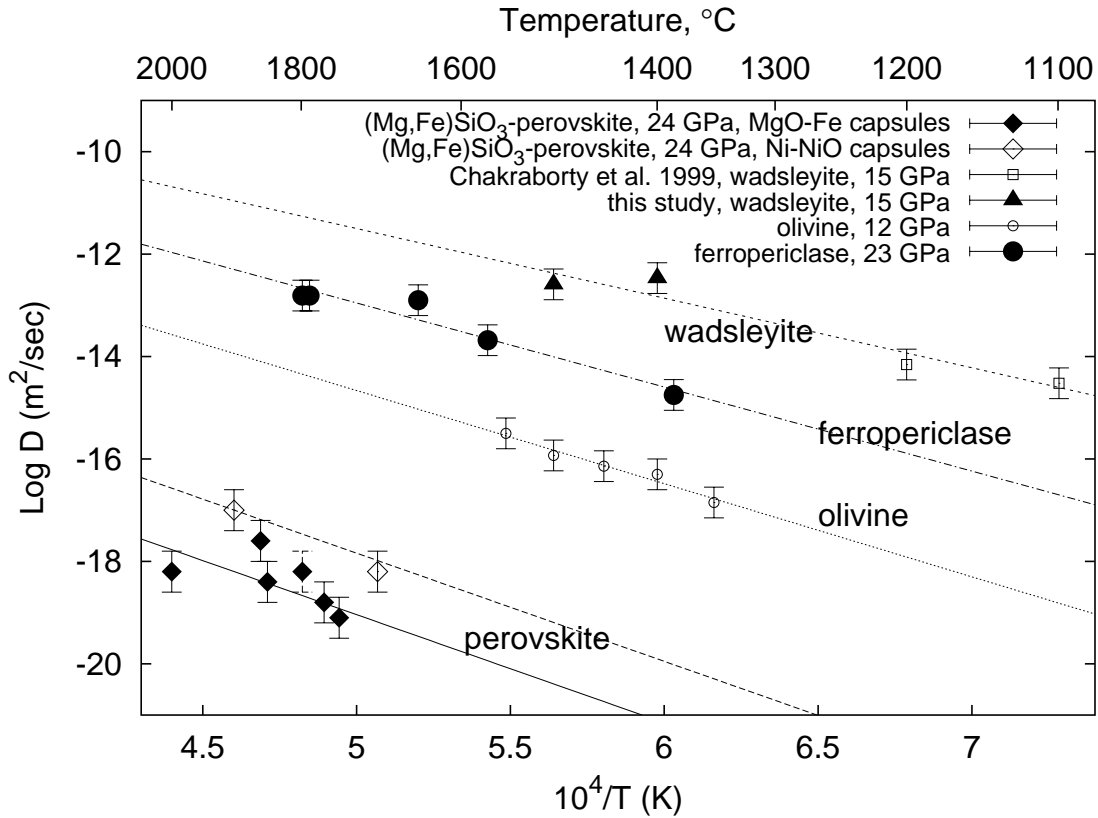


Figure 5.41: Overview of Fe-Mg interdiffusion coefficients for olivine, wadsleyite, ferropericlase, and silicate perovskite. Two datapoints for silicate perovskite obtained from experiments in Ni-NiO capsules lie ~ 1 order of magnitude above data obtained in MgO-Fe capsules.

ropericlase and (Mg,Fe)SiO₃ perovskite is shown. The fastest Fe-Mg interdiffusion coefficients are observed in wadsleyite, the mineral that dominates the upper transition zone. According to the results of Farber et al. (2000) interdiffusion in ringwoodite is as fast as in wadsleyite. The diffusive exchange of Fe and Mg is approximately two orders of magnitude slower in olivine, which is the main constituent phase of the upper mantle. In the lower mantle, Fe-Mg interdiffusion in perovskite is several orders of magnitude slower than in the main constituent phases of the upper mantle and the transition zone. However, ferropericlase shows relative fast Fe-Mg interdiffusion of a magnitude intermediate between olivine and wadsleyite. Because the lower mantle likely consists of ~ 80 vol.% perovskite (Poirier, 2000), processes depending on Fe-Mg

interdiffusion should be governed by very slow diffusivities (see further discussion in Section 6.5.2).

5.7 Diffusion experiments at high pressure: Experimental complications

5.7.1 High pressure versus low pressure experiments

At 1 bar, diffusion experiments are performed in furnaces that have a comparatively large hot spot region. Hence, at the position of the diffusion couple no significant temperature gradients are observed. In high pressure sample assemblies (Sections 2.2 and 2.5), the region of the hot spot is significantly smaller, potentially leading to significant thermal gradients. Knowing the diffusivities of the minerals investigated in this study (Sections 5.2 - 5.5), enables the effect of thermal gradients to be investigated by numerical simulations (Section 5.7.2). Another point of interest (at 1 bar and at high temperature) is the contribution of diffusion during initial heating of the experiments, especially if absolute diffusivities are relatively large and experimental durations short. As with temperature gradients, if diffusion coefficients are known, the role of the heating effect can be further investigated by numerical simulations (Section 5.7.3).

5.7.2 Temperature gradients

Temperature gradients in the 10/4 assembly can be as large as 100 K mm^{-1} (Trønnnes and Frost, 2002). The longest profiles investigated in this study were observed for ferropericlaase (Section 5.4), with a profile length of 100-200 μm . Therefore, Fe-Mg interdiffusion profiles in ferropericlaase are most likely to have been affected by thermal gradients across the diffusion zone. With a temperature gradient of 100 K mm^{-1} and a profile length of around 100-200 μm , the temperature variation along the diffusion profile is on the order of 10-20 K. Numerical simulations by finite differences using Equation 5.13, but allowing the temperature to vary linearly along the profile, were performed for the range of diffusivities obtained in this study. The temperature of the experiment T_{exp} was taken to be representative for the original interface of the diffusion profile. At the hotter end of the profile of the simulation, the temperature can then be expressed as $T_l = T_{exp} + grad \ 1/2 \ l_x$, where *grad* is the temperature gradient and l_x is the length of the profile

simulation. For the simulation, Equation 5.13 is inserted in Equation 1.2:

$$\frac{\partial C}{\partial t} = \frac{\partial}{\partial x} \left(D_0 \cdot \exp \left(-\frac{E_A - A \cdot X_{FeO} + (P - P_{ref}) \cdot \Delta V_A}{R \cdot (T_l - grad\ x)} \right) \frac{\partial C}{\partial x} \right) \quad (5.23)$$

Figure 5.42 illustrates the simulation at the conditions of experiment C48 (Table 5.5), which resulted in the longest profile observed in a 10/4 assembly in this study. The simulations employing

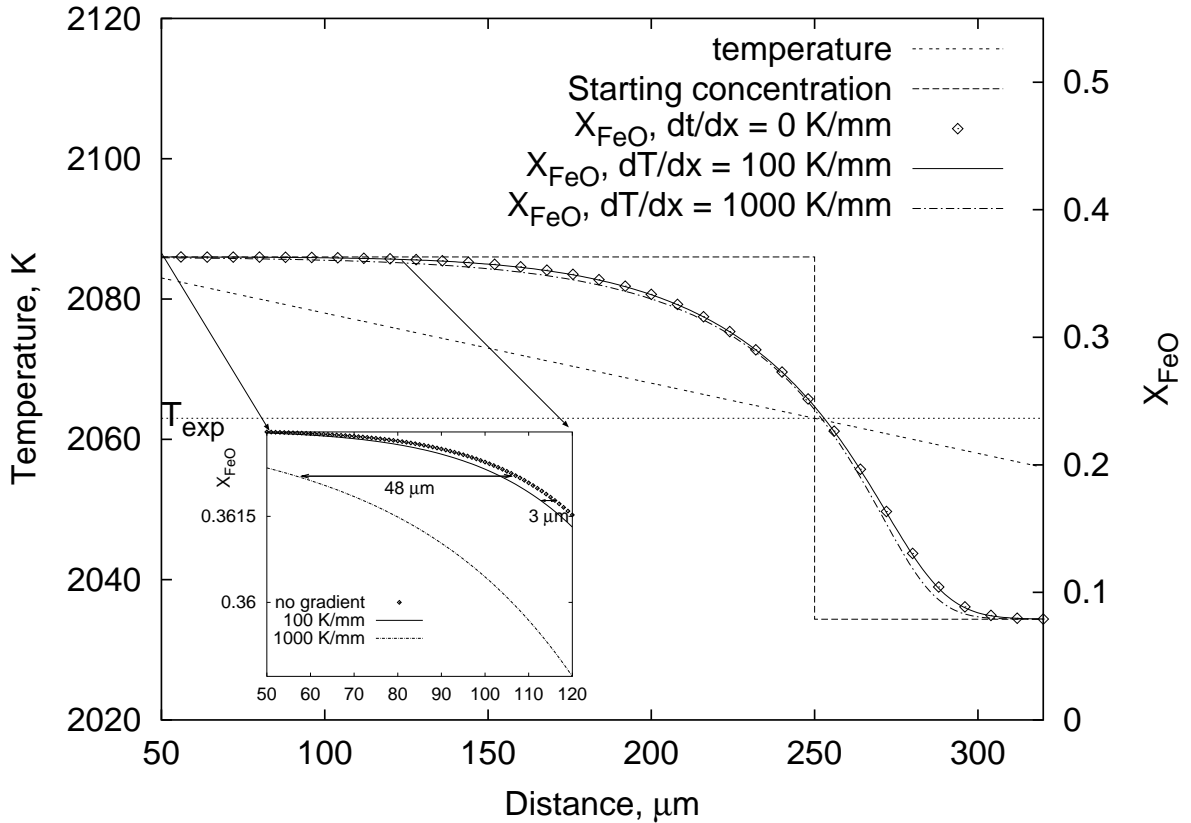


Figure 5.42: Effect of thermal gradients in the 10/4 assembly. The temperature varies linearly along the profile (left y axis, shown for a temperature gradient dT/dx of 100 K/mm). The simulations (right y axis) are shown for $dT/dx = 0, 100,$ and 1000 K/mm. The inset shows a blow up of the profiles in the region of $50-120 \mu\text{m}$ to show the extent of maximum profile lengthening.

Equation 5.23 show that effects of profile lengthening or shortening are negligible ($\sim 3 \mu\text{m}$ at the hot end and $\ll 1 \mu\text{m}$ at the cold end of the profiles) for a thermal gradient of 100 K/mm. The diffusion coefficient at $X_{FeO} = 0.3$, due to the thermal gradient, is $\sim 2.8 \%$ larger. This deviation is a factor of 10 smaller than the experimental error of $\sim 30 \%$ (0.3 log-units, Section 5.4.3). Hence, even for temperature gradients of 100 K/mm and a profile length of $\sim 200 \mu\text{m}$, the results would not be significantly affected. For temperature gradients much larger than 100 K/mm, the error

would become significant, for example approximately 30% at the profile ends for 1000 K/mm with a displacement of the profile of $\sim 48 \mu\text{m}$ at the hotter end (Figure 5.42).

Aside from pure distortion due to a change of diffusivity, temperature gradients can potentially also lead to Soret diffusion. For ferropericlase, this effect would be different in the two assembly types used in this study because temperature gradients in the 14/8 cell are much smaller in comparison to the 10/4 cell. Therefore a kink or discontinuity would appear in the pressure correlation if the Soret effect leads to a significant contribution of the diffusional flux. Such a kink is not observed however (Figs. 5.28, 5.29), so significant Soret diffusion can be excluded.

5.7.3 Heating effects

Some diffusion inevitably occurs while the sample is being heated. However, at 1873 K and 8 GPa, results of the time series shown in Fig. 5.27 indicate that this has little or no effect on the derived diffusion coefficients at these conditions. The contribution to the diffusion profiles during heating at all conditions was simulated by finite differences using Eq. 5.13. In an initial heating phase the temperature was varied from room temperature to the final temperature using the actual heating rates of the experiments. In practice this is achieved by approximating the heating with a step like temperature profile. At each step, normally with a stepsize of 1 K, diffusion is simulated and the resulting profile is taken as the initial distribution for the next temperature step. If the experimental temperature T_{exp} is reached, the calculations are continued in the same way as in all other profile simulations. Figure 5.43 shows an example of the ferropericlase system, taking a heating rate of 3.5 K/sec which is slightly smaller than the actual heating rate of 5 K/sec (worst case scenario).

The simulations show that diffusion profiles with lengths of several microns, depending on the heating rate and mineral system, develop during initial heating ($\sim 25 \mu\text{m}$ for the example in Figure 5.43). The difference between simulations employing these extended profiles as the initial condition and simulations using an ideal step function as the initial condition vanishes very quickly, however, with progressive diffusion. After less than 5 minutes no significant differences can be observed for the combinations of heating rate and high temperature annealing times used in this study. For C55, even for a longer heating time than the real heating time (Figure

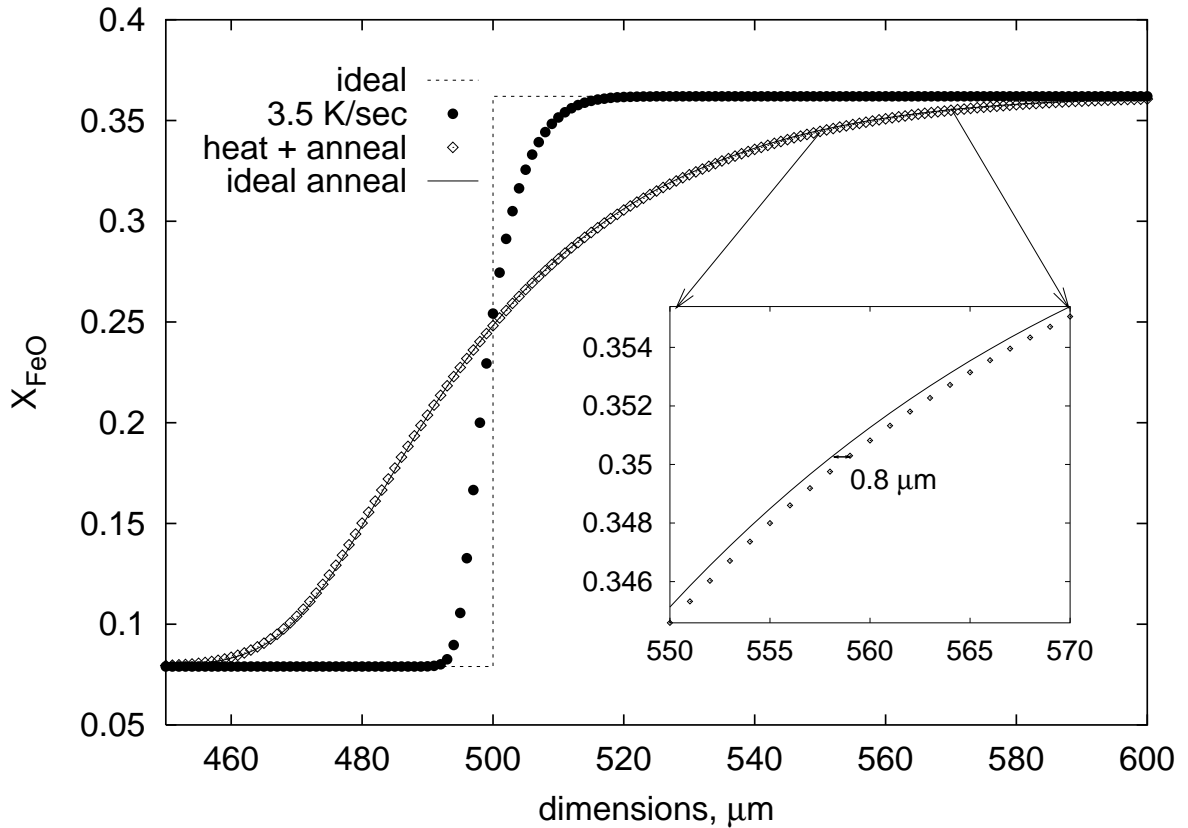


Figure 5.43: Effect of diffusion occurring during initial heating of experiment C55 (Table 5.5). The dashed line shows an ideal step function as initial condition (Eq. 4.2). The black dots show the profile that develops in the simulation solely due to the heating effect with a heating rate of 3.5 K/sec, slightly smaller than the actual heating rate of 5 K/sec. The diamonds represent the profile taking the heating effect into account and are compared to the profile simulated without heating effect (solid line). The deviation between the two profiles after 21 minutes (experimental duration) is on the order of $0.8 \mu\text{m}$ only.

5.43), the deviation of absolute diffusivities is smaller than 3 %, corresponding to better than 0.02 log-units (with an experimental error of 0.3 log-units). Experiments employing diffusion couples of olivine, wadsleyite and silicate perovskite were performed always with a larger ratio of experimental duration at high temperature to heating time. Hence, the effect of heating is even smaller for these minerals as compared to ferroprecipitate. Therefore the profiles observed in this work only contain information about the diffusional properties at high temperature and it is mathematically justified to use an ideal step function as the initial condition in the simulation of the profiles.

Chapter 6

Discussion

6.1 Introduction

The results obtained in this study can be used to calculate Fe-Mg interdiffusion coefficients at the oxygen fugacity of the Ni-NiO buffer for olivine in the upper mantle, wadsleyite in the transition zone and ferropericlase and silicate perovskite in the uppermost part of the lower mantle. The temperature and pressure conditions of the experiments directly correspond to the conditions prevailing in the mantle to a depth of 700 km. For constraining diffusivities and a better understanding of kinetics in the lower mantle, results for ferropericlase (Section 5.4) and silicate perovskite (Section 5.5) are extrapolated over the entire pressure and temperature range of the lower mantle in Section 6.2 using *ab initio* calculations to constrain the activation volume at pressures > 25 GPa (Ita and Cohen, 1997; Wright and Price, 1993). Taking an adiabatic model of temperature and the Preliminary Reference Earth Model (PREM, Dziewonski and Anderson, 1981) for the pressure variation with depth into account, diffusion coefficients, characteristic for the depth range of 0 to 700 km, are calculated in Section 6.3 together with estimates for the lower mantle. The slow Fe-Mg interdiffusion rates of silicate perovskite exert strong limitations on the experimental investigation of multiphase element partitioning involving this mineral. This problem is further discussed in Section 6.4.

The following sections highlight selected geological applications of the diffusion coefficients determined in this study. Olivine and wadsleyite Fe-Mg interdiffusion coefficients are used in Section 6.5.1 to constrain the kinetics of the olivine-wadsleyite phase boundary in the Earth's mantle. Because the lower mantle consists mainly of ferropericlase and perovskite, the diffu-

sional properties of a minor phase (ferropericlase) embedded in a matrix with a much smaller diffusion coefficient (perovskite) is investigated in Section 6.5.2. These results are then used to constrain the lifetime of heterogeneities of varying sizes in the lower mantle (Section 6.5.3) and the possible extent of interaction at the core-mantle boundary during Earth's history (Section 6.5.4). The final section (Section 6.5.5) gives an estimate of the extent of possible reequilibration in the lower mantle during core formation following an early magma ocean stage.

6.2 Extrapolations towards lower mantle conditions

6.2.1 Ferropericlase

In order to calculate Fe-Mg interdiffusion coefficients of ferropericlase over the entire pressure-temperature range of the lower mantle, the results of this study are combined with results of *ab initio* calculations on how the activation volume evolves as a function of pressure up to the pressure at the core-mantle boundary, which is approximately 136 GPa (Dziewonski and Anderson, 1981).

Theoretical considerations predict that the activation volume should decrease with increasing pressure (Karato, 1981; Poirier and Liebermann, 1984; Mills et al., 1991). Ita and Cohen (1997) calculated free energies for vacancy pair formation and migration of Mg and O in pure MgO at pressures from 0 to 140 GPa and temperatures from 1000 to 5000 K. Using these data together with calculated lattice parameters enabled these authors to calculate the decrease in the activation volume of the intrinsic Mg self-diffusion coefficient with increasing pressure. However, experimental and theoretical evidence shows that Mg diffusion in MgO occurs by an extrinsic diffusion mechanism at all experimental conditions so far investigated (Sempolinski and Kingery, 1980; Wuensch, 1983; Vočadlo et al., 1995; Van Orman et al., 2003). This is also likely to be the case for the Fe-Mg interdiffusion experiments reported in this study. Hence, to compare the results of Ita and Cohen (1997) with experimental results only the migration volume $V_m = \partial G_m / \partial P$, where G_m is the free energy of migration of the diffusion mechanism, has to be used. The activation volume of $3.0 \text{ cm}^3 \text{ mol}^{-1}$ for Mg tracer diffusion determined by Van Orman et al. (2003) agrees well with the migration volume of $3.1 \text{ cm}^3 \text{ mol}^{-1}$ calculated employing free energies of migration by Ita and Cohen (1997) between 0 and 20 GPa at 2000 K. It will be assumed here

that the data for the free energy of migration reported in Ita and Cohen (1997) can also be used to constrain the pressure dependence of the activation volume of $(\text{Fe}_x\text{Mg}_{1-x})\text{O}$ ferropericlase at pressures greater than 23 GPa.

The migration entropy S_m calculated as $S_m = \partial G_m / \partial T$ from the values of Ita and Cohen (1997) is approximately constant between 0 and 140 GPa indicating that the preexponential factor is pressure independent. In this case the activation volume $\Delta V_a(P)$ at any pressure P and constant temperature is given by (Poirier, 2000):

$$\Delta V_a(P) = -RT \frac{\partial \ln D(P)}{\partial P} = \frac{\partial \Delta H_a(P)}{\partial P}, \quad (6.1)$$

where $D(P)$ is the diffusion coefficient at pressure P and $\Delta H_a(P)$ is the activation enthalpy at pressure P . As an approximation, the average activation volume between 1 bar and pressure P was estimated from:

$$\Delta V_a^{avg}(P) = \frac{\Delta H_a(P) - \Delta H_a(1 \text{ bar})}{P - 1 \text{ bar}}. \quad (6.2)$$

Values for the activation enthalpy $\Delta H_a(T, P)$ at temperature T and pressure P can be calculated employing the results of Ita and Cohen (1997) from $\Delta H_a(T, P) = \Delta G_m(T, P) + T \cdot \Delta S_m(P)$, where $\Delta G_m(T, P)$ is the migration free energy at temperature T and pressure P and $\Delta S_m(P)$ is the migration free entropy at pressure P . Between 0 and 140 GPa at 3000 K an average migration volume of $1.35 \text{ cm}^3 \text{ mol}^{-1}$ was derived in this way for extrinsic Mg self-diffusion. Assuming a similar pressure effect on the activation volume for Fe-Mg interdiffusion leads to an average activation volume of $1.4 \text{ cm}^3 \text{ mol}^{-1}$ for calculation of diffusivities at the core mantle boundary.

The average activation volume between 0 and 140 GPa of $1.4 \text{ cm}^3 \text{ mol}^{-1}$ together with the experimentally determined value between 0 and 23 GPa of $3.3 \text{ cm}^3 \text{ mol}^{-1}$ (Section 5.4) can be used to constrain the pressure dependence of the activation volume of Fe-Mg interdiffusion in ferropericlase making a linear approximation:

$$\Delta V_a = \Delta V_a^0 + P \times \Delta V_a'. \quad (6.3)$$

The value for the zero pressure activation volume ΔV_a^0 is 0.367 J bar^{-1} and the pressure derivative $\Delta V_a'$ becomes $-1.624 \times 10^{-7} \text{ J bar}^{-2}$.

6.2.2 Silicate perovskite

Extrapolation of perovskite diffusion data to pressures in excess of 26 GPa is less well constrained than for ferropericlase because the activation volume of diffusion in silicate perovskite could not be determined by the experimental results of this study. This is due to the very restricted pressure range within the silicate perovskite stability field that can be generated by the multianvil apparatus employing sintered WC cubes. In addition, questions concerning the structural stability of this phase still remain unsolved (Section 1.3.1). Therefore, in the following sections two models of the activation volume of Fe-Mg interdiffusion in (Mg,Fe)SiO₃ perovskite are considered:

- The magnitude of the activation volume is considered to be zero. Thus, the activation energy determined at 24 GPa (404 kJ mol⁻¹, Equation 5.21 and 5.22) is valid over the entire pressure and temperature range of the lower mantle along the Ni-NiO buffer.
- The activation volume is 2.1 cm³ mol⁻¹, based on the value determined in a theoretical study of Mg self-diffusion in pure MgSiO₃ by Wright and Price (1993). In this approach it is assumed that, as for ferropericlase (see Section 6.2.1), the activation volume for diffusion of Mg in MgSiO₃ is also directly applicable to Fe-Mg interdiffusion in (Mg,Fe)SiO₃.

6.3 Fe-Mg interdiffusion along a present day geotherm

In Figure 6.1 diffusion coefficients along an adiabat for an average mantle below mid-ocean ridges (Herzberg and Zhang, 1996) are calculated below the base of the lithosphere, i.e. at pressures in excess of 3 GPa (depth > 96 km). For all minerals, results corresponding to the Ni-NiO buffer were used. The steps in temperature occurring at the phase transition boundaries are due to the heat of transformation. Depending on the mode of convection, these temperature steps would relax around the transition depth but the steps in diffusivity observed at the phase transition points would still be preserved. It should be emphasized that for olivine, above 3 GPa, the diffusivity decreases due to the effect of pressure on diffusion even though the temperature increases from ~ 1700 K to 1850 K. At 13.5 GPa the α - β phase boundary is reached. The diffusion coefficient for olivine at this pressure and a temperature of 1850 K is $D_{\text{Fe-Mg}} = (5.9 \pm 0.2) \times 10^{-16} \text{ m}^2 \text{ sec}^{-1}$ at the Ni-NiO buffer and $X_{\text{Fe}_2\text{SiO}_4} = 0.1$. This value is a factor of ~ 150 smaller than the value at 1 bar at the same temperature, composition and relative oxygen fugacity (Ni-NiO buffer). Hence, pressure effect has a large influence on the Fe-Mg interdiffusion coefficient at high pressure that was not taken into account in former studies (for example Solomatov and Stevenson, 1994).

For the high pressure polymorphs of olivine, wadsleyite and ringwoodite, the activation volume of $6.1 \text{ cm}^3 \text{ mol}^{-1}$ of Farber et al. (2000) was used in combination with Equation 5.12. It is assumed that Fe-Mg interdiffusion is equally fast in both high-pressure polymorphs of olivine (Chakraborty et al., 1999; Farber et al., 2000). As shown in Section 5.3.5 and Figure 5.22 a jump in the Fe-Mg interdiffusion coefficient by ~ 3.5 orders of magnitude occurs at the 410 km discontinuity. If the activation volume of $6.1 \text{ cm}^3 \text{ mol}^{-1}$ predicted by Farber et al. (2000) is correct, the effect of pressure on diffusion along the adiabat results in Fe-Mg interdiffusion coefficients for wadsleyite and ringwoodite which, at the 670 km discontinuity (~ 23 GPa), are relatively similar to the values derived for ferropericlase. On the contrary, Fe-Mg interdiffusion in silicate perovskite is orders of magnitude slower (approximately by a factor of 2×10^4 , see Section 5.5.5). An increase in diffusivity for silicate perovskite with increasing pressure along the adiabat shown in Figure 6.1 is observed because a possible effect of pressure ($V_a \neq 0$) was not taken into account in deriving the values for silicate perovskite shown in Figure 6.1 (compare with Equation 5.22). Depending on the oxidation state of the lower mantle, which is probably

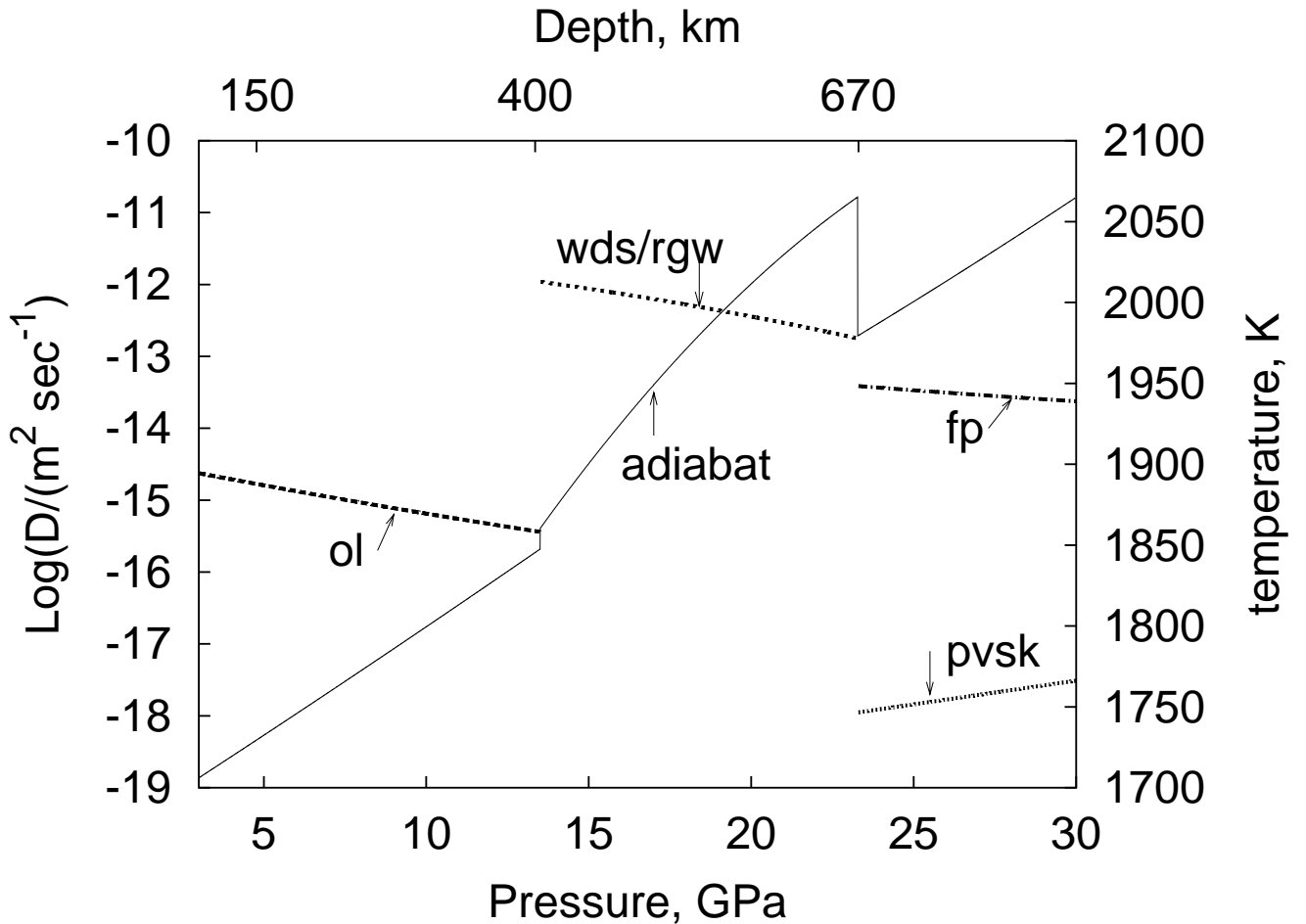


Figure 6.1: *Fe-Mg interdiffusion coefficients for different minerals in the upper mantle, the transition zone and the top of the lower mantle. All diffusion coefficients are given for an oxygen fugacity close to the Ni-NiO buffer, and an Fe component mole fraction of 0.1. The adiabat (right y axis) is from Figure 20 of Herzberg and Zhang (1996) and is representative of a present day average mantle beneath oceanic ridges. Olivine diffusion coefficients, given as $\log(D)$ on the left y axis, were calculated using Equation 5.11, and applying a correction factor of 1.6 to account for the compositional effect (see Section 5.2.3). Ringwoodite is considered to have the same diffusion properties as wadsleyite (Farber et al., 2000). In Equation 5.12 an activation volume of $6.1 \text{ cm}^3 \text{ mol}^{-1}$ (Farber et al., 2000) was used. For ferropericlase and silicate perovskite, Equations 5.14 and 5.22 were used, respectively.*

more reducing than the upper mantle (McCammon, 2002), Fe-Mg interdiffusion coefficients of ferropericlase and silicate perovskite might be 1-2 orders of magnitude smaller than the values shown here (see Equations 5.21 and 5.22).

For the lower mantle, Fe-Mg interdiffusion coefficients were calculated along a geotherm given by Anderson (1982). The geotherm was chosen because the temperature at the 670 km discontinuity is consistent with the adiabat given in Herzberg and Zhang (1996). Hence, diffusion coefficients in Figure 6.1 and 6.2 are comparable with each other. To extrapolate diffusivities

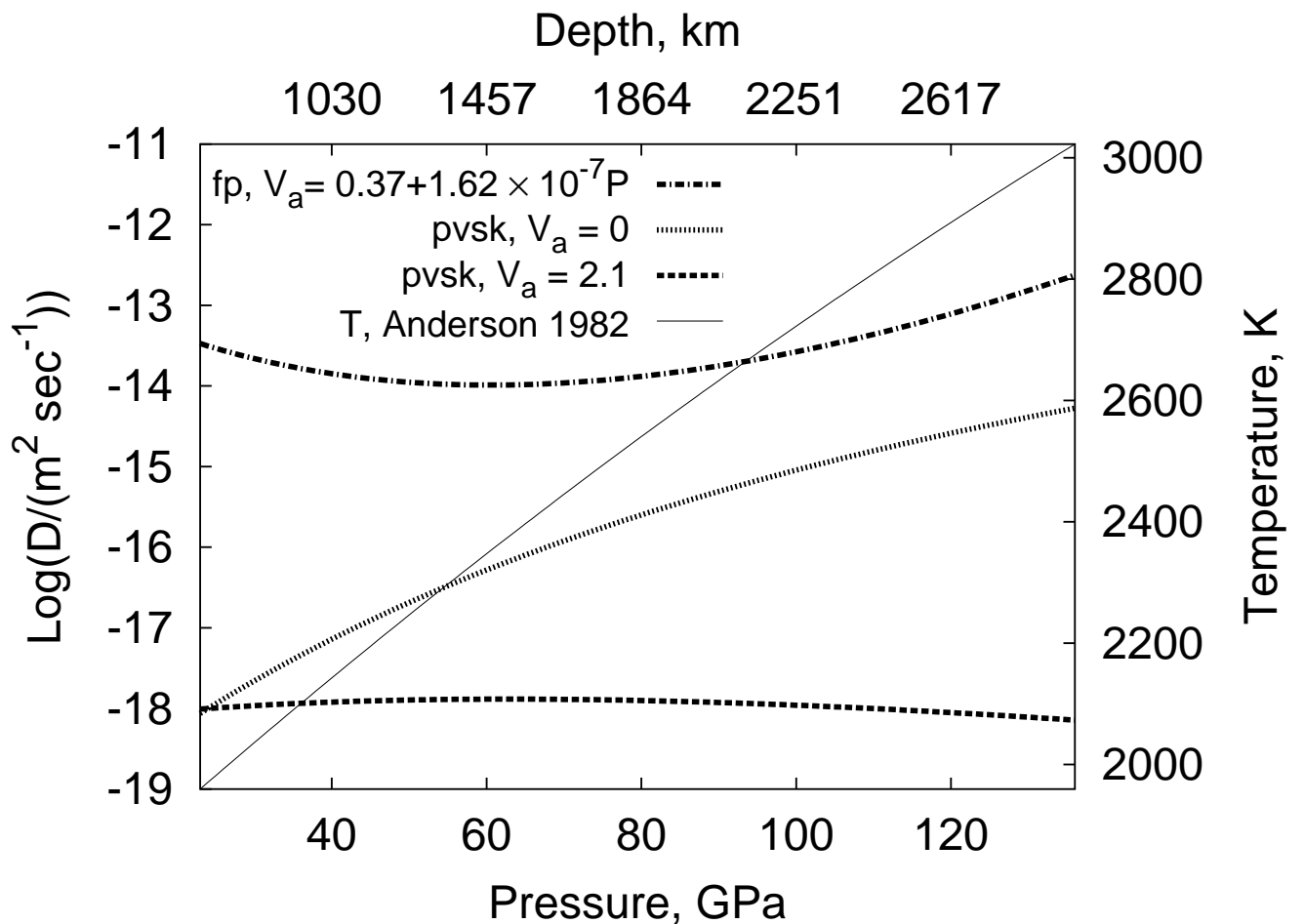


Figure 6.2: Fe-Mg interdiffusion coefficients for ferropericlase ($X_{\text{Feo}} = 0.1$) and silicate perovskite in the lower mantle. For perovskite the two models with an activation volume of $0 \text{ cm}^3 \text{ mol}^{-1}$ and $2.1 \text{ cm}^3 \text{ mol}^{-1}$ are shown, calculated using Equation 5.22. Diffusivities are given along the Ni-NiO buffer and, for perovskite, becomes a factor of ~ 15 smaller (Equations 5.22 and 5.21) at reducing conditions.

in ferropericlase, Equation 5.14 was employed together with the pressure-dependent activation

volume estimated in Equation 6.3. The calculated diffusion coefficients (Figure 6.2) show that in the upper part of the lower mantle the Fe-Mg interdiffusion coefficient would decrease slightly due to the pressure effect whereas in the lower part of the lower mantle the activation volume becomes essentially zero and diffusivities become faster due to the temperature effect. However, the Fe-Mg diffusion coefficient does not vary by more than a factor of 10. Therefore, a diffusion coefficient of $4 \times 10^{-14} \text{ m}^2 \text{ sec}^{-1}$ at $X_{\text{FeO}} = 0.1$ is a good estimate for the Fe-Mg interdiffusion coefficient of ferropericlase in the lower mantle along the Ni-NiO buffer and is almost independent of depth.

For silicate perovskite the two end-member models for the effect of pressure (Section 6.2.2) lead to a steady increase in diffusivities in the case where the activation volume $\Delta V_a = 0 \text{ cm}^3 \text{ mol}^{-1}$ (from $\sim 10^{-18} \text{ m}^2 \text{ sec}^{-1}$ at 24 GPa to $5 \times 10^{-15} \text{ m}^2 \text{ sec}^{-1}$ at 136 GPa), whereas diffusivities are essentially constant, approximately $10^{-18} \text{ m}^2 \text{ sec}^{-1}$, with $\Delta V_a = 2.1 \text{ cm}^3 \text{ mol}^{-1}$ (Wright and Price, 1993). These values are for oxygen fugacity conditions close to the Ni-NiO buffer. In the case of more reducing conditions (equivalent to f_{O_2} prevailing inside the MgO-Fe capsules) the Fe-Mg interdiffusion coefficients are a factor of 14 smaller (see Equations 5.21 and 5.22) leading to an effective diffusion coefficient of $7 \times 10^{-20} \text{ m}^2 \text{ sec}^{-1}$ in the case of $\Delta V_a = 2.1 \text{ cm}^3 \text{ mol}^{-1}$. In both models of the activation volume ($\Delta V_a = 0 \text{ cm}^3 \text{ mol}^{-1}$ or $\Delta V_a = 2.1 \text{ cm}^3 \text{ mol}^{-1}$), diffusivities in perovskite are always smaller than in ferropericlase, implying that silicate perovskite equilibration lengths are also smaller and equilibration times are longer compared to ferropericlase. Because the lower mantle is believed to be essentially a two-phase mixture of silicate perovskite and ferropericlase, the diffusional properties of a two-phase aggregate consisting of ferropericlase inclusions in a perovskite matrix is further discussed in Section 6.5.2.

6.4 Time scales of Fe-Mg partitioning experiments involving silicate perovskite

For different time scales, the characteristic diffusion length x_{diff} can be calculated by (Section 4.2):

$$x_{diff} = k \times \sqrt{Dt}, \quad (6.4)$$

where k is a proportionality factor as discussed in Section 4.2. The proportionality factor k depends on the nature of the diffusion problem and is estimated to be 6.6 in the case of two semi-infinite media (Figure 4.2) and 3.3 in the case of diffusion into a half-space.

The very small Fe-Mg interdiffusion coefficients of silicate perovskite, especially at reducing conditions, impose severe limits on the feasibility of Fe-Mg equilibrium partitioning experiments. In Frost and Langenhorst (2002), it was not possible to achieve equilibrium in experiments employing Fe-capsules. Equation 5.21 gives an equilibration distance of ~ 400 nm at 24 GPa and 1923 K for 24 hours at reducing conditions, comparable to the conditions of the experiments of Frost and Langenhorst (2002). Clearly, grains with a diameter of several microns can not fully equilibrate at such low oxygen fugacities. At more oxidizing conditions, Equation 5.22 predicts equilibration distances of 0.8-1.3 microns (for times of 8 - 20 h at 1923 K and 24 GPa), which are only slightly smaller than the grain size of 1-2 μm observed for Al_2O_3 -free perovskite by Frost and Langenhorst (2002).

It is also possible to estimate the time of reequilibration by using a solution for spherical particles (Equations 6.18, 6.19 and 6.21 in Crank, 1979). At reducing conditions (Equation 5.21) the time needed to equilibrate the center of a spherical grain with a diameter of 1 micron to 50% takes more than 10 days whereas for oxidizing conditions (Ni-NiO buffer, Equation 5.22) the same amount of equilibration is reached in 18 h and therefore within the experimental time frame. In addition, Frost and Langenhorst (2002) used Re capsules, where the oxygen fugacity is supposed to be even higher than in the Ni-NiO capsules used in this study. This is shown by the fact that one experiment of Frost and Langenhorst (2002) employing a Re- ReO_2 capsule showed exactly the same results for the partitioning data compared with the unbuffered Re capsules. In addition, the diffusion experiments performed by Yamazaki and Irifune (2003) using ferropericlase diffusion couples in Re capsules are consistent with very oxidizing conditions at pressures

of 23-26 GPa (but see the discussion in Section 5.4.7). Hence, microprobe analyses should be relatively close to the true equilibrium concentrations for experiments at oxidizing conditions. For more reducing conditions and the same pressure and temperature conditions as used by Frost and Langenhorst (2002) equilibration times should be at least on the order of a few weeks in order to result in an equilibrium distribution. Other phases like ferropericlasite or ringwoodite equilibrate within at least 2 orders of magnitude shorter times because diffusion coefficients are more than 4 orders of magnitude faster (Section 5.6).

6.5 Applications to geological problems

6.5.1 Kinetics of the olivine-wadsleyite phase boundary

As described in Rubie et al. (1993), the kinetics of the high-pressure phase transformation of olivine to wadsleyite are controlled by diffusion if nucleation occurs close to equilibrium. The growth rate should follow a parabolic rate law according to:

$$\dot{x} = \sqrt{\frac{D_{Fe-Mg}}{t}}, \quad (6.5)$$

where D_{Fe-Mg} is the Fe-Mg interdiffusion coefficient. Equation 6.5 is only valid as long as the diffusion halos of the matrix do not impinge on each other.

Figure 6.3 shows the physical model used in this study to constrain the kinetics of the phase transition in order to investigate a possible overstepping of the equilibrium phase boundaries which could lead in response to convective flow across the 410 km discontinuity to a broadening or narrowing of the transition. It is assumed that wadsleyite during convective descent and olivine during convective ascent nucleate heterogeneously on grain boundaries. Therefore, the distance over which diffusion has to occur is the grain diameter which is assumed to be 1 cm. A first estimate if the phase transition occurs close to equilibrium can be made by considering how long it takes to adapt to a new Fe-Mg equilibrium distribution along the P-T path inside the transformation boundaries by:

$$t = \frac{x^2}{k^2 \sqrt{D_{Fe-Mg}}}, \quad (6.6)$$

where k is the proportionality factor of Equation 6.4. As shown later in Section 6.5.3 the proportionality factor k is on the order of 1.6 for the equilibration of a spherical grain. Using the results obtained by Akaogi et al. (1989), the temperature across the phase transition for a mantle geotherm varies between 1695 - 1742 K at pressures between 13.3 and 14 GPa. Therefore, the time to equilibrate a grain of wadsleyite with a diameter of 1 cm is on the order of $3-5 \times 10^7$ sec depending on composition, temperature and pressure, whereas for olivine $\sim 1.5 \times 10^{11}$ sec are needed as shown in Table 6.1. Considering a convection velocity u_c of 5 cm year^{-1} , Table 6.1 shows that after convecting a distance $x = u_c t$ of 50-80 cm wadsleyite grains have already reequilibrated, whereas for olivine this characteristic distance is on the order of 240 m.

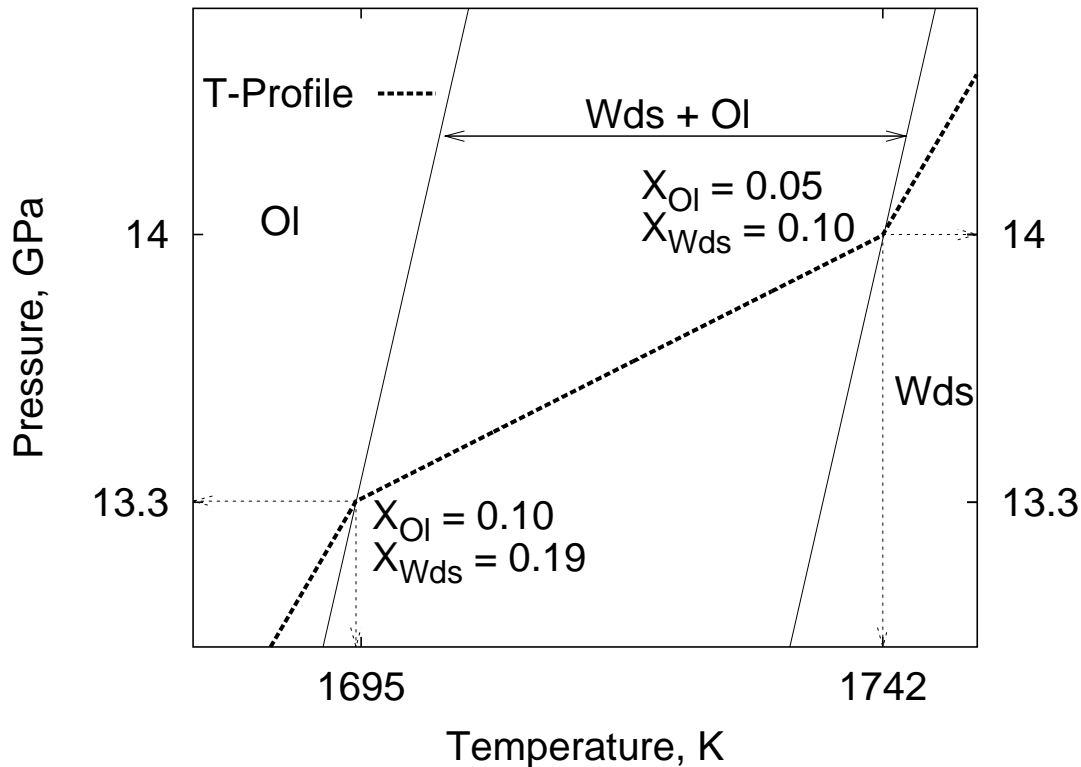


Figure 6.3: Physical model of the olivine-wadsleyite phase transition using results obtained in Akaogi et al. (1989). The dashed line is a temperature profile (T profile) in the normal mantle taken from Figure 10 in Akaogi et al. (1989) together with the phase boundaries. Also given are $X_{\text{Fe}_2\text{SiO}_4}$ of olivine and wadsleyite (X_{ol} , X_{wds}) coexisting in equilibrium at the phase boundaries. At intermediate points along the temperature profile the concentrations of wadsleyite and olivine change systemically between these values. The bulk Fe content is assumed to be $X_{\text{Fe}_2\text{SiO}_4} = 0.1$.

Clearly, the rate of diffusion in wadsleyite is always fast enough to reequilibrate to the new equilibrium concentration inside the transformation region. In order to see if the distance of 240 m, derived in Table 6.1 for olivine, can lead to a non-equilibrium distribution and hence to a metastable overstep of the phase boundaries, the evolution of concentration in wadsleyite and olivine during convection is modelled by finite difference simulations with a moving phase boundary. The moving boundary results from the difference in flux across the interface between growing wadsleyite and an olivine matrix or vice versa during progressive change of the equilibrium concentrations of coexisting olivine and wadsleyite within the transformation field leading

Table 6.1: Parameters relevant to reequilibration of the wadsleyite-olivine phase transition. Wds \rightarrow Ol corresponds to the high pressure boundary of the phase transition, and Ol \rightarrow Wds corresponds to the low-pressure boundary (Figure 6.3). D_{Fe-Mg} denotes the Fe-Mg interdiffusion coefficient at an oxygen fugacity close to the Ni-NiO buffer, t is the time of reequilibration of a spherical grain, where the proportionality factor k is 1.6 (see Section 6.5.3), r is the grain radius, assumed to be 0.5 cm, and x is the distance of convection needed to reequilibrate using a convection velocity v_c of 5 cm year $^{-1}$.

	Wds \rightarrow Ol		Ol \rightarrow Wds	
T , K	1742		1695	
P , GPa	14		13.3	
Phase	Wds	Ol	Wds	Ol
$X_{Fe_2SiO_4}$	0.1	0.05	0.19	0.10
D_{Fe-Mg} , m 2 sec $^{-1}$	1.9×10^{-13}	7×10^{-17}	3×10^{-13}	6×10^{-17}
$t = \frac{r^2}{k^2 D_{Fe-Mg}}$, sec	5.2×10^7	1.4×10^{11}	3.0×10^7	1.6×10^{11}
$x = v_c t$, m	0.08	221	0.05	258

to a consumption of either olivine or wadsleyite (Shewmon, 1989):

$$(C_{wds} - C_{ol}) \frac{dI_x}{dt} = -D_{wds} \frac{\partial C_{wds}}{\partial x} + D_{ol} \frac{\partial C_{ol}}{\partial x}, \quad (6.7)$$

where $C_{wds,ol}$ is the Fe concentration in olivine or wadsleyite, $D_{ol,wds}$ is the Fe-Mg interdiffusion coefficient, and $(dI_x)/(dt)$ is the change in position of the interface with time. In this work a one-dimensional approach was used to investigate the possible extent of a metastable persistence of olivine in the wadsleyite field or of wadsleyite in the olivine field during convection in a diffusion controlled regime. The profiles are modelled with a finite difference model where the composition dependence was not taken into account because of the limited variation of D_{Fe-Mg} with composition. In addition, as can be seen in Table 6.1, this assumption is also justified because of the concurrent change in composition and temperature along the geotherm in Figure 6.3 keeping D_{Fe-Mg} almost constant.

The width of the phase boundary is predicted to be on the order of 15 km from the phase diagram (Akaogi et al., 1989). In this case, the simulations show that for convection rates of 5 cm year $^{-1}$ and less, the composition of the coexisting olivine and wadsleyite can equilibrate by lattice diffusion even for grain sizes of 1 cm. However, the simulations also show that for rising mantle material close to the low-pressure boundary of the phase transition, where the kinetics of

olivine equilibration dominate, reequilibration becomes incomplete if temperatures are lower by more than 100 K or the convection velocity would be larger by a factor of 10. For a 100 K cooler mantle the displacement of the equilibrium phase boundary is on the order of 100 m.

6.5.2 Two-phase aggregates

In the following sections, processes occurring in the lower mantle are modelled. The lower mantle of the Earth is most likely composed of a mixture of 20 vol% ferropericlase and 80 vol% silicate perovskite (Poirier, 2000). Therefore, the diffusional properties of a two-phase aggregate have to be taken into account. There is no analytical solution of the diffusion equation (Equation 1.2), that describes the evolution of concentration in space and time during reequilibration in a multiphase aggregate. On the contrary, in the case of a steady state, effective diffusion coefficients D_{eff} , characteristic for two-phase composite materials and a variety of geometries, can be defined and are reviewed in Crank (1979). For a regular infinite series of alternating sheets A and B with diffusion coefficients D_A and D_B respectively, the series-parallel formula can be applied:

$$\frac{l_A}{D_A} + \frac{l_B}{D_B} = \frac{l_A + l_B}{D_{eff}}, \quad (6.8)$$

where $l_{A,B}$ are the thicknesses of layers A or B. As shown in Section 5.5.5, the diffusion coefficient D_{fp} of ferropericlase is approximately 20000 times larger than the diffusion coefficient D_{pvsk} of silicate perovskite. In this case, Equation 6.8 would predict an effective diffusion coefficient of $1.25 \times D_{pvsk}$ if instead of the lengths $l_{A,B}$ the volume fractions of ferropericlase and silicate perovskite of 0.2 and 0.8, respectively, in the lower mantle is used. However, the reequilibration processes considered in the next sections are not occurring at a steady state, because concentration is a function of both distance and time. Therefore, numerical simulations were performed in one and two dimensions to test if the series-parallel formula (Equation 6.8) gives reliable estimates for an effective diffusion coefficient also in the case of a non-steady state.

Reequilibration occurring in a two-phase aggregate was first simulated in one dimension using an explicit finite difference scheme similar as described in Section 4.3.2. Along the length of the simulated profile, alternating sections of perovskite and ferropericlase were assumed, separated by immobile boundaries. The initial concentration was set to a normalized concentration of zero before the equilibration event and the new equilibrium concentration is a normalized

concentration of 1. Hence, the boundary condition during equilibration is a fixed normalized concentration of 1.0 to the left of the profile:

$$C(x > 0, t = 0) = 0, C(x = 0, t) = 1.0. \quad (6.9)$$

For ferropericlase a diffusion coefficient at 2000 K and 23 GPa, conditions typical for the top of the upper mantle, of $5 \times 10^{-14} \text{ m}^2 \text{ sec}^{-1}$ was chosen. The diffusion coefficient of perovskite in the solutions was $2.5 \times 10^{-18} \text{ m}^2 \text{ sec}^{-1}$, $20000 \times$ smaller than for ferropericlase. The choice of the absolute diffusion coefficient values does not change the results of the simulation. The significant factors are the phase abundances and ratio of diffusivities.

For the simulations, a flux balance was taken into account at the position x_I of the interfaces:

$$D_A \frac{\partial C_A}{\partial x} = D_B \frac{\partial C_B}{\partial x} = F(C_I, t), \quad x = x_I, \quad (6.10)$$

where C is the normalized concentration and $F(C_I, t)$ is the diffusive flux, which has to enter medium A (either ferropericlase or silicate perovskite) at the same rate as it leaves medium B , at time t (Crank, 1979). The simulations were performed either assuming that the composition is continuous across the interface or assuming a range of distribution coefficients, resulting in a concentration discontinuity across the interface. Because the results are essentially the same with respect to the extent and distance of reequilibration, only the case of a continuous concentration profile will be discussed.

Figure 6.4 shows two selected simulated profiles. In the 1-dimensional simulations, the amount of ferropericlase was varied between $l_{fp} = 0.2$ and 0.5 , where l_{fp} is the fraction of the total length of the simulation. Equation 6.8 can then be applied with $l_A = l_{fp}$, $l_B = 1 - l_{fp}$ and $l_A + l_B = 1$. The ferropericlase grains are equally distributed along the profile and the absolute diameter was fixed at 1 mm. Consistent with the much faster diffusivity in ferropericlase, the profiles are nearly horizontal in regions where D_{fp} was used and much steeper in regions simulated with D_{pvsk} . In addition to the simulated profiles, analytical solutions with diffusion coefficients equal to D_{pvsk} , $1.25 \times D_{pvsk} = D_{eff}$ for $l_{fp} = 0.2$, $2 \times D_{pvsk} = D_{eff}$ for $l_{fp} = 0.5$, and D_{fp} are shown using Equation 6.8 for calculating D_{eff} . Figure 6.4 shows that due to the larger diffusivity of ferropericlase, the simulated profile is suppressed below the analytical solution with the corresponding D_{eff} calculated using Equation 6.8 at perovskite-ferropericlase interfaces. But, due to

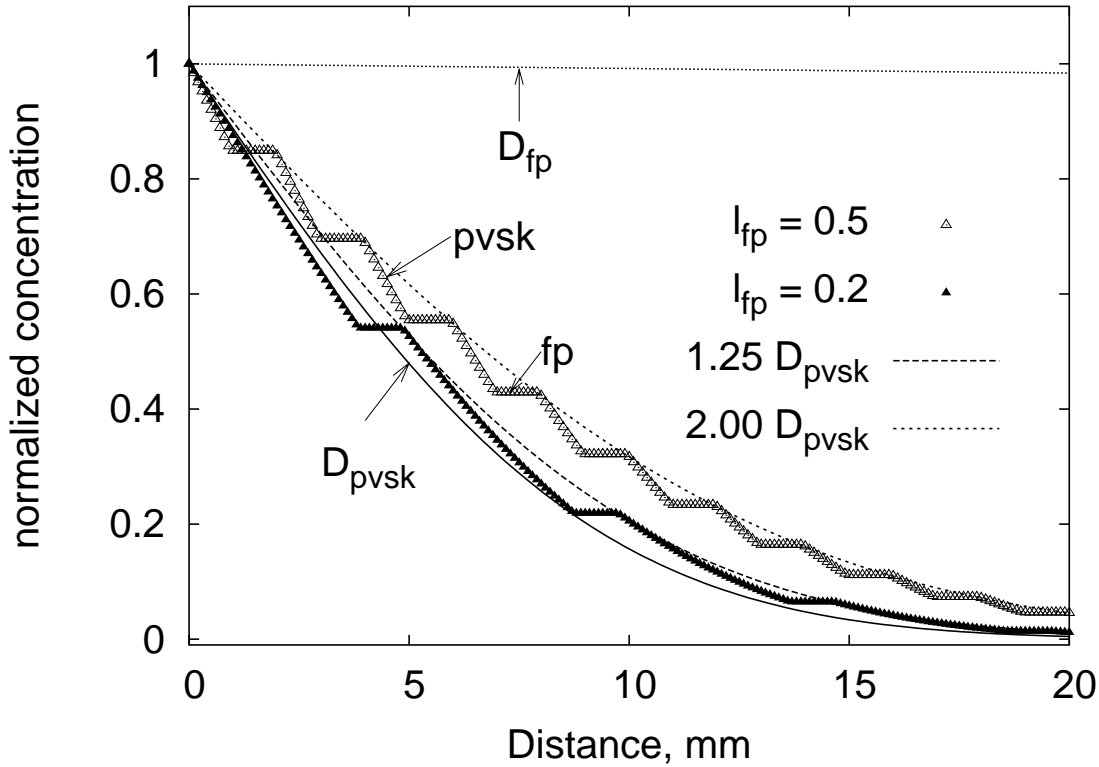


Figure 6.4: One-dimensional simulation of a two phase aggregate. In addition to the simulation, calculated profiles with the endmember diffusion coefficients D_{fp} and D_{pvsk} are shown together with profiles using effective diffusion coefficients consistent with Equation 6.8. l_{fp} is the fraction of the total length of the simulation occupied by ferropericlasite. The length of the individual ferropericlasite sections is 1 mm. A ferropericlasite section and a perovskite section are labelled *fp* and *pvsk* respectively.

the flat ferropericlasite profile, at ferropericlasite-perovskite interphases, simulated concentrations exactly match with concentrations calculated using the effective diffusion coefficients. Therefore, the series-parallel formula (Equation 6.8) for the effective diffusion coefficient is valid for the boundary conditions of the one-dimensional simulations with respect to diffusion distances. The amount of reequilibration in the 2-phase aggregate is slightly smaller due to the fact that concentrations of the simulated profile coincide with or are below the analytical solution.

The second model investigates two-dimensional diffusion in order to investigate the effect of a dispersion of individual ferropericlasite grains in a silicate perovskite matrix. The same diffusion coefficients as in the one-dimensional simulations were used. The boundary condition imposed by Equation 6.10 was applied at all perovskite-ferropericlasite interfaces. Figure 6.5

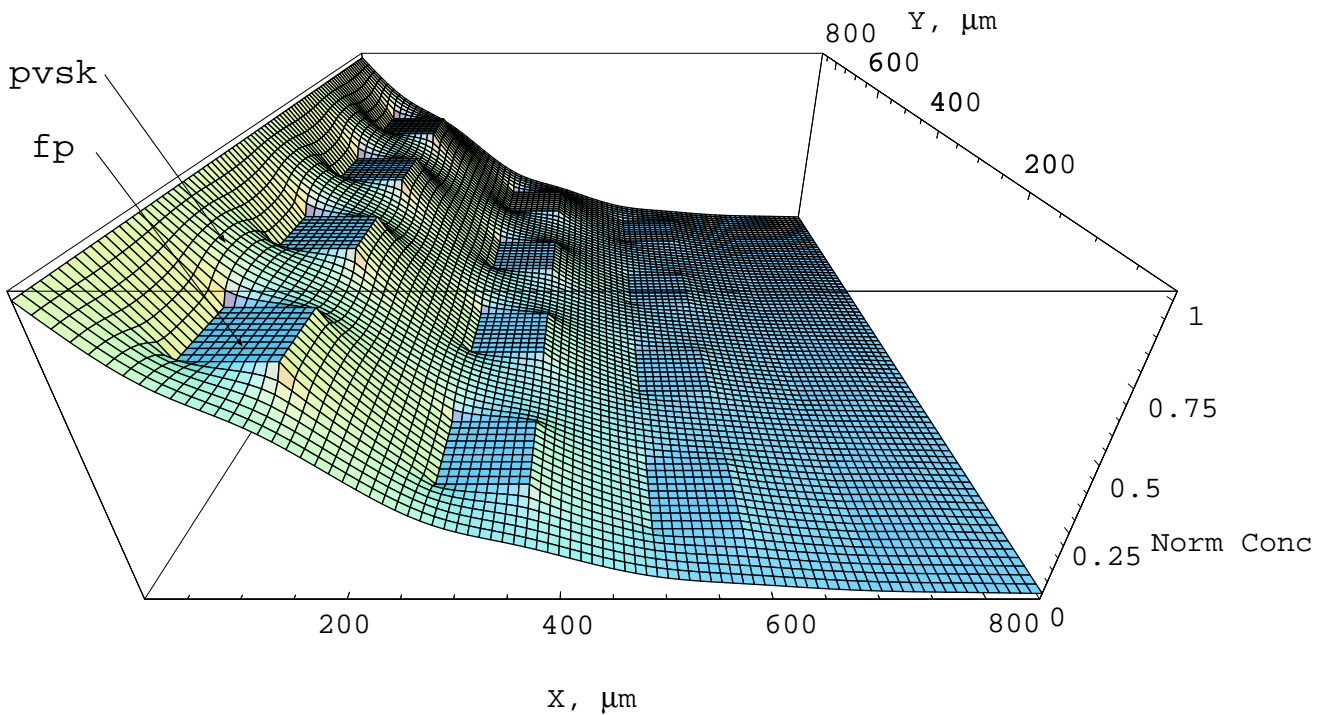


Figure 6.5: Two-dimensional simulation of diffusion in a two phase aggregate for 1×10^{10} sec. The initial normalized concentration was zero, the boundary conditions is a normalized concentration of 1 at $x = 0$, representative of a new equilibrium state. The minor phase has a square shape and a diffusion coefficient consistent with ferropericlase (fp), whereas the major phase has a diffusion coefficient consistent with silicate perovskite (pvsk). The edge length of the inclusions is 0.1 mm and the area fraction 0.2.

shows the normalized concentration after 1×10^{10} seconds (~ 317 years) of diffusion in a three-dimensional plot. The ferropericlase is assumed to form an array of square-shaped inclusions with an edge length of 0.1 mm in the perovskite matrix. The area fraction of ferropericlase is 0.2. As in the 1-dimensional case, the much larger diffusion coefficient of ferropericlase leads to an essentially flat composition distribution inside the ferropericlase grains embedded in the two-dimensional concentration profile of the silicate perovskite. Figure 6.6 shows a cross-section of Figure 6.5 along the x-direction crossing the center of the ferropericlase inclusions (profile 1) and a cross section located half-way between the inclusions (profile 2). In Figure 6.6 profiles calculated for various diffusion coefficients between $1 \times D_{pvsk}$ and $2 \times D_{pvsk}$ are superimposed on the numerically simulated profiles. In addition, the concentration profile calculated with D_{fp} is also shown. The simulated profile can be well described with an effective diffusion coefficient of

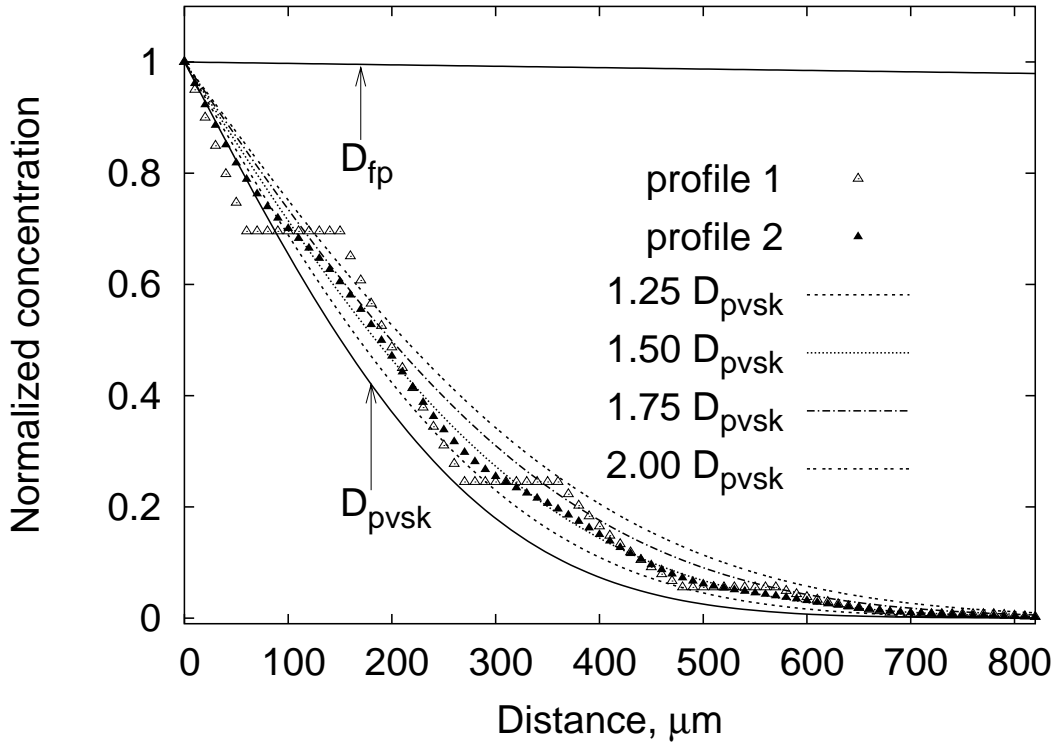


Figure 6.6: Two cross sections (profile 1 and profile 2 as discussed in the text) of the two-dimensional simulation of the two phase aggregate shown in Figure 6.5. The curves are analytical solutions of the diffusion equation for the same initial and boundary conditions as the simulation but with a constant diffusion coefficient given in the figure key.

$1.5 - 1.75 \times D_{pvsk}$. Equation 6.8 would predict an effective diffusion coefficient of $1.25 \times D_{pvsk}$ if the area fractions $A_{fp} = 0.2$ and $A_{pvsk} = 0.8$ for ferropericlase and perovskite, respectively, are used instead of l_A and l_B . This value is slightly smaller than estimated by the simulation.

Because in Equation 6.8 the thickness of alternating slabs is used, an alternative way of applying Equation 6.8 in the 2-dimensional case is to define a characteristic length of the ferropericlase inclusions instead of using the area fraction. This can be achieved by writing the area fraction as the ratio of the squares of characteristic lengths l_{fp}^c and l_{pvsk}^c :

$$A_{fp} = \frac{(l_{fp}^c)^2}{(l_{pvsk}^c)^2} = 0.2. \quad (6.11)$$

The effective diffusion coefficient, calculated using Equation 6.8 with $l_A = l_{fp}^c / l_{pvsk}^c = \sqrt{0.2}$ and $l_B = 1 - l_A$, is $1.8 \times D_{pvsk}$, only slightly larger than the value of $1.5 - 1.75 \times D_{pvsk}$ determined us-

ing the numerical simulations. This suggests, that in the 3-dimensional case, the ratio of lengths l_{fp}^* and l_{pvsk}^* derived by:

$$V_{fp} = 0.2 = \frac{(l_{fp}^*)^3}{(l_{pvsk}^*)^3}, \quad (6.12)$$

where $V_{fp} = 0.2$ is the volume fraction of ferropericlasite in the lower mantle (Poirier, 2000), should be a good estimate for characteristic length scales to use in Equation 6.8 to calculate the effective diffusion coefficient of the lower mantle with $l_A = l_{fp}^*/l_{pvsk}^* = \sqrt[3]{0.2}$, $l_B = 1 - l_A$ and $l_A + l_B = 1$.

From the results of the one-dimensional and two-dimensional simulations just described, it can be concluded that for a non-steady diffusional problem the average diffusion coefficient of a two-phase aggregate can be well described by the series-parallel formula, Equation 6.8, using appropriate values for l_A and l_B . For the three-dimensional case an effective diffusion coefficient of $2.4 \times D_{pvsk}$ is estimated using effective length scales defined by Equation 6.12. Therefore, the simulations presented in this section show that in the case of a dispersion of a minor phase in a matrix with a much smaller diffusion coefficient, the effective diffusion coefficient is very close to the diffusion coefficient of the matrix. Hence, diffusional reequilibration depending on Fe-Mg exchange in the lower mantle is almost completely governed by the rate of diffusion in silicate perovskite.

6.5.3 Reequilibration in the lower mantle

In this section, the time of persistence of a chemical heterogeneity in the lower mantle is discussed. A spherical geometry for the heterogeneity is assumed. For the solution of the diffusion equation (Equation 1.2), the boundary condition is a constant normalized concentration of 1 at the surface of the sphere, representing a new equilibrium concentration. The initial condition is a normalized concentration $C_i = 0$ throughout the sphere. The appropriate solution for the concentration at the centre of the sphere is given in Equation 6.19 of Crank (1979):

$$C = 1 + 2 \sum_{n=1}^{\infty} (-1)^n \exp\left(\frac{-D_{lm} n^2 \pi^2 t}{r^2}\right), \quad (6.13)$$

where C is normalized concentration, r is the radius of the sphere, and D_{lm} is the effective diffusion coefficient of the lower mantle. D_{lm} is estimated by the effective diffusion coefficient of a 2-phase aggregate of $2.4 \times D_{pvsk}$ (Section 6.5.2). As shown in Section 6.3, D_{pvsk} is essentially constant in the lower mantle ($7 \times 10^{-20} \text{ m}^2 \text{ sec}^{-1}$ for reducing conditions and $1 \times 10^{-18} \text{ m}^2 \text{ sec}^{-1}$ for more oxidizing conditions close to the Ni-NiO buffer) if the activation volume is assumed to be $2.1 \text{ cm}^3 \text{ mol}^{-1}$ (Wright and Price, 1989). Therefore D_{lm} lies in the range $(0.2 - 2.4) \times 10^{-18} \text{ m}^2 \text{ sec}^{-1}$ depending on the oxygen fugacity.

In Figure 6.7 the equilibration time of a heterogeneity with a certain diameter d is shown in a log-log plot. The equilibration time $t_{0.95}$ is defined as the time needed to equilibrate the grain to such an extent that the normalized concentration at the center is 0.95. As can be seen in Figure 6.7, $\log(t_{0.95}) \propto 2 \log(d)$, indicating that Equation 6.4 is valid for the definition of $t_{0.95}$ and a proportionality factor of $k = 1.6$ is determined from a fit of the results of the calculations employing Equation 6.13 for the Equation $r = k \times \sqrt{D t_{0.95}}$, where $r = 0.5 d$ is the radius of the heterogeneity.

Figure 6.7 shows that on experimental timescales of 1 day, equilibrium can only be achieved at conditions of the lower mantle on the submicron scale for reducing conditions and only a few microns for oxidizing conditions (see also Section 6.4). Grains with a diameter of 0.1 - 1 mm, which is the grain size expected for the lower mantle (Solomatov et al., 2002), equilibrate on timescales of 10-1000 years (oxidizing conditions) or 100-10000 years (reducing conditions), equivalent to a human lifetime or longer. During a timescale of the maximum duration of core

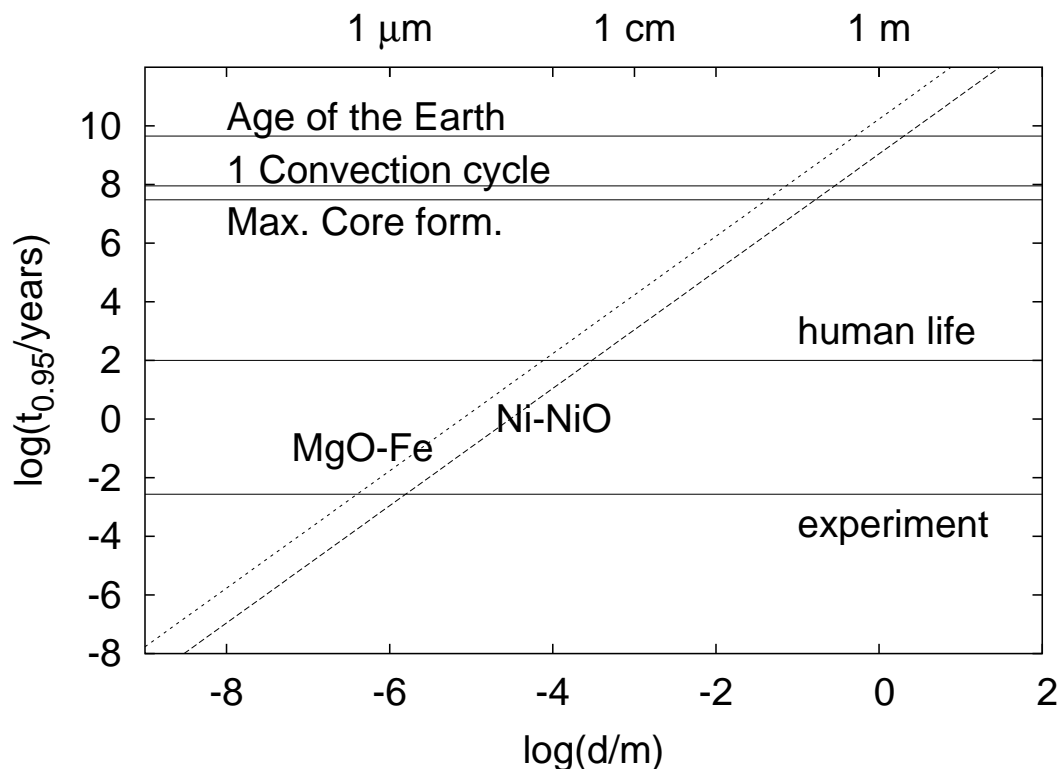


Figure 6.7: Equilibration times $t_{0.95}$ (defined in the text) as a function of the size of a chemical heterogeneity using the effective Fe-Mg interdiffusion coefficient of the lower mantle for reducing (corresponding to the fO_2 of the MgO-Fe capsule) and oxidizing conditions (corresponding to the fO_2 of the Ni-NiO capsules). The heterogeneity is assumed to have the form of a sphere with diameter d . Also shown are experimental timescales (experiment), the average human lifetime (human life), the maximum duration of core formation (Max. Core form.), the time for one convection cycle in the lower mantle (1 Convection cycle, $u_c = 5 \text{ cm year}^{-1}$), and the age of the Earth.

formation, assumed to be $\sim 30 \times 10^6$ years (Kleine et al., 2002), the size of a heterogeneity completely reequilibrating would be 4 - 17 cm, depending on the oxygen fugacity.

For one convection cycle with a convection velocity of 5 cm year^{-1} , chemical heterogeneities with diameters of only 7-30 cm would equilibrate. Hence, if one considers the thickness of the oceanic crust of $\sim 5 \text{ km}$, the diffusion distance of 30 cm shows that even complete subduction down to the core-mantle boundary and subsequent ascent in a rising plume could not eradicate the chemical difference between the basaltic composition and the surrounding mantle by lattice

diffusion in the lower mantle. Because of the larger ionic radius and/or higher valence states of radiogenic elements like Sr, Nd, Os or Re, these elements might have even smaller diffusion coefficients than the Fe-Mg interdiffusion coefficient and, hence, isotopic signatures of oceanic crust and continental sediments will essentially be unaltered by diffusion during convective recycling in the lower mantle. More critical might be the interaction in the upper mantle where diffusion properties are governed by olivine and its high-pressure polymorphs. The time to reach the 670 km discontinuity with a subduction rate of 5 cm year^{-1} is 1.3×10^7 years. Even if the effective diffusion coefficient of the subducting slab would be $1 \times 10^{-12} \text{ m}^2 \text{ sec}^{-1}$, corresponding to wadsleyite (Figure 6.1), the maximum exchange distance would be on the order of 70 m. Hence, considering that wadsleyite and ringwoodite are only stable in the transition zone and that olivine might metastably survive in cold subduction zones, interaction in the upper mantle by pure lattice diffusion also does not change significantly chemical heterogeneities during convection.

Over the entire history of the Earth (4.5×10^9 years), the diameter of heterogeneities that would reequilibrate by lattice diffusion is 50 cm for reducing conditions and up to 2 m for more oxidizing conditions. Clearly, heterogeneities larger than a few meters can survive several cycles of convection in the lower mantle if the only exchange process is lattice diffusion. Extreme strain rates would be required to stretch and subsequently thin heterogeneities to such an extent that reequilibration would be possible. In two recent review papers (Van Keken et al., 2002, 2003) numerical simulations are reported showing that convective mixing is vigorous enough to mix large-scale heterogeneities. This conclusion is in contradiction to geochemical observations (e.g. Hofmann, 1997). If one considers that even for extremely large strains the ultimate reequilibration most likely would occur by diffusion, the very short reequilibration lengths obtained using the Fe-Mg interdiffusion coefficients of this study provide an explanation for the existence of chemical heterogeneities.

For calculating the values given in this chapter a constant effective diffusion coefficient was used (see above), which is only valid if the activation volume of diffusion is $\sim 2 \text{ cm}^3 \text{ mol}^{-1}$ as calculated by Wright and Price (1989). As shown in Figure 6.2 the Fe-Mg interdiffusion coefficient of silicate perovskite would be increased approximately by a factor of 3000 in the lower mantle if the activation volume is essentially zero. Therefore, the maximum increase of the in-

teraction distances is a factor of $\sqrt{3000} \approx 55$. This maximum increase of diffusivity shows that the main conclusions of this section would be unaltered because the maximum size of a heterogeneity that can be reequilibrated over the entire history of the Earth would still be on the order of only 100 m. Of course, grain boundary diffusion may have some additional effect to the diffusion flux but this effect is difficult to estimate and most likely does not change the conclusions. Only in a thermal boundary layer at the core-mantle boundary are larger equilibration distances possible, as shown in the next section.

6.5.4 Interaction at the core-mantle boundary

Possible diffusive interaction at the core-mantle boundary is estimated using the effective diffusion coefficient for a two phase aggregate $D_{eff} = 2.4 \times D_{pvsk}$ where D_{pvsk} is the Fe-Mg interdiffusion coefficient of silicate perovskite (Section 6.5.2). These calculations can be applied to model reequilibration between the core and mantle for elements with diffusion coefficients close to the Fe-Mg interdiffusion coefficient such as Fe, Ni or Co. A possible physical process of reequilibration follows the formation of an FeO layer at the core-mantle boundary with subsequent divalent cation exchange similar to the experimental setup in the experiments of Rubie et al. (2000). The interaction length x_{diff} is then given by $x_{diff} = 3.3 \sqrt{D_{eff} t_e}$ (Equation 6.4), where t_e is the age of the Earth.

The pressure at the core-mantle boundary is approximately 136 GPa (Dziewonski and Anderson, 1981) but the temperature is poorly constrained. A value of 3000 K on the mantle side of the thermal boundary layer is derived from a mantle adiabat whereas for a core adiabat the temperature at the core-mantle boundary might be as high as 5000 K (Williams, 1998). Most of the parameters used in these estimates are highly uncertain, but according to Williams (1998) a temperature contrast of 1000-2000 K across D'' is likely. For the estimation of diffusion coefficients at the core-mantle boundary, 3000 K and 5000 K are adapted as limiting cases. According to Boehler (1996) the melting temperature of ferropericlase at 136 GPa is also ~ 5000 K. For silicate perovskite, several authors report melting temperatures in excess of 4000 K at around 60 GPa for Fe-free and Fe-bearing perovskite but no study has been performed at pressures corresponding to the core mantle boundary (see review in Shen and Heinz, 1998). A theoretical study of Wang (1999) predict a melting temperature of ~ 5000 K for $MgSiO_3$ perovskite at the core-mantle boundary. The oxygen fugacity relative to the iron-wüstite buffer at the core-mantle boundary ($\Delta_{fO_2} \sim -2$, Equation 5.20) should be close to the redox conditions of the experiments employing MgO-Fe capsules (Section 5.5.2). Hence, Equation 5.21 was used for estimating the Fe-Mg interdiffusion coefficient at the core mantle boundary.

In Table 6.2, the length of diffusive interaction x_{diff} is calculated as outlined above. The values of x_{diff} are on the order of 0.3 to 858 meters, depending on the activation volume and the temperature. This interaction distance leads to the conclusion that, based on Fe-Mg interdiffusion

Table 6.2: Diffusive interaction at the core-mantle boundary. T_{CB} is the temperature at the core-mantle boundary, ΔV_a is the activation volume, considered to be zero or $2.1 \text{ cm}^3 \text{ mol}^{-1}$ as discussed in Section 6.2.2, D_{eff} is the effective diffusion coefficient calculated using the Fe-Mg interdiffusion coefficient of perovskite (Equation 5.21) by $D_{eff} = 2.4 \times D_{pvsk}$ (see Section 6.5.2), and x_{diff} is the interaction length calculated by $x_{diff} = 3.3 \sqrt{D_{eff} t_E}$, where t_E is the age of the Earth.

T_{CB}, K	$\Delta V_a, \text{cm}^3 \text{ mol}^{-1}$	$D_{eff}, \text{m}^2 \text{ sec}^{-1}$	x_{diff}, m
3000	2.1	$6 \cdot 10^{-20}$	0.3
3000	0	$7 \cdot 10^{-16}$	34
5000	2.1	$2 \cdot 10^{-15}$	51
5000	0	$5 \cdot 10^{-13}$	858

coefficients, a significant interaction at the core mantle boundary over the entire history of the Earth cannot have occurred (see Section 6.2.1). In two recent papers, the diffusive interaction at the core mantle boundary was estimated based on diffusion coefficients for periclase (Van Orman et al., 2003) and ferropericlase (Holzapfel et al., 2003). Van Orman et al. (2003) calculated an effective diffusion coefficient based on the upper Hashin-Shtrikman bound (Hashin and Shtrikman, 1962), originally used to determine the effective magnetic permeability of multiphase materials. The Hashin-Shtrikman bounds are also widely used to calculate elastic properties of polycrystalline materials. The upper Hashin-Shtrikman bound as calculated by Van Orman et al. (2003) gives a diffusivity dominated by ferropericlase. This would correspond to a completely interconnected network of ferropericlase on perovskite grainboundaries. In this work this is assumed to be unrealistic given the fact that in samples synthesized at high pressure, microstructures always show isolated inclusions of ferropericlase in a perovskite matrix (see Figure 5.32). Van Orman et al. (2003) did not use the lower bound because of the lack of perovskite diffusion data. These become available in this study and the lower Hashin-Shtrikman bound for a volume fraction of ferropericlase of 0.2 gives an effective diffusion coefficient $D_{eff} = 1.7 \times D_{pvsk}$, very close to the effective diffusion coefficient of $D_{eff} = 2.4 \times D_{pvsk}$ derived in Section 6.5.2.

The interaction length deduced by Van Orman et al. (2003) for an effective diffusion coefficient employing the upper Hashin-Shtrikman bound is 0.7-2.8 km at 140 GPa, 4500 K. The values listed in Table 6.2 are much smaller even though temperatures up to 5000 K were used in

addition to a larger proportionality factor k in Equation 6.4. Only when an activation volume of $0 \text{ cm}^3 \text{ mol}^{-1}$ is used, does the interaction distance at 5000 K become comparable to the values of Van Orman et al. (2003). This is because, as shown in Figure 6.2, the diffusion coefficient of perovskite would then be smaller by a factor of only ~ 10 compared to ferropericlase. The interaction distances using data for ferropericlase are on the order of 0.4 - 15 km for compositions of $X_{\text{FeO}} = 0.1-0.2$ and temperatures between 3000 and 5000 K at an oxygen fugacity close to Ni-NiO buffer (Holzapfel et al., 2003).

Thus, it can be concluded that diffusive interaction at the core-mantle boundary is dominated by diffusion in silicate perovskite leading to interaction distances well below 1 km, hence, a significant chemical interaction between the mantle and the core based on Fe-Mg interdiffusion coefficients can be excluded.

6.5.5 Interaction during core formation

During early Earth's history, the separation of a metallic phase from silicates/oxides occurred which ultimately lead to the formation of the Earth's core. Different modes of separation and the physical processes involved are discussed by Stevenson (1990) and Rushmer et al. (2000).

Current models of core formation postulate equilibration between liquid silicate and liquid Fe-alloy in a magma ocean with a depth of 700-1400 km. This is based on the observation that partition coefficients at these conditions, for siderophile elements such as Ni and Co, achieve values that can explain their abundance in the mantle and the core (Thibault and Walter, 1995; Li and Agee, 1996; Righter et al., 1997; Gessmann and Rubie, 2000; Li and Agee, 2001; Righter, 2003). The kinetics of equilibration of metal and silicate liquid in the magma ocean were discussed recently by Rubie et al. (2003).

Subsequently, after equilibration in the magma ocean, the liquid metal has to descend through the solid lower mantle to form the core. It is still an open question whether this descent occurs in the form of large diapirs or by percolation along grain boundaries due to grain boundary wetting. The dihedral angle of core melts in lower mantle phases is approximately 71° , considerably smaller than for upper mantle phases (Shannon and Agee, 1998). Although this value is still larger than the critical angle of 60° , compositional effects or higher pressures might lower it below the percolation threshold. The two different modes of separation are shown schematically in Figure 6.8.

Because the partition coefficients of siderophile elements are a function of pressure, temperature and oxygen fugacity, their equilibrium distribution will be different in the lower mantle compared to the magma ocean. Hence, elements like Ni or Co will tend to be redistributed in the lower mantle by exchange with Fe. Fe-Mg interdiffusion coefficients can be used as a proxy for divalent cations such as Ni and Co as shown for the olivine system in Section 5.2. Also the length of interaction of NiO with ferropicrinite evident in Figure 5.23 indicates that the diffusion coefficient of Ni is similar to that for Fe-Mg interdiffusion. A similar conclusion was reached in the study of Rubie et al. (2000) in which the kinetics of equilibration between liquid metal (initially oversaturated in oxygen) and MgO single crystal capsules was investigated.

The length scales over which reequilibration has to occur are completely different in the two

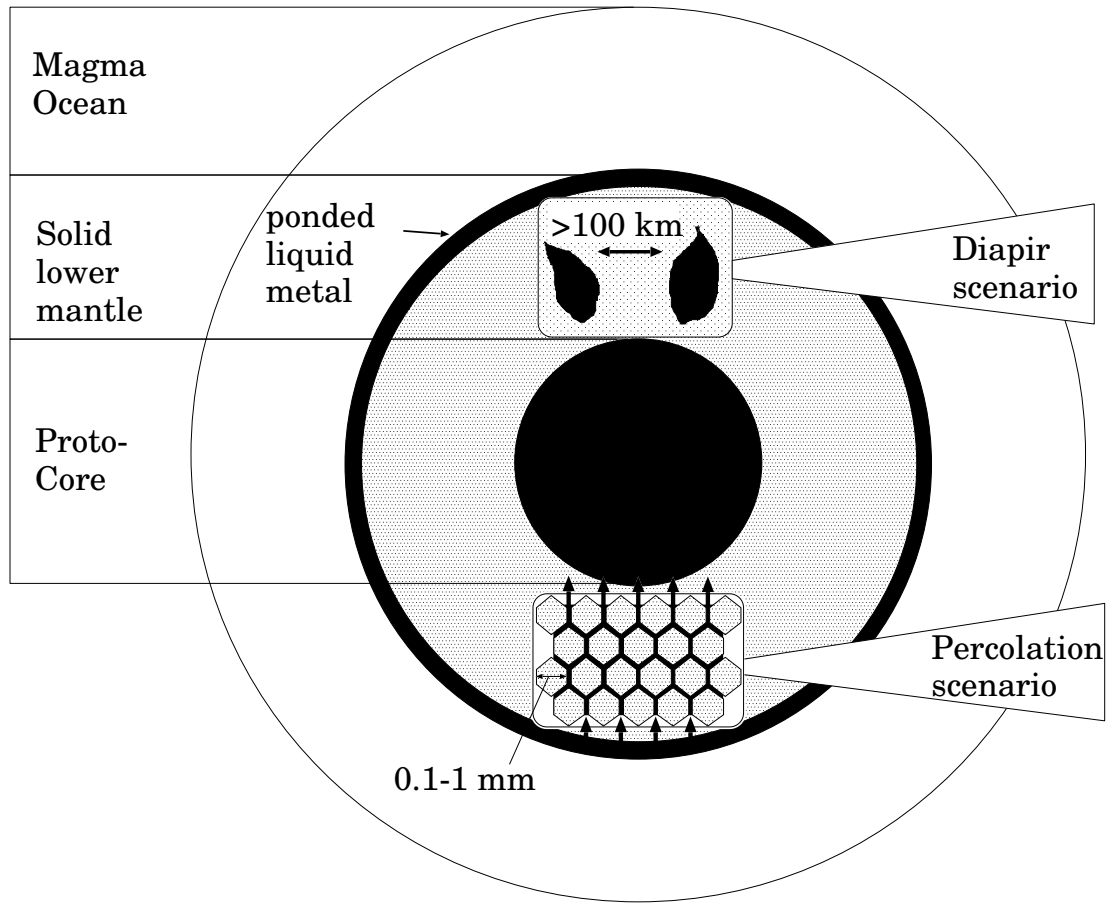


Figure 6.8: Current models of core formation postulate an equilibrium partitioning of siderophile elements at high pressure in a magma ocean. Subsequently, liquid metal sinks through the solid lower mantle to form the core either by large diapirs or by percolation due to grain boundary wetting.

core forming scenarios shown in Figure 6.8. In the percolation process, the grain size of 0.1-1 mm, estimated by Solomatov et al. (2002), is the dimension over which reequilibration has to occur, whereas for a diapir model the characteristic length scale depends on the distance X_d between individual diapirs. It is difficult to quantify X_d rigorously but according to a conservative estimate it should be much larger than several kilometers. In the latter case, even on the timescale of Earth's history and temperatures as high as 5000 K a significant reequilibration of more than 1 km cannot occur using a two-phase model (Table 6.2). For $\sim 30 \times 10^6$ years, which is the longest possible duration of core formation based on isotope constraints (Kleine et al., 2002), equilibration distances in the lower mantle are < 1 m (Section 6.5.3). Thus, in a diapir scenario

the composition of the lower mantle would not change significantly during final core formation.

The situation is much different in a percolation scenario. Even for relatively low temperatures corresponding to a present day adiabat, 0.1 to 1 mm of equilibration can be realized on timescales of less than 100000 years (Figure 6.7) using a two-phase model of the lower mantle (Section 6.5.3). This is further illustrated in Figure 6.9. In the case of percolation, it is also

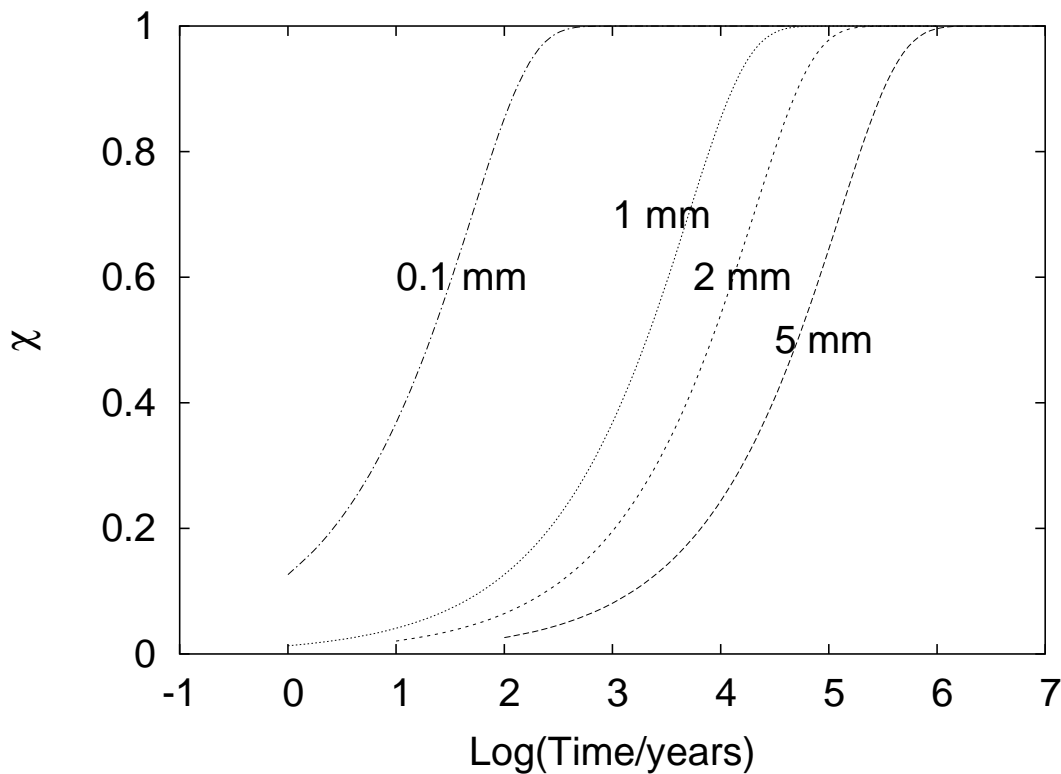


Figure 6.9: Amount of reequilibration χ (Equation 6.15) calculated using an effective diffusion coefficient for a two-phase aggregate composed of ferropericlase and silicate perovskite in a percolation scenario as a function of time and grainsizes between 0.1 and 5 mm. See text for further details.

possible to calculate the amount of reequilibration for silicate perovskite grains and ferropericlase grains individually (because every grain is in contact with the metallic liquid) and then average the results according to the phase abundance (20 vol% of ferropericlase and 80 vol% of silicate perovskite, Poirier, 2000). In order to derive the reequilibration curves in Figure 6.9, the distribution $C(r)$ of a siderophile element in spherical grains of radius r_g employing Fe-Mg interdiffusion coefficients as outlined in Section 6.2 and an analytical solution of Equation 1.2 was

calculated (Equation 6.21 in Crank, 1979). For silicate perovskite only the model with an activation volume of $2.1 \text{ cm}^3 \text{ mol}^{-1}$ was taken into account because in the case of $\Delta V_a = 0 \text{ cm}^3 \text{ mol}^{-1}$ reequilibration would be even faster. The surface concentration of an individual grain was fixed to a normalized concentration of 1 (taken to be the equilibrium value in contact with metallic liquid), implicitly assuming that during reequilibration, the concentration of the metallic liquid is not changed significantly and the bulk of the grain was initially at a normalized concentration of zero. The first assumption is justified because of the siderophile nature of Ni and Co and a corresponding much higher concentration of these elements in the metallic liquid. To calculate the amount of reequilibration, the average concentration of a grain with radius r_g at a certain depth in the Earth is determined by:

$$\xi = \frac{1}{\frac{4}{3}\pi r_g^3} \int_0^{r_g} C(r) 4\pi r^2 dr. \quad (6.14)$$

Subsequently Equation 6.14 is integrated over the whole depth range of the lower mantle between 670 to 2900 km, to calculate the overall amount of reequilibration:

$$\chi = \frac{1}{V_{lm}} \int_{x=670}^{2900} \xi(d) 4\pi d^2 dx, \quad (6.15)$$

where V_{lm} is the volume of the lower mantle between depth x of 670 and 2900 km.

The lower integration limit in Equation 6.15 corresponds to the depth of former equilibration in the magma ocean. The results are not very sensitive with respect to this depth because, due to the pressure effect of diffusion, the diffusion coefficients and therefore the amount of reequilibration effectively do not change with depth (see Figure 6.2). Figure 6.9 shows that, if metal separation occurred by percolation, the equilibration signature in a magma ocean would be completely destroyed within timescales much smaller than 100000 years and the present day distribution of at least Ni and Co between the mantle and the core would correspond to a depth integrated signature and not a single equilibration event in a magma ocean. However, partitioning in the lower mantle for Ni and Co may not be much different from in a magma ocean (Gessmann and Rubie, 2000). On the other hand, this is unlikely to be the case for all other siderophile elements.

It should be emphasized that the reequilibration times calculated by Equation 6.15 and shown in Figure 6.9 are maximum values with respect to temperature because a present day geotherm (Anderson, 1982) was employed due to the high uncertainties of estimates of temperatures in the early Earth. Temperatures might be significantly higher, for example on the order of 6000 K at the bottom of a magma ocean, as pointed out by Karato and Murthy (1997). Diffusion would have been much faster at these higher temperatures.

Chapter 7

Conclusions

In this work, multianvil experiments have been performed in order to study Fe-Mg interdiffusion at high pressures in minerals relevant for the Earth's interior. Single crystal and polycrystalline diffusion couples were employed. It has been shown that the experimental technique employing the multianvil apparatus is capable of producing diffusion data with a high accuracy due to temperature stability and low temperature gradients across the diffusion couples. Minerals investigated are olivine, wadsleyite, ferropericlase and (Mg,Fe)SiO₃ perovskite. The conditions of the experiments span a wide range of pressures between 6 and 26 GPa, temperatures between 1623 K and 2273 K at oxygen fugacity conditions close to the Ni-NiO buffer and, in the case of silicate perovskite, at reducing conditions approximately 2 log-units below the Fe-wüstite buffer. The duration of the experiments ranged from 5 min to 72 hours resulting in profile lengths between 150 nm and 200 μm . The longest profiles were observed in diffusion couples consisting of wadsleyite and ferropericlase, whereas the shortest profiles were found in experiments employing silicate perovskite. Whereas profiles in olivine are just long enough to be measured by electron microprobe analysis, profiles for silicate perovskite ($< 1 \mu\text{m}$) could only be measured by analytical transmission electron microscopy employing an energy dispersive X-ray detector (EDX-STEM). The combination of high pressure diffusion experiments with the analytical technique of EDX-STEM opens new perspectives of understanding diffusional properties of Earth materials. Because of the much smaller Fe-Mg interdiffusion coefficients found in silicate perovskite, which is assumed to be the major phase of the lower mantle, kinetic processes controlled by Fe-Mg exchange occur on much longer timescales in the lower mantle compared to the upper mantle. Interaction between subducting slabs and the surrounding mantle by bulk diffusion

is too slow to produce large scale homogenization even on timescales of convection overturn. Significant chemical interaction at the core-mantle boundary during Earth's history can be excluded based on Fe-Mg interdiffusion coefficients. Current models of core formation involving equilibration of metal and silicate in a magma ocean seem to predict abundances of siderophile elements correctly if subsequent descent of the metal through the solid lower mantle occurred by large diapirs. In the case of percolation by grain boundary wetting extensive reequilibration would be observed unless the distribution of siderophile elements between liquid metal and solid ferropericlase and silicate perovskite is pressure-independent in the lower mantle.

Appendix A

Multianvil Technique

The multianvil technique employs a two-stage compression mechanism (Figure 2.1) for reducing the area A at nominally constant force F to increase pressure P according to:

$$P = \frac{F}{A} \quad (\text{A.1})$$

Due to friction loss and the complicated geometry, as compared to opposing anvil designs, a direct calculation of pressure is impossible. Thus, an experimental pressure calibration has to be performed (Section 2.5), employing phase transitions of standard phases.

The main components of a multianvil system are (Figure 2.1):

- Hydraulic press generating a uniaxial force.
- first stage steel anvil system (cut from a sphere or cylinder) forming a cubic gap
- second stage WC cubes with truncated corners forming an octahedral pressure chamber (Figure A.1)
- Octahedral pressure medium containing the sample.

In this study different hydraulic presses were used depending on the pressure of the experiment. The different presses, their design and the pressure ranges investigated in this study are listed in Table A.1.

In all cases sintered WC cubes (with a Co sinter additive) were used as second stage anvils obtained from Toshiba tungaloy CO. LTD. (Japan) and WidiaValenite, Metalcutting Tools & Fluids (Germany). They are isolated from the first stage steel anvils by epoxy sheets (Figure

Table A.1: Presses installed at the Bayerisches Geoinstitut. The axial force is given in meganewton. The multianvil designs (MA-design) are: Walker-type apparatus (Walker, Walker et al., 1990), split-sphere Kawai-type (split-sp, Kawai and Endo, 1970; Kawai et al., 1973), and split-cylinder (split-cy, Ohtani et al., 1987). P denotes the pressure range that was studied in a specific press employing diffusion couples of minerals given in the last column (ol = olivine, fp = ferropericlasite, wds = wadsleyite, pvsk = silicate perovskite).

manufacturer	force, MN	MA-design	P, GPa	mineral
Voggenreiter	5	Walker	6-12	ol
Hymag	10	split-cy	8-26	fp, wds, pvsk
Sumitomo	12	split-sp	26	pvsk
Zwick	50	split-cy	22	pvsk

2.1). Only the two cubes that touch the upper and lower Mo discs of the assembly are brought into contact with the steel anvil by means of a copper foil (Figure 2.1).

Figure A.2 shows schematically a 10/4 assembly. Details of all assemblies are shown in Figure 2.2 and Figures 2.7-2.9. A copper coil protects the thermocouple in the gasket region (Figure A.1). The thermocouple EMF is converted to temperature with a Eurotherm controller.

In multianvil experiments the temperature effect on the electromotive force of the thermocouple is usually neglected due to a lack of a correction method. The electromotive force (*EMF*) of a thermocouple at high pressure *P* and temperature *T* can be expressed as (Spain and Paauwe, 1977b; Walter et al., 1995):

$$EMF = \int_{T_{ref}}^{T_{og}} S_r(T, 1 \text{ bar}) \frac{dT}{dx} dx + \int_{1 \text{ bar}}^{P_{exp}} \int_{T_{og}}^{T_{ig}} S_r(P, T) \frac{dT}{dx} dx \frac{dP}{dx} dx + \int_{T_{ig}}^{T_{exp}} S_r(T, P_{exp}) \frac{dT}{dx} dx \quad (A.2)$$

where T_{ref} is the reference temperature of the cold junction, x is the position along the circuit, T_{og} is the temperature outside the gasket, T_{ig} is the temperature on the high temperature side of the gasket, P_{exp} and T_{exp} are experimental pressure and temperature implicitly assuming that there are no pressure gradients inside the assembly and S_r is the relative Seebeck coefficient. Equation A.2 shows that the *EMF* is not developed at the thermocouple junction but along the individual wires where $dT/dx \neq 0$ and $dP/dx \neq 0$. Therefore, any correction depends not only on the type of thermocouple used but also on the temperature and pressure gradients across the gasket and the temperature gradient in the assembly and therefore on the experimental configuration and

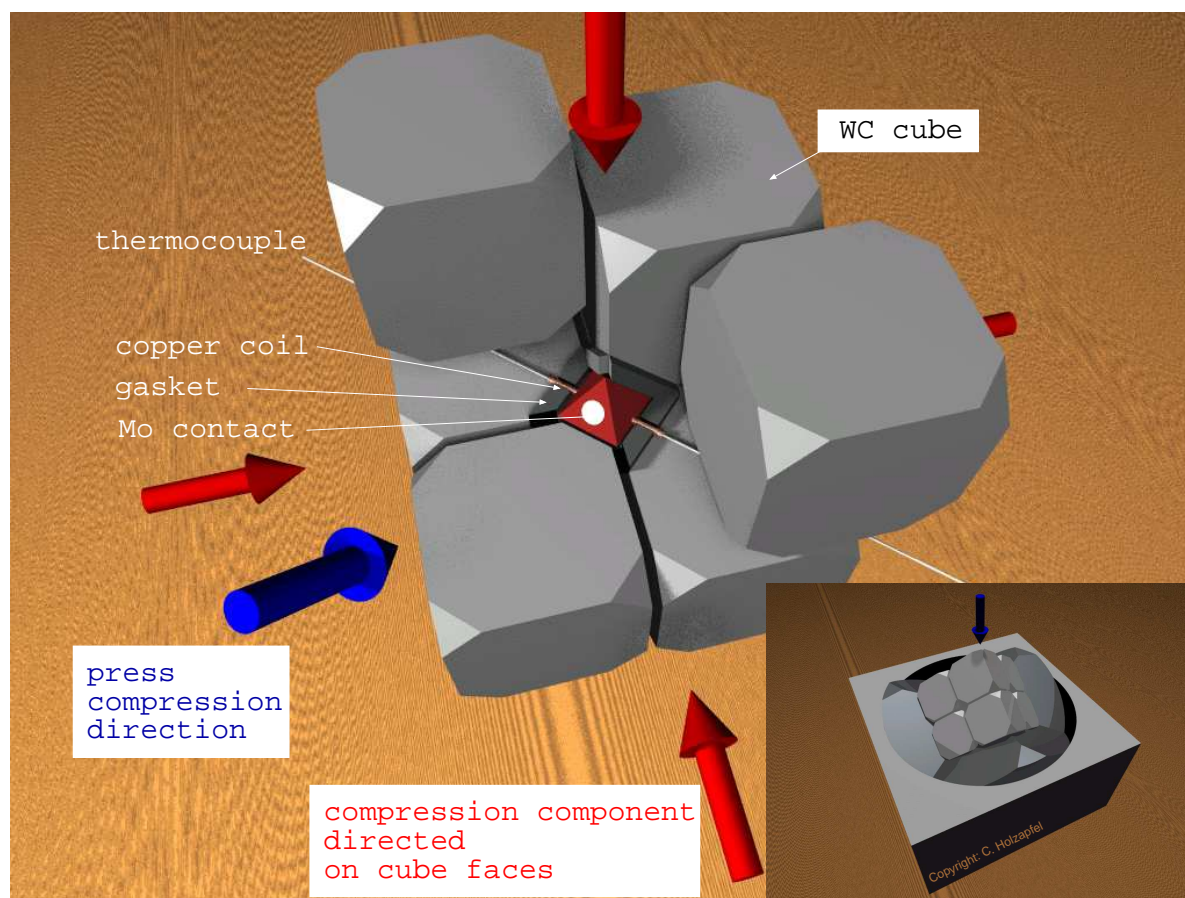


Figure A.1: Position of the Octahedron inside the 8 WC cubes. One cube is removed for clarity. Pyrophyllite gaskets are indicated with the thermocouple crossing enclosed by a Cu coil.

may even vary for a similar assembly from experiment to experiment.

Gettings and Kennedy (1970) measured the absolute effect on pressure on the *EMF* of Chromel-Alumel and Pt-Pt₉₀Rh₁₀ thermocouples using a differential technique in a piston-cylinder apparatus up to 3.5 GPa and 1273 K. Also Mao and Bell (1971) measured the pressure effect of the *EMF* in the piston-cylinder apparatus up to 4 GPa and 1773 K. Irifune (2002) extrapolated linearly the corrections proposed by Mao and Bell (1971) up to 25 GPa for an estimation of the *EMF*-pressure effect in the multianvil apparatus. At 1873 K and 20 GPa they derive an underestimation of T on the order of 80 K. As emphasized above, these corrections only give a first order estimate because pressure and temperature gradients can vary significantly for each assembly type.

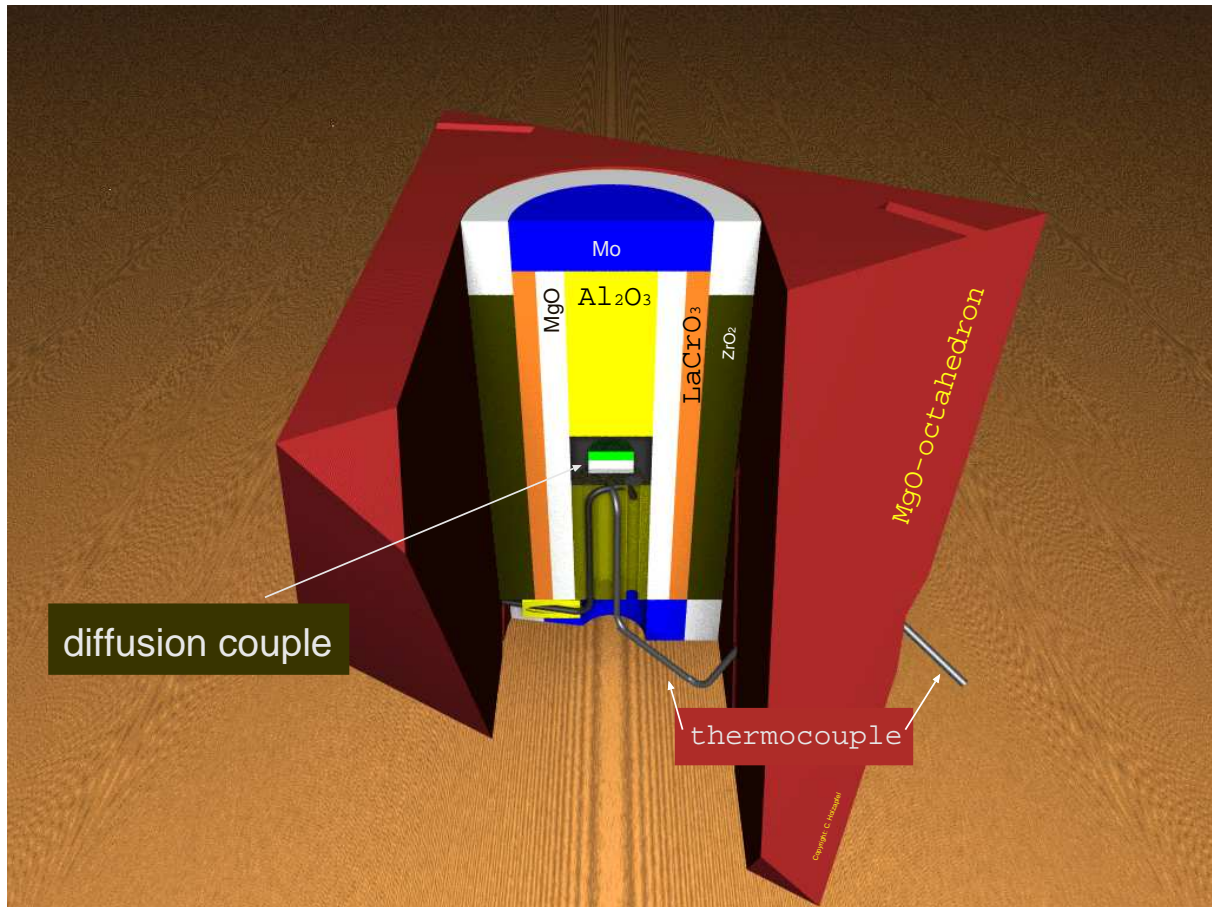


Figure A.2: Octahedron, cut open, to reveal the exact location of the thermocouple and the inner parts of the assembly. The inset is turned 180°.

Instead of measuring the absolute pressure correction for the *EMF*, different authors tried to determine the difference between different types of thermocouples (Ohtani et al., 1982; Kato and Kumazawa, 1985; Tsuzaki and Takahashi, 1992; Walter et al., 1995). Ohtani et al. (1982) derived a maximum deviation between a W-W₇₅Re₂₅ and a Pt-Pt₈₇Rh₁₃ thermocouple of 100 K. Using values of Getting and Kennedy (1970) at 5 GPa and 2370 K the correction would be ~ 30 K which is also the maximum deviation between the readings of a Pt-Rh and W-Re thermocouple in Walter et al. (1995). All evidence points to an underestimation of the real temperature in multianvil experiments. Taking the various estimates of the pressure effect of the thermocouple reading into account, the maximum underestimation of the absolute temperature is on the order of 100 K.

Because all data at high pressure are subject to that temperature shift, the absolute value of the activation energy determined in an Arrhenius plot would not be affected if the EMF pressure effect does not depend significantly on temperature. More critical is the determination of the activation volume where data at high pressure are compared to literature data at 1 bar. For a typical activation energy at 1 bar of 250 kJ mol^{-1} at a temperature of 1673 K and a temperature underestimation of 100 K the corresponding underestimation of the activation volume would be $1.2 \text{ cm}^3 \text{ mol}^{-1}$ comparing data at 1 bar and 12 GPa and $0.6 \text{ cm}^3 \text{ mol}^{-1}$ using data at 1 bar and 23 GPa. The real activation volume would be larger because the temperature of the experiment is underestimated according to the proceeding discussion and thus for comparison at 1 bar (slower) diffusivities at lower temperature would be used.

Appendix B

TEMQuant: A program for quantifying EDX-TEM analysis of ionic compounds

B.1 Principles of the program

Figure B.1 shows the principle algorithm of the program TEMQuant used for performing the absorption correction of EDX-STEM analysis following the procedure of Van Cappellen (1990) and Van Cappellen and Doukhan (1994, for details see also Section 3.3). In section B.2 the source code with some simplifications is given. Intensities are read from a data file provided by the Vantage software. If TEMQuant is used for reading intensities written in other file formats the class method `readdat` has to be changed according to the new format. For each data set (analysis) the uncorrected elemental ratios (relative to Si) are calculated (Equation 3.1). Assuming a density of $4 \text{ cm}^3 \text{ mol}^{-1}$ and a take off angle of 15° an absorption corrected analysis is calculated for a thickness of 10 nm (method `StoichDicke`). Using the electroneutrality constraint of ionic compounds (Van Cappellen and Doukhan, 1994) the thickness is varied systematically until the sum of charges of cations and anions is the same within error. Because the density and take-off angle are not optimized the thickness is only an apparent thickness. This makes no difference for the final result because it is the product of thickness, density, and take-off angle which determines the absorption-corrected k-factor in Equation 3.3.

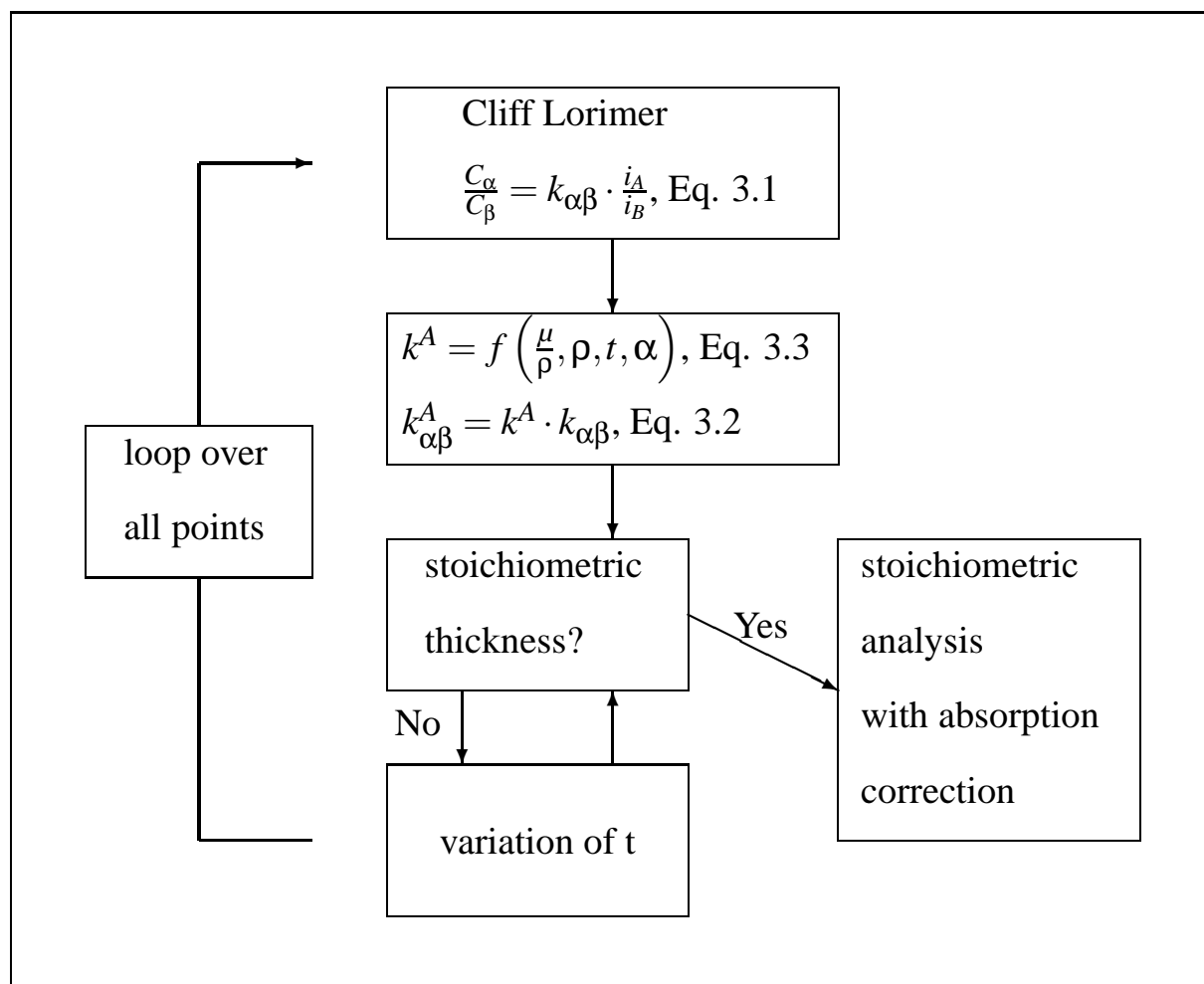


Figure B.1: Flow chart of program TEMQuant

B.2 Source code of TEMQuant

B.2.1 Header file of class TEMQuant

```

#include <iostream>
#include <fstream>
#include <string>
#include <cstring>
#include <vector>
#include <cmath>
#include <cstdio>

```

```
using namespace std;
```

```
class TEMQuant
{
```



```

private:
    vector<int> feld; // intensities
    vector<double> intensitaeten; // intensities of elements of interest (e.g. not carbon from coating)
    vector<int> interesse; // localize elements;
    vector<string> elemente; // elementsymbols (2 characters!)
    unsigned int Anz_Ele; // number of elements read from file
    unsigned int Anz_Analysen; // number of analyses
    double MassAbsorption[30][30]; // matrix of mass absorption coefficients
    double AtomicMass[100]; // matrix of atomic masses
    double wertigkeit[100]; // matrix of valences
    vector<int> Ord_Ele; // list of atomic numbers, only elements of interest
    unsigned int Anz_Ord; // number of elements to be calculated
    int Platz_Si; // position of Si in Ord_Ele?
    double k_factor[100]; // k-faktors, at position of atomic number
    vector<double> konzentrationen; // weight percent of cations
    vector<double> atomanteil; // atomic fraction of cations
    vector<double> atomprozent; // atomic percent of cations
    vector<double> KonzStoich; // composition calculated using algorithm of Van Capellen and
    Doukhan (1994)
    vector<double> thickness;

public:
    //constructors
    TEMQuant(void);

    // class methods
    void readdat(char *name);
    vector<double> success(void); // gives back intensitaeten, to check if reading was succesful
    void ausgabe_datei(char *ausgabe);
    void zuordnung(void);
    double concentration(double I1, double I2, double k12); // Cliff-Lorimer-equation
    void norm(vector<double> & var); // normalization of concentration ratio
    void toAtom(vector<double> & konz); // normalization of a vektor
    vector<double> MassAbs(const vector<double> & conc);
    vector<double> acf(const vector<double> & massX, double thick);
    void absorption(double dicke, vector<double> & intensity); // calculates the composition of an
    analysis without writing into private data members
    void toAtom(void); // wt% → atom%
    int StoichDicke(void); // calculates stoichiometric composition
};

```

B.2.2 Definition of class methods for class TEMQuant

```
#include "TEMQuant.h"
```

```
using namespace std;
```

```
TEMQuant::TEMQuant(void)
```

```
{
```

```
    Anz_Ele = 0;
```

```
    // Initialization of k-factors, only example!
```

```
    k_factor[8] = 1.546;
```

```
    k_factor[11]= 1.116;
```

```
    k_factor[12] = 1.095;
```

```
    k_factor[13] = 1.025;
```

```
    k_factor[14] = 1.0;
```

```
    k_factor[20] = 1.1658;
```

```
    k_factor[22]= 0.986;
```

```
    k_factor[24]=0.840;
```

```
    k_factor[25]=0.915;
```

```
    k_factor[26] = 1.314;
```

```
    k_factor[28]=1.0;
```

```
    // Initialisierung der Massenabsorptionskoeffizienten
```

```
    MassAbsorption[8][8]=1200.0;
```

```
    MassAbsorption[8][11]=3520.0;
```

```
    MassAbsorption[8][12]=5170.0;
```

```
    MassAbsorption[8][13]=6720.0;
```

```
    MassAbsorption[8][14]=8790.0;
```

```
    MassAbsorption[8][20]=22000.0;
```

```
    MassAbsorption[8][22]=22100.0;
```

```
    MassAbsorption[8][24]=3140.0;
```

```
    MassAbsorption[8][25]=3470.0;
```

```
    MassAbsorption[8][26]=4000.0;
```

```
    MassAbsorption[8][28]=5120.0;
```

```
    MassAbsorption[11][8]=4250.0;
```

```
    MassAbsorption[11][11]=591.0;
```

```
    MassAbsorption[11][12]=852.0;
```

```
    MassAbsorption[11][13]=1070.0;
```

```
    MassAbsorption[11][14]=1430.0;
```

```
    MassAbsorption[11][20]=4540.0;
```

```
    MassAbsorption[11][22]=5770.0;
```

```
    MassAbsorption[11][24]=7410.0;
```

```
    MassAbsorption[11][25]=8370.0;
```

```
    MassAbsorption[11][26]=9770.0;
```

```
    MassAbsorption[11][28]=10166.6;
```

```
    MassAbsorption[12][8]=2432.8;
```

```
    MassAbsorption[12][11]=5460.0;
```

```
    MassAbsorption[12][12]=463.6;
```

```
    MassAbsorption[12][13]=641.0;
```

```
    MassAbsorption[12][14]=802.2;
```

```
    MassAbsorption[12][20]=2656.7;
```

```
    MassAbsorption[12][22]=3646.4;
```

MassAbsorption[12][24]=4782.0;
MassAbsorption[12][25]=5443.6;
MassAbsorption[12][26]=6120.7;
MassAbsorption[12][28]=7709.5;
MassAbsorption[13][8]=1503.3;
MassAbsorption[13][11]=3359.4;
MassAbsorption[13][12]=4376.5;
MassAbsorption[13][13]=385.7;
MassAbsorption[13][14]=503.4;
MassAbsorption[13][20]=1667.0;
MassAbsorption[13][22]=2288.0;
MassAbsorption[13][24]=3000.5;
MassAbsorption[13][25]=3415.6;
MassAbsorption[13][26]=3840.6;
MassAbsorption[13][28]=4837.5;
MassAbsorption[14][8]=965.5;
MassAbsorption[14][11]=2168.1;
MassAbsorption[14][12]=2824.6;
MassAbsorption[14][13]=3493.2;
MassAbsorption[14][14]=327.9;
MassAbsorption[14][20]=1086.0;
MassAbsorption[14][22]=1490.6;
MassAbsorption[14][24]=1954.8;
MassAbsorption[14][25]=2225.3;
MassAbsorption[14][26]=2502.1;
MassAbsorption[14][28]=3151.6;
MassAbsorption[20][8]=115.8;
MassAbsorption[20][11]=265.9;
MassAbsorption[20][12]=346.4;
MassAbsorption[20][13]=431.7;
MassAbsorption[20][14]=530.6;
MassAbsorption[20][20]=139.4;
MassAbsorption[20][22]=191.3;
MassAbsorption[20][24]=250.8;
MassAbsorption[20][25]=285.5;
MassAbsorption[20][26]=321.1;
MassAbsorption[20][28]=404.4;
MassAbsorption[22][8]=65.7;
MassAbsorption[22][11]=151.9;
MassAbsorption[22][12]=197.9;
MassAbsorption[22][13]=247.0;
MassAbsorption[22][14]=304.3;
MassAbsorption[22][20]=772.2;
MassAbsorption[22][22]=110.6;
MassAbsorption[22][24]=145.0;
MassAbsorption[22][25]=165.1;
MassAbsorption[22][26]=185.6;

```
MassAbsorption[22][28]=233.8;
MassAbsorption[24][8]=39.4;
MassAbsorption[24][11]=91.4;
MassAbsorption[24][12]=119.1;
MassAbsorption[24][13]=149.0;
MassAbsorption[24][14]=183.8;
MassAbsorption[24][20]=469.2;
MassAbsorption[24][22]=583.0;
MassAbsorption[24][24]=88.2;
MassAbsorption[24][25]=100.5;
MassAbsorption[24][26]=113.0;
MassAbsorption[24][28]=142.3;
MassAbsorption[25][8]=30.9;
MassAbsorption[25][11]=72.0;
MassAbsorption[25][12]=93.8;
MassAbsorption[25][13]=117.4;
MassAbsorption[25][14]=145.0;
MassAbsorption[25][20]=371.0;
MassAbsorption[25][22]=472.5;
MassAbsorption[25][24]=69.9;
MassAbsorption[25][25]=79.5;
MassAbsorption[25][26]=89.4;
MassAbsorption[25][28]=112.6;
MassAbsorption[26][8]=24.5;
MassAbsorption[26][11]=57.2;
MassAbsorption[26][12]=74.6;
MassAbsorption[26][13]=93.4;
MassAbsorption[26][14]=115.5;
MassAbsorption[26][20]=296.2;
MassAbsorption[26][22]=377.5;
MassAbsorption[26][24]=474.2;
MassAbsorption[26][25]=63.5;
MassAbsorption[26][26]=71.4;
MassAbsorption[26][28]=90.0;
MassAbsorption[28][8]=15.8;
MassAbsorption[28][11]=37.2;
MassAbsorption[28][12]=48.4;
MassAbsorption[28][13]=60.7;
MassAbsorption[28][14]=75.2;
MassAbsorption[28][20]=193.7;
MassAbsorption[28][22]=247.3;
MassAbsorption[28][24]=310.7;
MassAbsorption[28][25]=343.6;
MassAbsorption[28][26]=379.6;
MassAbsorption[28][28]=58.9;
```

// Initialization of atomic weights, only example!

```

AtomicMass[1]=1.00794;
// insert other elements ...

// Initialization of valences, only example!
wertigkeit[1]=1.0;
// insert other elements ...

void TEMQuant::readdat(char *name)
{
    ifstream indat(name);
    char inp[160];
    string test;
    string vergleich1, vergleich2;
    int i=1;
    int zahl,zeile=0;
    vergleich1= string("-Sigma");
    vergleich2 = string("+/-");

    // Initialization
    Anz_Ele = 0;

    // open file
    if(indat)
    {
        indat.getline(inp,160);
        while(!indat.eof())
        {
            test=inp;
            if(test.find(vergleich1) != string::npos)
            {
                i++;
            }
            if(test.find(vergleich2)!=string::npos)
            {
                if(i==2)
                {
                    string str(test,2,4);
                    elemente.push_back(str);
                }
                test.erase(0,7);
                sscanf(test.c_str(),"%d",&zahl);
                feld.push_back(zahl);
                zeile++;
                // cout << test << " " << zahl << endl;
                if(i==2) Anz_Ele++;
            }
            indat.getline(inp,160);
        }
    }
}

```

```

    }
    Anz_Analysen = feld.size()/Anz_Ele;

    cout << "Anzahl der Analysen:  " << Anz_Analysen << endl;
}
}

vector<double> TEMQuant::success(void)
{
    vector<double> hilfe(intensitaeten);

    return(hilfe);
}

void TEMQuant::ausgabe_datei(char *ausgabe)
{
    ofstream outdat(ausgabe);
    unsigned int i;

    if(outdat)
    {
        for (i = 0; i < elemente.size();i++) outdat << elemente[i] << " ";
        outdat << endl;
        for (i=0; i< feld.size();i++)
        {
            outdat << feld[i] << " ";
            if (i % Anz_Ele == 6) outdat << endl;
        }
        outdat << endl << endl << endl;
        outdat << "Nach van Capellen bestimmte Zusammensetzung:  " << endl;
        outdat << "anzahl analysen:  " << Anz_Analysen << endl;
        for (i=0; i<KonzStoich.size(); i++)
        {
            if (i % Anz_Ord == 0) outdat << i/Anz_Ord+1 << " ";
            outdat << KonzStoich[i] << " ";
            if (i % Anz_Ord == Anz_Ord-1) outdat << thickness[i/Anz_Ord] * 10000000.0<< endl;
            if (i % (Anz_Analysen*Anz_Ord) == Anz_Analysen*Anz_Ord-1) outdat << endl << endl;
        }
    }
}

void TEMQuant::zuordnung(void)
{
    char test2;
    int test=0;
    unsigned int i,k;

```

```

int hilfsva;
double inttodouble; // Hilfsvariable
// debugging:
for (i=0; i<Ord_Ele.size(); i++)
{
    cout << Ord_Ele[i] << endl;
}
for (i=0; i<Anz_Ele; i++)
{
    if (elemente[i]=="C -K")
    {
        cout << "Element " << i << "= " << elemente[i] << endl;
        cout << "accept in matrix? - with y" << endl;
        cin >> test2;
        if (test2 == 'y') {
            test=1;
        } else {
            test=0;
        }
        if (test == 1)
        {
            Ord_Ele.push_back(6);
            interesse.push_back(i);
        }
    }
    if (elemente[i]=="Si-K")
    {
        cout << "Element " << i << "= " << elemente[i] << endl;
        cout << "accept in matrix? - with y" << endl;
        cin >> test2;
        if (test2 == 'y') {
            test=1;
        } else {
            test=0;
        }
        if (test == 1)
        {
            Ord_Ele.push_back(14);
            interesse.push_back(i);
        }
    }
}
// *****
// do the same for all other elements
// *****
// where is Si?
for (i=0; i<Ord_Ele.size(); i++)
{

```

```

    if (Ord_Ele[i]==14)
    {
        Platz_Si = i;
    }
} // implement control sequence!
Anz_Ord= Ord_Ele.size();
for (i=0; i<Anz_Analysen; i++)
{
    for (k=0; k<interesse.size(); k++)
    {
        hilfsvvar = feld[Anz_Ele*i+interesse[k]];
        inttodouble = double(hilfsvvar);
        intensitaeten.push_back(inttodouble);
    }
}

// debugging:
cout << "debug-information" << endl;
cout << Anz_Ord << " Elemente" << endl;
for (i=0; i<Ord_Ele.size(); i++)
{
    cout << Ord_Ele[i] << endl;
}
cout << " Si an " << Platz_Si+1 << ". Stelle" << endl;
cout << " elemente standen an den plaetzen: " << endl;
for (i = 0; i<interesse.size(); i++){
    cout << interesse[i];
}
}

double TEMQuant::concentration(double I1, double I2, double k12)
{
    double CAB;
    CAB = k12 * I1/I2;
    return(CAB);
}

void TEMQuant::norm(vector<double> & var)
{
    double summe = 0.0;
    unsigned int i;
    for (i=0; i<Anz_Ord; i++){
        summe = summe + var[i];
    }

    for (i=0; i<Anz_Ord; i++){
        var[i]=var[i]/summe;
    }
}

```



```

    }
}

vector<double> TEMQuant::MassAbs(const vector<double> & conc)
{
    unsigned int i,k;
    double absor=0;
    vector<double> hilfe;
    for (i=0; i<conc.size(); i++){
        for (k=0; k<conc.size(); k++){
            absor = absor + conc[k]*MassAbsorption[Ord_Ele[i]][Ord_Ele[k]];
        }
        hilfe.push_back(absor);
        absor=0;
    }

    return(hilfe);
}

vector<double> TEMQuant::acf(const vector<double> & massX, double thick)
{
    double dens=4.0;
    double takeoff=14.0*3.1415926535/180.0;
    double e1,e2,term1,fac;
    vector<double> E2,TERM1,factor;
    unsigned int i;
    e1 = 1-exp(-1* massX[Platz_Si]*dens*thick*1/sin(takeoff));
    for (i=0; i<massX.size(); i++){
        e2=1-exp(-1* massX[i]*dens*thick*1/sin(takeoff));
        E2.push_back(e2);
    }
    for (i=0; i<massX.size(); i++){
        term1 = massX[i]/massX[Platz_Si];
        TERM1.push_back(term1);
    }
    for (i=0; i<massX.size(); i++){
        fac = e1/E2[i]*TERM1[i];
        factor.push_back(fac);
    }
    return(factor);
}

void TEMQuant::toAtom(void)
{
    unsigned int k;
    unsigned int i,t;

```

```

double hilfe;
vector<double> NurZurNormierung;
for (i=0; i<konzentrationen.size()/Anz_Ord; i++){
    // konzentrationen might be larger than Anz_Analysen */
    for (k=0; k< Anz_Ord; k++){
        hilfe=konzentrationen[Anz_Ord*i+k]/AtomicMass[Ord_Ele[k]];
        atomanteil.push_back(hilfe);
    }
}
for (i=0; i<atomanteil.size()/Anz_Ord; i++){
    NurZurNormierung.clear();
    for (k=0; k< Anz_Ord; k++){
        hilfe = atomanteil[Anz_Ord*i+k];
        NurZurNormierung.push_back(hilfe);
    }
    norm(NurZurNormierung);
    for (t=0; t<NurZurNormierung.size(); t++){
        atomprozent.push_back(NurZurNormierung[t]);
    }
}
}

void TEMQuant::absorption(double dicke, vector<double> & intensity)
{
    vector<double> intensity_ratio,temp;
    vector<double> absorptions;
    vector<double> ACF;
    vector<double> kmod; // modified k-faktor
    unsigned int k;
    unsigned int t;
    double toleranz;
    // calculation of non-corrected intensity ratios (to Si)
    for (k=0; k<Anz_Ord; k++)
    {
        intensity_ratio.push_back(concentration(intensity[k],intensity[Platz_Si],k_factor[Ord_Ele[k]]));
    }

    norm(intensity_ratio);

    do {
        toleranz=0;
        kmod.clear();
        temp = intensity_ratio;
        absorptions = MassAbs(intensity_ratio);
        ACF = acf(absorptions, dicke);

```

```

    for (t=0; t<Anz_Ord; t++){
        kmod.push_back(ACF[t]*k_factor[Ord_Ele[t]]);
    }
    intensity_ratio.clear(); // clear, for optimized concentration ratios
    for (t=0; t<Anz_Ord; t++){
        intensity_ratio.push_back(concentration(intensity[t],intensity[Platz_Si],kmod[t]));
    }
    norm(intensity_ratio);

    for (t=0; t<Anz_Ord; t++){
        toleranz=toleranz+fabs(intensity_ratio[t]-temp[t]);
    }

} while (toleranz>0.000001);

// intensity_ratio → intensity
intensity.clear();
for (k=0; k<intensity_ratio.size(); k++){
    intensity.push_back(intensity_ratio[k]);
}
}

void TEMQuant::toAtom(vector<double> & konz)
{
    unsigned int k;
    // unsigned int i,t;
    double hilfe;
    vector<double> NurZurNormierung;
    vector<double> atom;
    for (k=0; k< Anz_Ord; k++){
        hilfe=konz[k]/AtomicMass[Ord_Ele[k]];
        atom.push_back(hilfe);
    }
    norm(atom);
    konz=atom;
}

int TEMQuant::StoichDicke(void)
{
    unsigned int i,l;
    unsigned int k;
    int ende=0; // break condition
    double debug; // debug variable
    double WieDick, add; // how thick is the sample, step size
    double summe1,summe2; // sum of charges, should become zero
    double hilfe; // help variable
    vector<double> datensatz; // for one data set

```

```

vector<double> temporaer; // reset of dataset
if (intensitaeten.empty()) {
    cout << "Kein Datensatz in atomprozent" <<endl;
    return(-1);
}

KonzStoich.clear();
thickness.clear();

// For each data set
for (i=0; i<intensitaeten.size()/Anz_Ord; i++){
    datensatz.clear();
    for (k=0; k<Anz_Ord; k++){
        hilfe = intensitaeten[Anz_Ord*i+k];
        datensatz.push_back(hilfe);
    }
    WieDick = 0.000001; // start with 10 nm
    summe1 = 0;
    summe2 = 0;
    temporaer = datensatz;
    absorption(WieDick,datensatz);
    toAtom(datensatz);

    for (l=0; l<datensatz.size(); l++){
        hilfe = datensatz[l]*wertigkeit[Ord_Ele[l]];
        debug = datensatz[l];
        debug = wertigkeit[Ord_Ele[l]];
        summe1=summe1+hilfe;
    }
    add = 0.00001; // 100 nm is first step size
    do{
        ende++; // number of iterations
        datensatz = temporaer;

        absorption(WieDick,datensatz);
        toAtom(datensatz);
        for (l=0; l<datensatz.size(); l++){
            hilfe = datensatz[l]*wertigkeit[Ord_Ele[l]];
            summe2=summe2+hilfe;
        }
        hilfe = summe1 * summe2; // if hilfe <0 ist, change of signs
        if (hilfe < 0) add = -1*add/2;
        summe1 = summe2;
        summe2 = 0;
        WieDick=WieDick+add;
    } while (fabs(summe1) > 0.00000001 && ende < 100);
if (ende >= 100) cout << endl << "MAXIMUM NUMBER OF ITERATIONS EXCEEDED" << endl;

```

```

    ende=0;
    cout << "AUSGABE VON ZWEITER BERECHNUNG" << endl;
    cout << "Nr. " << i << " ";
    for (k=0; k<Anz_Ord; k++){
        cout << datensatz[k] << " ";
    }
    cout << "d:  " << WieDick;
    cout << endl;
    for (k=0; k<Anz_Ord; k++){
        KonzStoich.push_back(datensatz[k]);
    }
    thickness.push_back(WieDick);

}

return(0);
}

```

B.2.3 Main function

```

#include "TEMQuant.h"

int main(int argc, char **argv)
{
    TEMQuant test;

    if (argc == 1){
        cout << "usage:  TEMQuant file" << endl;
        cout << "end nothing else" << endl;
        return(1);
    }
    if (argc == 2){
        test.readdat(argv[1]);
    }
    if (argc != 1 && argc != 2){
        cout << "something wrong with file input, probably to much" << endl;
        return(1);
    }
    test.zuordnung();
    vector<double> suc(test.success());
    if (suc.empty()) {
        cout << "reading data was not succesfull" << endl;
        return(2);
    }
    test.toAtom();
    test.StoichDicke();
    test.ausgabe_datei("raus.dat");
}

```

```
    return(0);  
}
```

Appendix C

ForwardLeastSquare: A program for finite difference simulation of a diffusion profile

C.1 Introduction

The program ForwardLeastSquare calculates a finite difference simulation of a diffusion profile assuming an exponential composition dependence (Equations 4.12 and 4.13). The simulated profile can then be compared with an input data file containing a measured profile in order to optimize the parameters D_0 and a of Equation 4.12. The format of the ascii input file must be "integer double", otherwise reading of the data file results in an error. An option of the main function allows to minimize the sum of squared deviations of the calculated and observed profile. Due to the implementation of the minimization, the distance values of the measured profiles must be integers. When converting noninteger distances to integer values by multiplying with a suitable number one has to keep in mind to update the units of the diffusion coefficient. The program calculates normalized concentrations. Therefore, the concentrations have to be normalized prior least square minimization. For calculating the preexponential factor and asymmetry parameter, an appropriate variable transformation must be performed.

The main function allows several options. By choosing options 1-3 the standard values of the number of space nodes (x), the preexponential factor D_0 ($d0$) or the composition dependence factor a can be changed and directly calculated for a specific combination of timesteps (nt) and factor (dt/dx^2). This combination can be changed with option 5. Option 6-8 allow to optimize one of the parameters x , $d0$ or a individually by minimizing the sum of squared deviations, whereas option 9 optimizes all three parameters. The progress is monitored in a log-file and is


```

void calcProfile(void);

///////////////////////////////////////////////////////////////////
// least square
///////////////////////////////////////////////////////////////////
void optimiseX(int initialx, int initialxstep); // change x: initialx → initialx+initialxstep, comparison
of sum of squared deviations (ssr)
void optimiseXsemiAuto(void); // minimize ssr by changing x
void optimiseD0(double initialD0, double initialD0step); // change D0: initialD0 →
initialD0+initialD0step, comparison of ssr
void optimiseD0semiAuto(void); // minimize ssr by changing D0
void optimiseA(double initialA, double initialAstep); // change a: initiala → initiala+initialastep,
comparison of sum of ssr
void optimiseAsemiAuto(void); // minimize ssr by changing a

///////////////////////////////////////////////////////////////////
// set-functions
///////////////////////////////////////////////////////////////////
void setParameters(void);

///////////////////////////////////////////////////////////////////
// get-Funktionen
///////////////////////////////////////////////////////////////////
void getParameters(void);
void print_parameters_into_file(void); // prints into file
long double ssr(void); // sum of squared residuals,  $\sum_{\delta x} (C_m - C_s)^2$ , Section 4.3.2
};

least_square::least_square(){
    string filename;
    double hilfe;

    ///////////////////////////////////////////////////////////////////
    // Initialization for profile parameters
    ///////////////////////////////////////////////////////////////////
    nt = 4100;
    nx=10;
    a=2.36;
    dnull=0.04;
    fak=0.5;

    cout << "Name of original data" << endl;
    cin >> filename;
    cout << filename << endl;

    hilfe = 0.0;

```

```

ifstream indat(filename.c_str());
if (indat)
{
    while(!indat.eof()) {
        if (indat.eof()){
            break;
        }
        indat >> hilfe;
        daten.push_back(hilfe);
    }
    daten.pop_back(); // because last element is to much
} else {
    cout << "no indat\n";
}
}

void least_square::calcProfile(void){
    int m=0,j=0;
    unsigned int ausgabe; // for output of result
    double hilfe; // when executing the finite differences
    ofstream aus("ausgabe.dat"); // output file

    alt_m.clear();
    neu_m.clear();

    ///////////////////////////////////////////////////////////////////
    // Initialization
    ///////////////////////////////////////////////////////////////////
    while (m<nx){
        if(m<nx/2){
            alt_m.push_back(1.0);
        } else {
            alt_m.push_back(0.0);
        }
        m+=1;
    }

    m=1;
    j=0;
    while (m<nt){
        while (j<nx){

            if (j==0) {
                neu_m.push_back(1.0); // left boundary condition
                j+=1;
                continue;
            }

```

```

    }
    if (j==nx-1) {
        neu_m.push_back(0.0); // right boundary condition
        j+=1;
        continue;
    }
    // finite difference formulation, exp composition dependence, Eq. 4.13 and 4.18
    hilfe = alt_m[j]+fak*(1.0/4.0*a*dnull*exp(a*alt_m[j])*(alt_m[j+1]-alt_m[j-1])*(alt_m[j+1]-
alt_m[j-1])+(dnull*exp(a*alt_m[j]))*(alt_m[j+1]-2*alt_m[j]+alt_m[j-1]));
    neu_m.push_back(hilfe);
    j+=1;
}
m+=1; // add 1 to m
j=0; // reset j
alt_m.clear(); // move elements
ausgabe=0;
while (ausgabe < neu_m.size()){
    alt_m.push_back( neu_m[ausgabe]); // make new out of old
    ausgabe += 1;
}
neu_m.clear();
}

// output
ausgabe = 0;
while (ausgabe<alt_m.size()){
    aus << ausgabe << " " << alt_m[ausgabe] << endl;
    ausgabe+=1;
}
aus.close();
}

void least_square::setParameters(void)
{
    cout << "number of timesteps" << endl;
    cin >> nt;
    cout << "faktor:  " << endl;
    cin >> fak;
}

void least_square::getParameters(void)
{
    cout << "current parameters" << endl;
    cout << "number of timesteps:  " << nt << endl;
    cout << "number of x-nodes:  " << nx << endl;
    cout << "D0:  " << dnull << endl;
    cout << "asymmetriefactor:  " << a << endl;
}

```

```

    cout << "faktor:  " << fak << endl;
}

void least_square::print_parameters_into_file(void)
{
    ofstream outdat("gefittet.log",ios::app);
    if(outdat){
        outdat << endl << "nx:  " << nx << " nt " << nt << " fak " << fak << endl;
        outdat << "assy-factor:  " << a << " dnull " << dnull << " ssr " << ssr() << endl;
    } else {
        cout << "can't open file gefittet.log" << endl;
    }
    outdat.close();
}

long double least_square::ssr(void){
    double hilfe=0;

    simuliert.clear();
    ifstream indat2("ausgabe.dat");
    if (indat2)
    {
        while(!indat2.eof()) {
            if (indat2.eof()){
                break;
            }
            indat2 >> hilfe;
            simuliert.push_back(hilfe);
        }
        simuliert.pop_back(); // because last element is to much, why?
    } else {
        cout << "can't open indat2" << endl;
    }
    // simulated must be larger than daten (size)
    while (simuliert.size() < daten.size()){
        simuliert.push_back(0.0);
    }
    indat2.close();

    for (unsigned int i=0; i<daten.size()/2; i++){
        hilfe=hilfe+(daten[2*i+1]-simuliert[2*int(daten[2*i]+1)]*(daten[2*i+1]-
simuliert[2*int(daten[2*i]+1)]);
    }
    return(hilfe);
}

void least_square::optimiseX(int initialx, int initialxstep) // optimising x

```

```

{
  string test="0";
  nx = initialx;
  double ssrnew,ssralt;

  calcProfile();
  ssrnew=ssr();
  nx = nx+initialxstep;
  ssralt = ssrnew;

  // print_daten();
  while ((test!="no") && (test!="n")){
    calcProfile();
    ssrnew = ssr();
    cout << "nx:  " << nx << "  ssrnew:  " << ssrnew << "  ssralt:  " << ssralt << endl;
    cout << "weiter, no mit n" << endl;
    cin >> test;
    if ((test=="n") || (test=="no")){
      break;
    }
    if(ssrnew > ssralt){
      cout << "minimum reached, return with smaller timestep?" << endl;
      cout << "only int allowed, though!!" << endl;
      cin >> initialxstep;
    }
    nx=nx+initialxstep;
    ssralt=ssrnew;
  }
}

```

```

void least_square::optimiseXsemiAuto(void) // optimising x
{
  string test="0";
  int initialxstep = 10;
  double ssrnew,ssralt;
  int lauf=0; // test, where is initialxstep?

  calcProfile();
  ssrnew=ssr();
  nx = nx+initialxstep;
  ssralt = ssrnew;

  while (1){
    calcProfile();
    ssrnew = ssr();
    cout << "nx:  " << nx << "  ssrnew:  " << ssrnew << "  ssralt:  " << ssralt << endl;
    if(ssrnew > ssralt){

```

```

    lauf=lauf+1;
    if (lauf==1){
        initialxstep = -1;
    }
    if (lauf==2){
        initialxstep =1;
        nx=nx+initialxstep;
        ssralt=ssrnew;
        calcProfile();
        ssrnew = ssr();
        cout << "nx:  " << nx << " ssrnew:  " << ssrnew << " ssralt:  " << ssralt << endl;
        break;
    }
}
nx=nx+initialxstep;
ssralt=ssrnew;
}
}

```

```

void least_square::optimiseD0(double initialD0, double initialD0step) // optimising D0
{
    string test="0";
    dnull = initialD0;
    double ssrnew,ssralt;

    calcProfile();
    ssrnew=ssr();
    dnull = dnull+initialD0step;
    ssralt = ssrnew;

    while ((test!="no") && (test!="n")){
        calcProfile();
        ssrnew = ssr();
        cout << "D0:  " << dnull << "step:  " << initialD0step << " ssrnew:  " << ssrnew << "
ssralt:  " << ssralt << endl;
        cout << "weiter, no mit n" << endl;
        cin >> test;
        if ((test=="n") || (test=="no")){
            break;
        }
        if(ssrnew > ssralt){
            cout << "minimum reached, return with smaller D0step?" << endl;
            cin >> initialD0step;
        }
        dnull=dnull+initialD0step;
        ssralt=ssrnew;
    }
}

```

```

}

void least_square::optimiseD0semiAuto(void) // optimising D0
{

    double ssrnew,ssralt;
    double initialD0step=0.01;

    calcProfile();
    ssrnew=ssr();
    dnull = dnull+initialD0step;
    ssralt = ssrnew;

    while (abs(initialD0step)>0.000001){
        calcProfile();
        ssrnew = ssr();
        cout << "D0:  " << dnull << "step:  " << initialD0step << " ssrnew:  " << ssrnew << "
ssralt:  " << ssralt << endl;
        if(ssrnew > ssralt){
            initialD0step = -1.0*initialD0step/10.0;
        }
        dnull=dnull+initialD0step;
        ssralt=ssrnew;
    }
}

void least_square::optimiseA(double initialA, double initialAstep) // optimising a
{
    string test="0";
    a = initialA;
    double ssrnew,ssralt;

    calcProfile();
    ssrnew=ssr();
    a = a+initialAstep;
    ssralt = ssrnew;

    while ((test!="no") && (test!="n")){
        calcProfile();
        ssrnew = ssr();
        cout << "a:  " << a << " step:  " << initialAstep << " ssrnew:  " << ssrnew << " ssralt:
" << ssralt << endl;
        cout << "weiter?  y or n" << endl;
        cin >> test;
        if (test=="no" || test=="n"){
            break;
        }
    }
}

```

```

    if(ssrnew > ssralt){
        cout << "minimum reached, return with smaller Astep?" << endl;
        cin >> initialAstep;
    }
    a=a+initialAstep;
    ssralt=ssrnew;
}
}

void least_square::optimiseAsemiAuto(void) // optimising a
{
    double ssrnew,ssralt;
    double initialAstep=0.1;

    calcProfile();
    ssrnew=ssr();
    a = a+initialAstep;
    ssralt = ssrnew;

    while (abs(initialAstep) > 0.00001){
        calcProfile();
        ssrnew = ssr();
        cout << "a: " << a << " step: " << initialAstep << " ssrnew: " << ssrnew << " ssralt: " << ssralt << endl;
        if(ssrnew > ssralt){
            initialAstep = -1.0*initialAstep/10.0;
        }
        a=a+initialAstep;
        ssralt=ssrnew;
    }
}

int main(int argc, char **argv)
{
    string auswahl;
    int startX,incrementX;
    double startD0,incrementD0,starta,incrementa;
    cout << "program for least square of numerical fits" << endl;
    least_square profileObject;
    while (1){
        cout << "What do you want to do?" << endl;
        cout << "there are several choices: " << endl;
        cout << "1 = optimise x" << endl;
        cout << "2 = optimise d0" << endl;
        cout << "3 = optimise a" << endl;
        cout << "4 = terminate program" << endl;
        cout << "5 = set nt and faktor" << endl;

```



```

cout << "6 = semiauto refinement of x" << endl;
cout << "7 = semiauto refinement of a" << endl;
cout << "8 = semiauto refinement of D0" << endl;
cout << "9 = 1000 durchgaenge" << endl;
cout << endl;
profileObject.getParameters();
cout << endl;
cin >> auswahl;
if ((auswahl != "1") && (auswahl != "2") && (auswahl != "3") && (auswahl != "4") &&
(auswahl != "5") && (auswahl != "6") && (auswahl != "7") && (auswahl != "8") && (auswahl !=
"9")){
    cout << "Mmmmh..." << endl;
    cout << "didn't I say something of giving a number" << endl;
    cout << "between 1 and 9?" << endl;
    cout << "next time I would try this" << endl;
    continue;
}
if (auswahl == "1"){
    cout << "startX incrementX" << endl;
    cin >> startX >> incrementX;
    profileObject.optimiseX(startX,incrementX);
}
if (auswahl == "2"){
    cout << "startD0 incrementD0" << endl;
    cin >> startD0 >> incrementD0;
    profileObject.optimiseD0(startD0,incrementD0);
}
if (auswahl == "3"){
    cout << "starta incrementa" << endl;
    cin >> starta >> incrementa;
    profileObject.optimiseA(starta,incrementa);
}
if (auswahl == "4"){
    return(0);
}
if (auswahl == "5"){
    profileObject.setParameters();
}
if (auswahl == "6"){
    profileObject.optimiseXsemiAuto();
}
if (auswahl == "7"){
    profileObject.optimiseAsemiAuto();
}
if (auswahl == "8"){
    profileObject.optimiseD0semiAuto();
}
}

```

```
if (auswahl == "9"){  
    int zaehler = 0;  
    for (zaehler = 0; zaehler < 1000; zaehler++){  
        profileObject.optimiseXsemiAuto();  
        profileObject.optimiseD0semiAuto();  
        profileObject.optimiseAsemiAuto();  
        profileObject.print_parameters_into_file();  
    }  
}  
}
```

Appendix D

Example profile analyses

In this section, example diffusion profile analyses also given in the Figures in Chapter 3 are listed. Profile analysis was performed either by electron microprobe (EPMA) or with energy dispersive X-ray spectrometry on a transmission electron microscope (EDX-STEM) as discussed in Chapter 5.

Table D.1: Profile analysis for olivine shown in Fig. 5.3 measured with EPMA. The experiment was performed at 12 GPa, 1623 K and annealed for 72 h. All concentrations are given in weight percent of the oxide.

Distance, μm	MgO	SiO ₂	MnO	FeO	NiO	Sum
0	51.67	41.66	0.179	6.46	0.237	100.20
1	51.59	41.95	0.178	6.21	0.251	100.18
2	51.38	41.34	0.174	6.27	0.244	99.40
3	51.69	41.67	0.164	6.29	0.267	100.08
4	51.41	41.55	0.172	6.33	0.232	99.70
5	51.30	41.76	0.151	6.25	0.279	99.74
6	51.59	41.46	0.148	6.36	0.263	99.82
7	51.38	41.52	0.155	6.34	0.251	99.64
8	51.51	41.43	0.139	6.21	0.239	99.53
9	51.60	41.32	0.148	6.19	0.277	99.53
10	51.46	41.43	0.146	6.24	0.248	99.53
11	51.59	41.51	0.141	6.22	0.232	99.69
12	51.58	41.67	0.165	6.28	0.269	99.96
13	51.74	41.59	0.155	5.96	0.269	99.70
14	52.25	41.64	0.134	5.78	0.227	100.03
15	52.37	41.73	0.118	5.43	0.215	99.86
16	52.69	41.78	0.116	4.82	0.213	99.61
17	52.88	41.70	0.096	4.33	0.201	99.21
18	53.39	41.82	0.080	3.70	0.187	99.18
19	53.94	42.00	0.085	2.94	0.141	99.11
20	54.59	42.26	0.063	2.16	0.073	99.15
21	55.02	42.49	0.071	1.50	0.038	99.11
22	55.66	42.42	0.018	0.94	0.061	99.11
23	56.14	42.70	0.000	0.39	0.037	99.27
24	56.06	42.74	0.009	0.18	0.006	99.00
25	56.27	42.98	0.000	0.14	0.000	99.37
26	56.24	42.72	0.000	0.08	0.017	99.05
27	56.11	42.90	0.000	0.12	0.000	99.13
28	56.34	42.69	0.003	0.10	0.009	99.14
29	56.19	43.00	0.000	0.04	0.011	99.25
30	56.34	42.87	0.008	0.10	0.018	99.34
31	56.32	42.82	0.000	0.06	0.000	99.20
32	56.34	43.05	0.013	0.12	0.018	99.54
33	56.49	43.10	0.005	0.12	0.032	99.75
34	56.35	42.66	0.019	0.08	0.018	99.13
35	56.32	42.83	0.001	0.06	0.000	99.22
36	56.37	42.87	0.009	0.06	0.000	99.31
37	56.10	42.92	0.006	0.06	0.010	99.10
38	56.35	43.00	0.012	0.05	0.014	99.43
39	56.28	42.95	0.008	0.06	0.045	99.34
40	56.16	42.82	0.005	0.06	0.034	99.08

Table D.2: Profile analysis for olivine shown in Fig. 5.4-A measured with EDX-STEM. The experiment was performed at 10 GPa, 1673 K and annealed for 24 h. All concentrations are given in atom%. EDX analyses are normalized to 100%

distance	O	Mg	Si	Fe	distance	O	Mg	Si	Fe
14	56.59	30.22	13.17	0.023	6.8	56.73	28.95	13.45	0.875
13.8	56.63	30.09	13.26	0.022	6.6	56.77	28.85	13.53	0.853
13.6	56.68	29.95	13.36	0.007	6.4	56.77	28.79	13.55	0.890
13.4	56.77	29.69	13.54	0.010	6.2	56.84	28.55	13.69	0.915
13.2	56.72	29.85	13.43	0.007	6	56.87	28.42	13.74	0.974
13	56.79	29.61	13.58	0.021	5.8	56.69	28.96	13.38	0.977
12.8	56.70	29.88	13.40	0.024	5.6	56.81	28.53	13.63	1.030
12.6	56.62	30.11	13.24	0.030	5.4	56.81	28.46	13.62	1.107
12.4	56.60	30.18	13.21	0.011	5.2	56.86	28.31	13.72	1.111
12.2	56.73	29.81	13.45	0.012	5	56.82	28.39	13.65	1.145
12	56.67	29.95	13.34	0.032	4.8	56.83	28.37	13.67	1.126
11.8	56.72	29.81	13.44	0.037	4.6	56.87	28.26	13.73	1.139
11.6	56.73	29.80	13.46	0.008	4.4	56.77	28.65	13.54	1.041
11.4	56.60	30.17	13.19	0.046	4.2	56.89	28.22	13.77	1.118
11.2	56.67	29.92	13.34	0.065	4	56.79	28.47	13.58	1.150
11	56.74	29.71	13.48	0.074	3.8	56.84	28.21	13.68	1.268
10.8	56.76	29.63	13.51	0.101	3.6	56.88	27.99	13.77	1.363
10.6	56.71	29.76	13.42	0.108	3.4	56.84	28.13	13.67	1.364
10.4	56.65	29.94	13.30	0.115	3.2	56.94	27.76	13.87	1.431
10.2	56.77	29.55	13.54	0.139	3	56.98	27.66	13.95	1.413
10	56.79	29.49	13.57	0.144	2.8	57.15	27.26	14.30	1.297
9.8	56.70	29.67	13.41	0.218	2.6	57.00	27.60	14.00	1.399
9.6	56.74	29.51	13.49	0.258	2.4	56.97	27.71	13.94	1.381
9.4	56.84	29.21	13.68	0.279	2.2	56.88	27.95	13.76	1.401
9.2	56.88	29.12	13.76	0.247	2	56.89	27.85	13.78	1.482
9	56.77	29.35	13.54	0.341	1.8	56.74	28.42	13.49	1.349
8.8	56.77	29.34	13.54	0.349	1.6	56.88	27.93	13.76	1.430
8.6	56.72	29.42	13.44	0.426	1.4	56.85	28.03	13.70	1.423
8.4	56.78	29.15	13.57	0.497	1.2	56.77	28.30	13.54	1.385
8.2	56.90	28.80	13.81	0.487	1	56.89	27.88	13.78	1.444
8	56.64	29.57	13.27	0.521	0.8	56.83	28.05	13.66	1.465
7.8	56.86	28.88	13.72	0.546	0.6	56.90	27.84	13.79	1.470
7.6	56.54	29.75	13.08	0.631	0.4	56.86	27.94	13.72	1.482
7.4	57.08	28.12	14.17	0.628	0.2	56.77	28.20	13.54	1.498
7.2	56.93	27.71	13.87	1.486	0	56.81	28.09	13.63	1.463
7	56.94	28.39	13.87	0.800					

Table D.3: Profile analysis for olivine shown in Fig. 5.4-B measured with EDX-STEM. The experiment was performed at 12 GPa, 1673 K and annealed for 24 h. All concentrations are given in atom%. EDX analyses are normalized to 100%

distance, μm	O	Mg	Si	Fe	Ni	Mn
0	57.29	26.32	14.53	1.706	0.107	0.052
0.5	57.35	26.14	14.63	1.718	0.105	0.057
1	57.31	26.22	14.59	1.731	0.101	0.037
1.5	57.35	26.16	14.67	1.720	0.071	0.032
2	57.36	26.13	14.67	1.699	0.094	0.054
2.5	57.25	26.47	14.44	1.668	0.098	0.071
3	57.20	26.62	14.37	1.683	0.090	0.041
3.5	57.22	26.53	14.39	1.716	0.109	0.044
4	57.22	26.58	14.37	1.694	0.081	0.059
4.5	57.23	26.55	14.41	1.663	0.105	0.039
5	57.29	26.46	14.54	1.562	0.109	0.040
5.5	57.25	26.70	14.44	1.475	0.087	0.052
6	57.14	27.00	14.24	1.507	0.069	0.042
6.5	57.26	26.89	14.48	1.264	0.077	0.034
7	57.24	27.09	14.45	1.108	0.094	0.024
7.5	57.42	26.91	14.81	0.797	0.040	0.022
8	57.28	27.34	14.54	0.768	0.059	0.017
8.5	57.08	28.13	14.14	0.573	0.058	0.013
9	56.90	28.81	13.80	0.466	0.016	0.002
9.5	57.10	28.35	14.18	0.325	0.036	0.015
10	56.99	28.80	13.98	0.179	0.043	0.002
10.5	56.81	29.47	13.60	0.068	0.049	0.015
11	57.09	28.66	14.18	0.028	0.038	0.004
11.5	56.97	29.05	13.94	0.016	0.029	0.000
12	57.06	28.76	14.12	0.021	0.036	0.000
12.5	57.65	27.00	15.29	0.024	0.035	0.000
13	57.12	28.58	14.23	0.027	0.043	0.000
13.5	57.21	28.31	14.42	0.014	0.042	0.002
14	57.17	28.44	14.34	0.022	0.019	0.006
14.5	57.21	28.33	14.42	0.015	0.021	0.000
15	57.08	28.72	14.14	0.016	0.031	0.014

Table D.4: Profile analysis for wadsleyite shown in Fig. 5.18 measured with EPMA. The experiment was performed at 15 GPa, 1773 K and annealed for 16 minutes. All concentrations are given in weight percent of the oxide.

d, μm	MgO	SiO ₂	FeO	NiO	Sum	d, μm	MgO	SiO ₂	FeO	NiO	Sum
500	55.61	43.05	0.049	0.000	98.71	556	56.49	42.34	0.113	0.000	98.94
501	55.87	42.71	0.085	0.055	98.72	557	56.08	42.52	0.133	0.013	98.75
504	56.06	42.23	0.058	0.025	98.37	559	55.63	42.13	0.179	0.067	98.01
505	56.17	42.13	0.091	0.067	98.46	560	56.14	42.41	0.215	0.032	98.80
506	56.11	42.16	0.035	0.017	98.32	561	55.75	42.11	0.143	0.090	98.10
507	55.94	42.13	0.049	0.023	98.15	562	55.77	42.30	0.178	0.087	98.33
508	56.46	42.38	0.072	0.025	98.93	563	56.13	42.73	0.279	0.000	99.14
511	56.45	41.99	0.090	0.029	98.56	564	55.30	43.39	0.160	0.006	98.85
512	56.08	42.14	0.030	0.029	98.28	568	55.71	42.60	0.516	0.122	98.95
513	55.98	42.26	0.126	0.029	98.40	569	55.25	42.42	0.718	0.036	98.43
514	56.31	42.39	0.100	0.087	98.88	570	55.79	42.16	0.926	0.061	98.93
515	56.19	42.65	0.081	0.064	98.99	571	54.47	42.87	1.128	0.010	98.48
517	55.97	42.23	0.077	0.004	98.28	574	54.72	41.92	2.184	0.067	98.90
518	56.24	42.20	0.072	0.055	98.57	575	54.85	41.93	2.451	0.095	99.33
519	55.79	42.28	0.059	0.000	98.13	576	54.47	41.81	2.893	0.032	99.20
520	55.75	42.25	0.058	0.004	98.06	577	53.90	41.62	3.495	0.000	99.01
521	55.77	42.19	0.059	0.051	98.07	579	53.00	41.42	4.299	0.080	98.80
522	56.67	42.17	0.077	0.025	98.94	580	52.67	41.56	4.666	0.070	98.96
523	56.16	42.28	0.084	0.116	98.64	581	52.58	41.36	5.034	0.051	99.02
524	56.22	42.13	0.068	0.048	98.47	582	52.05	41.11	5.654	0.010	98.82
525	55.53	42.95	0.000	0.070	98.54	583	51.93	40.85	6.018	0.118	98.93
526	52.67	45.42	0.134	0.048	98.28	584	51.20	40.79	6.255	0.042	98.28
527	55.72	42.93	0.046	0.000	98.70	585	51.19	41.07	7.089	0.048	99.39
528	56.23	42.32	0.064	0.000	98.61	586	50.83	40.89	7.270	0.115	99.10
541	56.12	42.22	0.120	0.010	98.47	587	50.51	40.57	7.763	0.137	98.98
542	56.07	42.29	0.109	0.051	98.51	588	50.05	40.69	8.203	0.130	99.06
543	56.46	42.10	0.078	0.000	98.64	589	49.61	40.57	8.435	0.134	98.75
544	56.46	42.43	0.111	0.042	99.04	590	49.34	40.34	8.998	0.092	98.77
545	56.25	42.05	0.096	0.048	98.45	591	49.20	40.44	9.587	0.286	99.51
546	56.39	42.18	0.091	0.000	98.66	594	47.92	39.93	10.275	0.289	98.41
547	56.63	42.04	0.133	0.000	98.80	595	48.11	40.15	10.879	0.153	99.29
548	55.98	42.62	0.104	0.064	98.76	596	47.43	40.27	10.792	0.193	98.69
549	53.47	45.15	0.207	0.025	98.85	597	47.42	40.07	11.017	0.266	98.77
550	56.63	42.49	0.169	0.036	99.32	598	47.41	40.06	11.231	0.317	99.01
551	56.37	42.47	0.126	0.055	99.03	599	47.13	40.00	11.425	0.234	98.79
552	56.36	42.34	0.149	0.019	98.87	600	46.74	39.88	11.783	0.221	98.62
553	56.24	42.30	0.152	0.000	98.69	601	47.00	39.71	11.868	0.313	98.88
554	56.02	42.38	0.122	0.000	98.52	602	46.84	39.81	12.117	0.225	98.99
555	56.35	42.25	0.091	0.090	98.78	603	46.69	39.91	12.228	0.307	99.13

Table D.4 continued.

d, μm	MgO	SiO ₂	FeO	NiO	Sum	d, μm	MgO	SiO ₂	FeO	NiO	Sum
604	46.23	40.02	12.183	0.370	98.80	651	43.74	39.08	16.657	0.302	99.78
605	46.19	39.94	12.462	0.234	98.83	652	44.66	38.78	15.732	0.416	99.59
606	45.98	39.65	12.653	0.326	98.62	653	44.33	39.15	15.727	0.350	99.55
607	46.67	39.15	13.256	0.319	99.39	654	44.44	38.79	15.709	0.299	99.24
608	45.58	38.96	13.277	0.354	98.17	655	44.64	38.92	15.803	0.249	99.62
610	45.46	39.31	13.634	0.262	98.67	656	44.15	39.08	15.947	0.410	99.58
611	45.45	39.06	13.756	0.294	98.56	657	44.50	39.06	15.856	0.277	99.70
612	45.68	39.49	14.093	0.149	99.41	658	44.29	39.13	15.631	0.237	99.28
613	45.44	39.37	14.124	0.249	99.18	659	44.02	39.05	15.569	0.230	98.87
614	45.78	39.64	14.293	0.262	99.97	660	44.27	38.97	15.669	0.303	99.21
616	45.11	39.46	13.982	0.347	98.90	661	43.44	39.61	15.285	0.286	98.62
617	44.82	39.18	14.388	0.382	98.77	662	43.96	39.22	15.519	0.290	99.00
618	44.80	39.34	14.539	0.252	98.93	663	44.27	38.94	15.653	0.265	99.13
619	45.08	39.55	14.765	0.297	99.69	664	44.47	39.13	15.712	0.293	99.61
620	44.72	39.46	14.886	0.239	99.31	665	44.23	39.14	15.785	0.406	99.57
621	45.02	39.34	14.984	0.318	99.67	666	44.18	38.93	15.605	0.327	99.05
622	44.64	39.40	14.762	0.258	99.06	667	44.49	39.14	15.672	0.327	99.63
623	44.78	39.22	15.047	0.221	99.27	668	43.97	39.36	15.425	0.344	99.10
624	44.46	39.04	14.748	0.196	98.44	669	44.04	39.32	15.478	0.308	99.15
625	44.49	39.29	15.094	0.328	99.20	670	44.39	38.92	15.992	0.314	99.62
626	44.42	39.23	15.455	0.256	99.36						
627	44.25	39.28	14.618	0.375	98.52						
630	45.42	38.47	14.825	0.350	99.07						
631	44.75	39.40	15.442	0.249	99.83						
632	44.34	40.12	15.021	0.504	99.99						
634	43.62	39.00	15.417	0.239	98.28						
635	43.80	39.21	15.390	0.275	98.68						
636	44.20	39.10	15.298	0.249	98.85						
637	44.33	38.98	15.292	0.331	98.93						
638	43.86	39.08	15.425	0.269	98.64						
639	44.27	39.31	15.658	0.280	99.52						
640	44.24	39.28	15.374	0.406	99.30						
641	43.89	39.00	15.286	0.322	98.49						
642	43.75	38.91	15.626	0.299	98.59						
645	43.85	39.00	15.379	0.466	98.70						
646	43.70	39.52	15.354	0.410	98.98						
647	44.19	39.03	15.667	0.239	99.13						
648	44.43	38.84	15.687	0.183	99.14						
649	44.36	38.87	15.770	0.218	99.22						
650	44.38	39.03	15.853	0.246	99.50						

Table D.5: Profile analysis for wadsleyite shown in Fig. 5.19 measured with EPMA. The experiment was performed at 15 GPa, 1673 K and annealed for 20 minutes. All concentrations are given in weight percent of the oxide. Sums smaller than 98% result from cracks crossed by the profile analysis.

d, μm	MgO	SiO ₂	FeO	NiO	Sum	d, μm	MgO	SiO ₂	FeO	NiO	Sum
0	51.60	42.96	0.053	6.947	101.56	42	56.66	42.79	0.075	0.229	99.76
1	53.39	41.73	0.003	6.349	101.47	43	56.66	43.01	0.035	0.229	99.93
2	53.72	42.24	0.039	4.793	100.80	44	56.67	42.98	0.078	0.107	99.84
3	54.79	42.52	0.045	3.627	100.98	45	56.72	42.86	0.089	0.247	99.91
4	55.81	42.58	0.021	2.432	100.84	46	56.90	43.01	0.035	0.213	100.16
5	56.43	42.85	0.000	1.785	101.06	47	56.59	43.01	0.037	0.235	99.87
6	56.74	43.08	0.050	1.033	100.91	48	56.52	43.04	0.060	0.241	99.86
7	56.51	43.11	0.057	0.839	100.51	49	56.50	43.09	0.077	0.172	99.84
8	56.86	43.06	0.040	0.744	100.71	50	55.99	43.29	0.023	0.216	99.51
9	57.04	43.03	0.044	0.654	100.76	51	56.67	42.86	0.033	0.188	99.74
10	56.50	42.61	0.054	0.556	99.72	52	56.49	42.34	0.041	0.159	99.03
12	55.69	42.41	0.000	0.550	98.65	53	56.33	42.34	0.081	0.279	99.02
13	56.93	43.06	0.064	0.468	100.51	65	57.14	44.20	0.000	0.153	101.49
14	57.13	43.20	0.030	0.484	100.83	66	56.68	43.39	0.010	0.191	100.27
15	57.05	43.02	0.068	0.490	100.63	67	55.64	43.94	0.044	0.101	99.73
16	57.12	43.32	0.004	0.503	100.94	68	56.53	43.36	0.000	0.176	100.06
17	56.70	42.97	0.063	0.503	100.24	69	56.23	43.12	0.031	0.182	99.57
18	56.84	43.25	0.019	0.496	100.60	70	56.34	43.21	0.021	0.135	99.70
19	56.83	42.76	0.023	0.430	100.04	71	54.48	45.13	0.010	0.153	99.77
20	56.45	42.85	0.046	0.330	99.68	72	56.20	43.21	0.044	0.103	99.55
21	57.08	42.97	0.000	0.392	100.45	73	55.23	44.93	0.024	0.157	100.33
22	57.16	42.92	0.031	0.512	100.63	74	53.64	46.56	0.054	0.101	100.35
23	57.05	42.88	0.033	0.414	100.38	75	56.34	43.38	0.081	0.122	99.93
24	56.99	43.09	0.051	0.342	100.47	76	56.58	43.26	0.062	0.084	99.99
25	56.36	42.94	0.067	0.448	99.81	77	56.46	43.32	0.068	0.213	100.06
26	56.74	43.08	0.030	0.445	100.29	78	56.33	42.78	0.037	0.107	99.25
27	56.49	43.17	0.046	0.330	100.03	79	56.48	42.96	0.035	0.116	99.58
29	57.09	43.25	0.003	0.251	100.60	80	56.44	42.92	0.035	0.081	99.47
30	56.04	43.00	0.087	0.272	99.41	81	56.42	43.03	0.078	0.193	99.73
31	56.82	43.19	0.000	0.349	100.36	82	56.76	43.14	0.087	0.081	100.07
32	56.79	43.24	0.040	0.330	100.39	83	56.60	43.18	0.068	0.060	99.91
33	56.97	43.02	0.057	0.351	100.40	84	56.11	43.20	0.064	0.182	99.56
34	56.65	43.17	0.040	0.283	100.14	85	56.65	43.02	0.004	0.050	99.73
35	56.70	42.83	0.044	0.279	99.85	86	56.46	42.87	0.037	0.088	99.46
36	56.81	43.21	0.013	0.238	100.27	87	56.33	43.03	0.084	0.116	99.56
37	56.69	43.15	0.054	0.270	100.17	88	56.46	43.07	0.048	0.223	99.80
38	56.76	43.24	0.054	0.263	100.32	89	56.29	43.07	0.051	0.141	99.56
39	56.82	42.97	0.035	0.248	100.08	90	56.41	42.96	0.091	0.081	99.54
40	57.10	42.97	0.033	0.272	100.37	91	56.63	43.04	0.084	0.182	99.93
41	56.69	42.95	0.008	0.169	99.82	92	56.45	42.92	0.087	0.062	99.51

Table D.5 continued.

d, μm	MgO	SiO ₂	FeO	NiO	Sum	d, μm	MgO	SiO ₂	FeO	NiO	Sum
93	56.46	42.85	0.054	0.107	99.47	145	56.31	42.87	0.091	0.069	99.34
94	56.41	42.69	0.019	0.165	99.29	146	56.38	42.90	0.075	0.062	99.42
95	53.34	41.44	0.060	0.094	94.93	147	56.87	42.85	0.154	0.000	99.87
96	39.30	32.90	0.098	0.159	72.45	148	56.78	42.73	0.154	0.081	99.74
97	56.58	42.11	0.108	0.129	98.93	149	56.50	42.71	0.139	0.113	99.47
98	56.56	42.59	0.064	0.103	99.31	150	55.63	42.93	0.117	0.032	98.72
99	56.60	43.19	0.040	0.144	99.98	151	56.05	42.86	0.154	0.019	99.08
100	56.66	42.85	0.073	0.103	99.69	152	56.60	43.00	0.144	0.116	99.86
102	57.10	42.91	0.071	0.056	100.13	153	56.62	43.00	0.148	0.103	99.87
103	56.63	42.56	0.085	0.144	99.42	154	56.24	42.73	0.161	0.060	99.19
105	56.53	43.24	0.073	0.038	99.88	155	50.33	43.53	0.073	0.113	94.05
109	56.64	42.90	0.098	0.103	99.74	156	40.27	55.35	0.117	0.081	95.82
110	56.77	42.90	0.058	0.038	99.77	157	39.22	58.40	0.098	0.000	97.72
111	56.76	42.84	0.125	0.148	99.86	158	39.35	58.65	0.134	0.073	98.20
112	56.34	42.97	0.064	0.073	99.46	159	39.30	58.49	0.151	0.060	97.99
113	56.87	43.04	0.094	0.090	100.09	160	40.37	57.64	0.086	0.003	98.10
114	56.65	43.17	0.062	0.150	100.02	161	46.17	50.51	0.194	0.000	96.88
115	56.56	43.13	0.058	0.107	99.85	162	50.97	42.21	0.198	0.022	93.41
116	53.32	42.41	0.051	0.034	95.82	163	52.92	43.77	0.252	0.006	96.95
117	56.42	43.68	0.041	0.103	100.24	164	53.82	40.46	0.338	0.000	94.62
118	56.80	42.96	0.071	0.113	99.95	165	41.78	36.36	0.354	0.107	78.60
119	56.62	42.85	0.050	0.041	99.56	166	51.47	41.13	0.383	0.066	93.05
120	56.07	42.28	0.058	0.137	98.55	167	56.76	43.34	0.562	0.003	100.67
121	56.16	43.20	0.084	0.041	99.49	168	56.32	42.85	0.634	0.000	99.80
122	55.80	42.79	0.046	0.113	98.75	169	56.16	43.01	0.723	0.025	99.92
123	56.07	42.48	0.095	0.041	98.69	170	56.52	42.93	1.023	0.122	100.59
124	56.20	43.17	0.024	0.041	99.44	171	55.99	43.07	1.328	0.088	100.48
125	56.37	42.74	0.060	0.022	99.20	172	55.44	42.46	1.582	0.000	99.48
126	56.87	42.96	0.068	0.000	99.89	173	55.40	42.54	1.717	0.028	99.69
127	56.67	42.98	0.095	0.000	99.74	174	54.93	42.46	2.091	0.075	99.56
128	56.17	42.34	0.129	0.107	98.75	175	54.81	42.46	2.300	0.022	99.59
129	53.98	44.08	0.108	0.107	98.27	176	54.32	42.57	2.690	0.019	99.60
136	39.69	59.17	0.108	0.088	99.05	177	54.04	42.39	3.160	0.101	99.69
137	39.59	58.16	0.075	0.013	97.83	178	53.73	42.18	3.521	0.081	99.51
138	40.83	54.07	0.064	0.107	95.07	179	53.24	41.86	4.036	0.135	99.27
139	54.05	44.36	0.125	0.047	98.58	180	53.20	42.07	4.200	0.122	99.60
140	52.10	42.38	0.078	0.182	94.73	181	53.28	41.79	4.703	0.025	99.80
141	56.28	43.29	0.148	0.034	99.74	182	52.88	41.71	5.146	0.078	99.81
142	57.15	43.02	0.138	0.073	100.38	183	52.24	41.79	5.452	0.047	99.53
143	56.47	42.72	0.117	0.073	99.38	188	50.57	41.26	7.685	0.071	99.58
144	56.65	43.03	0.140	0.000	99.82	189	50.14	41.08	7.721	0.150	99.09

Table D.5 continued.

d, μm	MgO	SiO ₂	FeO	NiO	Sum	d, μm	MgO	SiO ₂	FeO	NiO	Sum
190	50.54	41.08	8.143	0.131	99.90	234	45.50	40.00	14.225	0.345	100.07
191	50.01	41.30	8.550	0.140	99.99	235	45.70	40.11	14.169	0.326	100.31
192	47.99	40.07	8.686	0.174	96.92	236	45.72	40.06	13.753	0.239	99.77
193	49.94	41.08	8.816	0.200	100.03	237	45.71	40.09	13.490	0.333	99.63
194	49.41	40.86	9.198	0.200	99.66	238	45.24	40.06	14.477	0.243	100.02
195	49.45	41.01	9.406	0.118	99.98	239	44.39	39.76	16.408	0.313	100.87
196	48.36	40.54	9.524	0.211	98.63	240	45.31	40.16	13.493	0.299	99.26
198	49.79	41.28	9.970	0.112	101.15	241	45.81	40.09	13.617	0.299	99.81
199	48.80	41.14	10.055	0.293	100.29	242	43.96	39.78	15.866	0.391	100.00
200	48.17	40.75	10.620	0.221	99.76	243	42.79	39.30	17.724	0.372	100.18
201	48.45	40.79	10.336	0.209	99.79	244	45.63	39.97	13.773	0.314	99.68
202	48.54	40.59	10.788	0.330	100.24	245	45.28	40.05	13.866	0.267	99.46
203	48.20	40.67	11.044	0.293	100.20	246	43.79	40.30	14.636	0.230	98.95
204	48.20	40.62	11.029	0.323	100.17	247	42.16	39.15	18.223	0.272	99.81
205	47.86	40.61	11.126	0.308	99.90	248	41.44	39.28	19.823	0.415	100.96
206	47.80	40.75	11.713	0.237	100.50	249	41.64	39.34	19.171	0.325	100.48
209	47.38	40.36	11.972	0.205	99.91	250	43.13	39.56	15.907	0.308	98.91
210	47.19	40.39	11.837	0.261	99.67	251	41.50	38.97	19.629	0.372	100.47
211	47.16	40.44	12.099	0.364	100.06	252	43.89	39.63	15.750	0.347	99.62
212	47.30	40.14	12.209	0.289	99.93	253	45.87	40.07	13.795	0.355	100.09
213	47.25	40.42	12.300	0.230	100.20	254	44.06	39.46	17.483	0.267	101.27
214	47.22	40.36	12.188	0.265	100.03	255	44.82	39.82	14.580	0.144	99.36
215	46.99	40.53	12.402	0.342	100.27	256	42.37	39.35	18.720	0.356	100.79
216	46.76	40.30	12.403	0.289	99.75	257	40.72	39.06	19.744	0.458	99.98
217	46.82	40.48	12.667	0.153	100.13	258	43.94	39.49	15.487	0.246	99.16
218	46.28	40.63	12.784	0.326	100.02	259	44.02	39.49	17.252	0.280	101.04
219	46.58	40.48	12.519	0.215	99.79	260	44.37	39.55	15.651	0.181	99.75
220	45.22	40.80	12.156	0.286	98.46	261	42.85	39.45	18.595	0.328	101.22
221	46.72	40.12	12.659	0.342	99.83	262	45.50	40.03	14.072	0.286	99.89
222	46.65	40.25	13.017	0.323	100.23	263	45.70	40.18	13.921	0.256	100.06
223	43.41	39.35	18.554	0.300	101.61	264	45.44	39.80	14.580	0.200	100.02
224	42.33	38.95	18.720	0.305	100.31	265	43.79	39.83	16.629	0.333	100.58
225	41.54	39.03	19.254	0.389	100.22	266	44.68	40.30	14.230	0.316	99.52
226	41.80	38.85	19.188	0.417	100.25	267	45.36	40.27	14.281	0.265	100.17
227	44.34	39.53	15.492	0.279	99.65	268	44.40	39.88	16.163	0.333	100.77
228	45.91	39.75	13.702	0.317	99.68	269	45.46	39.88	13.948	0.241	99.53
229	44.35	39.70	16.468	0.276	100.80	270	45.87	40.15	14.182	0.249	100.46
230	45.19	39.86	14.221	0.220	99.50	271	45.67	40.21	14.154	0.265	100.29
231	45.96	40.14	13.432	0.330	99.86	272	45.79	40.12	13.828	0.215	99.96
232	45.98	40.20	13.626	0.293	100.10	273	45.96	39.79	14.120	0.256	100.13
233	45.68	40.10	13.695	0.246	99.72	274	44.59	39.77	15.547	0.355	100.26

Table D.5 continued.

d, μm	MgO	SiO ₂	FeO	NiO	Sum	d, μm	MgO	SiO ₂	FeO	NiO	Sum
275	42.95	39.25	17.365	0.252	99.81	316	45.25	39.47	14.759	0.326	99.80
276	45.19	39.99	14.564	0.269	100.01	317	42.93	39.27	18.828	0.342	101.37
277	45.90	40.09	13.612	0.350	99.95	318	41.14	39.01	20.306	0.355	100.82
278	45.41	40.08	14.766	0.249	100.51	319	40.60	38.99	20.141	0.295	100.03
279	44.05	39.65	16.693	0.293	100.69	320	40.92	38.88	20.714	0.386	100.90
280	43.22	39.60	16.283	0.308	99.42	321	41.67	39.04	18.901	0.325	99.93
281	45.20	39.95	14.409	0.249	99.81	322	45.44	39.90	14.236	0.304	99.88
282	42.36	39.06	19.299	0.403	101.12	323	45.70	40.13	13.947	0.232	100.01
283	45.64	39.93	14.090	0.241	99.90	324	45.55	39.87	13.939	0.300	99.66
284	45.98	39.97	14.028	0.384	100.36	325	42.01	38.87	20.063	0.411	101.35
285	45.55	39.83	14.061	0.260	99.69	326	43.44	39.33	16.454	0.337	99.57
286	45.70	39.94	14.223	0.247	100.11	327	44.78	39.76	15.653	0.304	100.50
287	45.48	39.97	14.420	0.213	100.08	328	44.37	39.67	15.116	0.322	99.48
288	44.51	40.59	14.217	0.249	99.57	329	45.73	39.86	14.181	0.214	99.99
289	45.40	40.29	14.380	0.309	100.38	330	40.82	38.74	20.566	0.442	100.56
290	45.68	40.01	14.063	0.365	100.12	331	40.70	38.84	20.808	0.377	100.72
291	46.05	40.20	14.330	0.354	100.93	332	40.21	38.67	20.628	0.364	99.87
292	45.79	40.33	14.059	0.238	100.42	333	40.19	38.69	20.397	0.333	99.62
293	45.84	40.18	14.285	0.197	100.50	334	41.13	39.09	19.741	0.277	100.24
294	45.77	40.05	14.189	0.244	100.24	335	44.30	40.06	15.004	0.294	99.66
295	45.92	40.10	14.406	0.260	100.68	336	45.54	40.08	14.163	0.272	100.06
296	45.36	40.16	14.537	0.232	100.29	337	45.85	39.90	13.979	0.276	100.00
297	45.32	39.99	14.442	0.279	100.04	338	45.54	39.96	14.361	0.216	100.08
298	45.56	39.99	14.127	0.279	99.96	339	45.20	39.83	14.865	0.248	100.15
299	44.58	40.36	13.997	0.241	99.17	340	41.98	39.06	19.975	0.462	101.47
300	43.83	39.66	16.620	0.293	100.41	341	40.58	39.03	20.034	0.419	100.06
301	42.13	39.18	17.950	0.321	99.58	342	40.28	38.93	20.103	0.281	99.59
302	45.40	40.15	14.176	0.204	99.93	343	41.62	38.44	15.321	0.319	95.70
303	45.69	40.25	14.584	0.347	100.88	344	45.81	39.79	14.483	0.285	100.36
304	44.95	40.59	14.135	0.229	99.91	345	45.81	39.98	14.248	0.330	100.37
305	44.53	41.06	13.828	0.191	99.61	346	45.50	39.85	13.828	0.295	99.48
306	45.96	40.19	14.259	0.172	100.57	347	45.73	39.93	14.122	0.239	100.02
307	45.73	40.13	14.124	0.263	100.24	348	45.68	40.03	13.996	0.257	99.96
308	43.62	39.42	17.881	0.361	101.28	349	45.53	39.81	14.270	0.274	99.88
309	41.12	39.06	20.069	0.305	100.55	350	45.63	39.77	14.257	0.280	99.93
310	40.59	39.09	19.683	0.523	99.88	351	45.89	39.93	14.433	0.336	100.58
311	40.76	38.69	20.393	0.420	100.27	352	45.44	39.99	13.951	0.289	99.66
312	40.53	39.00	19.978	0.504	100.01	353	45.33	40.03	14.328	0.323	100.00
313	41.19	38.84	19.457	0.411	99.90	354	44.85	39.77	14.203	0.358	99.18
314	44.79	39.58	15.018	0.328	99.71	355	44.23	39.73	14.687	0.330	98.98
315	45.40	39.78	14.159	0.251	99.59	356	43.99	39.45	15.660	0.235	99.34

Table D.5 continued.

d, μm	MgO	SiO ₂	FeO	NiO	Sum
357	42.45	39.36	17.689	0.241	99.74
358	41.67	38.80	19.560	0.400	100.43
359	42.70	38.80	18.807	0.397	100.71
360	42.75	38.92	19.270	0.316	101.25
361	41.21	38.89	19.889	0.440	100.43
362	41.39	38.89	19.497	0.318	100.09
363	41.24	39.29	20.429	0.325	101.28
364	41.70	39.13	19.996	0.284	101.11
365	44.20	39.50	16.897	0.317	100.92
366	44.97	39.79	14.810	0.293	99.86
367	45.07	39.94	14.400	0.387	99.79
368	45.43	39.79	14.275	0.286	99.79
369	45.53	39.85	13.993	0.265	99.64
370	45.54	39.76	14.106	0.336	99.74
371	45.59	39.74	14.276	0.305	99.91
372	45.32	39.77	14.428	0.317	99.84
373	44.80	39.28	14.846	0.342	99.27
374	44.56	39.43	14.284	0.280	98.55
375	45.49	40.40	14.434	0.336	100.66
376	45.38	40.19	14.400	0.323	100.30
377	45.65	40.09	14.400	0.280	100.42
378	45.04	39.84	14.389	0.359	99.62
379	45.15	40.05	14.419	0.229	99.86
380	45.65	39.93	14.623	0.199	100.40
381	45.40	40.11	14.250	0.286	100.05

Table D.6: Profile analysis for ferropericlasite shown in Fig. 5.24 measured with EPMA. The experiment was performed at 8 GPa, 1873 K and annealed for 15 minutes. All concentrations are given in weight percent of the oxide.

d, μm	MgO	FeO	Sum	d, μm	MgO	FeO	Sum
100	86.36	14.03	100.39	182	78.78	21.51	100.29
102	86.26	13.92	100.19	184	77.87	22.28	100.15
104	86.24	13.79	100.04	186	77.29	23.29	100.58
106	86.30	13.89	100.19	188	76.46	24.44	100.89
108	86.05	14.21	100.26	190	74.97	25.93	100.90
110	86.50	14.09	100.59	192	74.26	26.58	100.84
112	86.16	13.92	100.08	194	72.88	27.12	100.00
114	86.51	14.03	100.54	196	72.44	27.85	100.30
116	86.23	13.77	100.00	198	71.37	28.57	99.94
118	86.26	13.73	100.00	200	70.20	29.88	100.08
120	86.42	14.07	100.49	202	69.59	31.06	100.65
122	86.21	14.08	100.28	204	68.58	32.05	100.63
124	86.56	14.18	100.74	206	68.04	32.54	100.58
126	85.98	14.07	100.06	208	67.50	33.21	100.71
128	86.29	13.73	100.01	210	66.55	33.57	100.12
130	86.18	13.78	99.96	212	65.59	34.86	100.45
132	86.23	13.87	100.09	214	65.45	34.49	99.93
134	86.11	13.82	99.92	216	64.75	35.44	100.19
136	86.02	13.90	99.92	218	63.93	35.81	99.74
138	86.03	13.65	99.68	220	63.76	37.42	101.18
140	86.02	13.97	99.98	222	62.97	37.39	100.36
142	86.15	13.77	99.93	224	62.28	37.62	99.90
144	86.18	13.63	99.82	226	62.00	39.05	101.05
146	86.09	14.11	100.20	228	61.39	38.61	100.00
148	86.11	13.96	100.07	230	60.91	39.78	100.69
150	86.04	14.00	100.04	232	60.25	39.73	99.98
152	85.97	13.90	99.87	234	59.96	40.22	100.17
154	85.92	13.99	99.91	236	59.60	40.50	100.10
156	85.91	14.40	100.31	238	58.86	40.90	99.76
158	85.94	14.43	100.36	240	58.47	41.46	99.93
160	85.58	14.58	100.16	242	58.35	41.96	100.31
162	85.38	14.51	99.89	244	57.88	42.62	100.50
164	85.30	14.86	100.15	246	57.47	42.72	100.19
166	84.89	15.01	99.90	248	57.54	42.89	100.43
168	84.18	15.65	99.83	250	56.92	43.18	100.09
170	83.75	16.39	100.15	252	56.35	43.57	99.92
172	83.38	17.00	100.38	254	56.22	44.30	100.52
174	82.93	17.70	100.63	256	56.14	44.34	100.47
176	81.95	18.35	100.30	258	55.86	44.75	100.62
178	81.21	19.48	100.69	260	55.36	45.05	100.41
180	79.99	20.20	100.19	262	55.16	45.48	100.64

Table D.6 continued.

d, μm	MgO	FeO	Sum	d, μm	MgO	FeO	Sum
264	54.84	44.77	99.61	346	49.96	49.81	99.77
266	54.79	45.13	99.92	348	49.95	49.28	99.24
268	54.46	45.69	100.15	350	49.68	49.18	98.86
270	54.21	45.76	99.97	352	49.86	49.61	99.46
272	53.78	45.80	99.58	354	49.96	49.51	99.48
274	53.88	46.77	100.65	356	49.59	50.27	99.86
276	53.75	46.16	99.90	358	49.63	49.87	99.50
278	53.43	46.19	99.62	360	49.81	49.75	99.56
280	53.14	46.17	99.31	362	49.61	49.86	99.47
282	53.15	47.02	100.18	364	49.71	49.88	99.59
284	53.06	46.86	99.92	366	49.42	50.34	99.76
286	52.75	46.91	99.66	368	49.42	49.49	98.91
288	52.48	47.17	99.65	370	49.64	50.16	99.80
290	52.46	47.60	100.06	372	49.45	49.70	99.14
292	52.30	47.64	99.94	374	49.57	50.05	99.62
294	52.01	47.50	99.51	376	49.77	49.89	99.66
296	51.94	47.88	99.82	378	49.57	50.16	99.73
298	51.57	48.14	99.71	380	49.44	50.20	99.64
300	51.67	47.78	99.45	382	49.29	50.16	99.45
302	51.68	48.47	100.15	384	49.36	50.24	99.60
304	51.62	48.16	99.79	386	49.45	49.67	99.13
306	51.12	47.67	98.79	388	49.53	50.02	99.55
308	51.19	48.49	99.68	390	49.33	50.22	99.55
310	51.09	48.48	99.57	392	49.51	50.06	99.57
312	51.15	48.61	99.76	394	49.33	50.07	99.40
314	50.93	48.23	99.16	396	49.31	50.24	99.55
316	50.90	48.64	99.53	398	49.39	50.40	99.78
318	50.75	48.93	99.68	400	49.41	49.58	99.00
320	50.67	48.79	99.46	402	49.42	49.90	99.33
322	50.67	48.97	99.64	404	49.23	50.10	99.33
324	50.67	49.18	99.86	406	49.41	50.16	99.57
326	50.55	48.74	99.29	408	49.45	49.25	98.70
328	50.28	49.12	99.40	410	49.54	49.59	99.13
330	50.26	48.35	98.61	412	49.35	49.73	99.08
332	50.50	49.88	100.37	414	49.23	50.20	99.42
334	50.40	50.14	100.54	416	49.30	50.24	99.53
336	50.32	49.34	99.66	418	49.27	49.77	99.04
338	50.32	49.75	100.07	420	49.17	49.78	98.95
340	50.03	49.50	99.53	422	49.34	49.69	99.03
342	49.83	49.83	99.66	424	49.10	49.97	99.07
344	50.09	49.59	99.68	426	48.99	49.59	98.58

Table D.6 continued.

d, μm	MgO	FeO	Sum
428	49.17	49.62	98.80
430	49.30	50.23	99.54
432	48.95	49.67	98.62
434	49.19	49.99	99.18
436	49.16	49.99	99.15
438	49.41	50.21	99.62
440	49.21	50.22	99.43

Table D.7: Profile analysis for ferropericlasite shown in Fig. 5.25 measured with EPMA. The experiment was performed at 23 GPa, 1851 K and annealed for 183 minutes. All concentrations are given in weight percent of the oxide.

d, μm	MgO	FeO	Sum	d, μm	MgO	FeO	Sum
200	87.23	12.96	100.18	118	55.82	45.67	101.48
198	87.48	13.45	100.93	116	55.19	46.08	101.27
196	87.24	13.19	100.42	114	55.00	46.48	101.48
194	87.29	13.07	100.36	112	54.55	46.89	101.44
192	87.34	13.28	100.62	110	53.98	47.05	101.02
190	87.36	13.15	100.52	108	53.66	47.14	100.80
188	86.86	13.56	100.43	106	53.53	47.37	100.90
186	87.71	13.50	101.21	104	53.04	47.86	100.90
184	87.40	13.25	100.65	102	52.92	47.84	100.76
182	87.24	13.57	100.80	100	52.71	48.67	101.39
180	86.95	13.44	100.39	98	52.30	48.92	101.23
178	86.53	13.45	99.98	96	52.14	48.50	100.64
176	86.43	13.97	100.41	94	51.86	48.83	100.69
174	85.48	14.46	99.94	92	51.59	49.15	100.74
172	84.76	14.91	99.67	90	51.56	49.05	100.61
170	84.07	15.82	99.89	88	51.35	49.69	101.03
168	83.05	16.97	100.02	86	51.33	49.40	100.73
166	83.20	18.27	101.47	84	51.16	49.49	100.65
164	83.44	19.75	103.19	82	51.06	49.87	100.92
162	77.02	21.88	98.90	80	50.44	49.21	99.65
160	77.66	23.72	101.38	78	50.11	50.21	100.32
158	76.32	24.90	101.22	76	50.22	50.00	100.21
156	74.81	26.37	101.18	74	50.04	50.04	100.08
154	73.30	28.06	101.36	72	50.38	49.89	100.26
152	71.36	29.40	100.76	70	50.51	50.27	100.78
150	69.72	31.23	100.95	68	50.43	50.44	100.87
148	68.48	32.96	101.43	66	50.52	50.63	101.15
146	66.64	34.40	101.04	64	50.47	50.84	101.31
144	65.45	35.71	101.16	62	50.29	50.87	101.16
142	64.40	36.75	101.15	60	50.31	50.56	100.86
140	63.22	38.23	101.45	58	50.28	51.13	101.41
138	62.37	38.57	100.94	56	50.30	50.58	100.88
136	61.60	39.84	101.45	54	50.23	51.06	101.29
134	60.90	39.99	100.88	52	50.26	50.32	100.58
132	59.98	41.46	101.44	50	50.25	51.11	101.35
130	59.45	41.59	101.04	48	50.16	50.50	100.66
128	58.31	42.33	100.64	46	49.95	51.01	100.96
126	57.20	43.26	100.46	44	50.30	51.34	101.64
124	57.04	44.13	101.17	42	50.00	51.09	101.08
122	56.39	44.69	101.08	40	50.30	51.16	101.45
120	56.07	44.94	101.01	38	50.02	50.54	100.56

Table D.7 continued.

d, μm	MgO	FeO	Sum
38	50.02	50.54	100.56
36	49.99	50.27	100.25
34	50.28	51.42	101.70
32	50.46	51.15	101.61
30	49.85	50.80	100.65
28	50.24	51.16	101.41
26	50.20	51.22	101.43
24	50.22	50.80	101.02
22	50.10	50.76	100.86
20	50.09	51.05	101.14

Table D.8: Profile analysis for ferropericlasite shown in Fig. 5.26 measured with EPMA. The experiment was performed at 8 GPa, 1873 K and annealed for 20 minutes. All concentrations are given in weight percent of the oxide.

d, μm	MgO	FeO	Sum	d, μm	MgO	FeO	Sum
380	98.25	0.14	98.39	328	67.32	32.12	99.45
379	98.13	0.13	98.27	327	66.99	32.94	99.93
375	97.99	0.21	98.20	326	66.51	32.98	99.49
374	98.42	0.20	98.62	325	66.21	33.45	99.66
372	98.23	0.21	98.44	324	65.40	33.75	99.14
371	98.53	0.25	98.78	323	64.61	33.50	98.11
370	98.41	0.23	98.64	322	64.87	34.56	99.43
369	98.31	0.29	98.60	321	64.81	35.55	100.36
367	97.83	0.27	98.11	320	64.21	35.60	99.81
366	97.84	0.23	98.07	319	63.69	35.88	99.57
360	98.17	0.56	98.73	318	63.36	36.41	99.78
359	97.64	0.90	98.53	317	62.80	36.54	99.34
358	97.38	1.74	99.12	316	62.84	37.25	100.08
357	96.03	2.54	98.57	315	62.17	37.70	99.86
356	95.19	3.73	98.92	314	61.76	37.92	99.68
355	93.74	5.33	99.06	313	61.50	38.02	99.52
354	91.97	7.14	99.11	312	61.21	38.71	99.91
353	89.27	8.82	98.09	311	60.90	39.15	100.05
351	87.26	11.89	99.15	310	60.27	39.05	99.31
350	86.23	13.38	99.61	309	60.52	39.59	100.11
349	85.01	14.55	99.56	308	60.08	39.85	99.93
348	83.88	16.30	100.17	307	59.81	40.14	99.95
347	82.43	17.29	99.72	306	59.43	40.50	99.93
346	81.46	18.14	99.59	305	59.24	40.63	99.87
345	80.69	18.81	99.50	304	59.15	40.74	99.88
344	79.72	19.79	99.51	303	59.00	41.08	100.09
343	78.97	20.76	99.73	302	58.59	40.65	99.24
342	78.02	21.74	99.76	301	58.13	41.29	99.42
341	76.82	22.85	99.68	300	58.38	41.51	99.89
340	76.25	23.43	99.68	299	57.61	41.49	99.10
339	75.27	24.42	99.69	298	57.97	42.02	99.99
338	74.42	25.45	99.87	297	57.61	42.06	99.67
337	73.74	26.33	100.06	296	57.60	42.11	99.71
336	72.71	26.38	99.09	295	57.32	42.72	100.05
335	71.32	27.08	98.40	294	56.89	42.66	99.55
334	71.20	28.32	99.52	293	56.67	43.34	100.01
333	70.43	29.01	99.44	292	56.34	42.71	99.06
332	69.72	29.92	99.64	291	56.66	43.39	100.06
331	69.26	30.50	99.75	290	56.18	43.47	99.65
330	68.72	31.53	100.25	289	55.93	43.69	99.62
329	67.85	31.89	99.74	288	55.77	43.64	99.40

Table D.8 continued.

d, μm	MgO	FeO	Sum	d, μm	MgO	FeO	Sum
286	55.51	43.91	99.43	241	51.64	47.70	99.34
285	55.34	43.89	99.23	240	51.87	47.88	99.74
284	55.34	44.29	99.63	239	51.35	47.84	99.20
283	55.20	44.45	99.65	238	51.65	47.56	99.22
282	55.06	44.82	99.88	237	51.49	47.81	99.30
281	55.12	44.60	99.72	236	51.63	47.96	99.59
280	54.55	45.04	99.59	235	51.47	48.18	99.64
279	54.86	44.90	99.76	234	51.59	47.88	99.47
278	54.48	44.79	99.28	233	51.39	48.18	99.58
277	54.15	45.07	99.21	232	51.30	48.13	99.43
276	54.25	45.28	99.53	231	51.39	48.46	99.84
275	54.16	45.27	99.43	230	51.10	47.75	98.84
274	54.08	45.23	99.32	229	50.56	46.97	97.54
273	53.44	45.47	98.91	228	51.08	48.40	99.48
272	53.83	45.79	99.62	227	50.98	48.02	99.00
271	53.33	45.68	99.01	226	51.08	48.21	99.29
270	53.22	46.13	99.35	225	51.06	48.40	99.45
266	53.41	46.18	99.59	224	50.91	48.32	99.23
265	53.28	46.33	99.61	223	51.03	48.20	99.23
264	53.03	46.32	99.35	222	50.78	48.54	99.32
263	52.84	46.10	98.94	221	51.30	48.06	99.36
262	52.89	46.43	99.32	220	50.82	48.72	99.54
261	52.47	45.96	98.43	219	50.88	48.40	99.28
260	52.70	46.21	98.91	218	51.02	48.49	99.51
259	52.89	47.05	99.94	217	50.98	48.82	99.80
258	52.65	46.63	99.28	216	51.07	48.77	99.84
257	52.96	46.83	99.80	215	50.91	48.74	99.65
256	52.59	47.02	99.60	214	50.88	48.64	99.52
255	51.66	46.82	98.47	213	50.88	48.65	99.53
254	51.99	46.86	98.86	212	50.77	48.90	99.67
253	52.07	47.04	99.11	211	50.76	48.68	99.44
252	52.29	47.13	99.42	210	51.03	48.54	99.57
251	52.20	47.24	99.44	209	50.78	49.02	99.80
250	52.24	47.64	99.88	208	50.99	48.85	99.83
249	52.04	47.53	99.56	207	50.95	49.13	100.08
248	52.36	47.34	99.70	206	50.62	48.96	99.58
247	51.97	47.46	99.43	205	50.77	48.78	99.55
246	51.96	47.67	99.63	204	50.66	48.93	99.60
245	51.68	47.57	99.25	203	50.56	48.82	99.38
244	51.92	47.37	99.28	202	50.51	48.38	98.89
243	51.76	47.94	99.71	201	50.86	49.36	100.22
242	51.81	48.30	100.11	200	50.74	48.85	99.59
241	51.64	47.70	99.34				

Table D.9: Profile analysis for perovskite shown in Fig. 5.36 measured with EDX-STEM. The experiment was performed at 25 GPa, 2023 K and annealed for 483 minutes. X_{FeSiO_3} denotes mole fraction of FeSiO_3 in $(\text{Mg,Fe})\text{SiO}_3$ perovskite. MgO loss was corrected as discussed in Section 5.5.4

$d, \mu\text{m}$	X_{FeSiO_3}
0.105	0.045
0.132	0.047
0.158	0.047
0.184	0.051
0.211	0.047
0.237	0.049
0.263	0.043
0.289	0.037
0.316	0.026
0.342	0.015
0.368	0.012
0.395	0.006
0.421	0.004
0.447	0.002
0.474	0.002
0.500	0.003

Table D.10: Profile analysis for perovskite shown in Fig. 5.37 measured with EDX-STEM. The experiment was performed at 24 GPa, 2133 K and annealed for 1430 minutes. X_{FeSiO_3} denotes mole fraction of FeSiO_3 in $(\text{Mg,Fe})\text{SiO}_3$ perovskite. MgO loss was corrected as discussed in Section 5.5.4

$d, \mu\text{m}$	X_{FeSiO_3}
2.009	0.066
2.113	0.066
2.217	0.066
2.321	0.064
2.425	0.064
2.529	0.061
2.633	0.061
2.737	0.058
2.840	0.056
2.944	0.054
3.048	0.049
3.152	0.048
3.256	0.050
3.360	0.050
3.464	0.046
3.568	0.040
3.672	0.034
3.776	0.033
3.880	0.031
3.984	0.025
4.088	0.022
4.191	0.016
4.295	0.012
4.399	0.009
4.503	0.007
4.607	0.007
4.711	0.003
4.815	0.002
4.919	0.001

Table D.11: Profile analyses for perovskite shown in Fig. 5.39 measured with EDX-STEM. The experiment was performed at 26 GPa, 1973 K and annealed for 570 minutes. X_{FeSiO_3} denotes mole fraction of FeSiO₃ in (Mg,Fe)SiO₃ perovskite. MgO loss was corrected as discussed in Section 5.5.4

d, μm	X_{FeSiO_3}	d, μm	X_{FeSiO_3}	d, μm	X_{FeSiO_3}
0.0	0.107	1.6	0.103	0.0	0.107
0.2	0.113	1.7	0.079	0.1	0.108
0.4	0.112	1.8	0.060	0.2	0.106
0.6	0.115	1.9	0.043	0.3	0.107
0.8	0.114	2.0	0.034	0.4	0.105
1.0	0.114	2.1	0.020	0.5	0.104
1.2	0.114			0.6	0.103
1.4	0.112			0.7	0.101
1.6	0.113			0.8	0.102
1.8	0.111			0.9	0.098
2.0	0.111			1.0	0.097
2.2	0.106			1.1	0.100
2.4	0.091			1.2	0.098
2.6	0.040			1.3	0.096
2.8	0.018			1.4	0.085
3.0	0.010			1.5	0.059
3.2	0.006			1.6	0.036
3.4	0.001			1.7	0.024
3.6	0.001			1.8	0.018
3.8	0.001			1.9	0.014
4.0	0.001			2.0	0.012
4.2	0.001			2.1	0.011
4.4	0.002			2.2	0.009
4.6	0.002			2.3	0.008
4.8	0.002			2.4	0.007
5.0	0.002			2.5	0.006
				2.6	0.006
				2.7	0.005
				2.8	0.004
				2.9	0.004
				3.0	0.004

Appendix E

Example EDX-spectra of silicate perovskite

The example spectra are taken from sample C23, annealed at 24 GPa, 2123 K for 720 min. In Figure E.1 a spectrum of MgSiO_3 perovskite and in E.2 a spectrum of $(\text{Mg,Fe})\text{SiO}_3$ perovskite is shown. The Mo peak appears because scattered electrons produce X-ray emission from the Mo grid. In case of Cu grids, instead of Mo, Cu peaks are observed. Hence, in the Vantage software the Mo or Cu peak were considered for determination of the intensities (software option "present") but the intensities of Cu and Mo were than not used for the calculation of the absorption corrected concentrations. The relative intensity of the Mg peak especially on the Fe-poor side of the diffusion interface indicates Mg loss during the analysis (see Section 5.5.4 for further details). In all analysis performed in this study, spectra were recorded for a lifetime of 60 seconds. The dead time was usually between 15 and 30%.

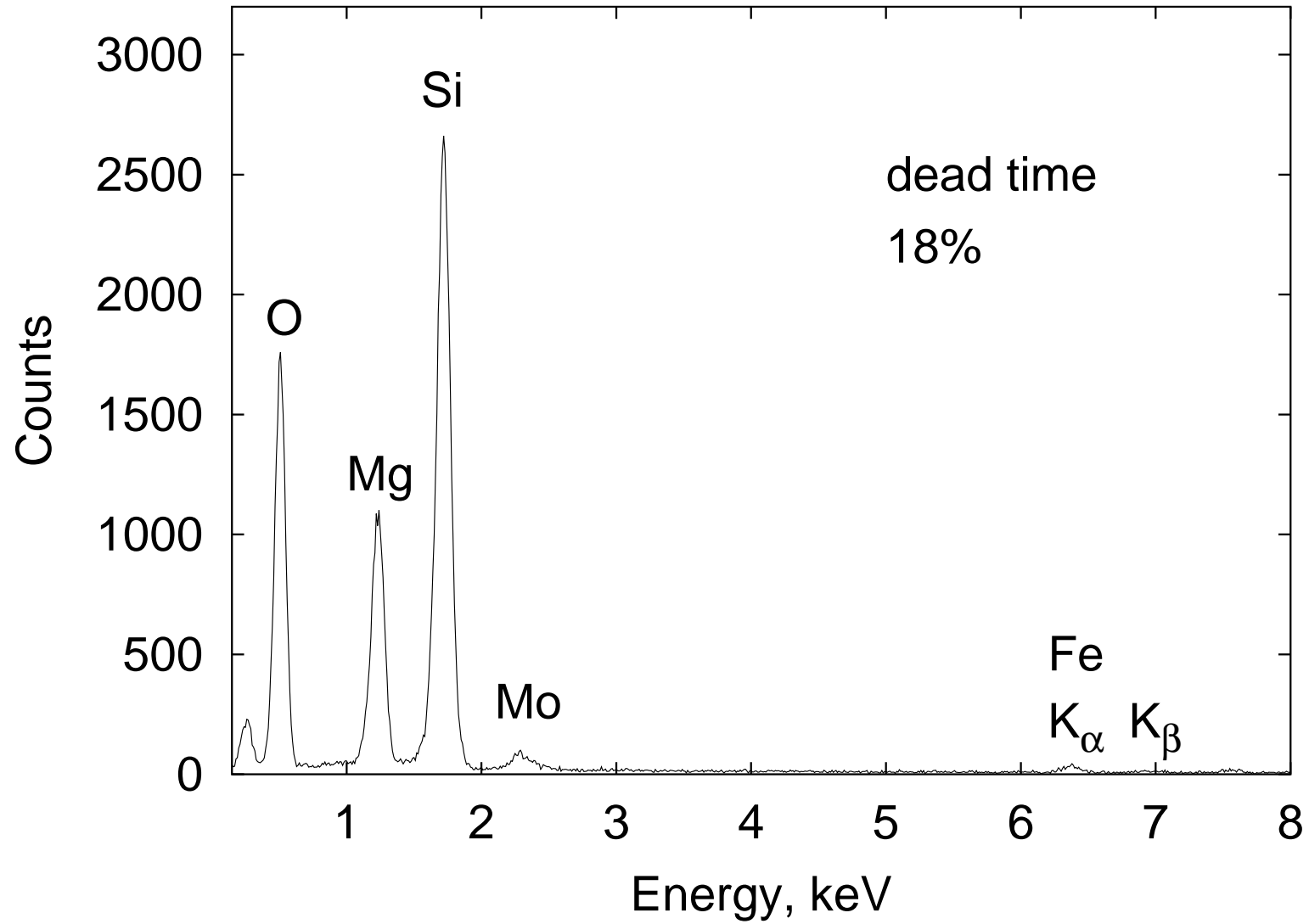


Figure E.1: Example EDX spectrum of an Fe-poor perovskite.

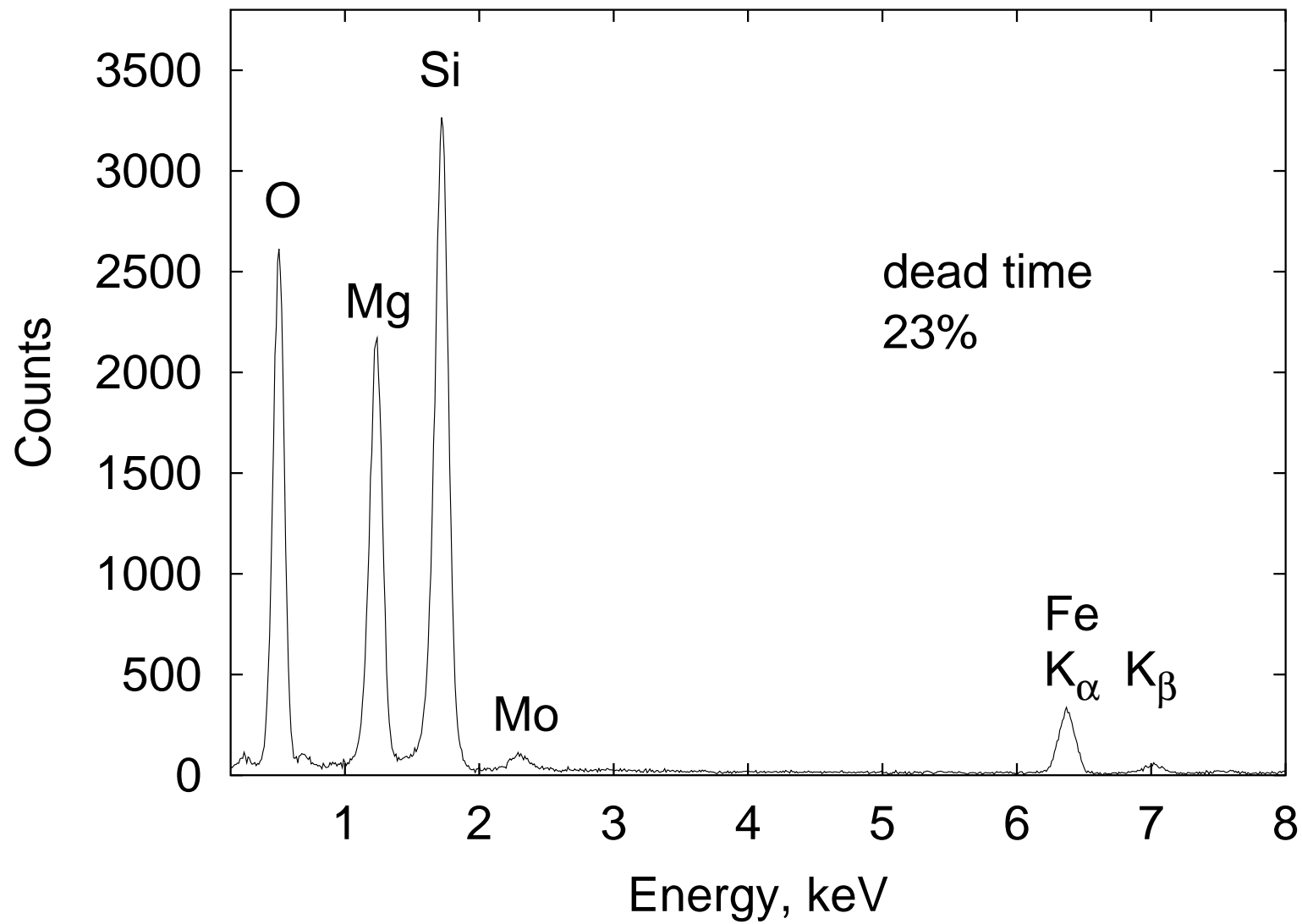


Figure E.2: Example EDX-spectrum of an Fe-rich perovskite.

Bibliography

- Akaogi, M. and Akimoto, S. (1977). Pyroxene-garnet solid solution equilibria in the systems $\text{Mg}_4\text{Si}_4\text{O}_{12}$ - $\text{Mg}_3\text{Al}_2\text{Si}_3\text{O}_{12}$ and $\text{Fe}_4\text{Si}_4\text{O}_{12}$ - $\text{Fe}_3\text{Al}_2\text{Si}_3\text{O}_{12}$ at high pressures and temperatures. *Physics of The Earth and Planetary Interiors*, 15: 90–106.
- Akaogi, M., Ito, E., and Navrotsky, A. (1989). Olivine-modified spinel-spinel transitions in the system Mg_2SiO_4 - Fe_2SiO_4 : Calorimetric measurements, thermochemical calculation and geophysical application. *Journal of Geophysical Research*, 94: 15671–15685.
- Akaogi, M., Ross, N., McMillan, P., and Navrotsky, A. (1984). The Mg_2SiO_4 polymorphs (olivine, modified spinel and spinel) - thermodynamic properties from oxide melt solution calorimetry, phase relations and models of lattice vibrations. *American Mineralogist*, 69: 499–512.
- Allnatt, A. R. and Lidiard, A. B. (1993). *Atomic transport in solids*. Cambridge University Press, Cambridge.
- Anderson, O. L. (1982). The Earth's core and the phase diagram of iron. *Philosophical Transactions of the Royal Society of London*, A306: 21–35.
- Appel, M. and Pask, J. A. (1971). Interdiffusion and moving boundaries in NiO-CaO and NiO-MgO single-crystal couples. *Journal of the American Ceramic Society*, 54: 152–58.
- Badro, J., Fiquet, G., Guyot, F., Rueff, J.-P., Struzhkin, V. V., Vankó, G., and Monaco, G. (2003). Iron partitioning in Earth's mantle: Toward a deep lower mantle discontinuity. *Science*, 300: 789–791.
- Bardeen, J. and Herring, C. (1952). *Imperfections in Nearly Perfect Crystals*. Wiley, New York.

- Barrer, R., Bartholomew, R., and Rees, L. (1963). Ion exchange in porous crystals. Part II - the relationship between self- and exchange-diffusion coefficients. *Journal of Physics and Chemistry of Solids*, 24: 309–317.
- Béjina, F. (1999). Activation volume of Si diffusion in San Carlos olivine: Implications for upper mantle rheology. *Journal of Geophysical Research*, 104(B11): 25529–25542.
- Béjina, F., Jaoul, O., and Liebermann, R. C. (2003). Diffusion in minerals at high pressure: A review. *Physics of the Earth and Planetary Interiors*, 139: 3–20.
- Blank, S. L. and Pask, J. A. (1969). Diffusion of iron and nickel in magnesium oxide single crystals. *Journal of the American Ceramic Society*, 52: 669–675.
- Bocquet, J. L., Brbec, G., and Limoge, Y. (1983). Diffusion in metals and alloys. In Cahn, R. W. and Haasen, P., editors, *Physical Metallurgy*. Elsevier Science Publishers.
- Boehler, R. (1996). Melting of mantle and core materials at very high pressures. *Philosophical Transactions of the Royal Society of London*, 354: 1265–1278.
- Bolfan-Casanova, N., Keppler, H., and Rubie, D. (2000). Water partitioning between nominally anhydrous minerals in the MgO-SiO₂-H₂O system up to 24 GPa: Implications for the distribution of water in the Earth's mantle. *Earth and Planetary Science Letters*, 182: 209–221.
- Bolfan-Casanova, N., Mackwell, S., Keppler, H., McCammon, C., and Rubie, D. (2002). Pressure dependence of H solubility in magnesiowüstite up to 25 GPa: Implications for the storage of water in the Earth's lower mantle. *Geophysical Research Letters*, 29: 89 – 1–4.
- Brady, J. (1995). Diffusion data for silicate minerals, glasses, and liquids. In Ahrens, T., editor, *Mineral Physics & Crystallography - A Handbook of Physical Constants*, volume 2 of *AGU Reference Shelf*, pages 269–290. American Geophysical Union, Washington.
- Brady, J. B. (1975a). Chemical components and diffusion. *American Journal of Science*, 275: 1073–1088.
- Brady, J. B. (1975b). Reference frames and diffusion coefficients. *American Journal of Science*, 275: 954–983.

- Buening, D. K. and Buseck, P. R. (1973). Fe-Mg lattice diffusion in olivine. *Journal of Geophysical Research*, 78: 6852–6862.
- Bygdén, J., Jakobsson, A., Sichen, D., and Seetharaman, S. (1997). Interdiffusion studies in the system MgO-FeO. *Zeitschrift für Metallkunde*, 88: 433–437.
- Carslaw, H. S. and Jaeger, J. C. (1946). *Conduction of Heat in Solids*. Oxford University Press, Oxford.
- Chakraborty, S. (1995). Diffusion in silicate melts. In Stebbins, J. F., McMillan, P. F., and Dingwell, D. B., editors, *Structure, Dynamics and Properties of Silicate Melts*, volume 32 of *Reviews in Mineralogy*, pages 411 – 503. Mineralogical Society of America, Washington.
- Chakraborty, S. (1997). Rates and mechanisms of Fe-Mg interdiffusion in olivine at 980°C–1300°C. *Journal of Geophysical Research*, 102(B6): 12317–12331.
- Chakraborty, S., Farver, J. R., Yund, R. A., and Rubie, D. C. (1994). Mg tracer diffusion in synthetic forsterite and San Carlos olivine as a function of P, T and fO₂. *Physics and Chemistry of Minerals*, 21: 489–500.
- Chakraborty, S. and Ganguly, J. (1991). Compositional zoning and cation diffusion in garnets. In Ganguly, J., editor, *Diffusion, Atomic Ordering and Mass Transport: Selected Topics in Geochemistry*, volume 8 of *Advances in Physical Geochemistry*, pages 120–175. Springer, New York.
- Chakraborty, S. and Ganguly, J. (1992). Cation diffusion in aluminosilicate garnets: experimental determination in spessartine-almandine diffusion couples, evaluation of effective binary diffusion coefficients, and applications. *Contributions to Mineralogy and Petrology*, 111: 74–86.
- Chakraborty, S., Knoche, R., Schulze, H., Rubie, D. C., Dobson, D., Ross, N. L., and Angel, R. J. (1999). Enhancement of cation diffusion rates across the 410-kilometer discontinuity in Earth's mantle. *Science*, 283: 362–365.

- Chen, W. K. and Peterson, N. L. (1980). Iron diffusion and electrical conductivity in magnesiowüstite solid solutions (Mg,Fe)O. *Journal of Physics and Chemistry of Solids*, 41: 335–339.
- Chudinovskikh, L. and Boehler, R. (2001). High-pressure polymorphs of olivine and the 660-km seismic discontinuity. *Nature*, 411(6837): 574–577.
- Clark, A. and Long, J. (1971). The anisotropic diffusion of nickel in olivine. In Sherwood, J., Chadwick, A., Muir, W., and Swinton, F., editors, *Diffusion processes*, pages 511–521. Gordon and Breach, London.
- Cottrell, E., Spiegelman, M., and Langmuir, C. H. (2002). Consequences of diffusive reequilibration for the interpretation of melt inclusions. *Geochemistry Geophysics Geosystems*, 3(5): U1–U26.
- Crank, J. (1979). *The Mathematics of Diffusion*. Oxford University Press, Oxford.
- Darken, L. (1948). Diffusion, mobility and their interrelation through free energy in binary metallic systems. *Am. Inst. Mining Metall Engineers Trans.*, 175: 184–201.
- Deer, W. A., Howie, R. A., and Zussman, J. (1992). *An Introduction to the Rock-Forming Minerals*. Longman Scientific & Technical, Harlow.
- Denbigh, K. (1981). *The Principles of Chemical Equilibrium*. Cambridge University Press, Cambridge.
- Dubrovinsky, L. S., Dubrovinskaia, N., Annersten, H., Hålenius, E., and Harryson, H. (2000a). Stability of (Mg_{0.5}Fe_{0.5})O and (Mg_{0.8}Fe_{0.2})O magnesiowüstites in the lower mantle. *European Journal of Mineralogy*, 13: 857–861.
- Dubrovinsky, L. S., Dubrovinskaia, N., Saxena, S. K., Annersten, H., Hålenius, E., Harryson, H., Tutti, F., Rekhi, S., and Le Bihan, T. (2000b). Stability of ferropericlasite in the lower mantle. *Science*, 289(5478): 430–432.
- Dubrovinsky, L. S., Saxena, S. K., and Lazor, P. (1998). High-pressure and high-temperature in situ X-ray diffraction study of iron and corundum to 68 GPa using internally heated diamond anvil cell. *Physics and Chemistry of Minerals*, 25: 434–441.

- Duffy, T. S., Hemley, R. J., and Mao, H. K. (1995). Equation of state and shear strength at multimegabar pressures: Magnesium oxide to 227 GPa. *Physical Review Letters*, 74: 1371–1374.
- Dziewonski, A. M. and Anderson, D. L. (1981). Preliminary reference Earth model. *Physics of the Earth and Planetary Interiors*, 25: 297–356.
- Edington, J. W. (1976). *The Operation and Calibration of the Electron Microscope*, volume 1 of *Monographs in practical electron microscopy in materials science, Philips technical library*. MacMillan.
- Einstein, A. (1905). Eine neue Bestimmung der Moleküldimension. *Annalen der Physik*, page 549.
- Eremets, M. (1996). *High Pressure Experimental Methods*. Oxford University Press.
- Farber, D. L., Williams, Q., and Ryerson, F. J. (2000). Divalent cation diffusion in Mg₂SiO₄ spinel (ringwoodite), β phase (wadsleyite), and olivine: Implications for the electrical conductivity of the mantle. *Journal of Geophysical Research*, 105(1): 513–529.
- Fick, A. (1855). Über Diffusion. *Poggendorff's Annalen der Physik und Chemie*, 94: 59–86.
- Finger, L., Hazen, R., Zhang, J., Ko, J., and Navrotsky, A. (1993). The effect of Fe on the crystal structure of wadsleyite β – (Mg_{1-x}Fe_x)₂SiO₄, 0.00 ≤ x ≤ 0.40. *Physics and Chemistry of Minerals*, 19: 361–368.
- Freer, R. (1980). Bibliography: self diffusion and impurity diffusion in oxides. *Journal of Materials Science*, 15: 803–824.
- Frost, B. (1991). Introduction to oxygen fugacity and its petrologic importance. In Lindsley, D., editor, *Oxide Minerals: Petrologic and Magnetic Significance*, volume 25 of *Reviews in Mineralogy*. Mineralogical Society of America, Washington, D.C.
- Frost, D., Poe, B., Trønnes, R., Liebske, C., Duba, A., and Rubie, D. (2003). A new large-volume multianvil system. *Physics of the Earth and Planetary Interiors*, submitted.

- Frost, D. J. and Langenhorst, F. (2002). The effect of Al_2O_3 on Fe-Mg partitioning between magnesiowustite and magnesium silicate perovskite. *Earth and Planetary Science Letters*, 199: 227–241.
- Gaetani, G. A. and Watson, E. B. (2002). Modeling the major-element evolution of olivine-hosted melt inclusions. *Chemical Geology*, 183(1-4): 25–41.
- Ganguly, J. (2002). Diffusion kinetics in minerals: Principles and applications to tectono-metamorphic processes. *EMU Notes in Mineralogy*, 4: 271–309.
- Ganguly, J., Bhattacharya, R. N., and Chakraborty, S. (1988). Convolution effect in the determination of compositional profiles and diffusion coefficients by microprobe step scans. *American Mineralogist*, 73: 901–909.
- Gessmann, C. K. and Rubie, D. C. (2000). The origin of the depletions of V, Cr and Mn in the mantles of the Earth and Moon. *Earth and Planetary Science Letters*, 184: 95–107.
- Getting, I. C. and Kennedy, G. C. (1970). Effect of pressure on the emf of chromel-alumel and platinum-platinum 10% rhodium thermocouples. *Journal of Applied Physics*, 41(11): 4552–4562.
- Ghez, R. (1988). *A Primer of Diffusion Problems*. Joh Wiley & Sons, Inc.
- Graham (1987). The multianvil press. In Sammis, C. G. and Henyey, T. L., editors, *Geophysics Part A, Laboratory Measurements*, Methods of experimental physics. Academic Press, Orlando.
- Harrison, L. (1961). *Trans. Faraday Soc.*, 57: 1191.
- Hashin, Z. and Shtrikman, S. (1962). A variational approach to the theory of the effective magnetic permeability of multiphase materials. *Journal of Applied Physics*, 33: 3125–3131.
- Haussühl, S. (1983). *Kristallphysik*. Physik Verlag, Verlag Chemie.
- Heinrich, K. F. J. and Newbury, D. E. (1991). *Electron Probe Quantification*. Plenum Press, New York and London.

- Hermeling, J. and Schmalzried, H. (1984). Tracerdiffusion of the Fe-cations in olivine ($\text{Fe}_x\text{Mg}_{1-x}$) 2SiO_4 (III). *Physics and Chemistry of Minerals*, 11: 161–166.
- Herzberg, C. and Zhang, J. (1996). Melting experiments on anhydrous peridotite KLB-1: Compositions of magmas in the upper mantle and transition zone. *Journal of Geophysical Research*, 101(B4): 8271–8295.
- Herzig, C. and Mishin, Y. (1998). Grain boundary diffusion in metals. In Kärger, J., Heitjans, P., and Haberland, R., editors, *Diffusion in Condensed Matter*, pages 90–115. Vieweg u. Sohn Verlag.
- Hofmann, A. W. (1997). Mantle geochemistry: the message from oceanic volcanism. *Nature*, 385: 219–229.
- Holzappel, C., Rubie, D., Mackwell, S., and Frost, D. (2003). Effect of pressure on Fe-Mg interdiffusion in ($\text{Fe}_x\text{Mg}_{1-x}$)O, ferropericlase. *Physics of the Earth and Planetary Interiors*, 139: 21–34.
- Holzheid (1996). *Aktivitäten von Metalloxiden geochemisch relevanter Elemente in silikatischen Schmelzen und deren Implikationen für die Kernbildung der Erde*. PhD thesis, University of Cologne.
- Huebner, J. S. (1971). Buffering techniques for hydrostatic systems at elevated pressures. In Ulmer, G., editor, *Research Techniques for High Pressure and High Temperature*, pages 146–177. Springer.
- Irifune, T. (1993). Phase transformations in the Earth's mantle and subducting slabs; Implications for their compositions, seismic velocity and density structures and dynamics. *Island Arc*, 2: 55–71.
- Irifune, T. (1994). Absence of an aluminous phase in the upper part of the Earth's lower mantle. *Nature*, 370: 121–123.
- Irifune, T. (2002). Application of synchrotron radiation and Kawai-type apparatus to various studies in high-pressure mineral physics. *Mineralogical Magazine*, 66(5): 769–790.

- Irifune, T., Naka, H., Sanehira, T., Inoue, T., and Funakoshi, K. (2002). In situ X-ray observations of phase transitions in MgAl_2O_4 spinel to 40 GPa using multianvil apparatus with sintered diamond anvils. *Physics and Chemistry of Minerals*, 29: 645–654.
- Irifune, T., Nishiyama, N., Kuroda, K., Inoue, T., Isshiki, M., Utsumi, W., Funakoshi, K., Urakawa, S., Uchida, T., Katsura, T., and Ohtaka, O. (1998). The postspinel phase boundary in Mg_2SiO_4 determined by in situ X-ray diffraction. *Science*, 279: 1693–1700.
- Ita, J. and Cohen, R. E. (1997). Effects of pressure on diffusion and vacancy formation in MgO from nonempirical free-energy integrations. *Physical Review Letters*, 79: 3198–3201.
- Ita, J. and Cohen, R. E. (1998). Diffusion in MgO at high pressure: Implications for lower mantle rheology. *Geophysical Research Letters*, 25: 1095–1098.
- Ito, M. and Takahashi, E. (1989). Post-spinel transformations in the system $\text{Mg}_2\text{SiO}_4\text{-Fe}_2\text{SiO}_4$ and some geophysical implications. *Journal of Geophysical Research*, 94: 10637–10646.
- Ito, M., Yurimoto, H., Morioka, M., and Nagasawa, H. (1999). Co^{2+} and Ni^{2+} diffusion in olivine determined by secondary ion mass spectrometry. *Physics and Chemistry of Minerals*, 26: 425–431.
- Jackson, I. and Rigden, S. M. (1998). Composition and temperature of the Earth's mantle: Seismological models interpreted through experimental studies of Earth materials. In Jackson, I., editor, *The Earth's Mantle: Composition, Structure, and Evolution*, page 566. Cambridge University Press, Cambridge.
- Jakobsson, A. (1996). Diffusion studies in the system NiO-MgO using high temperature X-ray technique. *Zeitschrift für Metallkunde*, 87: 55–60.
- Jaoul, O., Bertran-Alvarez, Y., Liebermann, R. C., and Price, G. D. (1995). Fe-Mg interdiffusion in olivine up to 9 GPa at $T = 600\text{-}900^\circ\text{C}$; experimental data and comparison with defect calculations. *Physics of the Earth and Planetary Interiors*, 89: 199–218.
- Jeanloz, R. and Thompson, A. B. (1983). Phase transitions and mantle discontinuities. *Rev. Geophys. Space Phys.*, 21: 51–74.

- Jost, W. and Hauffe, K. (1972). *Diffusion - Methoden der Messung und Auswertung*, volume 1 of *Fortschritte der physikalischen Chemie*. Dr. Dietrich Steinkopff Verlag, Darmstadt.
- Jurewicz, A. J. G. and Watson, E. B. (1988). Diffusion in olivine xenocrysts, with applications to petrology and mineral physics. *Contributions to Mineralogy and Petrology*, 99: 186–201.
- Karato, S.-I. (1981). Rheology of the lower mantle. *Physics of the Earth and Planetary Interiors*, 24: 1–14.
- Karato, S.-I. and Murthy, V. R. (1997). Core formation and chemical equilibrium in the Earth - I. Physical considerations. *Physics of the Earth and Planetary Interiors*, 100: 61–79.
- Kato, T. and Kumazawa, M. (1985). Effect of high-pressure on the melting relation in the system Mg_2SiO_4 - $MgSiO_3$. *J Phys Earth*, 33: 513–524.
- Katsura, T. and Ito, E. (1989). The system Mg_2SiO_4 - Fe_2SiO_4 at high pressures and temperatures: Precise determination of stabilities of olivine, modified spinel, and spinel. *Journal of Geophysical Research*, 94(B11): 15663–15670.
- Katsura, T., Yamada, H., Shinmei, T., Kubo, A., Ono, S., Kanzaki, M., Yoneda, A., Walter, M., Ito, E., Urakawa, S., Funakoshi, K., and Utsumi, W. (2003). Post-spinel transition in Mg_2SiO_4 determined by high P-T in situ X-ray diffractometry. *Physics of the Earth and Planetary Interiors*, 136: 11–24.
- Kawai, N. and Endo, S. (1970). The generation of ultrahigh hydrostatic pressures by a split sphere apparatus. *Review of Scientific Instruments*, 41: 1178–1181.
- Kawai, N., Togaya, M., and Onodera, A. (1973). *Proc. Jpn Acad.*, 49: 623–626.
- Kleine, T., Münker, C., Mezger, K., and Palme, H. (2002). Rapid accretion and early core formation on asteroids and the terrestrial planets from Hf-W chronometry. *Nature*, 418: 952–955.
- Kohlstedt, D. L., Keppler, H., and Rubie, D. C. (1996). Solubility of water in the α , β , and γ phases of $(Mg,Fe)_2SiO_4$. *Contrib. Mineral. Petrol.*, 123: 345–357.

- Langenhorst, F. (1995). Thermal and shock metamorphism of the Tenham chondrite: A TEM examination. *Geochimica et Cosmochimica Acta*, 59(9): 1835–1845.
- Lauterbach, S. (2000). *Der Oxidationsgrad des Eisens im unteren Mantel: Eine Studie des Fe³⁺-Gehaltes des Silikat-Perowskites in Abhängigkeit seines Al-Gehaltes mit Mössbauer-Spektroskopie und Elektronen-Energie-Verlust-Spektroskopie (EELS)*. phd, Universität Bayreuth.
- Lauterbach, S., McCammon, C. A., van Aken, P., Langenhorst, F., and Seifert, F. (2000). Mössbauer and ELNES spectroscopy of (Mg,Fe)(Si,Al)O₃ perovskite: A highly oxidised component of the lower mantle. *Contributions to Mineralogy and Petrology*, 138(1): 17–26.
- Li, J. and Agee, C. B. (1996). Geochemistry of mantle-core formation at high pressure. *Nature*, 381: 686–689.
- Li, J. and Agee, C. B. (2001). The effect of pressure, temperature, oxygen fugacity and composition on partitioning of nickel and cobalt between liquid Fe-Ni-S alloy and liquid silicate: Implications for the Earth's core formation. *Geochimica et Cosmochimica Acta*, 65(11): 1821–1832.
- Liebermann, R. C. and Wang, Y. (1992). Characterization of sample environment in a uniaxial split-sphere apparatus. In Syono, Y. and Manghnani, M. H., editors, *High-pressure research: Application to earth and planetary sciences*. American Geophysical Union, Washington, D.C.
- Liebske, C., Frost, D., Tronnes, R., Langenhorst, F., McCammon, C., and Rubie, D. (2003). The oxidation state of iron in the hadean lower mantle. *Geophysical Research Abstracts*, 5(06808).
- Litasov, K. and Ohtani, E. (2003). Stability of various hydrous phases in CMAS pyrolite-H₂O system up to 25 GPa. *Physics and Chemistry of Minerals*, 30: 147–156.
- Liu, L. (1975). Post-oxide phases of forsterite and enstatite. *Geophys. Res. Lett.*, 2: 417–419.
- Mackwell, S., Bystricky, M., and Sproni, C. (2004). Fe-Mg interdiffusion in (Mg,Fe)O. *Physics and chemistry of minerals*, submitted.

- Mackwell, S., Dimos, D., and Kohlstedt, D. (1988). Transient creep of olivine: Point-defect relaxation times. *Philosophical Magazine A*, 57: 779–789.
- Manning, J. (1968). *Diffusion kinetics for atoms in crystals*. Princeton Univ. Press, Princeton, NJ.
- Mao, H.-K. and Bell, P. (1971). Behavior of thermocouples in the single-stage piston-cylinder apparatus. *Carnegie Institution of Washington Yearbook*, 69: 207–216.
- Mapother, D., Crooks, H., and Mautter, J. (1950). Self-diffusion of sodium in sodium chloride and sodium bromide. *The Journal of Chemical Physics*, 18: 1231–1236.
- McCammon, C. (2002). From diamonds to defects: New ideas about the Earth's interior. *Hyperfine Interactions*, 141/142: 73–81.
- McDonough, W. F. and Sun, S.-S. (1995). The composition of the Earth. *Chemical Geology*, 120: 223–253.
- McMillan, P. and Akaogi, M. (1987). Raman spectra of β - Mg_2SiO_4 (modified spinel) and γ - Mg_2SiO_4 (spinel). *American Mineralogist*, 72: 361–364.
- Mei, S. and Kohlstedt, D. (2000). Influence of water on plastic deformation of olivine aggregates 1. Diffusion creep regime. *Journal of Geophysical Research*, 105(B9): 21457–21469.
- Meißner, E. (2000). *Messung von kurzen Konzentrationsprofilen mit Hilfe der analytischen Transmissionselektronenmikroskopie (TEM-EDX) am Beispiel der Bestimmung von Diffusionskoeffizienten für die Mg-Fe Interdiffusion in Olivin*. phd, Universität Bayreuth.
- Meißner, E., Sharp, T., and Chakraborty, S. (1998). Quantitative measurement of short compositional profiles using analytical transmission electron microscopy. *American Mineralogist*, 83: 546–552.
- Mills, D., Parker, S., and Wall, A. (1991). The effect of pressure on Schottky pair formation in mgo - a lattice dynamic approach. *Philosophical Magazine A*, 65(5): 1133–1144.

- Misener, D. J. (1974). Cationic diffusion in olivine to 1400°C and 35 kbars. In Hoffmann, A. W., Gilletti, B. J., Yoder, H. S., and Yund, R. A., editors, *Geochemical Transports and Kinetics*, pages 117–129. Carnegie Institution of Washington.
- Mitchell, R. H. (2002). *Perovskites - Modern and Ancient*. Almaz Press, Ontario.
- Moore, P. B. and Smith, J. V. (1970). Crystal structure of β - Mg_2SiO_4 : Crystal-chemical and geophysical implications. *Physics of the Earth and Planetary Interiors*, 3: 166–177.
- Morioka, M. and Nagasawa, H. (1991). Ionic diffusion in olivine. In Ganguly, J., editor, *Diffusion, Atomic ordering and mass transport*, volume 8 of *Advances in Physical Geochemistry*. Springer, New York.
- Morishima, H., Kato, T., Suto, M., Ohtani, E., Urakawa, S., Utsumi, W., Shimomura, O., and Kikegawa, T. (1994). The phase boundary between α and β - Mg_2SiO_4 determined by in situ X-ray observation. *Science*, 265: 1202–1203.
- Nakamura, A. and Schmalzried, H. (1983). On the nonstoichiometry and point defects of olivine. *Physics and Chemistry of Minerals*, 10: 27–37.
- Nakamura, A. and Schmalzried, H. (1984). On the Fe^{2+} - Mg^{2+} interdiffusion in olivine (II). *Ber. Bunsenges. Phys. Chem.*, 88: 140–145.
- Newbury, D. E., Joy, D. C., Echlin, P., Fiori, C., and Goldstein, J. I. (1984). *Advanced Scanning Electron Microscopy and X-Ray Microanalysis*. Plenum Press, New York and London.
- Nye, J. F. (1985). *Physical Properties of Crystals*. Oxford University Press.
- Ohtani, E., Irifune, T., Hibberson, W., and Ringwood, A. E. (1987). Modified split-sphere guide block for practical operation of a multiple-anvil apparatus. *High Temperatures - High Pressures*, 19: 523–529.
- Ohtani, E., Kumazawa, M., Kato, T., and Irifune, T. (1982). Melting of various silicates at elevated pressures. In Akimoto, S. and Manghnani, M. H., editors, *High-pressure research in geophysics*, pages 259–270. D. Reidel.

- O'Neill, H. S. and Pownceby, M. I. (1993). Thermodynamic data from redox reactions at high temperatures. I. An experimental and theoretical assessment of the electrochemical method using stabilized zirconia electrolytes, with revised values for the Fe-FeO, Co-CoO, Ni-NiO and Cu-Cu₂O oxygen buffers, and new data for the W-WO₂ buffer. *Contributions to Mineralogy and Petrology*, 114: 296–314.
- O'Neill, H. S. C. and Palme, H. (1998). Composition of the silicate Earth: Implications for accretion and core formation. In Jackson, I., editor, *The Earth's Mantle: Composition, Structure, and Evolution*, pages 3–126. Cambridge University Press, Cambridge.
- Ono, S., Katsura, T., Ito, E., Kanzaki, M., Yoneda, A. and Walter, S., Urakawa, W., Utsumi, K., and Funakoshi, K. (2001). In situ observation of ilmenite-perovskite phase transition using synchrotron radiation. *Geophysical Research Letters*, 28: 835–838.
- Paterson, M. (1982). The determination of hydroxyl by infrared absorption in quartz, silicate glasses and similar materials. *Bull. Mineral.*, 105: 20–29.
- Petry, C. (1999a). Abschlußbericht zur Sachbeihilfe II C 7 - PA 346/16-1.
- Petry, C. (1999b). *Experimente zur Ni-Diffusion in Olivin, Kalibration des Ni-Fe / Metall-Olivin - Austauschthermometers und deren Anwendung in der Kosmochemie*. PhD thesis, University of Cologne.
- Petry, C., Chakraborty, S., and Palme, H. (2003). Experimental determination of Ni diffusion coefficients in olivine and their dependence on temperature, composition, oxygen fugacity, and crystallographic orientation. submitted.
- Philibert, J. (1991). *Atom Movements - Diffusion and Mass Transport in Solids*. Les Editions de Physique, Les Ulis.
- Poirier, J.-P. (2000). *Introduction to the Physics of the Earth's Interior*. Cambridge University Press, Cambridge.
- Poirier, J.-P. and Liebermann, R. (1984). On the activation volume for creep and its variation with depth in the Earth's lower mantle. *Physics of the Earth and Planetary Interiors*, 35: 283–293.

- Pownceby, M. I. and O'Neill, H. S. (1994). Thermodynamic data from redox reactions at high temperatures. III. activity-composition relations in Ni-Pd alloys from EMF measurements at 850-1250 K, and calibration of the NiO + Ni-Pd assemblage as a redox sensor. *Contributions to Mineralogy and Petrology*, 116: 327–339.
- Putnis, A. (1992). *Introduction to Mineral Sciences*. Cambridge University Press, Cambridge.
- Ratkowsky, D. A. (1983). *Nonlinear regression modeling*, volume 48 of *STATISTICS: textbooks and monographs*. Dekker, New York.
- Reed, S. (1996). *Electron Microprobe Analysis and Scanning Electron Microscopy in Geology*. Cambridge University Press, Cambridge.
- Reed, S. J. B. (1975). *Electron Microprobe Analysis*. Cambridge Monographs on Physics. Cambridge University Press, Cambridge.
- Ride, R. (1991). *Handbook of Chemistry and Physics*. CRC Press, Inc.
- Rigby, E. B. and Cutler, I. B. (1965). Interdiffusion studies of system FeO-MgO. *Journal of the American Ceramic Society*, 48: 95–99.
- Righter, K. (2003). Metal-silicate partitioning of siderophile elements and core formation in the early Earth. *Annual Reviews of Earth and Planetary Science*, 31: 135–174.
- Righter, K., Drake, M. J., and Yaxley, G. (1997). Prediction of siderophile element metal-silicate partition coefficients to 20 GPa and 2800°C: The effects of pressure, temperature, oxygen fugacity, and silicate and metallic melt compositions. *Physics of the Earth and Planetary Interiors*, 100(1-4): 115–134.
- Rubie, D. (1993). Mechanisms and kinetics of reconstructive phase transformations in the Earth's mantle. In Luth, R., editor, *Short Course Handbook on Experiments at High Pressure and Applications to the Earth's Mantle*, pages 247–303. Mineralogical Association of Canada, Edmonton.
- Rubie, D., Fortenfant, S., and Gessmann, C. (2000). Kinetics of reactions between liquid iron and manganowüstite at high pressure. *Eos Trans.*, 81 (48): Fall Meet. Suppl., Abstract V61A-03.

- Rubie, D. C. (1999). Characterizing the sample environment in multianvil high-pressure experiments. *Phase Transitions*, 68: 431–451.
- Rubie, D. C., Karato, S., Yan, H., and O'Neill, H. S. C. (1993). Low differential stress and controlled chemical environment in multianvil high-pressure experiments. *Physics and Chemistry of Minerals*, 20: 315–322.
- Rubie, D. C., Melosh, H., Reid, J., Liebske, C., and Righter, K. (2003). Mechanisms of metal-silicate equilibration in the terrestrial magma ocean. *Earth and Planetary Science Letters*, 205(3-4): 239–255.
- Rushmer, T., Minarik, W. G., and Taylor, G. J. (2000). Physical processes of core formation. In Canup, R. and Righter, K., editors, *Origin of the Earth and Moon*. Univ. of Arizona Press.
- Sachs, L. (1997). *Angewandte Statistik: Anwendung statistischer Methoden*. Springer-Verlag.
- Salje (1990). *Phase Transitions in Ferroelastic and Co-elastic Crystals*. Cambridge University Press, Cambridge.
- Sammis, C. G., Smith, J. C., and Schubert, G. (1981). A critical assessment of estimation methods for activation volume. *Journal of Geophysical Research*, 86(B11): 10707–10718.
- Schmalzried, H. (1995). *Chemical Kinetics of Solids*. Verlag Chemie.
- Scott, V. D., Love, G., and Reed, S. J. B. (1995). *Quantitative Electron-Probe Microanalysis*. Ellis Horwood Limited, Hertfordshire.
- Sempolinski, D. and Kingery, W. (1980). Ionic conductivity and magnesium vacancy mobility in magnesium oxide. *Journal of the American Ceramic Society*, 63: 664–669.
- Shannon, M. C. and Agee, C. B. (1998). Percolation of core melts at lower mantle conditions. *Science*, 280: 1059–1061.
- Shen, G. and Heinz, D. (1998). High-pressure melting of deep mantle and core materials. In Hemley, R. J., editor, *Ultrahigh-pressure mineralogy: Physics and chemistry of the Earth's*

- deep interior*, volume 37 of *Reviews in Mineralogy*, pages 525–590. Mineralogical Society of America, Washington, D.C.
- Shewmon, P. (1989). *Diffusion in Solids*. The Minerals, Metals & Materials Society, Warrendale, Pennsylvania.
- Shim, S. H., Duffy, T. S., and Shen, G. Y. (2001a). The post-spinel transformation in Mg_2SiO_4 and its relation to the 660-km seismic discontinuity. *Nature*, 411(6837): 571–574. Article NATURE.
- Shim, S. H., Duffy, T. S., and Shen, G. Y. (2001b). Stability and structure of MgSiO_3 perovskite to 2300 kilometer depth in Earth's mantle. *Science*, 293(5539): 2437–2440.
- Shimozuku, T., Kubo, T., and Ohtani, E. (2002). Cation diffusion of wadsleyite. *The review of high pressure science and technology, special issue*, 12.
- Smith, G. D. (1985). *Numerical Solution of Partial Differential Equations - Finite Difference Methods*. Oxford applied mathematics and computing science series. Clarendon Press, Oxford.
- Solomatov, V. S., El-Khozondar, R., and Tikare, V. (2002). Grain size in the lower mantle: constraints from numerical modeling of grain growth in two-phase systems. *Physics of the Earth and planetary interiors*, 129: 265–282.
- Solomatov, V. S. and Stevenson, D. J. (1994). Can sharp seismic discontinuities be caused by non-equilibrium phase transformations? *Earth and Planetary Science Letters*, 125: 267–279.
- Spain, I. L. and Paauwe, J. (1977a). *High Pressure Technology*, volume 1. Marcel Dekker, Inc, New York.
- Spain, I. L. and Paauwe, J. (1977b). The measurement of pressure and temperature in high pressure systems. In Spain, I. L. and Paauwe, J., editors, *High Pressure Technology*, volume I, pages 281–313. Dekker, New York.
- Stevenson, D. J. (1990). Fluid dynamics of core formation. In Newsom, H. E. and Jones, J. H., editors, *Origin of the Earth*, pages 231–249. Oxford University Press, New York.

- Suzuki, A., Ohtani, E., Morishima, H., Kubo, T., Kanbe, Y., Kondo, T., Okada, T., Terasaki, H., Kato, T., and Kikigawa, T. (2000). In situ determination of the phase boundary between wadsleyite and ringwoodite in Mg_2SiO_4 . *Geophysical Research Letters*, 27: 803–806.
- Thibault, Y. and Walter, M. J. (1995). The influence of pressure and temperature on the metal/silicate partition coefficients of Ni and Co in a model C1 chondrite and implications for metal segregation in a deep magma ocean. *Geochimica et Cosmochimica Acta*, 59: 991–1002.
- Trønnes, R. G. (2000). Melting relations and major element partitioning in an oxidized bulk Earth model composition at 15–26 GPa. *LITHOS*, 53 (3–4): 233–245.
- Trønnes, R. G. and Frost, D. J. (2002). Peridotite melting and mineral-melt partitioning of major and minor elements at 22–24.5 GPa. *Earth and Planetary Science Letters*, 197: 117–131.
- Tsuzaki, E. and Takahashi, E. (1992). Pressure correction on thermocouple emfs with a multi-anvil apparatus. *Int. Geol. Congr. 29th Abstr. 1*, page 58.
- van Aken, P., Liebscher, B., and Styrsa, V. (1998). Quantitative determination of iron oxidation states in minerals using Fe $L_{2,3}$ -edge electron energy-loss near-edge structure spectroscopy. *Physics and Chemistry of Minerals*, 25: 323–327.
- Van Cappellen, E. (1990). The parameterless correction method in X-ray microanalysis. *Microsc. Microanal. Microstruct.*, 1: 1–22.
- Van Cappellen, E. and Doukhan, J. C. (1994). Quantitative transmission X-ray microanalysis of ionic compounds. *Ultramicroscopy*, 53: 343–349.
- Van Keken, P. E., Bellentine, C. J., and Hauri, E. H. (2003). In Turekian and Holland, editors, *Geochemistry of the Mantle and Core*, volume 2 of *Treatise of Geochemistry*. Elsevier.
- Van Keken, P. E., Hauri, E. H., and Bellentine, C. J. (2002). *Annual Reviews of Earth and Planetary Sciences*, 30: 493–525.

- Van Orman, J. A., Fei, Y., Hauri, E. H., and Wang, J. (2003). Diffusion in MgO at high pressures: Constraints on deformation mechanisms and chemical transport at the core-mantle boundary. *Geophysical Research Letters*, 30: Art.No 1056.
- Vočadlo, L., Wall, A., Parker, S. C., and Price, G. D. (1995). Absolute ionic diffusion in MgO - computer calculations via lattice dynamics. *Physics of the Earth and Planetary Interiors*, 88: 193–210.
- Wagner, C. (1969). The evaluation of data obtained with diffusion couples of binary single-phase and multiphase systems. *Acta Metallurgica*, 17: 99–107.
- Walker, D., Carpenter, M. A., and Hitch, C. M. (1990). Some simplifications to multianvil devices for high pressure experiments. *American Mineralogist*, 75: 1020–1028.
- Walter, M. J., Thibault, Y., Wei, K., and Luth, R. W. (1995). Characterizing experimental pressure and temperature conditions in multianvil apparatus. *Can. J. Phys.*, 73: 273–286.
- Wang, Y. B., Guyot, F., and Liebermann, R. C. (1992). Electron-microscopy of (Mg,Fe)SiO₃ perovskite - evidence for structural phase-transitions and implications for the lower mantle. *Journal of Geophysical Research*, 97(B9): 12327–12347.
- Wang, Z. (1999). The melting of Al-bearing perovskite at the core-mantle boundary. *Physics of the Earth and Planetary Interiors*, 115: 219–228.
- Wei, G. C. T. and Wuensch, B. J. (1973). Composition dependence of ⁶³Ni diffusion in single-crystal NiO-MgO solid solutions. *Journal of the American Ceramic Society*, 56: 562–565.
- Williams, D. B. and Carter, C. B. (1996). *Transmission Electron Microscopy: A Textbook for Material Science*. Plenum Press, New York.
- Williams, Q. (1998). The temperature contrast across D". In Gurnis, M., Wysession, M. E., Knittle, E., and Buffett, B. A., editors, *The Core-Mantle Boundary Region*, volume 28 of *Geodynamics Series*. American Geophysical Union, Washington, D.C.
- Wood, B. J. (2000). Phase transformations and partitioning relations in peridotite under lower mantle conditions. *Earth and Planetary Science Letters*, 174: 341–354.

- Wright, K. and Price, G. D. (1989). Computer-simulations of iron in magnesium-silicate perovskite. *Geophysical Research Letters*, 16(12): 1399–1402.
- Wright, K. and Price, G. D. (1993). Computer-simulation of defects and diffusion in perovskites. *Journal of Geophysical Research-Solid Earth*, 98(B12): 22245–22253.
- Wuensch, B. J. (1983). Diffusion in stoichiometric close-packed oxides. In Bénérière, F. and Catlow, C. R. A., editors, *Mass Transport in Solids*, volume 97 of *NATO ASI Series*, pages 353–370.
- Yamazaki, D. and Irifune, T. (2003). Fe-Mg interdiffusion in magnesiowüstite up to 35 GPa. *Earth and Planetary Science Letters*, 216: 301–311.
- Yamazaki, D., Kato, T., Yurimoto, H., Ohtani, E., and Toriumi, M. (2000). Silicon self-diffusion in MgSiO₃ perovskite at 25 GPa. *Physics of the Earth and Planetary Interiors*, 119: 299–309.
- Young, D. (1991). *Phase Diagrams of the Elements*. University of California Press.
- Yund, R. A. and Tullis, J. (1991). Compositional changes of minerals associated with dynamic recrystallization. *Contributions to Mineralogy and Petrology*, 108: 346–355.
- Zhang, J., Utsumi, W., and Liebermann, R. C. (1996). In situ X-ray observations of the co-site stishovite transition: Reversed phase boundary and kinetics. *Physics and Chemistry of Minerals*, 23: 1–10.

Index

- Boltzmann-Matano analysis, 71
 - fitting functions, 71
- boundary conditions, 68
- convolution effect, 90
- diffusion
 - definition, 22
 - direction dependence, 29
 - mechanism, 23
 - oxygen fugacity dependence, 26
 - pressure effect, 20, 28
 - temperature dependence, 27
 - types of diffusion coefficients, 24, 25
- diffusion couple, 43
- diffusion data
 - literature
 - ferropericlasite, 36
 - olivine, 34
 - silicate perovskite, 38
 - wadsleyite, 35
 - this study
 - ferropericlasite, 121, 132
 - olivine, 85, 104
 - overview all systems, 154
 - perovskite, 148
 - wadsleyite, 109, 119
- electron microprobe, 59, 60
 - measurement conditions, 61
- ferropericlasite
 - structure, 32
- Ficks's laws, 22
- finite difference method, 73
- initial conditions, 67
- Matano interface, 71
- Mg-loss, 66
- MgO-Fe capsule, 52
- multianvil apparatus, 20, 42, 193
- multianvil assembly
 - 10/4, 42, 53, 54
 - 14/8, 42, 53, 54
 - 18/8, 53, 54
- Ni-NiO capsule, 53
- normalization, 67
- olivine
 - structure, 30
- perovskite
 - structure, 32

resolution, 61, 64, 70, 90

ringwoodite

 structure, 32

solution diffusion equation

 composition-dependent, 71

 composition-independent, 68, 88

stability criterion, 76

synthesis, 45, 46, 48

TaMED, 24

TEMQuant, 199, 200

transmission electron microscopy, 59

 conditions of thinning, 63

 measurement conditions, 63

 quantification, 64

wadsleyite

 structure, 32

Danksagung

Hiermit möchte ich mich bei allen bedanken, die mir die Durchführung dieser Arbeit ermöglicht haben.

Besonders danken möchte ich meinen Betreuern Prof. Dr. D. C. Rubie und Prof. Dr. H. Palme, die mich stets engagiert unterstützt haben. Für die Einführung in die experimentelle Hochdruckforschung danke ich Dr. D. J. Frost und für die Einweisung in die Kurzprofilmessung mit dem Transmissionselektronenmikroskop Dr. F. Langenhorst. Hervorheben möchte ich auch die stete Diskussionsbereitschaft und Unterstützung von Prof. Dr. S. Chakraborty.

Desweiteren gilt mein Dank allen Kollegen, die mir bei der Durchführung meiner Experimente, Analysen und sonstigen Arbeiten unschätzbare Hilfe geleistet haben:

G. Gollner, H. Fischer, G. Herrmannsdörfer, D. Krauß, L. Kison-Herzing, K. Klasinski, O. Leitner, S. Linhardt, H. Schulze, P. Ständner, S. Keyssner, F. Heidelberg sowie allen anderen Mitarbeitern des Bayerischen Geoinstituts.

Für viele Anregungen und Diskussionen danke ich auch D. Dobson, R. Dohmen, C. Liebske, S. Mackwell und J. Mecklenburgh.

Ohne die unermüdliche Unterstützung meiner Eltern wäre diese Arbeit in ihrer hier vorliegenden Form nicht möglich gewesen.

Erklärung

Ich versichere, daß ich die von mir vorgelegte Dissertation selbständig angefertigt, die benutzten Quellen und Hilfsmittel vollständig angegeben und die Stellen der Arbeit - einschließlich Tabellen, Karten und Abbildungen -, die anderen Werken im Wortlaut oder dem Sinn nach entnommen sind, in jedem Einzelfall als Entlehnung kenntlich gemacht habe; daß diese Dissertation noch keiner anderen Fakultät oder Universität zur Prüfung vorgelegt hat; daß sie - abgesehen von unten angegebenen Teilpublikationen - noch nicht veröffentlicht worden ist sowie, daß ich eine solche Veröffentlichung vor Abschluß des Promotionsverfahrens nicht vornehmen werde. Die Bestimmungen dieser Promotionsordnung sind mir bekannt. Die von mir vorgelegte Dissertation ist von Prof. Dr. H. Palme und Prof. Dr. D. C. Rubie betreut worden.

Teilpublikationen

C. Holzapfel, D.C. Rubie, S. Mackwell, D.J. Frost, 2003. Effect of pressure on Fe-Mg interdiffusion in $(\text{Fe}_x\text{Mg}_{1-x})\text{O}$, ferropericlase. *Physics of the Earth and Planetary Interiors*, 139: 21-34

Lebenslauf

Christian Holzapfel

*24 September 1971 in Köln

Schulbildung

1978 - 1982	Städtische katholische Grundschule Frankenforst, Bergisch-Gladbach
1982 - 1991	Städtisches Otto-Hahn-Gymnasium Bensberg, Bergisch Gladbach
Juni 1991	Allgemeine Hochschulreife

Zivildienst

Sept. 1991 - Nov. 1992	Zivildienst im Marien-Krankenhaus, Bergisch Gladbach
------------------------	--

Hochschulausbildung

April 1993 - Aug. 1999	Studium am Institut für Mineralogie und Geochemie, Universität zu Köln
Dez. 1995	Vordiplom in Mineralogie
Aug. 1999	Diplom in Mineralogie Diplomarbeit bei Prof. Dr. H. Palme: Bestimmung partieller molarer Volumina von Ga_2O_3 und GeO_2 in Silikatschmelzen durch Dichtemessungen und ihre Anwendung zur Berechnung der Druckabhängigkeit von Metall-Silikat-Verteilungs- Koeffizienten
Jan. 2000 - Mai 2004	Promotionsvorhaben am Institut für Mineralogie und Geochemie, Universität zu Köln, in Zusammenarbeit mit dem Bayerischen Geoinstitut, Universität Bayreuth, Betreuer: Prof. Dr. H. Palme und Prof. Dr. D. C. Rubie
